DEVELOPMENT OF A FIRST-YEAR RIDGE KEEL
LOAD MODEL
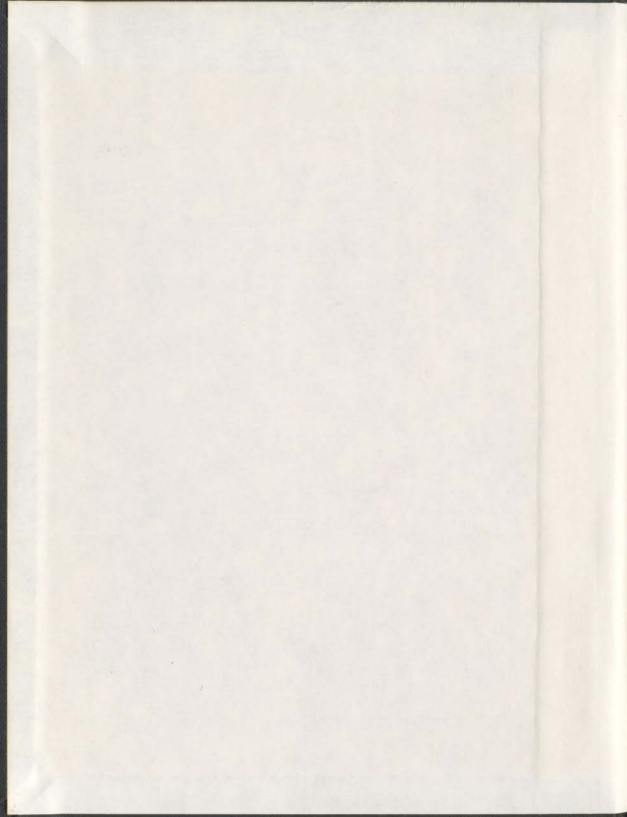
STEPHEN E. BRUNEAU

001311

INFORMATION TO USERS

This manuscript has been reproduced from the microfilm master. UMI films the text directly from the original or copy submitted. Thus, some thesis and dissertation copies are in typewriter face, while others may be from any type of computer printer.

The quality of this reproduction is dependent upon the quality of the copy submitted. Broken or indistinct print, colored or poor quality illustrations and photographs, print bleedthrough, substandard margins, and improper alignment can adversely affect reproduction.

In the unlikely event that the author did not send UMI a complete manuscript and there are missing pages, these will be noted. Also, if unauthorized copyright material had to be removed, a note will indicate the deletion.

Oversize materials (e.g., maps, drawings, charts) are reproduced by sectioning the original, beginning at the upper left-hand corner and continuing from left to right in equal sections with small overlaps.

Photographs included in the original manuscript have been reproduced xerographically in this copy. Higher quality 6" x 9" black and white photographic prints are available for any photographs or illustrations appearing in this copy for an additional charge. Contact UMI directly to order.

UMI®

Your file Votre référence

Our file Notre référence

0-612-47507-7

Canada

DEVELOPMENT OF A FIRST-YEAR RIDGE KEEL LOAD MODEL

By

© Stephen E. Bruneau, B.Eng, M.E.Sc. P.Eng

A THESIS SUBMITTED TO THE SCHOOL OF GRADUATE STUDIES IN
PARTIAL FULFILMENT OF THE REQUIREMENTS FOR THE DEGREE OF
DOCTOR OF PHILOSOPHY

ABSTRACT

This thesis documents the development of a new modelling approach for first-year ridge keel loads. The development involves a detailed review of previous and new ice rubble indentation and shear strength experiments. A systematic regression analysis of compiled laboratory data sets is used to establish a basic approach to keel load modelling, analogous to that for soil retaining problems. Experiments pioneering the modelling of first-year ridge keels with sand are also described. The dry sand tests afforded a high degree of control which led to the development of a new sand force prediction model that was adapted and calibrated for ice keel modelling.

The advantage of the new first-year ridge keel load model is that new effective structure width and keel shape models are utilized, ridge width is factored in and surcharge effects are considered. The model shows excellent agreement with a large body of new experimental data and the best field data available. Also, it is closed-form, has been successfully applied to both vertical and conical structures, and is based on fundamental earth pressure equilibrium mechanics as are other approaches already in the literature. A further advantage is that ice rubble shear strength yield criteria used in the model have been thoroughly examined so that associated parametric uncertainties are quantified and reduced. An *in situ* technique for testing the shear strength of ridge keels is developed and direction for future field work and modelling efforts is given.

ACKNOWLEDGEMENTS

TABLE OF CONTENTS

LIST OF TABLES

LIST OF FIGURES

NOMENCLATURE

A	specified cross-sectional area	K_p	passive earth pressure coefficient
A_c	acceleration	K_o	at rest earth pressure coefficient
A_p	projected area	k	thermal conductivity
A_r	aspect ratio	L	latent heat of fusion
a	keel angle	L_i	ice blocks: thickness (minimum dimension)
B	specified length dimension		
b	limit sail height exponent	L_x	ice blocks: median of maximum dimension
C	limit sail height constant		
C_d	drag coefficient	M	mass
C_m	inertia coefficient	Ma	added mass
c	cohesion	m	rupture distance for cone
c_i	specific heat of ice	m_c	shape factor
D	diameter/width of a structure	n	void ratio
D_b	cone base diameter	P	specified pressure
D_{eff}	effective structure width	P_{en}	penetration distance
D_f	furrow width	q	Dolgopolov *et al.* (1975) shape factor
D_s	neck diameter		
d	vessel depth	R	radial distance
E	modulus of elasticity	R_f	ridge factor
e	porosity	r	forward rupture distance
F	specified force	r^2	regression correlation coefficient
F_c	crushing force	r_a	radius
F_{keel}	keel failure force	S	salinity
F_l	level ice failure force	s	side rupture distance
F_n	normal force	T	temperature
F_r	ridge failure force	T_f	freezing point temperature
F_s	shear force	T_i	ice surface temperature
F_{sail}	sail failure force	t	duration
f	specified function	U_o	far field velocity
f_c	contact factor	u	longitudinal velocity component
g	gravitational constant	V	specified speed or velocity quantity
H	keel depth		
H_f	furrow depth	v	lateral velocity component
H_{kz}	total ridge thickness ($H + H_s$)	W	ridge or keel width
H_p	depth at point of peak load	W_s	sail width
H_s	sail height	w	specified weight
H_{sur}	surcharge height	x	specified quantity
H_t	total height of sand at structure	x_m-x_{sd}	mean, standard dev. of quantity
h	level ice thickness	Z_h	Weaver inertia force
I	indentation coefficient	z	specified vertical position
K_a	active earth pressure coefficient		

Nomenclature continued

α	structure angle from vertical
β	flare angle
β'	apex angle
β''	half-apex angle
γ	specified unit weight
δ	surcharge angle from horizontal
θ	specified angle
λ	Weaver added mass factor
ν	dynamic viscosity
ν_p	Poisson's ratio
ξ	$= 90 - \alpha + \phi_i$
π	3.1415926
ρ	specified density
ρ_i	density of ice
ρ_w	density of water
σ	specified stress
$\sigma_1\sigma_2\sigma_3$	principal stresses: major, intermediate, minor
σ_{fl}	flexural strength
σ_h	horizontal stress
σ_{max}	maximum confinement stress
σ_n	normal stress
σ_v	vertical stress
τ	shear stress or strength as specified
ϕ	internal friction angle
ϕ_i	soil or ice against structure friction
ψ	Keinonen bow flare angle
$\psi2$	Keinonen stem angle
$\psi3$	Keinonen entrance angle
ω	rupture angle

Chapter 1

INTRODUCTION

1.1 Scope of problem

First-year pressure ridges usually form at the boundary of two ice sheets or spontaneously within an ice sheet due to compressive stresses. The crushing and fracturing of the ice sheet produce blocks and brash ice that are ultimately forced beneath the surface forming the *keel* and to a lesser extent are forced upwards to form the *sail* of a ridge (Figure 1.1). In time, the keel becomes interlocked with a refrozen core that forms at the waterline and may exceed parent ice sheet thickness. First-year pressure ridges and ice rubble features will control the design ice loads for offshore structures in those regions where icebergs and multi-year ice are absent.

During a ridge interaction with a structure the clearing of the blocks which form the keel may contribute substantially to the total applied force, yet there are significant uncertainties in the modelling of the process. The problem involves both model and parametric uncertainty and stems from a scarcity of field observations and data, the complex characteristics of submerged ice rubble and the complicated task of reproducing the natural environment in scaled laboratory tests. Though previously identified, this problem came to the fore as a research issue during design work on the Northumberland Strait Crossing Project (NSCP). The bridge project, between Prince Edward Island and New Brunswick involved placing concrete gravity-based piers in a dynamic first-year ice environment. During the project, consensus was not achieved amongst international ice experts on the first-year ridge keel failure loads. This underscored the need for

fundamental research and provided the impetus for this thesis.

The NSCP design experience indicated that efficiencies in new offshore developments can be expected if first-year ridge load models were improved. The commercial significance of this research area continues as interests expand in oil and gas exploration in Canada, including the West Coast of Newfoundland, and abroad, in the Sea of Okhotsk and the Pechora Sea.

1.2 Purpose and methodology

The purpose of this thesis is to improve the modelling of first-year ice ridge loads on structures. This is a complex multi-faceted problem, which has not been fully understood, in spite of many investigations. This thesis provides additional insight based on a systematic organisation and analysis of prior work and new experimental investigations.

The body of this thesis is partitioned into background research, exploratory experimentation and model development phases. The background chapter provides a state-of-the-art basis for new work by interpreting, grouping and examining a broad range of new and old literature sources. The subjects of the background chapter include physical characteristics of ridges, parent ice properties, ice rubble shear strength, field and laboratory investigations of ridge loads, and, first-year ridge load models.

Following the background chapter several unique exploratory experiments are introduced. They include rubble property investigations, small- and large-scale ridge interaction tests

and ice rubble shear experiments. Collectively these programs represent the most significant body of first-year ridge force data known. When this new data are grouped with the literature sources a new opportunity for the development an analytical force model arises.

Chapters 4 through to 7 describe the process in which this opportunity for model development is exploited. The first phase, Chapter 4, is a multi-variable regression study which isolates the fundamental parametric form of equations describing rubble shear strength and ridge interaction forces. Chapter 5 describes a series of experiments which pioneer the use of sand as an analogue for ice rubble. The sand indentation tests afford a high level of control which enables a calibration and adaptation of earth pressure formulas for ridge keel boundary conditions. Reconciling the sand-based models from Chapter 5 with laboratory ice ridge experiments is the subject of Chapter 6. The performance of force prediction models for both vertical and conical structures is judged through sensitivity studies and regression techniques. Chapter 7 considers fluid dynamics, inertia effects and the application of the newly calibrated ice load model to full-scale.

It is the goal of this thesis to provide an approach to force modelling that is mainstream; that is, a model which is heavily supported by the broadest possible range of experimental and field data, and practical for contemporary probabilistic modelling methods. The structure of this thesis permits the attainment of this objective while providing a series of studies which independently document useful reference material and provide impetus for new research thrusts.

Ice floe

First-year ridge sails

Ice floe

Approximately one
square kilometer of 50%
sea ice concentration

First-year pressure ridge idealization

Sail: the above-water ice
rubble accumulation

Refrozen core (consolidated layer)

Keel: the submerged
accumulation of broken
ice rubble

Keel depth may
exceed 20m

Cross-section
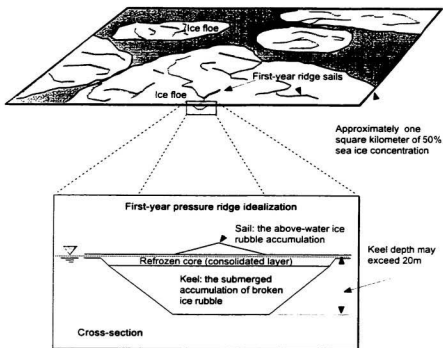
Figure 1.1 First-year pressure ridge schematic.

Chapter 2
BACKGROUND

In the first section of this chapter first-year ridges are defined and the geometry and composition of ridge keels are investigated. The shear strength of ice rubble is reviewed from the open literature in Section 2.2. Forces resulting from ridge interactions with structures are described in Section 2.3 where laboratory and full-scale data are documented. Section 2.4 reviews the evolution of keel load models and looks at the performance of several models in a sensitivity analysis.

2.1 First-year ridge characteristics

2.1.1 Definitions and formation processes

According to the Canadian Code for Offshore Structure Design (CAN/CSA-S471-92) *first-year ice* is defined as "sea ice not more than one winter's growth". A *ridge* is defined as "an approximately linear ice feature of broken ice blocks, created by pressure due to relative motion, that can be categorized as a shear ridge or a compression ridge". A *compression ridge* is formed at the boundary of two ice sheets or spontaneously within an ice sheet as the result of excessive compressive stresses (Figure 2.1). A ridge formed in this way through the dynamic action of current and wind driving forces is often irregular in direction, height and depth. Compression ridges can be quite large with extreme sail heights 10 m or more and keel depths of 40 m or more (CSA-S471-92). Most first year ridges, however, have sail heights less than 6 m (Wright *et al.* 1978) in the Beaufort Sea and less than 2.5 m in the Northumberland Strait (Brown, 1989).

A *shear ridge* is formed by lateral movement between ice sheets and, in contrast to more common compression ridges, is straight and dense with near vertical walls. They do not arise spontaneously from level ice but rather result from the shear action between already separate ice sheets, at the interface between moving and landfast ice, or from compression ridges which have undergone a change in driving force direction. The distinction between shear and compression ridge keels is not made in this thesis.

Ridging occurs in most of the arctic and subarctic seas and estuaries and is also a common occurrence on larger freshwater lakes, for example, Lake Erie. Rubble *pile-up* and *ride-up* occur when floes are driven ashore or grounded leading to significant rubble mounds. Similarly, ice rubble *jams* are formed when passage of floes is obstructed and *bridging* occurs. *Rubble fields* may be formed when a pressure ridge grounds and sustained driving forces cause continued floe ice failure leading to the significant broadening of the rubble formation. This thesis is concerned with floating first-year ridges which in some circumstances may be laterally extensive making them indistinguishable from floating rubble fields.

The process of compression ridge formation is not well documented though it is thought to be fairly rapid - a matter of hours and minutes to form. It involves the crushing and fracture of the ice sheet into blocks and brash that are ultimately forced beneath the surface forming the keel and to a lesser extent are forced upwards to form the sail, thus maintaining hydrostatic equilibrium. The multi-failure mode process of formation may grade rubble and contrasts to other rubble formation mechanisms. At the Kemi-1 lighthouse in the Gulf of Bothnia level ice interacting with the lighthouse structure penetrated a stationary rubble pile and failed directly against the conical shield. The

rubble formed in this way was regular in shape and almost uniform in size (Hoikkanen, 1985). The thrusting and mixing action during ridge formation may be expected to sort blocks somewhat, with slush at the waterline and large blocks on the bottom of the keel and the top of sail. The same action may also rupture freeze-bonds between newly submerged cold blocks or cause rubble *clumps* to form.

In time, through heat transfer, pressure bonding, sintering and/or other processes, compression ridges may become partially *consolidated*, the term used to describe the freezing of pore water and the bonding of juxtaposed blocks. An irregular solid ice layer (referred to as a refrozen or consolidated core) which forms at the waterline within a ridge separates the keel from the sail and may exceed the parent ice layer thickness by two or three times (Eranti *et al.* 1992). This three-part ridge approximation is shown in Figure 2.1. Variations of this ridge representation are common in the literature. Eranti *et al.* (1992) prefer to separate the keel into two regions; an upper one comprised of heavily compacted and consolidated blocks, and a lower one comprised of loose and partially adfrozen blocks. Gladwell (1976) and others describe significant slush layers below the core, and Lepparanta *et al.* (1995) document a distinct mid-keel low porosity region. Most field studies indicate that ridge structure is likely to vary spatially and temporally. Keel form is probably influenced by formation temperature and speed, parent ice salinity and thickness, ridge depth, sail size, the elapsed air and current exposure, and local snow regime. Ridges which survive the first melt season as second-year and multi-year ice features consolidate further, reducing porosity and increasing strength to become formidable obstacles to any structure. Second-year and multi-year ridges occur mostly in arctic regions and are not considered in this thesis.

2.1.2 Parent ice properties

Detailed information on the physics of ice is found in Pounder (1965), Hobbs (1974) and Michel (1978). Cammaert and Muggeridge (1988) and Sanderson (1988) document investigations of ice properties and ice interactions with offshore structures. A review of the mechanical properties and formation processes of sea ice, the constituent material of ridges, was carried out as part of the work for this thesis and published in Bruneau (1995a). Sea ice formation processes, morphologic and strain rate characteristics and strength and friction properties were documented in that study. Table 2.1 summarizes some of these first-year ridge parent ice properties for reference later in the text.

2.1.3 First-year ridge geometry

Several researchers (Weeks and Kovacs, 1970, Wright and McGonigal, 1982, Kankaanpaa, 1989) have documented the geometry of first-year ridges in detail. Others (Acres 1987, Cammaert *et al.*, 1993, Croasdale *et al.*, 1995, Burden and Timco, 1995) have sought to classify ridge geometries for interpretive or design purposes. A summary of first-year ridge characteristics from the literature is presented in Table 2.2, and significant keel parameters are reviewed below.

Keel size and shape

Dolgopolov *et al.* (1975) describe the geometry of first-year ridges in temperate regions around Russia. They observed that the design ratio of ridge draft to depth may be taken as 1/4 to 1/5 and that an individual ridge may have a trapezoidal cross-section. Kankaanpaa (1989) in a survey of 8 ridges in the Baltic Sea found the sail height to keel depth ratio was 1/5.8 on average though it ranged from 1/3.8 to 1/8.6 and local isostatic imbalance was common. In another Baltic study this ratio ranged from 1/4 to 1/8 (Veitch

et al., 1991a). Burden and Timco (1995) produced a catalogue of sea ice ridge morphology in which one hundred and seventy-six multi-year and first-year ridge profiles from the literature are documented. The keel depth to sail height ratio for first-year ridges in temperate regions was found to be 3.96, almost identical to that of keel width to depth, 3.94. Considerable scatter was observed in the data and it was noted that the power law fit, $W = 5.76H^{0.86}$ (where H is keel depth and W is keel width) may be more appropriate than the linear model. Note that the keel depth, H, is usually measured from the waterline. When considering ridge force models, keel depth is typically reduced by the thickness of the submerged portion of the refrozen core (Cammaert *et al.* 1993).

Kankaanpaa (1989) found average slope angles of the sail to be 21° and keel slopes to be around 32°. Cammaert and Muggeridge (1988) report that a typical first year ridge keel has a mean keel angle of 32°. This implies that a keel width to depth ratio of 3.2 can be expected for triangular-sectioned ridge keels. Lepparanta and Hakala (1992) note that in the six ridges they studied they found the largest maintained a well developed triangular cross section (depth of 14 m) whereas the medium-sized (depth approximately 5 m) were more trapezoidal. Smaller ridges lost the appearance of being identified as a ridge as the keel was more closely described by an irregular rubble field. Lepparanta *et al.* (1995) suggest that ridge keels may start out triangular in shape but evolve towards a trapezoidal form. The *keel angle* defined by Burden and Timco as "the angle of decline for each side of the keel in degrees" for 35 temperate region ridges had a mean of 27.6° and a standard deviation of 13.9°, suggesting considerable variation.

Apparently, the limiting vertical size of ridge sail height (H_s) depends upon the thickness of the parent ice sheet, h. The relation to keel width and depth is thus implied from

ratios given above and in Table 2.2. Lepparanta and Hakala (1992) present the formula as

$$H_z = Ch^b \qquad (1)$$

where C and b are constants. Parmerter and Coon (1972), Lepparanta (1981), Tucker *et al.* (1984) and Timco and Sayed (1986) obtained different values for b, typically between 0.5 and 1. Kankaanpaa (1989) determined that the best positive correlation occurred when $C = 2.2$ and $b = 0.5$. Many statistical aspects of arctic ridge height, depth and spacing are considered by Hibler *et al.* (1972). They found remarkably good characterization of ridging using just the ridge height and ridge spacing within a floe, and also found a linear relationship between those parameters.

Keel porosity

The porosity of ridge sails and keels has been studied by several researchers (Kovacs and Mellor, 1974, Keinonen, 1977, Tucker *et al.*, 1984, Kankaanpaa, 1989, and Lepparanta and Hakala, 1992). Some results are listed in Table 2.2. Keel porosity is usually determined by mapping the resistance felt while drilling a vertical hole through a keel. In Baltic research it is common to categorize resistance into regions of slush, solid ice, no ice and loose blocks. Other sources from elsewhere cite void ratio only. Careful excavation and block measurement in the sail (Veitch *et al.*, 1991b) have also provided insight into ridge porosity by an assumed equivalence or through buoyancy equilibrium calculations. Since interpretive techniques vary and significant spatial and temporal variability is expected, porosity measurements in most respects are approximate.

Field drilling results in the Baltic indicate that the average porosity for a whole ridge is

29% but varies with a standard deviation of around 4-6%. Keel porosity is typically larger than sail porosity (8% more according to Kankaanpaa, 1989). According to Lepparanta and Hakala (1992) there is little explanation for this but that block size distributions may vary - this is as yet unproven. Eranti et al. (1992) describe a layering in the ridge keel but this is more a boundary between a region of heavily and loosely packed blocks at around 1/3 of the ridge depth. Lepparanta et al. (1995) describe porosity layering (minimum at mid-keel range) and evolution though results are based on a single ridge. Note that the maximum packing density of uniform spheres gives a porosity of 25%, which is quite close to the rubble values.

Ice block size, shape and placement

Weeks and Kovacs (1970) investigated first-year ridge keels near Barrow Alaska. Results from one ridge indicated that the keel was comprised of two different parent ice thicknesses: 15 to 20 cm and 50 to 60 cm. The coring of the keel showed a heterogeneous layering of sea ice and snow and slush ice that was poorly bonded. Larger blocks on the outer edge of the keel were rounded indicating appreciable melting. Other ridges had parent ice thicknesses of the order of 15 to 20 cm.

The piece size distribution of ice blocks in the sails of Baltic sea ridges has been investigated by Veitch et al. (1991a, 1991b). In two separate studies it was found that the sample distribution for both long and short ice block axis was near lognormal, and was thus represented by

$$f(x) = \frac{1}{x\sqrt{2\pi}\ln x_{sd}}\exp\left[-\frac{1}{2}\left(\frac{\ln x - \ln x_m}{\ln x_{sd}}\right)^2\right], \quad 0 \leq x < \infty \qquad (2)$$

where x_m is the geometric mean and x_{sd} the geometric standard deviation of the distributed quantity x. In one study of two ridges in the same vicinity Veitch *et al.* (1991a) determined that the mean block long axis lengths were 55 cm and 49 cm and the mean short axis lengths were 36 cm and 34 cm respectively for the two ridges. The long axis standard deviations were 2.2 and 1.7 cm. The long-to-short axis ratio for the two were 1.52 and 1.49 with a mean thickness recorded at 0.18 m and 0.19 m respectively. Over one hundred ice blocks were measured in that study. In another ridge study located elsewhere in the Baltic, Veitch (1991b) found that the mean thickness, long axis and short axis dimensions for two different locations in a ridge sail were 16 cm, 71.2 cm and 69 cm, and 15 cm, 54 cm and 50 cm respectively. Distribution lognormality was again established.

Lepparanta and Hakala (1992) studied 6 ridges in the Baltic and found the average thickness of ice blocks to be around 10-30 cm and the average length to be 60-90 cm. They determined that the block size distribution was quite narrow, the maximum lengths being less than twice the average length. The ice blocks in the keel were characterized as platy, well-rounded and often very porous. The blocks also appeared to be randomly arranged and the existence of the occasional very large block (some ten times bigger than the average in length) situated in the middle or near the bottom of the keel, was noted.

2.1.4 Temporal ridge keel processes

Evidence that ridges undergo considerable changes through a season is provided by the research of Peschansky (1963), Weeks and Kovacs (1970) Lepparanta *et al.* (1995) and others. Mechanical and thermodynamic processes result in erosion, re-packing, creep, melting, freezing, brine ejection and recrystallization. How these and other processes

interact is not known but by the following description the changes are significant (from Lepparanta *et al.* (1995) describing the life-cycle of a Baltic first-year ridge):

"The ridge structure underwent considerable evolution. The external geometry became smoother. The keel depth and sail height decreased and the cross-section developed from triangular toward trapezoidal form. The volume of the ridge showed no significant changes in the mid-winter but decreased by 25% during one spring month. The porosity of the ridge decreased from 28 to 18%; it varied vertically through the keel and showed a persistent minimum of 20 to 23% in the mid-keel region. The decrease was in midwinter and was due to further consolidation and packing of ice blocks while in spring packing compensated the porosity increase by melting for the mid-range data. During the melting season, below the consolidated layer the melting of the ice blocks was found to be uniform and the same as the overall ice volume decrease; mechanical erosion of the keel was insignificant."

Practically no information is available on ice block erosion and other mechanical "aging" processes. Since this is not the intended focus of research for this thesis the topics are not discussed further, however, they may be important and should be considered in future research efforts. Keel consolidation, block bonding and creep are reviewed below to provide some background for a discussion later on rubble shear strength.

Refrozen core formation

Depending on the air temperature when compression ridges form, the parent ice may often be a few degrees cooler than freezing (according to the air temperature). The

negative sensible heat of ice blocks in the keel must then be considered for both the potential contribution to the growth of the refrozen layer and in the freeze-bonding of ice blocks. Lepparanta and Hakala (1992) illustrate this capacity in the following example. Consider a rubble layer of thickness, H, porosity e and temperature T. This layer may produce in water a surface ice layer of thickness h which is obtained from

$$\rho_i L h' = \rho_i c_i (T_f - T)(1-e)H \qquad (3)$$

where c_i is the specific heat of ice, L is the latent heat of fusion and T_f is the freezing point temperature. If $T_f - T = 5^\circ$ and $H = 5$ m, then $h' = 10$ cm. Further, the decrease in porosity that may be expected as a result of the cold content of the blocks being used up in freeze bonding alone would be 3% if the ice block temperature were 5 degrees below freezing upon formation.

The long-term growth of a refrozen core in a ridge is predominantly attributed to heat conduction to the cold atmosphere. Stefan's model for level ice growth is often used to predict this growth. It is commonly represented as

$$h'^2 = \frac{2k}{\rho_i L} \int_{t_s}^{t_f} (T_f - T_i) dt \qquad (4)$$

where T_f and T_i are the freezing temperature and ice surface temperature respectively. and the constants k, L and ρ_i are the mean thermal conductivity, latent heat, and density of ice. The time t_o is the time at which the ice begins to form. In a ridge or rubble field only the water in the voids of the rubble must be frozen for the increase of vertical core ice thickness. Given that the square of the ice thickness is inversely proportional to ice density and latent heat (typically around 333 J/g) and directly proportional to thermal conductivity (approximately 2 W/m °C) it is evident that the square of the thickness

should also be inversely proportional to the rubble porosity. This hypothesis was tested by Veitch *et al.* (1991c) in a laboratory experiment in which ridges were produced under controlled conditions and the degree of ice growth was measured. It was determined that core ice grew at a rate of 1.8 that of level ice when rubble porosity, e, averaged 39.5%. The predicted growth based on the $e^{1/2}$ ratio suggests a ratio of 1.6, a reasonable agreement given that the conditions under which these tests were conducted were somewhat ideal (little temperature variation, and with natural insulation from snow and ice not modelled).

Croasdale, Allyn and Marcellus (1990) devised a comprehensive computer model for predicting the refreezing of ice rubble. Their model considers air temperature, wind speed, radiation, ice temperature, rubble porosity, rubble height, snow cover, salinities and other significant parameters. Their results indicated that the parameter which has the biggest degree of uncertainty and which is most important, is the initial porosity of the ice rubble. It is suggested that this parameter could vary with the initial effective stress state in the rubble due to sintering and creep consolidation, emphasizing the need for a better understanding of the state of ice rubble when it first forms and prior to refreezing.

In the design load calculation for the NSCP bridge (Cammaert *et al.* 1993) a model was developed from work by Nakawo and Sinha that considered the measured temperature regimes, ice thickness and snow deposition regimes in, and around, the Northumberland Strait. It was assumed that the region of the keel that undergoes consolidation had a porosity of 30% but that the pores were completely filled with brash ice and snow with a porosity of 50%, thereby reducing the porosity for freezing purposes to 15%. This assumption was precautionary and is expected to produce an upper bound for refrozen

ice layer growth.

It is generally accepted that the refrozen core thickness varies considerably over short distances. This variation is in part the result of randomly oriented blocks being partially incorporated into the core layer but is also due to non-uniform insulation above. Near the highest part of the sail (which often acts as a snow fence) the consolidated ice thickness is generally thinner than in most other areas above the keel. This would lead to the weakening of the level ice in this area which may influence ridge failure mechanisms. Most modelling strategies assume the core is a uniform thickened plate.

Keel block bonding

Some examinations of keel ice rubble *in situ* have been reported in the literature (Pilkington *et al.*, 1982, Shinde and Kemp, 1983, Brown, 1989, Lepparanta and Hakala, 1992, Eranti *et al.*, 1992 and others). Most describe rubble in the keel as highly variable in texture and geometry. Blocks may vary from porous and highly deteriorated to apparently solid plates (Weeks and Kovacs, 1970). Observations are typically limited though by lack of access to the outer surface of keels. Inter-block contacts are usually coherent ice bridges but are often weak enough that blocks may be dislodged by hand. In the Beaufort, Shinde and Kemp (1983) reported contact lengths less than 10% of block length in mature first-year ridges in April. The ice blocks were very easy to dislodge indicating that "the cohesive strength of the contact was less than 35 kPa (judged by comparison with observations with cohesive clays)". The crystallographic examination indicated that the frozen junction between blocks was comprised of relatively course granular congealed frazil ice. Ice blocks in the keel ranged from 0.3 to 1.8 m thick with lengths from 0.6 to 3.0 m and widths typically around one-half the length.

Inter-block freeze-bonding below the consolidated core may arise as a result of several processes. As mentioned previously the negative sensible heat in the blocks at the time of ridge formation may be converted to latent heat at block surfaces by (or during) fusion. Bonding by heat conduction may reach below the consolidated core through partially incorporated blocks or highly saline pore fluid. However, temperatures throughout the keel are usually at, or very near, the block melting point (Lepparanta *et al.*, 1995, Weeks and Kovacs, 1970, and others) so that this mechanism is probably not predominant. It is more likely that bonds result from *pressure consolidation, sintering* and other recrystallization processes which are briefly described below.

The freeze bonding that occurs between two ice pieces brought together was first described by Faraday in 1859. In the paper "On Regelations and the Conservation of Force" Faraday demonstrated that if two ice blocks are placed in contact they will form a solid bond even when the temperature of the ice and surroundings is such as to keep them in a thawing state. To explain this Faraday postulated the existence of a liquid-like layer on the ice surface which, when enclosed by ice at the point of contact, freezes. Disputing this, Thompson in 1857 argued that the minute areas over which the asperities on the ice surfaces contact one another were sufficiently small to create contact pressures which lower the equilibrium melting point. The melting which results then relieves the pressure which in turn causes the water to re-freeze and bond the pieces together (pressure consolidation). It is currently believed that the driving mechanism for bond growth between two ice pieces is an unstable thermodynamic system in that the surface free energy is not minimized. The energy of the system can be reduced if material is transferred to the region of contact thereby causing the bridge to develop (sintering). Although this theory is broadly accepted today, the mechanism by which the initial neck

forms between the two ice particles still remains uncertain.

Schaefer and Ettema (1986) carried out experiments investigating pressure consolidation/sintering between two flat surfaces of uniform freshwater ice blocks. Apparently, much stronger (greater than four times) freeze bonds develop between fresh ice blocks when immersed in fresh water than when in air, unless the water is a saline solution. In a saline solution (salts greater than 12.5% by weight) bonding is weaker than that in air. The strength of the freeze-bond between blocks in fresh water increased linearly with increased normal pressure and duration of contact. However, in saline solutions (salts 3% or greater) the increase with normal pressure is much weaker and no bond strength increase was observed for increased contact durations. Schaefer and Ettema concluded:

- Stronger freeze bonds form in water than in air (submerged rubble will have a pronounced cohesive character, and associated with this is a pronounced effect of loading rate in which strength decreases with increased rate).

- Cohesion in a floating rubble ice layer probably increases with increasing depth due to higher normal pressures.

- Contributing to the scatter of data from rubble shear strength tests in the literature is the time between experiments since stronger freeze bonds form with increased duration.

Bulk pressures in ridge keels are usually determined by the product of rubble buoyant

weight and position above the keel bottom, z, as follows:

$$\sigma_v = (\rho_w - \rho_i)(1-e)gz \qquad (5)$$

where ρ_w and ρ_i are the densities of the water and ice, σ_v is the bulk vertical stress in the rubble, e is the bulk porosity of the rubble, and g is the gravitational acceleration. Initially first-year ice blocks may have densities ranging from 860 to 920 kg/m^3 (σ_v changes by a factor of two in this range). In time, though, all submerged rubble probably has a density greater than pure ice (917 kg/m^3) since evacuated brine channels are likely to fill with water (anomalously, the "heaviest" blocks may become the "lightest"). For example, maximum bulk pressures for a 20 m deep keel of porosity 30%, and block density of 900 kg/m^3 in sea water of density 1028 kg/m^3 are around 17.6 kPa. Pressures between blocks are, of course, much higher. If contacts were 10% of block length as described by Shinde and Kemp (1983), then notionally contact areas may be 1% of total so that pressures would be 1.76 MPa. This pressure exceeds the crushing strength of warm unconfined sea ice and so contact areas would grow. This example is probably overly-simplistic, but it serves to illustrate the stress level which may lead to pressure bonding.

Pressure consolidation and sintering may be important bonding mechanisms but other complicated processes may also be at work. Circulation is likely to be important for redistribution of brine and or frazil ice. Lewis and Perkin (1986) describe the phenomenon of an *ice pump* which is a naturally occurring heat engine driven by the change of freezing point with pressure. It causes ice to melt at lower depths in sea water and to form at a shallower location - and is a self-starting mechanism. The pumping is not dependent upon the availability of sensible heat in the water column and its effects

are added to any melting caused by the advection of warmer water to the ice-water interface. It is conjectured that, due to the significant ice surface area in an ice rubble keel, level ice growth and keel deterioration may be enhanced appreciably via the *ice pump* mechanism.

Creep

Though ice deforms in several ways under pressure (as described in Table 2.1) irreversible secondary creep (viscous) strain is the most likely mechanism for causing noticeable global deformations in ridge keels. Blocks juxtaposed and under high contact pressure will deflect and contact areas will grow as ice "flows" in accordance with grain size, grain orientation, stress patterns and salinity. Sea ice containing brine flows more easily than pure ice since brine cannot support shear stress. Pockets of brine also cause stress concentrations which further enhance creep rate. Though bulk rubble has a relatively low buoyant weight it was shown earlier that stresses between blocks in a keel can be high. Edge-on contacts between blocks may have contact areas defined by the compressive strength of the ice. Furthermore, the action of leverage from eccentrically applied buoyancy forces on blocks may promote near-failure stresses within blocks or at inter-block bonds. At 1 MPa the uniaxial strain rate for horizontal compression may be between 10^{-6} s^{-1} and 10^{-4} s^{-1} (Sanderson 1988) suggesting the potential for large deformations during the typical life expectancy of a ridge (around 100 days or $10^{6.94}$ s).

Table 2.1 Typical first-year ridge parent ice characteristics.

Ice type	Vertical Columnar S2 resulting from preferential growth perpendicular to 'c' axis.
Ice salinity	5-12 ppt brine in ice when sea ice comprised of 35 ppt dissolved salts.
Freezing point	-1.91 C at 35 ppt ; -1.1 C at 20 ppt ; -0.3 C at 5 ppt
Ice density	860-920 kg/m^3 first-year ice ; 916.8 kg/m^3 fresh water ice
Sea water density	1028 for S = 35 ppt, T = -1.8C, 1016 for S = 20 ppt, T = -1.1 C
Ice friction	Dynamic ice-ice = 0.016-0.13 for -19 C to -5 C and from 0.06 to 0.83 m/s.
	Static sea ice-steel = 0.3-0.7 ; kinetic sea ice-steel = 0.025-0.25
	Sea ice-aluminum: static increases 4 orders from -1 C to -25 C.
	Sea ice-aluminum: dynamic decreases 1 order when speed rises 0.3 to 5 m/s.
Ice friction causes	Adhesion at contact asperities where weld-bonds form from high pressure.
	Liquid layer from loose surface molecules, pressure melting or surface friction may lubricate. Water vapour and surfaces gases also decrease friction.
Ice frictrion notes	Sea ice has higher friction coefficient than pure ice. At high normal loads friction coefficients decrease with increased pressure, esp. near freezing point.
Latent heat of fusion	264 J/g for ice salinity 8 ppt, temp = -2 C
	334 J/g for ice salinity 0 ppt, temp = 0 C
Thermal conductivity	2.13 W/(m C) for ice salinity 4.7 ppt, temp = -5 C
	2.22 W/(m C) for ice salinity 0 ppt, temp = 0 C
Specific heat	7.97 J/(g C) for ice salinity 10 ppt, temp -5.6 C
	3.25 J/(g C) for ice salinity 2 ppt, temp -5.6 C
Elastic modulus	Sea ice modulus varies with temperature and air plus brine volume.
	Dynamic values typically range between 3.5-9.4 GPa.
Morphology	Visco-elastic crstaline near melting point as when submerged.
Strain types (figure below)	Ductile, transitional, brittle.
Strain factors	Load rate, load concentration, load history, temperature,ice purity, porosity.
Ductile strain	For tension and compression: strain is immediate elastic then transient, delayed elastic, followed by time-dependant, non-linear viscous creep.
Brittle strain	Vacancy diffusion and dislocation velocities are too slow for ductility.
Ice strength - brittle	Governed by grain size, and brine volume. It is not as rate sensitive as ductile.
Compressive strength	Usually determined by uniaxial compression tests.
	May vary inversely with log of contact area.
	Typical measurements in lab between 1 and 10 MPa, for larger scale < 1 MPa.
	Confinement suppresses crack propogation and enhances creep.
Tensile strength	Determined with direct tension tests.
	Influenced by salinity and temperature.
	Same order but slightly less than pressure strength values for compression.
Shear strength	Shown to vary with brine volume - wide range reported in literature.
	0.5 MPa approximate average.
Flexural strength	Function of brine volume (salinity and temperature dependent).
	Usually lies between 0.1 and 1.0 MPa.
References:	**Sanderson (1988), Hobbs (1971), Pounder, (1968),**
	Cammaert and Muggeridge (1988), Molgard and Jordan (1994)

Rheologic model of solid ice ductile strain
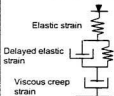
Strain history for constant stress

Elastic strain

Delayed elastic strain

Viscous creep strain

Brittle fracture
HIGH STRESS
LOW STRESS
Tertiary creep
Delayed elastic strain
Viscous strain
Elastic strain
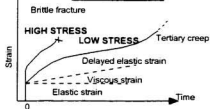
Table 2.2 First-year ridge characteristics reported in the literature.

Property	Symbol	Description	References
Keel width	W	3.94H or 5.76 H^0.86	Burden and Timco (1995)
		3.2H	Cammaert & Muggeridge (1988)
		4.4H	Lepparanta and Hakala (1992)
Keel depth	H	4Hs - 5Hs	Dolgopolov et al. (1975)
		3.96Hs	Burden and Timco (1995)
		5.8Hs	Kankaanpaa (1989)
		14h - Beaufort, 25h - Bering	Vaudrey (1983)
		7Hs-12Hs	Palosuo (1975)
		3Hs-9Hs, 4.5Hs (av)	Kovacs (1972)
		H distribution is exponential	Weeks and Kovacs (1970)
Keel porosity	e	mean 29% and std. dev. 5%	Kankaanpaa (1989)
		29%	Lepparanta and Hakala (1992)
		13% + 0.72x(Sail porosity)	Burden and Timco (1995)
Keel angle	a	32 deg	Kankaanpaa (1989)
		32 deg	Cammaert & Muggeridge (1988)
		mean = 27.6 deg, std.dev. = 13.9 deg	Burden and Timco (1995)
		32 deg	Weeks and Kovacs (1970)
		15-60 deg, 39 deg (av)	Palosuo (1975)
Keel Shape		Trapezoidal	Dolgopolov et al. (1975)
		Triangular for large ridges	Lepparanta and Hakala (1992)
		Trapezoidal for small ridges	Lepparanta and Hakala (1992)
Sail width	Ws	Wsh = 17.1/(h^0.5)	Tucker and Govoni (1981)
Sail height	Hs	2.2 h^0.5	Kankaanpaa (1989)
		H/3.96	Burden and Timco (1995)
		H/5.8	Kankaanpaa (1989)
		3.69 h^0.5	Tucker and Govoni (1981)
		Spatially highly variable	Tucker and Govoni (1981)
Sail porosity		19%	Lepparanta and Hakala (1992)
		21%	Kankaanpaa (1989)
		25 - 33%	Veitch et al. (1991b)
		30%	Gladwell (1975)
		36 - 43 %	Keinonen (1977)
Sail slope angle		21 deg	Kankaanpaa (1989)
		10-50 deg, 30 deg (av)	Palosuo (1975)
		25 deg	Weeks and Kovacs (1970)
		25 deg	Wright et al. (1978)
		10-55 deg, mean = 24 deg	Kovacs (1972)
		8.8-51.3 deg, mean = 26.1 deg	Tucker and Govoni (1981)
		mean = 20.4, std.dev. = 11 deg	Burden and Timco (1995)
Keel brine salinity	S	40 - 120 ppt	Weeks and Kovacs (1970)
Keel block Temp.		-0.2 C throughkut keel (freezing point)	Lepparanta et al. (1995)
Keel block flex. st.		0.2-0.4 MPa	Weeks and Kovacs (1970)
Ice block length	Li	0.6-0.9 m	Lepparanta and Hakala (1992)
		1.5 x width, 2.8 x thickness	Veitch et al. (1991b)
Ice block thickness	h	0.1-0.3 m	Lepparanta and Hakala (1992)
		0.15-0.19 m	Veitch et al. (1991b)
		0.15-0.2 and 0.5-0.6 m	Weeks and Kovacs (1970)
Ice block area		0.67 e^(1.86h) or 4.48 h^2	Tucker and Govoni (1981)
Ice block size distn.		Tight, maximum length < 2 times average	Lepparanta and Hakala (1992)
		Log-normal	Veitch et al. (1991b)
		Bi-modal	Weeks and Kovacs (1970)
		Multi-modal	Tucker and Govoni (1981)
Ice block shape		Platy, rounded and porous	Lepparanta and Hakala (1992)
		Deternorated, rounded	Weeks and Kovacs (1970)
Ice block placement		Random, large blocks at bottom	Lepparanta and Hakala (1992)
Ridge spacing		Distribution is exponential	Weeks and Kovacs (1970)

Pressure ridge formation schematic

Compression in
parent ice

Compression
ridge

Cross-section schematic

h

Level Ice

Sail

Hs

Refrozen core

a

Keel

H

W
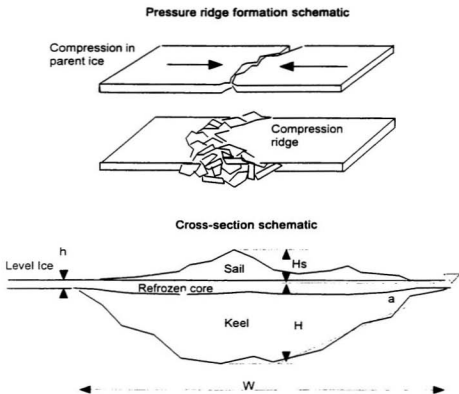
Figure 2.1 Schematic of first-year ridge formation and cross-section.

2.2 Ice rubble strength

2.2.1 Keel failure modes

It is commonly assumed that ridge keels interacting with structures fail in shear. Simple tension, compression or other failure modes may be expected when support boundary conditions are conducive to global flexural or crushing failure. This more likely when keels are a relatively small factor in the total ridge resistance or when ridges are small or poorly supported. Experience from the NSCP has shown that the most resistant ridges are either core or keel-dominated. Ultimately "design" ridges for the NSCP were characterized by very large keels and quite modest cores. Very little information is presently in the open literature regarding first-year ridge failure modes not to mention what is happening in the keel. Based on the NSCP design strategy and broad support in the literature (Dolgopolov *et al.* 1975, Keinonen 1979, Croasdale 1980 and others) it is assumed that "design" keels and thus the keels to be studied in this thesis, fail in shear. This assertion may be subject to scrutiny in the near future as the NSCP bridge approaches completion and monitoring of ice interactions begins.

2.2.2 Rubble shear mechanics

Although ice rubble has been shown to be a multi-phase, highly complex material, it accumulates predictably in specific configurations (keels for instance). Since it is practically incoherent during formation frictional resistance must be active. In time, blocks bond which makes rubble coherent also so that both frictional and cohesive qualities coexist (Prodanovic, 1979).

Friction is the tangential force required to move one surface past another and is defined for static and kinetic conditions. For a granular material *internal* friction results from the slip movement between the surfaces of "blocks" of fixed particles (Bridgwater, 1987). For soils these regions, termed *failure zones*, are typically about ten particle diameters in width and are actually made up of substantial particle rolling, sliding and in some cases attrition (both fragmentation and abrasion). Typically, internal friction is primarily influenced by density and grain packing and to a lesser extent dependent upon a sliding friction component. The reason is that considerable *interlock* occurs between grains so that for sliding and rolling to occur grains must be lifted over one another or else fail in flexure, shearing or crushing. Sliding friction is mostly a material property which varies with surface roughness, pressure, speed and the presence of interstitial water, gases and chemicals, but interlock and thus internal friction, varies with gradation and densification. When sheared, granular materials often undergo volumetric change (dilation) due to the effects of interlock and grain packing (Figure 2.2).

Cohesion is the finite shear strength a granular material possesses when it is not subjected to confining stresses. In ice rubble this property is believed to arise from freeze-bonding between blocks. Freeze-bonding has been shown to be a function of contact pressure, contact period, temperature, salinity, size and shape of the ice blocks, and other factors.

Shear resistance in granular materials is influenced by the presence of fluid in pores. Surface tension acts only when air and water are present together and is not expected to play a role in rubble shear mechanics. On the other hand fluid dynamics may be important. For instance, increased pore pressures have been shown to enhance and reduce shear resistance in soils. At high speeds a submerged dilatant soil may have

appreciably higher shear resistance in accordance with reduced pore pressures (resulting from volume expansion and lower permeability). When bulk compression takes place, pore pressures may be enhanced which causes effective stresses between particles to be relieved, diminishing shear resistance. For ice rubble in keels, open channels between blocks are large so permeability is very high and pore pressure is not expected to vary much. However, with increased particle scale, the drag and inertia of blocks and suction between adjacent ice plates may become significant. A simple calculation reveals that an average sized ice block (0.6 x 0.45 x 0.15 m) ascending perpendicular to its principal axis in water has a terminal velocity of 0.5 m/s (free fall in air would be 45 m/s). Fluid flow around a structure or through a keel during failure can exceed this *critical* velocity causing suspension. The degree of suspension will depend on the state of coherent bonds between blocks. More will be said on this topic later in the thesis.

2.2.3 Yield criteria

At low loads or loading rates and before shear failure, rubble may behave visco-elastically, like a highly porous solid ice. When sheared appreciably, though, unconsolidated ice rubble deforms plastically since the change in shape is irreversible. At failure, behaviour has been shown to be neither *perfectly* plastic (Tresca-Saint Venant condition) nor elastoplastic (as per Prandtl material). The two limiting states or plastic failure theories most relevant to the study of soil mechanics are Von Mises and Mohr-Coulomb. The Mohr-Coulomb model is the most commonly used limit states model in soil and ice rubble mechanics. It was first proposed as a hypothesis of the shear strength for soil by Coulomb (ca 1773) as

$$\tau = c + \sigma_n \tan\phi \qquad (6)$$

where τ is the shear resistance resulting from the slip movement between two "surfaces" within a soil, c is the cohesion of the soil, σ_n is the normal stress on the slip surface and ϕ is the angle of internal friction. Mohr later presented a similar generalized theory and so the limiting state plasticity model became known as Mohr-Coulomb.

The widespread acceptance of the Mohr-Coulomb model has apparently resulted from observations in laboratory tests for ice rubble (Keinonen and Nyman 1978, Prodanovic 1979, Hellmann 1985, and others) that show linearly increasing yield strengths with increased confining pressure (Figure 2.3). Most experiments have also indicated a non-zero cohesive intercept when shear strength data is plotted against a normal stress. Some researchers argue that the Mohr-Coulomb failure criterion may not be appropriate for modelling ice rubble because the internal friction angle and apparent cohesion are a function of normal stress (Ettema and Urroz, 1989). Many researchers would agree that stress history influences the rubble strength and that failure criterion are considerably influenced by many other environmental conditions. Never-the-less the Mohr-Coulomb approximation prevails as it is a simple and effective interpretive tool for laboratory testing and allows the easy adaptation of (Mohr-Coulomb based) soil failure mechanics to keel load models.

In situ materials often have shear stresses on the octahedral plane since all three principal stresses are most often not equal ($\sigma_1 \neq \sigma_2 \neq \sigma_3$). The intermediate stress, σ_2, is commonly ignored, however, or assumed equal to σ_3. The resulting two-dimensional stress state greatly simplifies computation efforts without too much error in most cases (Bowles, 1984).

Considering the two-dimensional case further the equations for normal stress, σ_n, and shear stress, τ, on an arbitrarily inclined plane passing through a rubble body are:

$$\sigma_n = \frac{\sigma_1 + \sigma_3}{2} + \frac{\sigma_1 - \sigma_3}{2}\cos2\theta \quad ; \quad \tau = \frac{\sigma_1 - \sigma_3}{2}\sin2\theta \qquad (7)$$

which were first recognised by Mohr (1882) as those representing a circle of radius $(\sigma_1 - \sigma_3)/2$ and origin $(\sigma_1 + \sigma_3)/2$. The Mohr's circle diagram is a graphic means of identifying the stresses at a point as shown on the right-hand side of Figure 2.4.

Early researchers noted that in a triaxial compression test the axial stress σ_1, at failure depends on cell pressure $\sigma = \sigma_3$. Successive tests at different σ_3 stress levels provide more values for σ_1 and are sufficient to draw a series of Mohr circles. The failure shear strength as a function of normal stress could be reasonably well predicted from the line (or envelope) drawn tangent to the circles as shown in Figure 2.4. The Mohr-Coulomb failure criterion in two dimensions is the equation representing this line. Typically at least three tests are performed for averaging to get a representative value for slope, ϕ, and intercept, c.

A triaxial cell (as per Wong *et al.* 1987) for controlled confinement tests is the most rigorous of all procedures for determining Mohr-Coulomb failure criterion but is also the most complicated and expensive. A biaxial cell (plane stress) has been used by Sayed (1989) whereby controlled ice rubble confinement pressure in one direction, perpendicular to an increasing normal stress, was achieved (Figure 2.4b). Direct and simple shear devices in a variety of shapes, sizes and orientations are most commonly used for testing shear strength (Figure 2.4c and 2.4d). Direct shear involves the

placement of a sample in a box or cylinder which is split so as to allow relative tangential motion of the two parts. A pressure is applied normal to the slip plane of the sample through any number of means - pneumatic bladder, hydraulic pistons, weight placement etc. Direct shear test results are plotted on a graph to yield the best fit failure envelope since the shear stress itself is measured "directly" (Keinonen and Nyman 1978, Prodanovic 1979, Hellmann 1984, and others). Some consider this to be a plane strain test since only lateral and vertical motions can take place. Simple shear tests attempt to produce a state of pure shear for samples undergoing plane strain (Urroz and Ettema, 1987). The problems with the direct shear device (changing sectional area and assumed failure surface orientation) are partially overcome in simple shear devices although stroke length is reduced and equipment is more complicated.

Often the repose angle of an accumulation of a cohesionless granular material is considered a lower-bound estimate of internal friction angle. For instance, when carefully poured into a pile, sand is close to a minimum density state and usually has a repose angle around 30° which is around the low density internal friction angle determined from direct shear tests (Bowles, 1984). For cohesive granular materials this approximation does not apply.

2.2.4 Investigations of ice rubble shear strength

Summaries of laboratory investigations into the shear behaviour of ice rubble are found in Wong *et al.* (1987), Ettema and Urroz (1989), Case (1991), Chao (1993) and others. Few references citing full-scale rubble experiments or strength tests are available. Lepparanta and Hakala (1992) and Coon *et al.* (1995) describe field trials where ridge keel strength was tested and others have estimated strength from observations in the field.

Lavender (1973) for instance describes obtaining estimates of friction angle and cohesion from river ice jams, and Williams *et al.* (1993) describe keel resistance while coring ridges in the Northumberland Strait. Some inferences can be made by observation of rubble repose angle shown earlier to be around 27° on average for keels. Laboratory experiments dominate the literature record of rubble shear strength measurements. A collection of references with reported conditions and results are listed in Table 2.3. Some experiments on solid ice are also listed on the bottom of the table as a reference for extreme upper-bound strengths for highly consolidated rubble (as in multi-year ridge keels).

Few obvious trends emerge as one scans the data columns of Table 2.3. Rubble shear strength shows huge variations from source to source with reported ranges of internal friction angle, ϕ, from 11° (Weiss *et al.* 1981) to 65°+ (Loset and Sayed, 1993) and cohesion, c, anywhere from 0 (Urroz and Ettema, 1987) to as high as 10 or 20 kPa for cold and dry ice (Sayed, 1987). High values for both rarely coincide. Reconciling these results with those for other materials proves to be difficult even for friction angle which is seemingly less dependent upon parent material than cohesion. For example, gravels have internal friction angle varying anywhere from 32° to 36° for loose accumulations and from 35° to 50° for dense packing. These values are comfortably bounded by the extremes reported for ice rubble. Curiously, Urroz and Ettema (1987) found the internal friction angle of polyethylene blocks to be around 35° and that for similarly sized and shaped ice blocks to be 51° when packing densities and testing procedures were identical. Remarkably, Lepparanta and Hakala (1992) report full-scale friction angles to be less than 10° though an adequate explanation is not given.

Clearly, ice rubble shear strength is **state-dependent** and **not unique**. There are many control variables, trends are weak, and multicollinearity is highly probable. Regression analyses on this sort of data are complicated since testing and analysis procedures vary widely. For example, many different shear apparati, rubble types and handling procedures have been used. Compounding the difficulty is an incomplete record of control parameters for each program. In this thesis multiple regression techniques are used to test the relevance of control parameters and to develop best-fit empirical relations to the shear strength data available in the literature.

Table 2.3 Review of ice rubble shear information in the literature.

Author(s)	Ice Properties	Test type	Maximum confining pressure kPa	Temp	Porosity %	Maximum Layer Depth mm	Speed mm/s	Friction angle deg	Cohesion Pa	Notes
Cheng and Tatinclaux (1977)	Fresh ice 2 types 10x20x8 mm blocks, and crushed ice	Direct vert. 2 sided 244.609 x 450 mm Rotary vane shear	0.087	Submerged 0 C	-na-	90/275	0.25-6	0-86+	0-3350	Wide range of tests Merry (1974) records similar result with same apparatus (cf. Cheng and Tatinclaux)
Keinonen and Nyman (1978)	Saline parent sheet < 20 mm Salinity scaled 1/10-1/50 Blocks: b 2.5h x 2.5h Max block = 8h Salinity 6 ppt, b = 32 mm, natural sheet ice use, higher than natural	Direct horiz. shear 300 mm square box	1.47	Submerged 0 C	32/37	300	"Slow" by hand	47	11.3	Parent sheet t= 19 mm Parent sheet t= 38 mm
Prodanovic (1979)	Uniaxial freezing saline water Strength scaled 1/50: block = 19 mm sand 54 mm, max block size= 4h Flexural str. = 16 kPa, E=5.9 MPa Compressive 49 - 25.5 kPa	Direct vert. shear 300x457 mm box	2.7	Submerged 0 C	38	304	Rate varied 0.1-8	47 53	250 560	Parent sheet t= 19 mm Parent sheet t= 38 mm
Weiss et al (1981)	Saline parent sheet < 60 - 200 mm Flexural strength = 30-80 kPa Strength scale approximately 1/10 Max block size 4h Uses disjoint columnar individual grains	Direct vert. shear 1 m x 1.5 m	31	Submerged -2.5 to 5 C	19-50	1000 1000 1000 1000	4 25 3 24 5 25	13 18 26 25 36 34	1700 1200 2300 1400 3200 3450	Parent sheet t= 60 mm Parent sheet t= 60 mm Parent sheet t=150 mm Parent sheet t=150 mm Parent sheet t=200 mm Parent sheet t=200 mm
Hellmann (1984)	Three types: Fresh ice chips: 10-20 mm Fresh ice cylinders: 30-50 mm Uses cylinders or individual grains	Direct vert. shear "cross-shaped" 2 sides at 0.7x0.7 m in 2 m total	4.2	Submerged ice < 0 C water = 2 C	-na-	700 700 700 700	10.9 1.6 10.7 10.7	54 61 64 64	580 420 280 0	Ice chips Ice chips Cylinders Object
Fransson and Sandkvist (1985)	Three ice types Fresh ice x 39, L x 110, flex = 1000kPa Fresh ice: h = 46mm, L x = 6 mm, flex = 780 kPa Flexural strength = 38 kPa	Direct horiz. shear 500 mm square	3	Submerged ice = 0 C water = 2 C	20	500 500 500	10 10 10	34 14 13	350 450 240	Parent sheet h=39, length=110 mm Parent sheet h=46, length=6 mm Approx results from saline Parent sheet h=52, length=4 mm
Urroz and Ettema (1987)	Three sizes fresh ice and 1 plastic: small: tiles 58 mm med: tiles 63 mm large: 95x95x38 mm polyethylene: 38x31x9.5 mm	Simple shear Rubble in vertically unconstrained 530x609 mm	0.46	Floating layer, 0 C	36-41	76-229 76-229 133-229 152-229 152-76	2 2 2 2 2	36.6 51.6 30.5 51 35	0 0 0 0 0	small (blocks) med (blocks) large (blocks) large plastic (blocks)
Sayed (1987)	Fresh ice 30 mm cubes Not submerged	Confining press. = 25 diam. = 130		-10 C	Initial 40-46 Final 30-40		0.032-0.85	27-45	10000-20000	Biaxial plane strain cold, dry fresh ice 500x500x300 mm

Table 2.3 (Continued)

Author(s)	Ice Properties	Test type	Maximum confine pressure kPa	Temp	Porosity %	Iceramor Layer Depth mm	Speed mm/s	Friction angle deg	Cohesion Pa	Notes
Wong et al. (1987)	Crushed fresh ice cubes Max size = 4.75 and 9.5 mm (3 mm av.) Internally coefficient 2.6 - 4.0	Direct horiz. shear 300 mm square	(very high) 140	2 C Brine & Dry	Initial 41.5	200	Very slow	No peak 0.0096-0.040 monotonic increase	-na-	Gale et al. (1986) similar testing arbitrary max selected for phi c but tests similar to these
Case (1991)	EGADS (doped fresh) ice sheet 50 mm thick, broken into blocks 3.2k average length, 8k maximum size	Direct vert shear 600x450 mm box	2.41	Submerged 0 C	34-37	450 450 450 450	1 1 1 1	48.9 37.6 34.9 27.2	523 597 674 824	7.5 ms warmup 8.5 ms warmup 10 ms warmup 11 ms warmup
Leppanen and Hakala (1992)	Unknown ice type (scale =1:13) 15 mm thick pased sheet	Direct horiz. shear 800x400 mm box Punch tests 150 mm	1.5	Submerged 0 C	20	450	-na-	8.4	800-2400	Punch and direct shear results Reported results unclear
Eranti et al. (1992)	Few grained model ice (FGI GX) Scale 1:40 to 1:50, E = 20-30 MPa	Shear box	-na-	-na-	-na-	-na-	-na-	34 30	350 2000	Average for loading rate Amount of slush and consol- ideration of rubble tested
Sayed et al. (1992)	EGADS (doped fresh) ice sheet 30-40 mm thick, broken into blocks max. size = 20-25 cm, min. size = 5 cm Submerged tests reported here	Biaxial plain-strain 1 m x 1 m x 0.5 m vert shear zone	100	Aw = 2 C Wat = 0.3 C	24-34 CW wet tests	500	0.27-5	47.7 59.7 48.4 30.6	0 460 333	Strain rates: 23 test 10 kPa only Strain rates: 51 Test 50 kPa only Strain rates: 23 test 10 kPa only Strain ratio 0.9 test 10 kPa only
Load and Sayed (1993)	Freshwater ice blocks ranging from 25 mm to 130 mm	Biaxial plain-strain 1 m x 1 m x 0.5 m vert shear zone	90+	Dry = 2 Wet ice = 2 C for varying durations	Initial 36-39	500	3.34-5.3	dry 37-65 wet higher than dry	-na-	Tested different size distributions and varied strain rates
Lehmus and Karna (1995)	Fresh water ice sheet cases into parallelepipeds approx. 40x150 mm largest = 300 mm	Direct horiz. shear 800x600 mm box below rubicon layer	1.6	Submerged 10 C	29-42	800	20 & 10	-na-	-na-	Consolidation time and temp varied at constant pressure
Cornett and Timco (1996)	Saline ice parent sheet + 0.5% salt by wt h= 10 cm, pieces broken by hammer to <150m in length varying in size, angular in shape	Biaxial plain-strain 1 m x 1 m x 0.5 m vert shear zone	60	Dry -na- Ice + 10 C Water + 1 C	-na-	500	4.0-5.3	45-70 Saline higher than fresh	-na-	Friction angle decreases with confining pressure

Table 2.3 (Continued)

Author(s)	Ice Properties	Test type	Maximum confine pressure kPa	Temp	Porosity %	Maximum Layer Depth mm	Speed mm/s	Friction angle deg	Cohesion Pa	Notes
FULL SCALE										
Lavender (1973)	Apparent cohesion from large scale river ice joints	Analyzed from data						Not publ	0-3800	
Leppäranta and Hakala (1992)	Baltic first-year ridge keels	Punch shear through keels	12 kPa (11.7 m keel depth)	Submerged	23-33	3300-1170	Very slow <1 mm/min		1700-4000+ 3400	Total shear strength reported Median for keel depth <3.9 m
SOLID ICE										
Rogaczewski (1978)	Solid columnar freshwater ice	Large shear box	1.69	-2.5 C	0	-na-	0.06-0.12	22.8 / 25.2	500000 / 750000	Peak strength / Ultimate strength
Zsongai et al. (1993)	Solid sea ice	Direct shear box	3 MPa	0 to -20C	0	-na-	10^-3 to 10^-1 /s	up to 56	(0.3-1.2MPa)	Range of results given
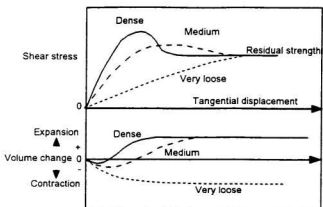
Figure 2.2 Volumetric change of a granular material undergoing shear.
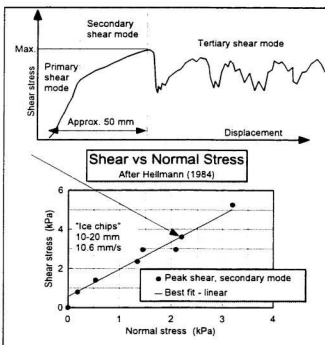
Figure 2.3 Shear behaviour of ice rubble (after Hellmann, 1984).
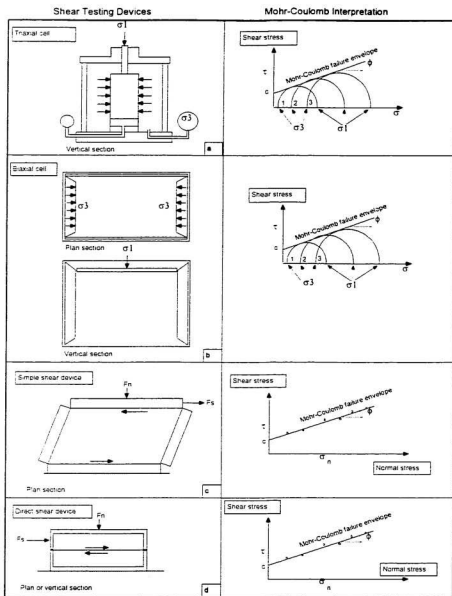
Figure 2.4 Shear testing devices and interpretation procedures.

2.3 First-year ridge forces on structures

2.3.1 Overview of ridge forces

The force on a structure exposed to the action of sea ice is the lesser of the *limit force* condition due to environmental driving forces and momentum, and, the *limit stress* condition due to the strength of ice features. When driving forces are sufficient, competent sea ice crushes, spalls and buckles against vertical structures while for sloping structures it fails at much lower loads in flexure. Dynamic loads, either quasi-static or resonant, result from cyclic ice failure which is pronounced for crushing-dominated modes. Sloping structures thus diminish the threat of resonance but tend to increase vertical forces, underwater exposure and construction complexities. The literature is silent about keel dynamic loads probably because keels are assumed to produce transient loads that are generally not "long" enough or "high" enough to excite resonant structural frequencies.

Keel failure mechanisms vary with global support boundary conditions and scale as described in Subsection 2.2.1. Design ridges in the NSCP were large and keel-dominated so that shear failure was expected (Cammaert *et al.* 1993). In general, the refrozen core of a first-year ridge is assumed to be a uniformly thickened homogeneous plate, interlocked with the keel. Usually, it is assumed that failure of the core and keel are independent and peak forces are simultaneous. Both assumptions are analytically conservative but necessary since proof of less severe interaction mechanics is not openly available.

Interpretation of measured ice forces on structures is complicated work. Often strain measurements are indirect or pressures are measured over representative areas, few cases of direct global measurement of loads where ridges interact have been made (and much of that remains proprietary). In the open literature there are some references to either design loads based on field observations or actual measured data. More often than not *ridge factors* are given which represent the increase in level ice load when ridges are encountered. A significant drawback of this factor is the unknown state of the refrozen core which may, at maturity, be twice the surrounding level ice thickness. None-the-less the keel loads can be bounded somewhat by looking at ridge factors. In the absence of any competent core a ridge factor, R_f, is representative of rubble clearing forces alone (as a ratio of level ice resistance). When a refrozen core is similar in thickness and strength to the surrounding ice then R_f - 1 indicates the rubble clearing force ratio (including confinement effects of the refrozen core). Level ice forces on vertical structures are fairly well understood and are often approximated using the generalized crushing force equation

$$F_c = I f_c m_c \sigma_c D h \qquad (8)$$

where I is indentation coefficient, f_c is the contact factor, m_c is shape factor, σ_c is the strain dependent crushing strength, D is structure width or diameter and h is the ice thickness. Values for coefficients are broadly quoted in a number of publications and texts (Cammaert and Muggeridge 1988, Sanderson 1988).

In the following subsections laboratory investigations and field monitoring programs associated with ridge loading are reviewed. The information from the laboratory programs will be revisited later in Chapters 3, 4 and 6 of this thesis.

2.3.1 Laboratory investigations of rubble indentation

Laboratory investigations which simulate either ridge interactions or generic rubble indentation are reviewed in Table 2.4. Cheng and Tatinclaux (1977) and Keinonan and Nyman (1978) investigated the "two-dimensional compressive resistance" of a floating ice rubble layer. In a tank containing floating ice rubble, a full-width vertical plate was translated horizontally giving rise to bulk compressive resistance forces. Load traces indicated peak and residual strengths, while rubble depth and interaction speed influenced results.

Prodanovic (1979) describes the interaction process for a vertical cylinder translating through a continuous floating rubble field.

> "As the model structures penetrated into the rubble field, the rubble was compressed, the compression zone extending up to 1 m in front of the structure (of diameter 0.304 m, and rubble depth 0.28 m). The ice pieces were mostly moving relative to each other and hence the resistance force was mainly frictional. The ice pieces separated in tangential directions and gradually slid around the structure. The rubble field failure was predominantly planar, with little upward and downward ice activity. Large ice pieces were slightly crushed and occasionally split. Thicker rubble fields created small pile-ups and plugs in front of the structure."

The development of surcharge and other transient load mechanisms appears, from this description, to be down-played.

Hellmann (1984) punched a circular plate horizontally through the centre of a floating rubble mass. Though the interaction process at the structure could not be directly observed it is implied that rubble did flow around all edges of the advancing plate (not just a compression test). A ten-fold increase in resistance resulted from decreasing indentation speed from 250 to 1 mm/s.

Rogachko *et al.* (1994) studied ridges both in the laboratory and in the field. From the paper, reviewed in the next section, it is difficult to determine the exact source of the information given. Timco and Cornett (1995) indented simulated first-year ridges in a study investigating ridge loading on the Northumberland Strait bridge piers. The force contribution of the unconsolidated rubble in the keel portion of the model ridges were roughly estimated from global force measurements.

2.3.2 Full-scale ridge load research

This section describes some field programs in which first-year ridge loading was studied. A review of the programs is provided in Table 2.5. These data and other full-scale load issues will be discussed and analyzed in Chapter 7.

Cook Inlet

In a study lasting several years Blenkarn (1970) investigated ice loading on offshore jacket structures in Cook Inlet, Alaska. Pressure ridges which occur naturally around the periphery of many floes in that region were associated with the peak loading events on the structures. The ratios between peak forces and steady forces for uniform floes were in the range between two and three. Similar values for the "pressure ridge factor" were also determined for a test pile in Cook Inlet. Ridge line loads of 878 to 1042 kN/m were

approximated. Blenkarn was able to discriminate between dynamic and static components of the peak force, concluding that the equivalent static peak force ratio with uniform floe force was less than two.

Gulf of Bothnia

This body of work centres on an instrumented light pier "Kemi-1" in the Northern Gulf of Bothnia near the coast of Finland. There, typical annual ice thicknesses are 0.8 m and ridge keels deeper than 12 m are common. The structure is 10 m wide at average water level and has a slope angle of 55°. Krankkala and Maattanen (1984) report Maattanen's use of a ridge factor of 2.5 based on Baltic experience to that date.

Two principal ice failure mechanisms were observed during ice interaction during the first seasons of Kemi-1 operation (1984/85 and 1985/86); one corresponding to low speeds and the other to high speeds (Maattanen 1986). The former involved the ductile bending of the sheet ice with some single ice layer ride-up, the latter process involved bending, crushing and shearing modes leading to a stationary rubble pile at the leading edge of the pier. Rubble clearing on the cone was "efficient" as pieces climbed and flowed around the cone without the formation of a stationary bow. Maximum ice forces were always associated with pressure ridges, the largest of which resulted from an adfrozen grounded ridge stationary for a week in cold weather and then broken up in a storm. Quantitative force measurements remain proprietary so little data have become available, however, loads were lower than expected at the time of publication (1986) leaving Maattanen to conclude that "... earlier predictions of ice failure models against a conical structure have to be modified".

Hoikkanen (1985) noted the formation of an ice "stack" when pressure ridges rode up on the Kemi-1 cone base. As penetration increased there was a strong flow of ice blocks and brash upwards from the inner parts of the ridge. He noted the presence of large ice blocks longer than 3 m and 1.5 m thick which appeared to be the result of two or three level ice layers frozen together. The level ice following the ridge tended to penetrate the rubble pile or ride up on it. Hoikkanen agreed that the loose parts of a pressure ridge can be treated as a granular material and may be analyzed using the principles of soil mechanics. He further observed that if the structure were narrow and vertical it could further be assumed that the consolidated part fails by crushing, although the Kemi-1 cone showed no clear failure pattern emerging; "... sometimes thick rafted ice was bent but some ridges seemed to be crushed completely". He also noted the inability of model tests to reproduce the crushing failure of the level ice and ridge core observed at Kemi-1.

Recently, Maattanen (1994a) discussed the design of a smaller conical light structure for the Gulf of Bothnia. The structure was 2.6 m at the waterline and had a 60 degree cone angle (from horizontal). The results of the load analysis indicate that a 3.0 MN load can be expected from a design ridge keel, this being greater than the load from a 0.8 m thick level ice interaction but less than the 5.8 MN load predicted for a 1.2 m thick rafted ice layer.

Frederking and Sayed (1994) report that Palosuo (1970) estimated the maximum first-year pressure force on a cylindrical caisson to be in the order of 700 kN/m in the Gulf of Bothnia. The block ice thickness was 0.3 to 0.5 m (personal notes of L.W.Gold) but he did not give a ridge size for this estimate. Palosuo did say that the biggest ridges, comprised of blocks with thickness 0.4 to 0.5 m, were 20 m deep therefore the load

estimate is probably for 15 to 20 m deep keels.

Sea of Okhotsk and other Russian temperate seas

Dolgopolov et al. (1975) present methods for calculating ice loads on isolated piers of marine structures which include rafted and ridged ice. Their work is based on field, experimental and analytical data. They state that a uniform solid ice sheet is rarely seen in open seas but that ice fields with ridges of different sizes, shapes and directions are much more common. They refer to the use (prior to 1975) of a ridge factor of 2.2 in Canada and the USA as reported by Dinkla and Sluymer (1970) whereas in the USSR a factor of 1.3 to 1.5 has been taken for temperate seas. In their opinion they felt that data then available permitted the refinement of those numbers. New factors were obtained in an ice basin where vertical and cone shaped piers indented ridge formations. The results obtained were as follows: "the magnification factor for the vertical pier made up 1.54 with loose ice blocks in the underwater part of the ridge whereas it amounted to 2.5-2.7 with the ice blocks frozen together. The magnification factor for a cone-shaped pier was 1.45 if ice blocks in the lower part were not bonded together".

In a paper by Rogachko et al. (1994) an "ice-hummock" or pressure ridge coefficient was studied in large scale controlled experiments for a continuous rubble field. They based their experimental parameters on field observations from the Sea of Okhotsk. It is reported that the thickness of the middle consolidated portion of the ridge varies within 1 - 1.5 times the level ice thickness surrounding the ridge and the keel is 4-5 times greater in depth than sail height.

In their experiments an extensive rubble field was built in front of an extensive level ice

sheet and the two were systematically indented with vertical rigid cylinders. Results were obtained for two consolidation levels - the case where the refrozen core thickness in the rubble field was equal to the level ice thickness, and the other when it was 1.5 times the level thickness. The experimental results for the two cases were plotted on a graph of ridge coefficient, R_f versus sail height-level ice ratio (H_s/h) from which the following empirical relations were developed:

$$R_f = \frac{F_R}{F_l} = 1.23 + 0.65\left[\frac{H_s}{h}\right] - 0.054\left[\frac{H_s}{h}\right]^2 \qquad (9)$$

for refrozen core thickness equal to level thickness, and

$$R_f = \frac{F_R}{F_l} = 2.07 + 0.66\left[\frac{H_s}{h}\right] - 0.0455\left[\frac{H_s}{h}\right]^2 \qquad (10)$$

for the thickness ratio of 1.5. For example, a given ridge with a refrozen core 1.5 times the level ice thickness and sail height 4 times level ice thickness, the keel would be statistically 16 to 20 times deeper than the level ice thickness (10.6 to 13.3 times the consolidated layer thickness) and the total ridge force would be four times the level ice force. This value corresponds to the asymptotic limit of the ridge factor for the thickness ratio of 1.5 in Rogachko et al. (1994). If a ridge has a consolidated core thickness equal to the level ice, and keeping the same sail height ratio, the ridge factor becomes 3, also the limit for that thickness ratio. A factor of 3 implies that the rubble resistance is twice the level ice resistance if similar core and level ice thicknesses equate to similar resistances (when confinement and failure modes are considered).

Beaufort Sea

Field monitoring of first-year ridge interactions with the Molikpaq caisson have recently been revisited in Croasdale *et al.* (1995). Above-water observations indicated that many modes of failure were common but that larger ridges generally failed in shear. Ridge load factors were found to be in the range of 1 to 3 and line forces of 0.5 MN/m for keels interacting with the 100 m structure were suggested.

Frederking (1994) states that the line load (load per unit meter) of a cold strong multi-year floe 7-10 m thick was around 2.5 to 5 MN/m from experience with the Molikpaq in the Beaufort sea. He believes that even a 20 m deep first-year ridge in the Northumberland Strait would not be capable of generating line loads anything near *half* of that for the multi-year floe.

Grounded rubble

Grounded rubble fields which form around some arctic structures have been studied by researchers typically interested in load transmission to the structure (Sayed *et al.* 1986, Marshall *et al.* 1991, Poplin and Weaver 1992 and others). Croasdale *et al.* (1994) review field measurements, physical model tests, laboratory tests and theoretical models for grounded rubble and point out that there are no known cases where ice rubble has reduced structural stability and created a problem. On the contrary, ice rubble has often significantly reduced the transmission of ice loads to structures and can significantly mitigate the potential for dynamic excitation of the structure. A study of the sliding resistance of grounded rubble may provide some upper bound limits on unconsolidated rubble shear strength for ridges though this line of work has not been pursued in this thesis.

Table 2.4 Laboratory rubble indentation tests.

Reference	Range of Structural Width m	Range of Rubble Width m	Range of Rubble Depth m	Range of Rubble Area m^2	Range of Speed m/s	Range of Peak Load N	Range of Fric Angle Phi deg	Range of Cohesion c Pa
Cheng and Tatinclaux (1977)	0.91	Contin*	0.076 -0.22	- na -	0.00015 - 0.0028	19 - 386	46	1
Keinonen & Nyman (1978)	0.3	Contin	0.174	- na -	0.025	24	47	10
Prodanovic (1979)	0.152 - 0.304	Contin	0.09 - 0.28	- na -	0.001 - 0.009	8 - 285	50	500
Hellmann (1984)	0.1	Contin	0.2 - 0.8	- na -	0.001 - 0.25	60 - 600	54 - 61	580 - 420
Rogachko et al. (1994)		Contin						
Timco and Cornett (1995)	0.333	0.8 - 1	0.003 - 0.45	0.002-0.45	0.09 - 0.27	70 - 1900	45	1000

* Contin. means that rubble was continuous in the direction of structure displacement.

Table 2.5 Estimations of full-scale loads based on field observations.

Reference	Location	Structure	Ridge factor	Maximum load	Notes
Blenkarn (1970)	Cook Inlet, Alaska	Vertical cylinders Jacket rig	2-3	876-1024 kN/m	Test pile and full structures tested Dynamics analysed
Dinka and Sluymer (1970)	Canada	Vertical structure	2.2		Reference from Dolgopolov et al (1975)
Palucao (1970)	Gulf of Bothnia, Fin.	Vertical cylinder caisson type		700 kN/m	Includes keel and consol. layer Ridge depth approx. 15- 20 m
Dolgopolov et al (1975)	Sea of Okhotsk	Vertical structure	1.3-1.5		Old ridge factor in USSR
Maattanen (1983)	Baltic, Finland	Vertical structure	2.5		Design recommendation for lighthouses
Maattanen (1994)	Baltic, Finland	Conical ice shield small light structure	2-3	Approx 1 MN/m	Keel, c = 5.0 kPa, phi = 45 deg keel, level and rafted ice models are compared for design
Frederking & Sayed (1994)	Beaufort Sea	Vertical structure		500 kN/m	For first year ice up to 2 m thick
Rogachev et al. (1994)	Sea of Okhotsk	Vertical cylinder	2-4		From lab and field observations Formulas for ridge factor in thesis text
Croasdale et al. (1995)	Beaufort	Molikpaq caisson	1-3		Many modes observed
		Ranges:	1-4	500-1024 kN/m	
		Averages:	2.3	800 kN/m	

2.4 First-year ridge keel load models

2.4.1 First-year ridge modelling

When a ridge interacts with an offshore structure loads are created by the breaking of the core and the clearing of the keel and sail when sufficient driving forces prevail. Engineering analyses of loads often include the sail with either keel or core load models and treat the remaining component processes separately (Prodanovic 1981, Eranti *et al.* 1992, Cammaert *et al.* 1993, Croasdale *et al.* 1995). Though it is understood that the core provides an important boundary condition which influences keel failure, the simultaneity of failure and the interaction dynamics are not well understood. Thus the peak loads resulting from both keel and core models are typically added to obtain a resultant peak.

Croasdale *et al.* (1995) assert that design ridges are keel-dominated in size and strength. The failure of the core is said to change keel boundary conditions reducing confining stresses near the structure and slightly increasing them further away. The change is small however, and the error introduced to the keel model over the entire ridge is negligible. Since the discussion in Croasdale *et al.* (1995) appears limited to a class of structures with upward breaking cones at the waterline these statements must be interpreted cautiously. Nevertheless, if one assumes that the keel is plastic behaving as a frictional granular material and that the core is a rigid plastic brittle solid then the former may retain most of its strength after yielding whereas the latter may not. Thus it is assumed in this study that the influence of core failure on keel processes is not significant enough for most structural configurations to alter the independent approach to keel modelling.

Several modelling practices for first-year ridge keels are investigated in Krankkala and Maattanen (1984), Kitazawa and Ettema (1985), Bruneau (1994) and Croasdale *et al.* (1995). The following section reviews the historical development and demonstrates the variety of approaches to keel modelling.

Dolgopolov et al. (1975)

One of the earliest and most influential modelling approaches proposed for ridge keels is provided by Dolgopolov *et al.* (1975). The authors describe that the model was developed from experimental studies in which the physical patterns of interactions were observed. There is little novelty to the approach, however, as it is, in form, the passive earth pressure equation for retaining structures, written as:

$$F = qDH_{df}\left(H_{df}/2\gamma K_p + 2c\sqrt{K_p}\right)$$ (11)

where

$$K_p = \tan^2\left(45 + \frac{\phi}{2}\right) \quad , \quad H \leq H_{df} \leq H + \frac{D}{2} \quad , \quad q = \left(1 + \frac{2H}{3D}\right)$$ (12)

and where F in this and other equations presented here is the maximum longitudinal horizontal force on the structure of width D, H is keel depth, γ is the ice rubble weight, c is rubble cohesion and ϕ is rubble internal friction angle (Figure 2.5a). The suggested adjustments to keel depth for surcharge and to structural width for the spatial behaviour of the ice medium appear reasonable, though little guidance is given in assigning a value to H_{df}. This is a significant stumbling block for the application of the model since, by example, if the structure is twice as wide as the keel depth then loads may vary by 100% for arbitrary assignments of surcharge. The shape factor, q, in Dolgopolov's approach

is explained by Maattanen (1994) as originating from the contribution of *side wedges*, "a common assumption for the shape of a failure surface in soil mechanics" (Figure 2.5b). The ice rubble buoyancy applicable in this formula is usually assumed to be

$$\gamma = (\rho_w - \rho_i)(1-e)g \tag{13}$$

where ρ_w and ρ_i are the water and ice densities, e is the bulk porosity of the ice rubble and g is the gravitational acceleration 9.81 m/s^2.

Keinonen (1979)

Keinonen (1979) developed a model for ship resistance in first-year ice rubble and brash. Since this situation is analogous in some ways to ridge interactions with stationary structures it is considered here. The assumption of linear Mohr-Coulomb ice rubble behaviour allowed the formulation of a passive pressure model similar to that of Dolgopolov *et al.* (1975) but with attention to a variety of structural geometries. Through equilibrium of forces it was shown that:

$$\frac{F}{D} = 1/2H^2(1-e)(\rho_w - \rho_i)gK_{\eta} + HcK_{hc} \tag{14}$$

where

$$K_{\eta} = \frac{(\sin\psi + \tan\phi_1\cos\psi)(\sin\theta + \tan\phi\cos\theta)\sin(\psi+\theta)}{[(1-\tan\phi_1\tan\phi)\sin(\psi+\theta) + (\tan\phi_1+\tan\phi)\cos(\psi+\theta)]\sin\psi\sin\theta} \tag{15}$$

$$K_{hc} = \frac{\sin\psi + \tan\phi_1\cos\psi}{[(1-\tan\phi_1\tan\phi)\sin(\psi+\theta) + (\tan\phi_1+\tan\phi)\cos(\psi+\theta)]\sin\theta} \tag{16}$$

in which ψ is bow flare angle, θ is the slip plane angle, ϕ_I is the ice-structure friction angle and ϕ is the internal angle of friction of the ice rubble (Figure 2.6). The value of the slip plane angle, θ, was determined using differentiation to minimize the resistance formula above. While dealing with the complications of bow entrance, stem and flare angles it is not clear how Keinonen deals with the slope of the surcharge or the effective depth over which the bow is said to act. The resistance formula was shown (in Kitazawa and Ettema, 1985) to be altered to account for the slippage of ice rubble under a vessel in the "developed condition" so that the $1/2H^2$ term became Hd where d is the depth of the vessel. However, this adjustment does not conform to the passive pressure state as sketched in Figure 2.6 (where the rubble depth is $H+d$ at the point of failure). Keinonen maintained that in the "developed condition" the total force on a ship was actually the summation of five components:

$$F = F_{su} + F_{sl} + F_{se} + F_{PB} + F_{PS} \tag{17}$$

where the first three represent resistance from upper, lower and end bow slip-planes and the last two are for middle body ship resistance on the bottom and side. It was also suggested that the confining pressure along the vertical end slip planes at the bow was in the neutral state so that

$$\frac{\sigma_h}{(1-e)(\rho_w - \rho_i)gz} = \frac{\nu_p}{1 - \nu_p} \tag{18}$$

where σ_h is the horizontal pressure at depth z, and, ν_p is Poisson's ratio. Since adjustments for depth and surcharge are in accordance with ship-like clearing processes, and may be *rule of thumb*, the applicability of Keinonen's formulation to first-year ridge interactions with offshore structures may be limited.

Mellor (1980)

Mellor (1980) developed a passive shear failure model for ship resistance in unconsolidated level brash ice. The form of the model was similar to Keinonen's above when a vertical frictionless plate is considered. The differences are Mellor's treatment of rubble depth, buoyancy and effective bow form. The formulation is given by,

$$\frac{F}{D} = (1 + \tan\phi\cot\beta'') \left[\frac{1}{2} H_{ks}^2 K_p \left[(1-e)\rho_i g \left(1 - \frac{\rho_i}{\rho_w} \right) \right] + 2cH_{ks}\sqrt{K_p} \right] \qquad (19)$$

where H_{ks} the full brash depth (keel plus sail), and the value in square brackets is the assumed rubble buoyancy (Figure 2.7). The friction angle and cohesion of submerged brash in water is assumed to be the same as that in air. The factor $(1 + \tan\phi\cot\beta'')$ represents the effective width of the ship bow in accordance with the formation of a false bow with half apex angle of β'' (Figure 2.7). The angle β'' appears to be a function of bow form, bow roughness and assumed failure criteria for the brash. For plain strain indentation in a Von Mises material a flat faced rough indentor produces a false bow with $\beta'' = 45°$. For Mohr-Coulomb $\beta'' = (45-\phi/2)$. For an arbitrary friction angle of 35° the bow factor $(1 + \tan\phi\cot\beta'')$ becomes 2.34. By comparison the shape factor in the formula by Dolgopolov *et al.* (1975) is 2.34 when $H = 2D$. The similarity suggests the Dolgopolov formulation may be based on a similar approximation.

Croasdale (1980 - 1994)

Croasdale (1980) modelled first-year ridge loads assuming that the ridge keel is comprised of ice blocks held together by buoyancy, gravity and frictional forces alone. Thus the ice keel was said to act as a granular material with an assumed friction angle and no cohesion. A plug-type failure was suggested whereby two parallel shear planes

form at either side of a structure during the initial stages of an interaction (Figure 2.8a). The force required to shear through the rubble keel was determined by vertically integrating shear stress and area through an assumed triangular keel cross-section. Since it was also assumed that no consolidation had taken place a horizontal shear plane was not considered. The formula reduced to

$$F = \frac{2WH^2}{3}\rho g \tan\phi \qquad (20)$$

where F is the peak horizontal force on the structure, W is the keel width, H is keel depth, ρ is the buoyant density of the ice, g is gravitational acceleration and ϕ is the internal friction angle of the keel rubble. Horizontal confining stresses were assumed to be equivalent to vertical hydrostatic pressure, an assumption which suggests a stress state slightly higher than the neutral but short of passive conditions.

If cohesive bonds are sufficient to disable frictional sliding, Croasdale suggested that the force required to shear completely through a triangular ridge keel (as described above) would be

$$F = cWH \qquad (21)$$

Based on a downwards breaking wedge of width D with failure plane pitch angle of 45°, an approach for wider keels or rubble fields for purely cohesive rubble was proposed by Croasdale (1993) as shown in Figure 2.8b and written as:

$$F = c(2HD + H^2) \qquad (22)$$

The force to clear rubble from the path of the structure was also determined as

$$F = \gamma \frac{H^2}{2} W \left[\frac{1+\nu_p}{1-2\nu_p} \right]$$

where ν_p is poisson's ratio, γ is the buoyant weight of the submerged rubble and W and H are the ridge width and depth. However, this was not to be added to the cohesive rupture failure as the two were not assumed to act together. Croasdale (1993) also considered a footing failure for rubble fields (Figure 2.8c). Formulated in accordance with Figure 2.8c it was shown that

$$F = c(\pi DH + \frac{\pi D^2}{2}) \qquad (24)$$

where D is the structure width and also the radius of the failure slip surface. The first term reflects shear along the vertical circumferential slip surface, the second is for shearing on the interface between the ridge consolidated core and the rubble.

Croasdale (1994) updated the friction plug model (from 1980) to include the effects of friction on the underside of a refrozen core. If a horizontal shear plane, of width D, fails simultaneously with the two sides of the plug, the friction plug model becomes

$$F = [WDH/2 + WH^2/3](\rho_w - \rho_i)g(1-e)\tan(\phi) \qquad (25)$$

Prodanovic (1981)

Prodanovic (1981) developed a plasticity upper bound model for ridge forces on vertical (cylindrical and flat-sided) structures. The model, which accommodates both crushing

and shearing, assumes the ice rubble behaves as an elastic-perfectly plastic material, described by the corresponding yield functions, and that the associated flow rule relates current plastic strain rates to current stresses. The model conservatively estimates maximum loads by constructing admissible velocity fields and applying the upper bound theorem of plasticity theory (note that Prodanovic assumes the simultaneous failure of the consolidated level ice zone and the keel rubble in the determination of the maximum ice loads).

Two failure mechanisms commonly observed in first-year ridge model tests are described by Prodanovic as "plug-type" shearing and "gate-type" crushing modes (Figure 2.9). Shearing is the more common failure mode in model tests when the structure diameter is large in comparison to the ridge thickness (ie $D/H > 0.5$). The crushing failure mode follows a classical Prandtl velocity field with ice blocks flowing and clearing on both sides of the indentor in a log-spiral fashion. This mechanism is postulated to occur more often when the structure diameter is small and plain strain conditions are approached.

Prodanovic (1981) assumed that rubble behaves as a Mohr-Coulomb material (homogeneous and isotropic - strength increasing linearly with confinement). A three-dimensional extrapolation of the yield function was applied to construct a rubble force upper bound solution. The formulas reduced to

$$F = 2Ac \qquad (26)$$

for rubble shearing, where A is the keel cross-sectional area and c is the cohesion, and,

$$F = 2cDH\tan(45^\circ+\phi/2)\left[1+a'\frac{H}{D}\left(1+b'\frac{H}{D}\right)\right] \qquad (27)$$

where

$$a' = 0.89[1+1.82(\phi-17^\circ)] \quad , \quad b' = 0.31[1+2.01(\phi-8^\circ)] \qquad (28)$$

(cit. Croasdale *et al.* 1995) for rubble crushing.

Prodanovic's (1981) work illustrated the dominance of rubble shearing at high aspect ratios (structural diameter to level ice thickness) and the mechanism of crushing providing cut-offs at lower aspect ratios.

Eranti et al. (1992)

In Eranti *et al.* (1992) the authors report that the keel force component of first-year ridge interaction models can be estimated by classic soil mechanics as Prodanovic (1979) did assuming rubble plastic flow shear reaches the Mohr-Coulomb yield criterion. They suggested the use of Dolgopolov's model (attributed to Eranti and Lee in Krankkala and Maattanen, 1984) as a "fair first-estimate" of the ridge keel load if the structure is narrow when compared to the keel. It is pointed out that a more sophisticated analysis taking into account the cohesion profile among other things is required for final design.

When the structural width is large compared to the size of the keel Eranti *et al.* (1992) believe the penetration angle (oblique angle between direction of advance and keel long axis) and keel geometry become important. Eranti *et al.* suggest the use of a *cross-over* load estimating technique in which the maximum keel load is determined as the

intersection of passive and plug failure mode models - computed as a function of penetration into the ridge (Figure 2.10).

According to Allyn (1994), Eranti now uses a Brinch-Hansen "pile" model (Brinch-Hansen, 1961) which represents the ultimate resistance of rigid piles in earth against transverse movement. He has used this model which considers the slope angle of the keel, in the calculation of ice loads for the design of the bridge to span between Denmark and Sweden. Eranti is credited as having calibrated his model based on much Baltic sea ice data. Eranti presently believes, according to Allyn (1994), that there is only one model required which calculates the failure planes as a function of indentation into the ridge, and which he bases on the extensive model testing that he has directed.

Maattanen (1983, 1994b)

Maattanen (1983), as reported in Krankkala and Maattanen (1984), did not use soil mechanics arguments to formulate a ridge load model. He assumed the pressure distribution caused by a first-year ridge against a vertical structure to be comprised of a triangular sail and keel contribution and a uniform sheet ice contribution, apparently all acting simultaneously (Figure 2.11) . The sail height is assumed to be two times level ice thickness, h, and the keel depth is $10h$. The total load due to a ridge (sheet ice and rubble) is obtained by

$$F = F_c + F_{sail} + F_{keel} = F_c + F_c/2 + F_c = 2.5F_c \qquad (29)$$

where F_c is the sheet ice crushing load, F_{sail} is the sail load contribution and F_{keel} is the keel load contribution. Thus the ridge load is dependent only upon the level ice sheet crushing load. This also implied the dependence upon the ice/structure aspect ratio. Maattanen points out that rafted ice (layered ice) contributes only to the level ice portion and that adfreezing (understood here to mean cohesion between blocks) may serve to influence the sail strength independent of the other two factors. Therefore it is concluded in Krankkala and Maattanen (1984) that the above formula may be used but if better estimates of individual components are known then they should be used instead.

Maattanen (1994b) believes that a downward wedge failure model, ie. Dolgopolov et al. (1975), is applicable in the case where the ratio of keel depth to structural diameter is small (2 or less). This type of failure model has also been developed by Broms (1964) for the lateral resistance of piles in cohesive soils. Maattanen believes that when the ratio is large one would expect a Prandtl type failure. Actual failure surfaces for first-year ridge keels would have a Prandtl mode at the centre and wedge modes both at the top and bottom (at top if consolidated layer does not restrict it). He goes on to state that the shape factor as used in Dolgopolov's approach will be more complicated in the mixed mode case and it will depend upon H/D. Also a turnover into a shear plug mode is more likely so that ridge ice loads will be lower than the pure Prandtl mode suggests. For the case of a conical structure as in the Kemi-1 lighthouse in the Baltic Sea, Maattanen has concluded that omitting the shape factor from Dolgopolov's model results in more realistic ridge loads but that it is a "good detail" to observe the increased keel depth due to displaced rubble during the initial penetration into the keel.

Maattanen (1994b) reiterates that, in plastic limit analysis, failure surfaces are similar

both in cohesive and frictional materials. He says weaknesses in many keel load strategies include the separation of cohesive effects from frictional effects, the over-simplification of keel and structural geometry (constant depth keel and vertical instead of sloped surface for example) and the use of planar failure surfaces. Maattanen says that one might expect non-parallel failure surfaces and that due to high roughness, the consolidated core bottom will not attract shear plane formation but would cause failure surfaces to curve downwards. This has been independently verified by Allyn (1994) who states that the plug failure plane is not at the underside of the consolidated layer as determined in model tests. According to Allyn, Eranti also believes this to be the case and suggests that it reduces loads by 20% over typical horizontal failure surface calculations.

Hoikkanen

As cited in Krankkala and Maattanen (1984), Hoikkanen (no date given) suggests the formation of a "pseudo bow" in front of the structure which interacts with the oncoming first-year ridge or rubble field (Figure 2.12). He formulates two horizontal load expressions; the first for the sail, and second for the keel, based on soil mechanics. For the sail

$$F_{sail} = \left\{1 + \frac{\tan\phi}{\tan\beta'}\right\}\left[(P_1 + P_2)rH_s - (\frac{2}{3}P_1 + \frac{1}{3}P_2)H_s^2\cot(90 - \alpha)\right] \tag{30}$$

and for the keel

$$F_{keel} = \left\{1 + \frac{\tan\phi}{\tan\beta'}\right\}\left[(P_3 + P_4)rH_k + (\frac{1}{3}P_3 + \frac{2}{3}P_4)H_k^2\cot(\alpha - 90)\right] \tag{31}$$

where ϕ is the angle of internal friction, β' is half the leading angle of the pseudo bow (though β' is shown in the paper as the full apex angle, it is likely meant to be half of this), and,

$$P_1 = 2c_s(K_{ps})^{1/2}$$

$$P_2 = 2c_s(K_{ps})^{1/2} + K_{ps} \gamma_i H_s n$$

$$P_3 = 2c_k(K_{pk})^{1/2} + K_{pk} \gamma_i H_s n$$

$$P_4 = 2c_k(K_{pk})^{1/2} + K_{ps} \gamma_i H_s n - min\{(\gamma_w - \gamma_i)H_k , \gamma_i n H_s\}$$

$r = D/2 = $ radius of structure at waterline,

H_s is the sail height,

H_k is the keel depth,

α is the inclination angle of a conical or an inclined structure from vertical,

$K_p = \tan^2(45 + \phi/2)$ is the passive pressure coefficient for sail (s) and keel (k),

$c_{i,}$ is the cohesion of ice mass; subscript s for sail and k for keel,

n is the void ratio of the ridge, and

γ_i and γ_w are the specific weights of ice and water.

There is little reference to the basis of this extensive formulation by Hoikkanen as described in Krankkala and Maattanen (1984). A numerical comparison between different methods done by the latter party suggest that loads computed by Hoikkanen's approach are similar to those of Prodanovic. The study is somewhat confusing, however, with uncertainty about the conditions and parametric values prevailing for each of the models.

Joensuu (1981)

Reference to ice load modelling of first-year ridge interactions with conical structures is made in Krankkala and Maattanen (1984). A formulation attributed to Joensuu (1981) who in turn based the work on ridge piling by Parmerter and Coon (1973) is given as:

$$F \approx 10\rho_w g H_s^2 D + 45\rho g \frac{H_s^3}{\tan(\alpha)} \qquad (32)$$

where ρ_w is the density of water, g is gravitational acceleration, H_s is the sail height, D is the structural width and α is the cone angle. The first term calculates the force required to increase the potential energy of the ridge, and the second term calculates the force required to overcome the friction between the blocks in the ridge. The authors avoid explaining what the structure width, D, represents since for a cone this varies with height. Also it is not clear whether or not this model includes level ice failure loads.

Sayed and Frederking (1988)

Sayed and Frederking (1988) propose a calculation model of ice rubble pile-up for three dimensional ridge keel geometries. The formulation can be applied to the case of ridge failure and takes the form of an expression for the wall force in the passive stress state. The only difference is in the (material) constant relating line force to keel depth. The line force model suggested by Sayed and Frederking (1988) is:

$$F = 0.76\gamma H^2 \qquad (33)$$

where γ is the buoyancy of the keel H is keel depth and the constant 0.76 replaces $K_p/2$ (a factor decrease of about 4 for ϕ of 35°).

Frederking and Sayed (1994) review the works of Broms (1964) on the lateral resistance of piles in cohesive soils since the formulas Broms developed have been considered for ice rubble/structure interaction. Concern over the use of these formulations arises from the semi-empirical nature of the derivations that assume deflections, pile stiffness, compressibility and interaction geometries that pertain to soils and not ice rubble. The

greatest reservation they have in the use of Broms models is the assumption that piles are imbedded in a semi-infinite "half space" and as a result are highly confined, whereas ridge keels are much less so - leading to different failure modes and lower pressures. They advocate the use of a three dimensional non-linear finite element analysis or a discrete element analysis for a more rigorous solution to the problem.

Cammaert et al. (1993)

The Northumberland Strait Bridge Project provided the research incentive and direction for this thesis. Computing the design loads for the main span piers was a challenge undertaken by C-CORE and then CODA led by A.B. Cammaert. The approach used to model to ridge loads on the piers evolved as the structural design progressed from preliminary to advanced stages. A continuous stream of model updates was produced due to the exceptional scrutiny by a review engineering team, new results from laboratory experiments, new environmental data and ongoing rigorous model analysis. In the end the client was satisfied that the approach and results presented by CODA were sound. The strategy incorporated the Dolgopolov *et al.* (1975) passive failure approach and the updated Croasdale (1994b) frictional plug model in a *cross-over* technique as described in Eranti *et al.* (1992). The algorithm was buried in a lengthy simulation routine which used Monte Carlo sampling and assumed parametric distributions to compute extremal distributions from which return period loads were assessed.

In the *CODA* model both passive and plug models were rewritten as a function of penetration into the keel. Additionally, accommodation was made for the flaring of vertical shear planes across the width of the keel as were observed and reported in Bruneau (1994b) (Figure 2.13). Incorporating these changes into Croasdale's model

resulted in

$$F = \left[(W-x)D + (W-x)^2 \tan(\beta)\right](\gamma H/2) \tan(\phi)$$
$$+ \left[W^r H - 2(x^r)^2 H/W^r\right](\gamma H/3) \left[\frac{1-\sin\phi}{1+\sin\phi}\right] \cos\beta \qquad (34)$$

where γ is the bulk weight of the submerged ice rubble, x is the penetration of the structure into the ridge in the approach direction, and primed terms are distances along the flared failure planes at angle β to the direction of travel. The pressure on the divergent side failure planes was assumed to be in the active state.

The passive failure model (from Dolgopolov *et al.* 1975) was rearranged to represent the load as a function of penetration into a symmetrical triangular keel of depth H as follows:

$$F = qD(2xH/W)[K_p \gamma xH/W + 2\sqrt{K_p} \, c] \qquad (35)$$

Peak load was said to occur at the point where passive loads exceeded plug resistance whereupon it was assumed a plug failure would occur and stresses would be relieved. This peak was said to act simultaneously and independently of core failure since it could not be proven that they did not. Thus the total ridge resistance was said to be the sum of the instantaneous maximum failure loads of both the core and keel.

Through algebraic manipulation it was shown that a quadratic equation, for which there is a closed-form solution, could be used to solve for the point of intersection between the two models. This adaptation was attempted since it simplified and shortened the probabilistic simulation routine. Complications arose, however, when considerations of alternate keel geometries were necessary so the original iterative technique prevailed.

The assumption of a triangular and or trapezoidal keel form while simplifying many aspects of the model, complicated matters when penetration occasionally went beyond the slope discontinuity before plug failure was attained. Special consideration was required in such cases.

Brown and Bruce (1995)

Brown and Bruce (1995) attempted continuum finite element modelling of first-year ridge keel interactions with vertical structures (both wide, two-dimensional and cylindrical types). They found that loads and failure modes resulting from keel interactions were less dependent on the ice rubble cohesion than the friction angle. The model indicated the dominance of rubble clearing mechanisms, including surcharge accumulations, during interactions and the tendency for shear failure in the keel to stay below the core-keel interface. Results also indicated that the loads were proportional to the square of the keel depth. Unfortunately model uncertainty was estimated to range as high as 40% and profound numerical difficulties were encountered at high strains. Non-linear material models additionally complicated the iteration process for solution equilibrium and as a result the use of continuum finite element procedures was discouraged.

Sayed (1995)

In Sayed (1995) a discrete element model is introduced which simulates ridge keel interactions with cylindrical structures. The principal advantages of the discrete or particle element model over continuum finite element methods are the ability to deal with large deformations and discontinuities which usually arise during failure and the realistic simulation of the interaction conditions between ice blocks. Sayed deals heavily with existing techniques for ridge keel load modelling suggesting that failure mechanisms have

so far been chosen completely arbitrarily and that they involve gross inaccuracies. His preference is for "a more accurate approach" which involves solving a set of governing momentum balance and constitutive equations.

Numerical results indicated a linear force dependency on keel depth and an increase in load as one exchanged a triangular keel with a larger trapezoidal one. "Plug formation" was questioned as a distinct failure mechanism since a continuum of velocities without distinct boundaries was observed in the simulations. It was reported, however, that plugs formed perpendicular to the length of a ridge regardless of the direction of ridge motion. Loads were shown to decrease by a factor of two when keel depth was halved, unlike the result from Brown and Bruce (1995).

The developments in particle element modelling reported in Sayed (1995) hold some promise. As described in Croasdale et al. (1995) however, the approach may best be used at this early stage of development as a calibration tool. Some issues which must be addressed include the unverified yet significant velocity dependency reported, inertia effects which do not consider the fluid in which the particles are suspended, and failure modes which do not agree with the model calibration test (in which Sayed compared results with a sand experiment by Bruneau, 1994b). The discrete element model would be improved if simulated interactions which began with the model stationed half way through the keel were to start at the leading edge of the keel. Almost all peak simulation loads are reported by Sayed to have occurred within one meter advance from the ridge centerline which may be a sign that this position is past the point of peak load for some interactions with the full keel cross-section (as demonstrated by most *cross-over* simulations).

Weaver (1995)

Croasdale *et al.* (1995) describe the development of a general passive failure model for ridge keels which incorporates structure slope angle, structure rubble friction angle and keel inertia. Dr. J. Weaver was the principal researcher behind the formulation. From first principles, a force equilibrium was established between adjacent rubble zones which comprise the mobilized rubble leading the penetrating structure. The complex formulation involves the pre-selection of rubble zone shape, flare, pitch and confining pressure, as well as the extent of rubble accumulation and the added mass factor of the bulk ice rubble mass. Ice rubble failure criteria were selected on a friction only or cohesion only basis. The model is written as

$$F = \frac{w + 2C_a \left[\dfrac{Z_h}{2\sin\theta} + F_2 \left[\dfrac{\tan\phi}{C_b} - \dfrac{\sin\omega\tan(\theta-\phi)}{C_a} \right] + F_1\tan\phi + \dfrac{c_2}{C_b} + c_1 + \dfrac{c_{12}}{2} \right]}{\tan(\theta-\phi) - \tan(\phi_1+\alpha)} \qquad (36)$$

where

$$C_a = \cos\theta[1 + \tan\theta\tan(\theta-\phi)]; \qquad C_b = \sqrt{1 + \tan^2\alpha\sin^2\theta} \qquad (37)$$

and Z_h is the horizontal inertia force associated with decelerating the failed rubble mass from the initial ridge speed to zero, written as

$$Z_h = \lambda \Delta M \frac{V^2}{2\Delta x} \qquad (38)$$

where λ is a factor that accounts for hydrodynamic added mass and ΔM is the additional mass of rubble and pore water incorporated into the failure wedge due to incremental penetration, Δx. It is not clear if this factor discounts the fluid dynamic inertia affects (drag) already present when currents free of ice flow past the structure. In the

formulation above, V is the velocity of the ridge and is assumed constant for the entire interaction, F_1 and F_2 are the horizontal forces acting normal to mobilized rubble adjacent to (region 1), and distant from (region 2), the structure, and c_1, c_2 and c_{12} are the cohesive shear strengths of the vertical shear planes for regions 1 and 2 and inclined at angle θ respectively. The weight of the multi-faceted failure wedge, w, is computed separately for each step of the advancing structure.

In Croasdale et al. (1995) the model is shown to compare favourably with laboratory results by Bruneau (1994b) and its ability to deal with progressive changes in the failure wedge form, structure slope, wall friction and keel inertia are emphasized. The model possesses a high degree of flexibility and it is not clear how sensitive the model is to some of the input assumptions about which little is known. Though this is presently a stumbling block the model does provide a promising framework for enhanced modelling in the future.

2.4.2 Comparison of models

Several of the models described above have been programmed into a spreadsheet as shown in Figure 2.15. The intention is to investigate the relative performance of various models and to demonstrate the variability between approaches and sensitivity to keel input parameters. Reference to other model comparisons can be found in Krankkala and Maattanen (1984), Croasdale et al. (1995) and others. Some models reviewed in the previous section were not suitable for spreadsheet application and as a result were either not included in the study or pre-computed results of specific case scenarios were quoted directly.

There are five scenarios considered in the upper table in Figure 2.15. The first corresponds to an arbitrary default case which is somewhat based on design conditions for ridges in the Northumberland Strait. The shaded blocks in the table indicate the parameters varied for each test while all other terms remain constant. Scenarios 2 to 5 consider a shallower ridge keel, greater cohesion, greater friction angle and broader structure respectively. In the lower table computed force values for each model and scenario are listed. The computed forces are also plotted. The results shows that, for predicted loads, the coefficient of variation across the board for the models shown was in excess of 50% on average. The range of results was greater than twice the average for some scenarios. Constant values for different scenarios (within a row in the lower table) attest to the insensitivity of some models to parametric change.

Despite the significant model uncertainty underscored by the jagged appearance of the horizontal chart, some interesting trends emerge. The average force for all models increases 43% over the default value when structure diameter is doubled. A decrease of 78% occurs when keel depth is decreased by a factor of two. Only an 11% increase is experienced when cohesion is doubled. The sensitivity to friction angle appears to be higher than cohesion though a linear comparison cannot be made.

The apparent lack of consensus amongst models comes as little surprise when one considers the data with which they have been calibrated. Laboratory experiments offer little guidance with hugely varying approximations of rubble shear strength. Field force measurements are scarce and, subject to interpretation, may have a higher degree of variability than the models. Even the simple parametric inputs such as ridge geometry show significant degrees of natural variability; for instance, the standard deviation of the

ridge keel slopes measured in the field was one-half the mean.

Improvement on the state of the art in ridge keel modelling will require an approach that deals with parametric and model uncertainty simultaneously. The combined approach will enable the optimization of a force model. sensitive to parameters proven significant and adapted to a relevant range of ridge boundary conditions.
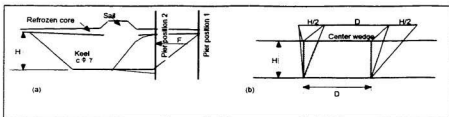
Figure 2.5 Passive failure model after Dolgopolov *et al.* (1975). (a) Interaction sketch (b) effective width model.
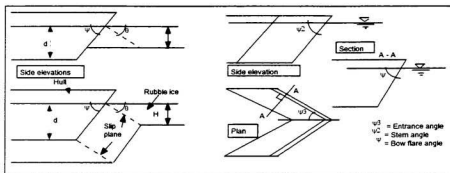
Figure 2.6 Ship resistance in first-year ice rubble after Keinonen (1979).
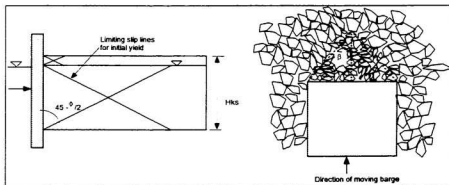
Figure 2.7 Passive shear failure model for ship resistance after Mellor (1980).
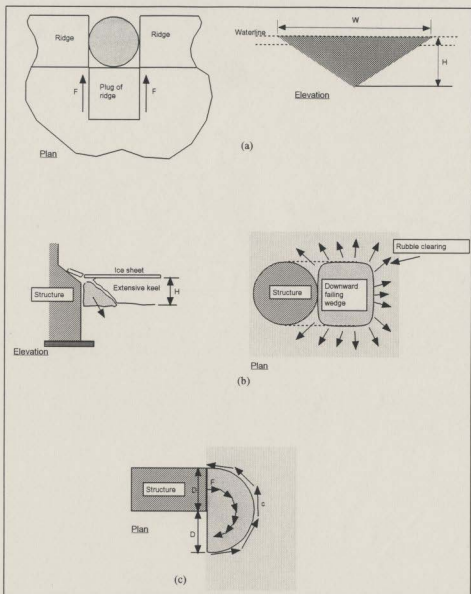
Figure 2.8 First-year ridge keel failure scenarios after Croasdale (1980, 1994). (a) Shear plug (b) wedge and (c) "footing type" failures.
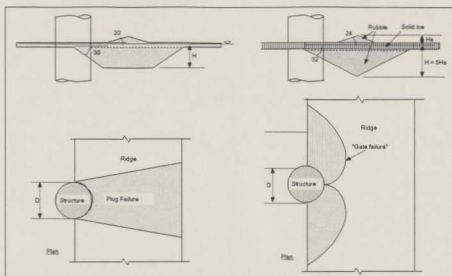
Figure 2.9 "Plug-type" (a) and "gate-type" (b) ridge failures after Prodanovic (1981).
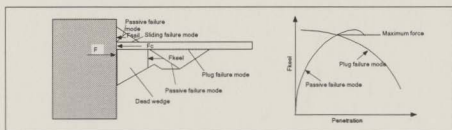
Figure 2.10 Ridge interaction schematic from Eranti *et al.* (1992).
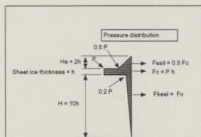
Figure 2.11
Maattanen's ridge pressure (cit. Krankkala and Maattanen, 1984).
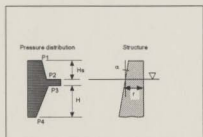
Figure 2.12
Hoikkanen's ridge pressure (cit. Krankkala and Maattanen, 1984).
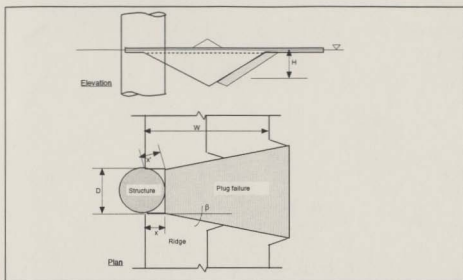
Figure 2.13 Ridge failure schematic from Cammaert *et al.*, (1993).
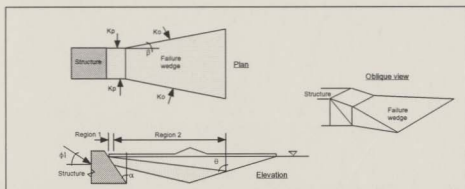
Figure 2.14 Ridge failure schematic from Weaver (cit. Croasdale *et al.*, 1995).

Parameters	Units	Default (1)	Shallower keel (2)	Greater cohesion (3)	Greater friction (4)	Broader structure (5)	Description/Notes
H	m	20	10	20	20	20	Keel depth below datum
W	m	64	32	64	64	64	Keel width = 3.2H
D	m	10	10	10	10	20	Structure projected width
α	rad	0.00	0.00	0.00	0.00	0.00	Structure slope
ρ_i	Kg/m^3	920	920	920	920	920	Density of ice blocks
ρ_w	Kg/m^3	1020	1020	1020	1020	1020	Density of sea water
e		0.3	0.3	0.3	0.3	0.3	Bulk porosity of ice rubble
c	Pa	2500	2500	5000	2500	2500	Apparent cohesion
φ	rad	0.61	0.61	0.61	0.87	0.61	Apparent friction angle
V	m/s	0.20	0.20	0.20	0.20	0.20	Interaction speed
q		2.33	1.67	2.33	2.33	1.67	Dolgopolov shape factor
Kp^.5	N/m^3	687	687	687	687	687	Square root of passive pressure coef
Hs	m	3.33	1.67	3.33	3.33	3.33	Sail height = Hi6
Ko		0.43	0.43	0.43	0.23	0.43	At-rest earth pressure coef = 1-sinφ

Model References		Predicted loads					
Dolgopolov et al (1975)	MN	9.4	2.3	12.6	12.7	13.4	Equation 11 (no surcharge)
Croasdale (1980)	MN	8.2	1.0	8.2	14.0	8.2	Equation 20
Prodanovic (1981)	MN	3.2	0.8	6.4	3.2	3.2	Equation 26
Mellor (1981)	MN	4.8	1.5	6.2	6.5	9.6	Equation 19
Joensuu (1981)	MN	11.1	2.8	11.1	11.1	22.2	Equation 32
Croasdale (1994)	MN	2.0	0.8	4.0	2.0	3.0	Equation 32
Croasdale (1994)	MN	7.2	1.3	7.2	12.2	10.3	Equation 25
Brown & Bruce (1995)	MN	16.0					input parameters are approximate
Sayed (1995)	MN	1.0					input parameters are approximate
Frederking (1994)	MN	2.1	0.5	2.1	2.1	4.2	Equation 33
Average	MN	6.5	1.4	7.2	8.0	9.3	
Standard Deviation	MN	4.6	0.7	3.2	4.8	6.0	
C.O.V	MN	0.7	0.5	0.4	0.6	0.6	
Minimum	MN	1.0	0.5	2.1	2.0	3.0	
Maximum	MN	16.0	2.8	12.6	14.0	22.2	
Range	MN	15.0	2.3	10.5	12.0	19.2	

Figure 2.15 Sensitivity study and comparison of ridge keel models.

Chapter 3

EXPLORATORY EXPERIMENTS

In the previous chapter the nature of ice rubble shear strength was explored. It was found that rubble behaviour is state-dependent and non-unique with very little full-scale data from the field for guidance. It was then shown that few laboratory programs have been undertaken specifically to model structures interacting with unconsolidated ridge keels. Keel load models in the literature were reviewed and a sensitivity study demonstrated that significant variation exists in model flexibility and output. Thus it has been shown that considerable parametric and model uncertainties exist, that the two are correlated and that this problem, at least in part, arises from a scarcity of field and laboratory data.

In this chapter a succession of exploratory experimental programs are described in which the purpose was to establish a database for ridge keel model development and calibration. The first, a broad study using simple techniques, looked at many ice rubble properties and keel-structure interaction scenarios. This program was followed by larger-scale sophisticated interaction experiments, sponsored by government and industry, and carried out at IMD by a research team. As in the first experimental program the failure mechanisms of unconsolidated ridges were observed and associated interaction forces were recorded. The last laboratory program described in this Chapter is one in which an *in situ* direct shear technique was developed for measuring ridge keel shear strength.

Data from these programs are analyzed collectively later in this thesis to provide direction for further experimentation and the development of an analytical force model.

3.1 Pilot experiments for first-year ridge modelling[1]

In this section small-scale laboratory experiments modelling first-year ridge interactions with structures are described. Tests were aimed at determining the mode of failure of ice rubble accumulations under varying loading conditions and the stress levels required for failure. The packing density and shear behaviour of the laboratory ice rubble were also examined under varying conditions since these properties influence the strength of ridge keels and are necessary for model calibration. The first attempt to substitute sand for ice rubble as a modelling tool for studying keel rubble failure mechanics is also described.

3.1.1 Scope of experiments

Experiments were undertaken in the summer and fall of 1994 with the intention of replicating first-year ridge keel encounters with fixed offshore and coastal structures. For logistical reasons the experiments involved translating a rigid indentor (or model pier) into stationary ice rubble. This preserves the relative motions of the pier, rubble and water yet simplifies testing. The tests are designed to demonstrate the trends in failure mode and loads as control parameters are varied.

All experiments were conducted at C-CORE in a cold room at 0° C. Commercially available freshwater ice cubes were used for the tests. Floating accumulations of ice rubble were systematically indented by a mechanically driven, instrumented cylinder in the first test series. Similar procedures were used to test the ice rubble in a dry state, stacked on a false floor inside the tank. First-year ridges may reach depths of over 20

---

[1]A version of this section was prepared for K.R.Croasdale and Associates, sponsored by National Energy Board and titled *Bruneau, S.E (1994a) Ice load models for first-year ridges and rubble fields - physical laboratory tests*.

m so that hydrostatic pressure due to buoyancy can be high, up to 15 kPa as one approaches the waterline from the keel bottom. For a cohesive granular material (obeying linear Mohr-Coulomb failure criteria) the frictional shear resistance would be relatively high, theoretically three times cohesion if $c = 5$ kPa and $\phi = 45°$. It may be expected, however, that for accumulations of rubble at the laboratory scale, cohesion would dominate rubble shear strength since buoyant stresses are low. The "dry" tests, which effectively increase inter-block stresses by as much as an order of magnitude for similar sized accumulations, attempted to examine this effect. Pore fluid and boundary conditions also change the behaviour of ice rubble so that normal stress effects were not perfectly isolated in these experiments, considered exploratory in nature.

Overall dimensions of ridge keels and ratios were geometrically scaled at approximately 1 to 100 (for the case of the Northumberland Strait Crossing Project) but particle scaling and dynamic modelling (forces mainly) were not intended or achieved in the lab. The control parameters considered for the ice rubble indentation tests were the ice temperature upon placement, the rubble contact duration before indentation and the width and depth of the rubble accumulation.

Model "sand keels" were indented to demonstrate the potential for this approach to aid in ridge keel model development. The properties of silica sand are well-defined and some load formulas used in ridge keel modelling are geotechnical in origin. Thus it was postulated that sand tests, which are easier and faster to perform, would provide a meaningful analogue for ice rubble experiments. Furthermore, parametric control and observation capabilities are greatly enhanced.

A shear box apparatus was developed and used to determine the cohesive and frictional properties of the ice rubble studied, and, rubble porosity and repose angle were determined.

3.1.2 Apparatus

A steel tank one meter square at the top and 0.76 m deep was used in the study (Figure 3.1). Its heavy steel frame and rugged support legs provided a stable platform for the drive mechanism used in the indentation and shear tests. Two plexiglass windows (0.6 m square) were installed in the side and rear of the tank for underwater lighting and viewing. The drive mechanism was an assembly of aluminum and steel structural parts, a traversing block which rigidly supported the model indentors, a threaded lead screw and a stepper motor. The motor was controlled through a power supply unit by a Zenith 386 laptop PC supporting stepper motor software.

Data acquisition was handled through a 286 PC with a 10 V data acquisition card on board using **Snapshot** software. Two, 1.1 kN, waterproofed, cantilever load cells, on loan from the Institute for Marine Dynamics (IMD-NRC, St. John's), were used for load measurement. Using the two single axis load cells as model supports permitted the resolution of the resultant load. A "yoyo" displacement potentiometer was attached to the top of the drive mechanism to measure the absolute displacement of the traversing block relative to the tank frame. All experiments were recorded using a Super VHS recorder mounted on a high tripod beside the tank.

Ice and sand properties

Ice used in the studies was purchased from a commercial supplier of ice cubes. Unused,

the individual pieces were roughly cylindrical, concave at the ends and had a diameter of 25 mm and a length of 30 mm. The pieces changed shape after some use by losing sharp edges and concavity and some grading occurred through agglomeration and splitting. The ice temperature during testing ranged from -24° to 0.0° C.

Subangular silica sand type 'O' with a dry weight of at 13880 N/m³ was used for all sand tests. The internal friction angle at this specific weight is around 32 degrees and the effective grain size is 0.325 mm (Paulin, 1992).

3.1.3 Structure interaction experiments with ice rubble and sand

Floating ice rubble indentation experiments

Air, water and ice temperatures were recorded before each indentation test. The placement time and test time were also taken so that static contact duration of the bulk ice rubble samples was known. Ice stored in a deepfreeze was removed and mechanically separated by striking and applying pressure to the containment bags. This ensured that all freeze-bonds between ice pieces were broken prior to placement in the tank support frame. After a few moments the central gate section of the support frame was removed to provide a clear path for the model structure (Figure 3.2). The remainder of the frame acted as a rigid (moment-bearing) connection for the ice formation adjacent to the exposed area. The indentor was computer-controlled to advance at a rate of 6 mm/s with a 2 mm/s² acceleration and deceleration at the beginning and end of each test. The motor drive was stopped at a prescribed distance into the rubble. The deformed rubble accumulation was observed after each test and a recording of the unloading process was made. The support frame was partially removed from the tank to allow access to the ice

rubble for removal, drainage, bagging and storage.

With the exception of calibration files all experiments were recorded digitally at 50 Hz for a 120 second interval and later lowpass filtered digitally at 3 Hz. The calibration coefficients determined in a pretest calibration experiment were applied to each of the raw voltage data time series. A time channel was established and the results from the two load cells were added to establish a 5 channel data file of the calibrated data time series. After plotting the complete series for each test the exact starting point for the indentation was found and the first 60 seconds of each test was isolated.

Nine floating ice rubble indentation experiments were recorded as listed in the table in Figure 3.3. The settings for the first two experiments represented the default values of the control variables. Tests were performed to determine the sensitivity of load and failure mode to ice temperature and contact duration, rubble depth, rubble width, and support boundary conditions. Since the temperature of the ice after placement in the water was not measured the residency of the ice in the tank (at $0°$ C) is given.

The table also lists the maximum force on the pier model during the first 60 seconds of each test and the failure modes observed. The bar chart in Figure 3.3 indicates the relative influence of the control parameters. From this figure some trends in measured forces emerge:

- load is highly sensitive to rubble depth,

- warmer ice rubble results in reduced strength,

- the width of the rubble accumulation influences indentation resistance,

- continuous "rubble fields" have greater resistance than discrete "ridges", and

- rubble shear resistance increases with contact duration.

Additional analysis indicated that over the first 60 seconds maximum loads were, on average, double the mean loads for both discrete rubble and continuous rubble accumulations while the standard deviation was between 1/4 and 1/2 the mean.

The load traces for tests RF012 and RF08 are shown in Figures 3.4 and 3.5. These traces are representative of the indentation of discrete (ridge-like) and continuous (rubble field-like) accumulations. Failure modes observed on video records were synchronized with force records and are summarized on each figure.

The plug failure observed in the floating ice rubble tests is generally preceded by some local failure. A few tests saw plugs form simultaneously with first ice contact. Most often, however, the indentor was embedded in the rubble formation when the plug forms. On average plug movement started when the indentor penetrated 12% of the rubble width. The geometry of the plug varied considerably. Often failure planes flared tangentially from the pier model outwards towards the support points at the rear of the rubble mass. Occasionally though straight shear planes formed between fore and aft support points leaving much of the ice around the indentor undisturbed. Usually, the plug tended to advance in stages as it remained partially interlocked with the rest of the ice.

The local (non-plug) failure mechanism was characterized by an upward shifting of ice pieces which formed a raised elliptical crescent around the indentor. Some large scale shifting of rubble in the outer reaches of formation were observed. The raised ice formation extended out in front of the indentor approximately the depth of the ice but

tapered around the sides and fell off to below level ice grade and ultimately to water level behind the indentor. The depth of the pile-up at the highest point was approximately 2-4 cube widths above level ice grade.

At least three dynamic load mechanisms (or load release mechanisms) were recognised in all load traces. The highest frequency appears to correspond to the repositioning of individual ice pieces within the coherent formation. Clumps of ice rubble periodically shift in the vicinity of the indentor leading to lower frequency events. The lowest frequency corresponds to the global repositioning of bulk rubble blocks during plug-like failure.

Dry ice rubble indentation experiments

A series of eleven "dry" ice rubble indentation tests were conducted in the tank in the C-CORE cold room. A false floor made of high density polyethylene and a new, shorter pier model were placed in the tank after water was removed. The pier was positioned so that it swept over the smooth plastic floor with a spacing of 6 mm throughout. Ice rubble was placed on the floor in a fashion similar to the tests performed in water using the same holding pen and positioning system. Ice temperature, rubble depth and the slope of the leading and trailing edge of the accumulations were varied. Indentation rate was 6 mm/s.

The table in Figure 3.6 lists the conditions under which the tests were performed. Load traces for test DR03, for a "ridge-like" formation and DR05, for a "rubble field-like" formation are shown in Figures 3.7 and 3.8. The two traces reveal distinctly different force patterns which also correspond to dissimilar failure modes observed during testing.

Trends in peak loads observed in Figure 3.6 are essentially the same as those for floating rubble when similar control parameters are varied. Some of the "dry" rubble test results are as follows:

- load is sensitive to rubble depth and sectional area,
- warmer ice rubble results in reduced strength,
- continuous "rubble fields" have greater resistance than discrete "ridges", and
- rubble shear resistance increases with ice contact duration.

The maximum loads for both discrete ridge and continuous rubble tests were roughly double the mean and the standard deviation was very near 1/2 the mean. Uniform cyclic loading was observed in tests DR01, DR02, DR10 and DR11. This corresponded to a ratchet-like advance of the indentor, originally believed to be lock-in resonance at the structure fundamental mode. However, further inspection of the time histories revealed that cycles were around 1.7 Hz - one-tenth of the fundamental frequency of the structure. Thus it is more likely that the dynamic loading is a complicated interaction between the ice and the structure, controlled by advance rate, structural stiffness, and ice extrusion processes associated with creep, compressibility and crushing strength.

Plug failure geometry and movement was difficult to observe in the "dry" tests. The ice shifted in quick steps making it difficult to discriminate where failure planes had formed. It appeared that rubble movement occurred across a flaring wedge shaped rubble block which leads the indentor. The first plug movements were noticed 30 seconds into the indentation at 180 mm or 40% of the rubble width on average. The local (non-plug) failure mechanism may be characterized as a cyclical rearrangement, lifting and translation of clumps of ice pieces. The raised formation was elliptic and tapered. The

depth of the pile-up was approximately 2-4 ice cube diameters.

Maximum forces in the "dry" tests were anywhere from 2.5 to 10 times greater than those in similar floating rubble tests where the ratio of dry weight to buoyant weight was approximately 11. Assuming loads from inertia, fluid dynamics and floor friction to be relatively low, one would expect little difference between indentation forces for wet and dry tests if the rubble were purely cohesive. Also, if the rubble were purely frictional then the indentation forces should be proportional to normal forces, *i.e.* weight. Since results are somewhere in between one may infer that both properties act, though the probable dependency of ice rubble cohesion on confining stresses complicates this interpretation.

Sand indentation experiments

Experiments on damp sub-angular silica sand were performed utilizing the apparatus as configured for the dry ice tests (Figure 3.9). Figure 3.10 lists and illustrates the results for the four "sand keel" tests performed. Loads appear to be directly proportional to the sectional area of the "sand keels". Plug failure occurred approximately 30% of the way through the pile widths though the ratio is probably a function of sand depth, width and structure diameter. The continuous sand layer yielded the highest resistance - a 30% increase over the others. Figure 3.11 indicates that the load levels and patterns at penetrations up to 30% of keel width were the same for all tests, which supports the basis of the *cross-over* modelling approach as described in Section 2.4 and illustrated in Figure 2.10 (where peak loads occur at local and plug failure transition). The three plug failure force traces are remarkably similar to the force trace DR03 for a similarly shaped "dry" ice rubble accumulation. The pattern is again seen in the first 20 seconds of

RF012, a floating ice rubble experiment. This is evidence that gross failure modes for sand are somewhat representative of those for ice rubble.

Failure patterns easily distinguished in the damp sand are sketched in Figure 3.12 for test SA02. The local plastic deformation of the sand was characterized by an uplifted area of sand that increased in height, broke and was divided as the indentor approached and passed. In the slightly damp sand there was a tendency for the sand to terrace as repeated passive failures occurred.

The origins of the plug failure shear planes were not distinctive but appeared to be within the compressed passive failure zone adjacent to the indentor. The planes propagated outward towards the far side of the sand formation breaking at an increased angle near the free edge. They did not appear to be vertical planes nor did the sand within the plug translate uniformly. The leading edge of the plug fanned out, cracking and falling in height. The entire plug appeared to slide on the plastic floor so that sand did not remain in the rear path of the structure.

3.1.4 Shear box experiments

The shear strength of the ice rubble used in the indentor tests was investigated. Both normal stress and ice temperature at placement were controlled so that Mohr-Coulomb yield criteria could be established for different temperature regimes. A shear box was fabricated from heavy polyethylene and PVC as shown in Figure 3.13. The experiments involved placing ice rubble into the shear box which was positioned in the water so as to allow neutral buoyancy of the ice when the box was full. The top shear ring of the box was pulled horizontally by a load cell on the traversing block at 1 mm/s relative to the

stationary bottom ring.

Eighteen tests were performed in which ice temperature, contact duration and normal stress were controlled. Five tests were performed without any ice to monitor and calibrate the friction of shear box mechanism, before and after tests. All test results have been corrected for no-load box friction.

The maximum shear stress in the first 60 seconds for each test is listed in the table in Figure 3.14. Sample force time-histories are shown in Figures 3.15 and 3.16 for SB08 and SB14.

Load traces for the shear box exhibited 2 scales of load and release. The first at high frequency and low load amplitude (1-30 N and 1-5 second periods), the second at low frequency and high load amplitude (hundreds of Newtons at 25 second periods). The small force fluctuations probably resulted from incremental shifts in ice pieces as the rubble mass was compressed. The large fluctuations resulted from the global shearing of the bulk rubble sample. With interest it is noted that the dominant low frequency high load cycle occurs at a displacement approximately equal to one ice cube diameter (25 mm). The predominant shape of this load trace is saw-toothed with the load drop occurring earlier in tests with lower normal pressure (surcharge).

Shear strength was calculated from the first peak before a major drop in load. In a few tests secondary cycles achieved higher loads but may have involved jamming so these results were not considered. The normal stress was determined by adding the buoyant weight of ice beneath the shear plane to the steel weights and plastic platen used for surcharge, and then dividing the sum by the original cross sectional area of the shear

box.

Figure 3.14 shows the plots of maximum shear stress versus normal stress for both cold and warm ice rubble in the lab. The Mohr-Coulomb approximation is shown for each. Values fall in the range of those reported in the literature as described earlier. The friction angle was similar for tests with warm and cold ice (54° and 59°). Cohesion, on the other hand, appeared to be significantly affected by the temperature of the rubble with an apparent threefold increase for colder ice (720 to 2460 kPa).

3.1.5 Ice rubble repose angle experiments

Repose angle experiments were aimed at detailing the influences of ice rubble temperature and block shape on repose angle (Figure 3.17). Ice was piled lightly with a scoop into a mound centred around a vertically positioned measuring rod. Ice used in these tests fell into three categories; dry unused ice cube rubble from the deepfreeze ($\approx$ -21 C), previously used (in the wet tank) rubble also taken from the deepfreeze, and warm ice (0 C) which was used in wet tank experiments. After five trials with each sample the cold, new ice (the most angular of all) exhibited the steepest repose angle at 36°. The warm ice averaged an angle of 34° and the cold used ice was measured at 33° on average. Repose angle is often considered a lower bound estimate of the internal angle of friction for cohesionless soils (Bowles, 1985).

3.1.6 Ice rubble porosity experiments

The bulk porosity (volume of voids to total volume ratio), e, of the ice used in the experiments was determined in both dry and submerged states. To determine the ratio of the volume of ice to the bulk volume of a sample (1-e), a large container of known

volume was loosely filled with experimental ice and weighed. The volume of ice was determined from the measured weight assuming an ice density of 919 kg/m³. The ratio of open volume to the total volume of the container was then determined. Results are shown in Figure 3.18. Ice that had been previously used in wet tests had 36% porosity while new, unused (more angular) ice was around 44%. Ice taken directly from the tank in a wet state had a porosity of around 39%.

In an effort to determine the porosity of floating ice rubble *in situ*, a large plastic container of known volume was placed in the test tank so that it was approximately 80% submerged. The bottom and sides of the container had been perforated with 5 mm holes so as to allow the free flow of water. Ice was added to the container until it was completely filled - apparent when ice obscured the visibility through the lower holes in the container wall. With the ice flush across the top, the container was slowly removed allowing complete drainage of the sample. The porosity was then determined (through weighing and volume calculations) to be 29%.

The drop in porosity for the "submerged" ice rubble was unexpected since it was anticipated that ice deposited in water would be subject to lower normal stresses leading to a decreased packing density. This may, however, have been more than offset by both the mode of deposition (always added from the top and pushed down), the melting of asperities and the fact that the ice used in this test had been utilized in other experiments and may have been somewhat graded. The bonding of some blocks and breaking up of others in prior experiments would lead to a tighter packing arrangement than new, sorted ice rubble.

3.1.7 Summary of C-CORE pilot test series

The resistance to indentation of floating laboratory ice rubble accumulations increased non-linearly with rubble depth, decreased with rubble width and decreased with higher ice temperature (at time of placement). Continuous rubble indentation resulted in higher loads than discrete "ridge-like" indentation. Plug failure occurred 12% of the way into the rubble formation on average. The plug geometry varied considerably as shear planes formed in parallel, flared and curved patterns for different tests. Maximum loads were on average double the mean and standard deviations were between 1/4 and 1/2 the mean for the first 60 seconds of the tests.

"Dry" ice rubble indentation test loads decreased with rubble sectional area, increased with decreased ice temperature at placement and increased when plug failure was not permitted (continuous rubble layer over discrete ridge tests). Loads were 2.5 to 10 times greater that similar tests on floating rubble (the ratio of effective weights being 11). Plug failure occurred 40% of the way into the rubble formation on average. Mean loads were approximately 1/2 the maximum and standard deviations were 1/2 the mean.

Indentation tests on "sand keels" yielded smooth load traces and highly reproducible results. The two failure mechanisms, local passive and global plug-like, were easily distinguished in the force-time histories and video records. Plugs were "bell" shaped and occurred 30% of the way into the formation. Similarities between "sand keel" force trace patterns and those for ice rubble supported the hypothesis that sand may be used as a modelling tool for looking at failure modes of ice rubble.

Shear box experiments on floating ice rubble demonstrated the sensitivity of rubble shear

strength to ice temperature at the time of submergence. Mohr-Coulomb criterion established from the shear box tests produced friction angle values of 59° and 54°, and cohesion values of 720 Pa and 2460 Pa for warm and cold ice respectively. Tests also revealed two scales of load cycling in the force traces. The first was a high frequency low load event, the second was a low frequency and high load event occurring at a displacement around one ice block diameter.

The repose angle of the lab ice varied from 36° when cold and angular, to 33° when cold and used. Ice rubble porosity varied from wet to dry states and with the degree of prior use. Values ranged from 44% porosity for highly angular, cold, dry ice to 29% for submerged, used ice.

The physical laboratory tests described have demonstrated that the shear resistance and structural strength of ice rubble at laboratory scale are highly influenced by the temperature of ice upon placement (whether it is submerged or not), normal stresses, residence time (in a static position), and to a certain degree the geometry of the lab ice pieces and boundary conditions. The geometries of plug and local passive failure surfaces are complex and somewhat random. Sand provided a useful tool for demonstrating force trends and failure modes and may provide the simplest approach for parametric investigations of other ridge keel failure properties.
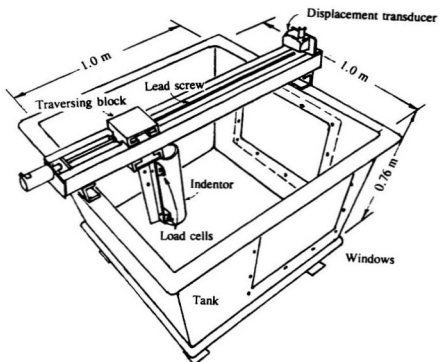
Figure 3.1 Oblique view of apparatus.
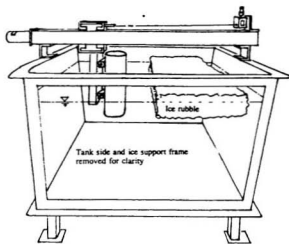
Side view
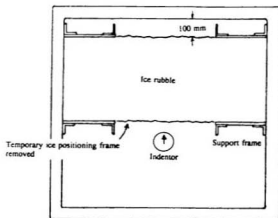
Plan view

Figure 3.2 Setup for floating "wet" ice rubble experiments.

Test	Test description	Ridge depth mm	Ridge width mm	Ice temp/ condition*	Duration in frame min.	Max force (first 60 s) N	Mean force (first 60 s) N	Failure modes observed
RF01	Default conditions	200	450	-24 C	7	40.0	n/a	Local then plug at 25% wid
RF012	Default conditions	200	450	-24 C	7	30.1	18.0	Immediate plug
RF04	Warmer ice and increased duration	200	450	1 hr in tank	30	19.6	13.1	Mixed: local and plug
RF02	Shallower rubble keel	100	450	-24 C	8	10.7	6.2	Mixed: flexure and plug
RF06	Deeper rubble keel	250	450	20 mins & -24C	7	43.1	26.9	Local then plug at 25% wid.
RF03	Narrower rubble keel	200	300	-24 C	7	16.2	7.8	Plug immediately
RF05	Continuous rubble field	200	Contin.**	50 & 30 mins	8	60.0	27.9	Local
RF07	Contin.** and warmer ice	250	Contin.	1hr & 10 mins	10	47.4	20.7	Local
RF08	Contin. and warmer ice	250	Contin.	1hr & 30 mins	9	55.3	27.0	Local
RF09	Contin. and warm ice, long duration	250	Contin.	21 hrs	1140	167.0	36.3	Local

* Temperature given if ice is new, if time is given it is the period since the ice was removed from a freezer at -21 C and placed in water at 0 C.
** Contin. means that the rubble layer was continuous to the back wall of the tank.
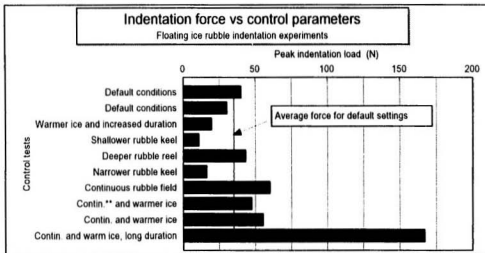
Figure 3.3 Floating ice rubble test conditions and results.
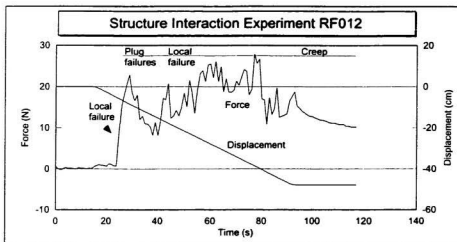
Figure 3.4 Force trace for "ridge-like" interaction (floating rubble).
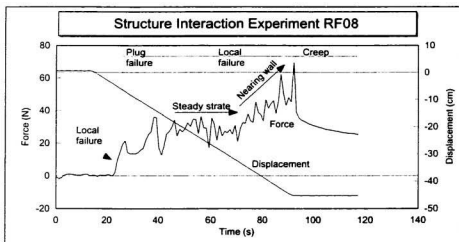
Figure 3.5 Force trace for "rubble field-like" interaction (floating rubble).

Test	Test description	Ridge depth mm	Ridge width mm	Ice temp./ condition	Duration in frame min	Max force (first 60 s) N	Failure modes observed
DR01	Default**	200	450	-24 C	15	169.9	Local (w/resonance) - plug
DR03	Warmer	200	450	3 hrs @ 0 C	7	119.6	Local then plug
DR04	Warmer, sloped	200	450	3 hrs @ 0 C	7	51.5	Local then plug
DR06	Warmer, sloped	200	450	4 hrs @ 0 C	5	58.4	Mixed: local and plug
DR10	Shallower, warmer**	100	450	27 hrs @ 0 C	7	99.2	Local then plug, repeated
DR11	Shallower, warmer v.low slope**	100	450	27 hrs @ 0 C	7	106.8	Local then plug repeated
DR07	Long duration and warmer*	200	450	26 hrs @ 0 C	1320	218.9	Local - test incomplete
DR02	Contin.**	200	Contin.	-24 C	15	173.0	Local (w/resonance)
DR05	Contin. sloped	200	Contin.	4 hrs @ 0 C	5	88.6	Local
DR06	Contin., sloped, warmer	200	Contin.	26 hrs @ 0 C	7	254.4	Local - test incomplete
DR09	Contin. shallower, warmer*	100	Contin.	26 hrs @ 0 C	7	106.7	Local: mixed modes

Indentation force vs control parameters

Dry ice rubble experiments

Peak indentation load (N)

Control tests:
- Default**
- Warmer
- Warmer, sloped
- Warmer, sloped
- Shallower, warmer**
- Shallower, warmer v.low slope**
- Long duration and warmer*
- Contin.**
- Contin. sloped
- Contin., sloped, warmer
- Contin. shallower, warmer*

Average force for default settings

* : Motor stalled as 200N system threshold was surpassed
**: Ratchetting of indentor occurred - Ultimate peaks shown on graph

Figure 3.6 Dry ice rubble test conditions and results.
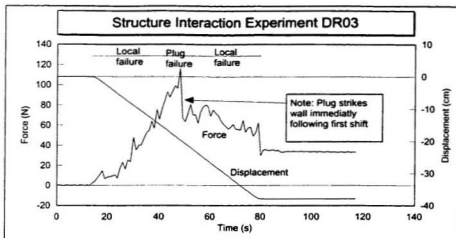
Figure 3.7 Force trace for "ridge-like" interaction (dry rubble).
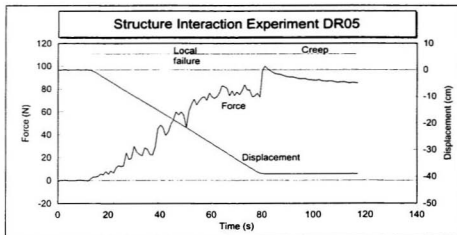
Figure 3.8 Force trace for "rubble field-like" interaction (dry rubble).

Cylindrical
structure
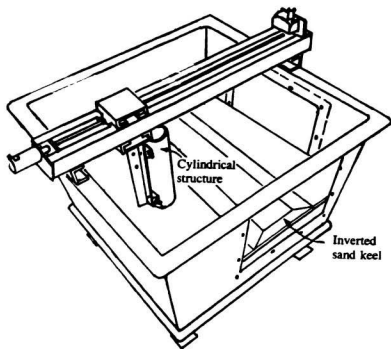
Inverted
sand keel

Oblique view

Figure 3.9 Setup for inverted "sand keel" experiments.

Test	Test description	Sand depth mm	Sand width mm	Sand area mm^2	Moisture content	Max. Force N	Failure modes observed
SA01	Triangle, damp	110	450	25000	Damp sand	44.0	Local then plug
SA02	Trapezoid, damp	75	450	30000	Damp sand	47.3	Local then plug
SA03	Trapezoid (narrower), less dam	75	400	25000	Sl. less damp	43.8	Local then plug
SA04	Continuous, less damp	75	Contin	n/a	Sl. less damp	61.3	Local

Indentation force vs control parameters

"Sand keel" experiments
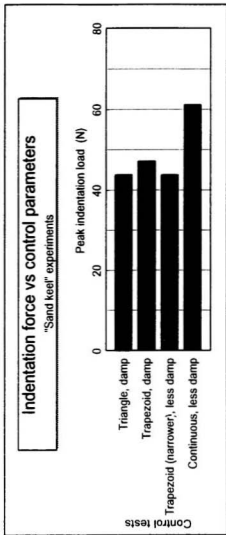
Figure 3.10 Sand test conditions and results.
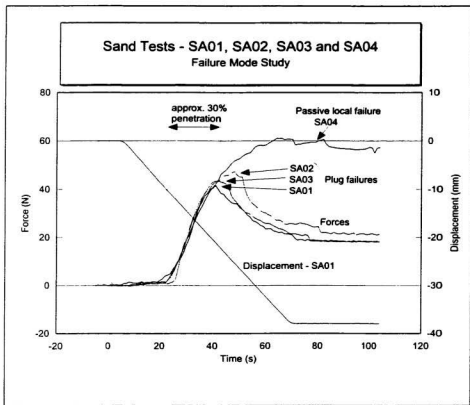
Figure 3.11 "Sand keel" force traces superimposed.
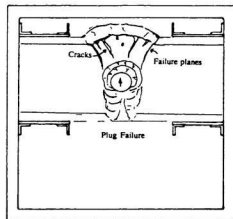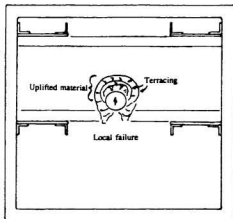
Figure 3.12 Failure patterns in an indented "sand keel" (SA02).

0.25 m diam.

0.24 m full ht.

Platen

Tension rod

Top ring

Guides

Bottom ring

Platform

Oblique view

Drainage holes

Sliding blocks

Plan view
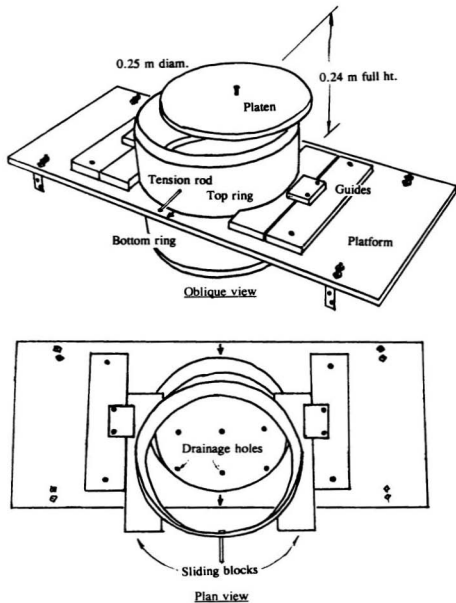
Figure 3.13 Polyethylene shear box for ice rubble.

Test	Ice temp / condition*	Contact duration Min	Speed mm/s	Over-burden + kg	Max force (first 60mm) N	Confining pressure Pa	Max. shear Pa	Mean shear Pa	Std. dev. shear Pa
SB05	-21C	6		ice	122	115	2407	1281	608
SB06	-21C	6		ice	158	115	3154	1989	760
SB07	-21C	6		ice + 2.57	143	638	2849	2129	609
SB08	-21C	6		ice + 2.58	162	640	3237	2101	746
SB09	-21C	6		ice + 2.58	221	1251	4452	2830	709
SB12	5 hrs @ 0 C	1		ice	36	115	633	291	133
SB13	5 hrs @ 0 C	1		ice + 2.58	86	115	1660	1356	671
SB14	wet ice (0C)	1		ice	63	115	1183	671	291
SB15	wet ice (0C)	1		ice + 2.58	132	640	2621	1556	576
SB16	wet ice (0C)	1		ice + 1.58	132	1251	2605	1883	557
SB17	wet ice (0C)	1		ice + 1.58	50	437	913	779	234

* Temperature given if ice is new, if time is given it is the period since the ice was removed from a freezer at -21C and placed in water at 0 C.

Shear vs normal stress

Direct shear - submerged ice rubble

■ Cold ice slope=54 deg, intercept = 2460 Pa
◇ Warm ice slope=59 deg, intercept=720 Pa
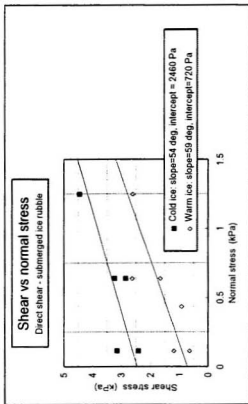
Figure 3.14 Shear box test conditions and results.
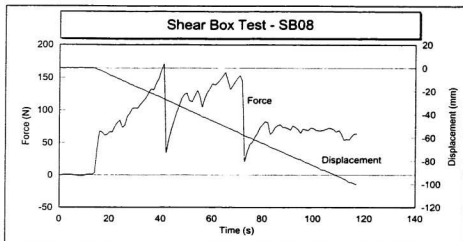
Figure 3.15 Force trace for "cold" ice rubble shear test - with surcharge.
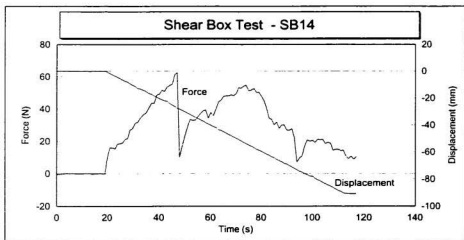
Figure 3.16 Force trace for "warm" ice rubble shear test - without surcharge.
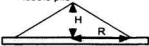
Ice		Trial 1	Trial 2	Trial 3	Trial 4	Trial 5	Average
Dry/used	(x 2.5 cm)	6	7	5	5.5	6	
Cold	(x 2.5 cm)	10	9	9	8.5	9	
	Angle	31	38	29	33	34	33
Dry/new	H	8	8	7.5	6.5	7	
Cold	R	11	10	11	10	9	
	Angle	36	39	34	33	38	36
Wet/used	H	6	6	5	5.5	5	
Warm	R	9	9	8	8	7	
	Angle	34	34	32	35	36	34
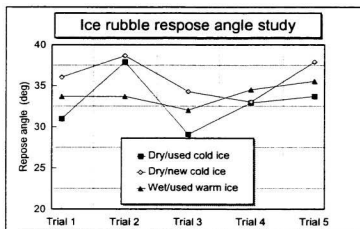
Figure 3.17 Ice rubble repose angle test conditions and results.

Test	Mass bucket Kg	Mass full bucket Kg	Mass water Kg	Volume water l	Porosity (%gas) %
Liquid water	1.78	21.09	19.31	19.31	0
Used ice, dry	1.78	12.94	11.16	12.40	36
New ice, dry	1.78	11.47	9.69	10.77	44
Wet ice	1.78	12.56	10.78	11.98	38
Drained wet ice	1.78	12.27	10.49	11.66	40
Submerged	1.10	15.70	14.60	16.22	29
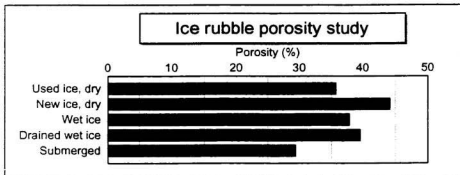
Figure 3.18 Ice rubble porosity test conditions and results.

3.2 Ridge failure at oblique approach angles[1]

3.2.1 Introduction

The physical laboratory tests with sand described in the previous section (and in Bruneau, 1994a) were extended so that some ridge failure patterns could be examined in more detail. They were motivated by the successful application of Section 3.1 results to the calibration of load prediction models for the Northumberland Strait Crossing Project. For example, the distinct local and plug-like failure modes observed justified the use of the *cross-over* modelling approach, and the consistent flaring of plug rupture planes was newly incorporated.

The experimental program described here was undertaken to determine model keel failure modes and load levels for certain loading conditions with a view towards resolving some outstanding issues in ice load modelling for the NSCP. In particular, the effects of ridge *obliquity* were not known. In principle, when a ridge is oriented at an angle other than 90° to the direction of travel the cross-section through which a structure must pass is extended. Seabed anchor pull-out experiments (reported by Vesic 1971, and others) indicated that rupture would strike out towards the nearest free surface and not follow the direction of travel. Otherwise, little guidance was found in the literature on the potential influence of oblique interactions on loads and rupture patterns. Experiments were undertaken to determine these obliquity effects and to investigate the influence of floor roughness and structure-to-keel size ratio on these effects.

---

[1] This study was sponsored by Public Works Canada at the request of K.R. Croasdale and Associates and reported as *Bruneau S.E. (1994b) The indentation of sand formations*.

3.2.2 Scope of tests

The laboratory apparatus and testing procedures were similar to those in Subsection 3.1.3. Obliquity was expected to produce lateral loading on the structure so both longitudinal and lateral loads were measured. This was achieved by changing the support position of the uniaxial cantilever load cells. Experiments were repeated with opposite approach directions so that any bias in the axial measurement of "non-axial" loads would become evident.

Roughening the false floor was achieved by adhering sandpaper sheets (with grit size equivalent to sand particle size) to the entire floor area. The rough surface was intended to model the interlock expected between an ice ridge keel and the overlying refrozen core. Oblique "sand keels" were aligned according to painted angle markings on the floor.

3.2.4 Oblique ridge experimental results

Eight test series are reported in Table 3.1. The first four ("00", "10", "70", "80") refer to tests carried out on a smooth polyethylene floor inside the tank. The next two test series ("110", "120") were repeats of earlier ones, only they were performed on a roughened floor. The last two ("130" and "140") were performed on a rough floor and with a larger keel (depth H) and smaller structure (diameter D). These tests were aimed at determining the influence H/D on the obliquity force trends.

Figures 3.19 and 3.20 show plotted results and include schematics of the test series. Test series "10" and "70" are repeats of the default conditions with opposite approach directions. Similar results (for "00" and "80" also) confirmed that the data were

independent of the direction of loading on the cantilever load cells. For all the tests, the angle of obliquity was shown to increase longitudinal loads by a maximum of 20% though almost no effect was measured at angles below 50°. In fact, loads were sometimes reduced by as much as 10% at low oblique attack angles. Both longitudinal test series with the rough floor ("110" and "130") showed even less sensitivity to obliquity although it can been seen from Table 3.1 that roughening the floor increased structural loads by 10 to 25%. At a higher H/D ratio the influence of obliquity on longitudinal forces appeared to be diminished slightly at high obliquity angles but otherwise was similar to other test series.

Lateral loads ranged from almost zero for perpendicular entry to approximately half of the longitudinal force. Maximum lateral loads typically occurred at an oblique angle of 60°. The "exit force" (lateral force when structure leaves the "sand keel") often exceeded the "entry force" and was opposite in direction.

The modest influence of obliquity angle seen in these tests persuaded engineers to exclude it the design load strategy for the NSCP. The sensitivity of loads to the floor roughness was interpreted to suggest that, when modelling keel failure analytically, the internal friction angle of the rubble should be used as a friction coefficient on the horizontal shear plane.

Table 3.1 "Sand keel" obliquity experiments.

Test	Ridge obliquity deg	Keel width mm	Keel depth mm	Model diameter mm	Floor surface	Maximum force N	Minimum force N
						Lateral	Lateral
AN00	0	160	38	114	Smooth Poly.	0.558	-1.95
AN01	10	160	38	114	Smooth Poly.	0.639	-1.84
AN02	20	160	38	114	Smooth Poly.	0.607	-2.5
AN03	30	160	38	114	Smooth Poly.	0.853	-2.93
AN04	40	160	38	114	Smooth Poly.	1.03	-2.8
AN05	50	160	38	114	Smooth Poly.	1.35	-3.77
AN06	60	160	38	114	Smooth Poly.	1.49	-4.16
AN07	70	160	38	114	Smooth Poly.	1.71	-3.77
AN09	90	160	38	114	Smooth Poly.	0.51	-2.35
						Longitudinal	
AN10	0	160	38	114	Smooth Poly.	6.56	
AN11	10	160	38	114	Smooth Poly.	6.18	
AN12	20	160	38	114	Smooth Poly.	5.93	
AN13	30	160	38	114	Smooth Poly.	6.44	
AN14	40	160	38	114	Smooth Poly.	6.2	
AN15	50	160	38	114	Smooth Poly.	6.85	
AN16	60	160	38	114	Smooth Poly.	6.95	
AN17	70	160	38	114	Smooth Poly.	7.16	
AN18	90	160	38	114	Smooth Poly.	7.98	
						Longitudinal	
AN77	10	160	38	114	Smooth Poly.	6.54	
AN78	20	160	38	114	Smooth Poly.	6.66	
AN70B	30	160	38	114	Smooth Poly.	6.3	
AN71	40	160	38	114	Smooth Poly.	6.8	
AN72	50	160	38	114	Smooth Poly.	6.77	
AN73	60	160	38	114	Smooth Poly.	7.07	
AN74	60	160	38	114	Smooth Poly.	7.32	
AN75	70	160	38	114	Smooth Poly.	7.44	
AN76	90	160	38	114	Smooth Poly.	7.93	
						Lateral	Lateral
AN80	0	160	38	114	Smooth Poly.	2.26	-0.84
AN81	10	160	38	114	Smooth Poly.	2.25	-1.31
AN82	20	160	38	114	Smooth Poly.	2.45	-0.755
AN83	30	160	38	114	Smooth Poly.	3.05	-0.576
AN84	40	160	38	114	Smooth Poly.	3.8	-1.24
AN85	50	160	38	114	Smooth Poly.	3.97	-1.63
AN86	60	160	38	114	Smooth Poly.	4.08	-1.72
AN87	60	160	38	114	Smooth Poly.	4.23	-1.61
AN88	70	160	38	114	Smooth Poly.	4.49	-1.78
AN89	90	160	38	114	Smooth Poly.	2.85	-1.81
						Longitudinal	
AN113	0	160	38	114	Rough grit	8.27	
AN116	30	160	38	114	Rough grit	8.68	
AN114	60	160	38	114	Rough grit	8.42	
AN115	90	160	38	114	Rough grit	8.7	
						Lateral	Lateral
AN120	0	160	38	114	Rough grit	0.43	-2.3
AN121	30	160	38	114	Rough grit	0.64	-2.52
AN122	60	160	38	114	Rough grit	1.71	-4.07
AN123	90	160	38	114	Rough grit	0.95	-1.62
						Longitudinal	
AN130	0	320	76	60	Rough grit	23.17	
AN131	0	320	76	60	Rough grit	23.17	
AN132	30	320	76	60	Rough grit	22.02	
AN133	50	320	76	60	Rough grit	24.44	
AN134	90	320	76	60	Rough grit	22.15	
AN135	0	160	76	60	Rough grit	5.72	
						Lateral	Lateral
AN140	0	320	76	60	Rough grit	0.64	-3.17
AN141	30	320	76	60	Rough grit	1.44	-6.25
AN142	50	320	76	60	Rough grit	2.82	-7.64
AN143	90	320	76	60	Rough grit	0.4	-3.63
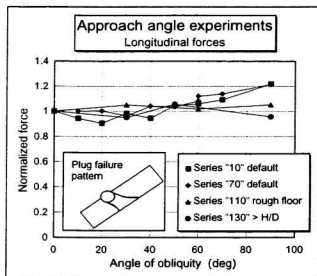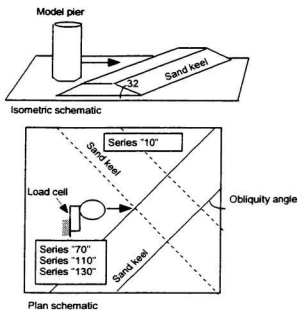
Figure 3.19 "Sand keel" longitudinal forces.
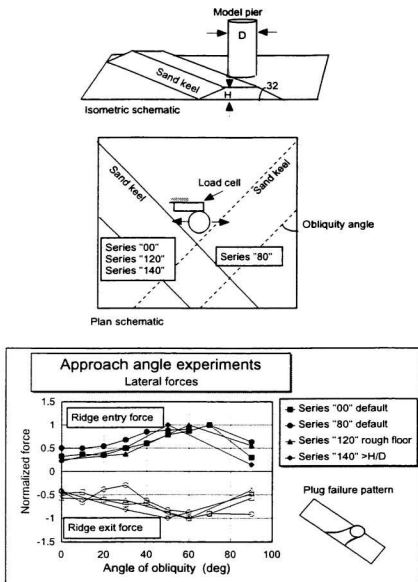
Figure 3.20 "Sand keel" lateral forces.

3.3 Pilot experiments with a cylindrical structure in unconsolidated ice ridges[1]

3.3.1 Introduction

To assess the feasibility of large scale first-year ridge indentation experiments in the ice tank at the Institute for Marine Dynamics a pilot experimental program was carried out. The details of the experiments are reported in McKenna *et al.* (1995a). The experiments were sponsored by the National Energy Board/ Panel on Energy Research and Development Project 6A5014, and were conducted in February, 1995. In the experiments unconsolidated ridges were considered and the focus was on the relation between the forces and the observed failure mechanisms. The influence of interaction speed was also given attention and the coincidence of peak load with shearing events and penetration distances was noted.

The geometric scale of the tests was roughly 1:31.5 and some inferences about scaled loads were made though scaling was not the primary goal of the tests. Some new experimental techniques were introduced: an acoustic system, developed at C-CORE, attached to a moving underwater carriage was used to profile the underside of ridge keels. Ridges were formed using a "dumptruck" technique which involved the service carriage being used to dump level ice collected elsewhere into a pre-cut slot the size of the desired ridge. This allowed the development of a relatively uniform ridge cross

---

section across the 12 m wide tank. A digital video image processing technique to determine block size distribution and under and above water time-encoded video systems were used to document the tests.

3.3.2 Scope of experiments

The structure was a 0.32 m diameter aluminum cylinder. Two parallel ridges with a space of 3 m between were built from a 3 cm thick ice sheet. Ridges were not consolidated as tests commenced shortly after ridges were built at a room temperature of 2° C. The ice around the test area remained intact for the test period to provide support boundary conditions for the ridges during indentation. The first ridge, 2 m wide, was indented twice and the second, 3 m wide, was indented four times. Interaction speed was systematically varied over one order of magnitude. Video records of the interactions were obtained from two positions above and two beneath the water surface.

3.3.3 Experimental results

Results are summarized in Figure 3.21. Of the six tests all but the first failed in patterns characterized by local failure giving way to plug formation. Ridge failure in front of the structure for the first 20 to 40% of the width was characterized by a local repositioning of blocks with some above water surcharge developed but none below. Beyond this position a large wedge of intact rubble was mobilized up to the speed of the advancing structure. Before the structure exited the ridge the wedge was forced off to one side of the structure's path (without directional preference) and under the level ice layer. The first experiment, at the lowest speed, resulted in a global shift of the ridge as it failed in flexure and slid under the supporting ice layer to the rear.

As shown in Figure 3.21 longitudinal forces were insensitive to interaction speed over the range of test conditions. A non-linear increase in load with ridge sectional area was observed. Of particular interest was the close correspondence of incipient plug failure with maximum longitudinal loads. Lateral loads were, on average, 30% of longitudinal and lagged behind also so that resultant loads were only marginally greater than longitudinal. Remarkably, almost exactly the same loads were measured for the first two tests in which observed failure modes differed considerably. If further substantiated, this result could play an important role in future modelling efforts.

These experiments were of value for a number of reasons. The observed failure modes and associated load levels supported the accepted analytical modelling strategy for design loads on the Northumberland Strait Bridge. The acoustic profiler was successful in mapping the bottom profile of the ridge, and, the "dumptruck" ridge construction technique yielded a block size distribution that was strikingly similar to that which was measured in the field in Veitch *et al.* (1991a).

The robust procedure developed in this test series provided the groundwork for larger scale first-year ridge experiments to be undertaken at IMD.

	Run 1	Run 2	Run 3	Run 4	Run 5	Run 6
RIDGE PROPERTIES						
Ridge #	1	1	2	2	2	2
Ridge width (m)	2	2	3	3	3	3
Ridge sail x-section area (m^2)	0.1	0.1	0.15	0.15	0.15	0.15
Ridge keel x-section area (m^2)	0.59	0.59	1	1	1	1
Total ridge x-section area (m^2)	0.69	0.69	1.15	1.15	1.15	1.15
Block density (kg/m^3)	857	857	871	871	871	871
Ridge porosity	0.26	0.26	0.27	0.27	0.27	0.27
INTERACTION DATA						
Speed (m/s)	0.019	0.187	0.187	0.131	0.075	0.019
Ice/structure friction coef.	0.13	0.13	0.13	0.13	0.13	0.13
Structure diameter (m)	0.32	0.32	0.32	0.32	0.32	0.32
Longitudinal						
Peak longitudinal force (N)	332	331	852	592	692	541
Displacement to peak longit. (m)	0.342	0.595	1.336	1.177	1.05	0.681
Fraction of ridge to peak longit.	0.171	0.298	0.445	0.392	0.350	0.227
Lateral						
Peak lateral force (N)	68	73	121	177	171	347
Displacement to peak lat. (m)	0.674	1.74	2.18	1.283	1.16	1.418
Fraction of ridge to peak lat.	0.337	0.870	0.727	0.428	0.387	0.473
Resultant						
Peak resultant force (N)	332	332	852	594	703	557
Displacement to peak res. (m)	0.342	0.595	1.336	1.203	1.05	1.272
Fraction of ridge to peak res.	0.171	0.298	0.445	0.401	0.350	0.424
VIDEO DATA						
Distance to plug (m)	0.38	0.81	1.17	1.1		0.64
Fraction of ridge to plug	0.19	0.41	0.39	0.37	0.33	0.21
Wedge flare angle (deg)	-	30	30	30	45	-
Max. wedge width (in diameters)	-	3 D	4 D	3-4 D	>5 D	-
Surcharge height above water (cm)	13	12	20	21	21	12

Average block statistics:
Block thickness = 3 cm
Block width = 9.2 cm
Block width = 6 cm
Block L*W = 63.8 cm^2
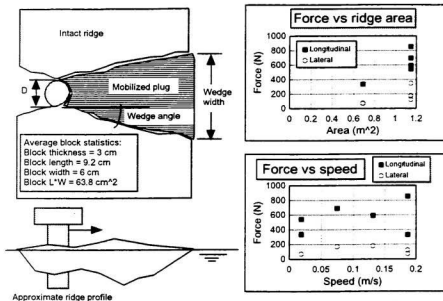
Figure 3.21 Test conditions and results - pilot experiments at IMD.

3.4 Large-scale ridge interaction experiments[1]

3.4.1 Introduction

Two sets of experiments, independently planned and sponsored but similarly executed, are described in this thesis section. Both programs utilized test procedures developed in McKenna *et al.* (1995a) and described in Section 3.3. The two programs represent the largest scale first-year ridge indentation laboratory experiments in the literature (though proprietary). The first program was conducted to address the interaction between a model pier from the Northumberland Strait Crossing Project and first-year ridges (McKenna *et al.* 1995b). Experiments were conducted at the Institute for Marine Dynamics in June 1995. The tests were requested by the Ice Interaction Subcommittee for the Northumberland Strait Crossing Project and were sponsored by Public Works and Government Services Canada (PWC). The committee was seeking to establish whether design ice loads for the NSCP had been computed properly. The intent was to determine the degree of success in matching experimental forces with analytically predicted loads using the modelling approach used for the NSCP.

The second experimental program was conducted in September 1995 and was sponsored by a joint industry project headed by K.R.Croasdale and Associates for which the laboratory program is reported in McKenna (1996). The primary focus was again to establish a data base for developing and calibrating keel load models. As the author was a member of the research team conducting these experiments the data is available for use

---

[1]A portion of this study, **McKenna R.F. and Bruneau S.E. (1997) Ice rubble build-up on conical structures during ridge interactions**, has been prepared for POAC/OMAE, 1997. Yokahama, Japan.

in this thesis (though it remains proprietary).

3.4.2 Scope of experiments

The model pier used in both experimental programs was comprised of a conical ice shield at the waterline and a cylindrical shaft below (see the figure in Table 3.2). The shaft diameter was 0.8 m and the cone was 1.825 m at the base and had an angle of 45°. The cone and the cylinder were instrumented separately. In total, twenty-nine experiments were performed on fifteen ridges most of which were constructed from an entire ice sheet using the "dumptruck" technique. The focus of the test program was on the forces exerted on the structure by the rubble in the ridge keels. Most ridges were refrozen to form a thin consolidated core at the waterline which provided a realistic boundary condition for the keel. The cone lifted the core and sheet ice so that ice crushing was avoided, preserving the structural configuration and function of the NSCP bridge piers. The test parameters were water level, speed, rubble strength, ridge shape, ridge orientation and structure diameter. In the second test program a few experiments were conducted with the lower cylinder replaced by a large one (1.8 m diameter) and with no consolidated core present.

In an attempt to ascertain the shear strength of ice rubble in the ridge keels at IMD a "punch" shear technique was developed. The tests were similar to subsea plate anchor pull-out experiments except that they were inverted (push down) and the refrozen core needed to be presawn. Details of the experiments, the analysis technique and results are found in McKenna R., Bruneau S. and Williams, M. (1996). In Table 3.2 the shear strength of the ice rubble is shown to remain constant for all tests. It is quite possible that the rubble shear strength varied from test to test, however, there was considerable

scatter in the punch shear data set. Without a consensus amongst the research team on how to interpret the data, only the approximate mean value for unconsolidated keel rubble strength has been quoted.

3.4.3 Experimental results

Details of the test conditions and results are found in McKenna *et al.* (1995b) and McKenna (1996) (referred to as the PWC and JIP tests respectively). Table 3.2 lists most key test conditions and results. With so many test variables, some of which may be correlated, it is difficult to conclusively isolate singular effects. Nevertheless, some general trends are exposed in the figures which accompany the table. They show that keel forces on the cylinder are strongly influenced by keel depth and structural diameter, are influenced much less by apparent block flexural strength and are quite insensitive to ridge width and approach speed. Also from the table one can deduce that ridge keel shape and structure roughness are not key control parameters. Peak cylinder and cone forces were not simultaneous and the peak resultant was on average 5.8% less than the sum of the two. However, it cannot be readily concluded that the core and keel will not fail simultaneously in the field since lab ridges were not heavily consolidated and tended to be double-keeled with the sail arched between (probably an artifact of the "dumptruck" building technique).

Forces on the cone were not the focus of these experiments. However, the data set provides a unique opportunity for development and testing of models for rubble forces on conical structures. The topic is discussed later in this thesis.

Table 3.2 Large-scale test conditions and results.

Test program		PWC	PWC	PWC	PWC	PWC	PWC	PWC	PWC	PWC	PWC	PWC
Ice sheet		1	1	2	2	3	3	4	4	5	5	6
Run		1	2	1	2	1	2	1	2	1	2	1
Cylinder diameter	m	0.8	0.8	0.8	0.8	0.8	0.8	0.8	0.8	0.8	0.8	0.8
Cylinder surface		smooth	smooth	smooth	smooth	smooth	smooth	smooth	smooth	smooth	smooth	smooth
Cone base diameter	m	1.825	1.825	1.825	1.825	1.825	1.825	1.825	1.825	1.825	1.825	1.825
Cone angle		45	45	45	45	45	45	45	45	45	45	45
Cone angle		45	45	45	45	45	45	45	45	45	45	45
Speed	m/s	0.424	0.141	0.141	0.141	0.141	0.0283	0.141	0.141	0.141	0.141	0.141
Water level to cone base	m	0.08	0.08	0.08	0.32	0.08	0.08	0.08	0.32	0.08	0.08	0.32
Ridge orientation		90	90	90	90	90	90	90	90	90	90	90
Keel width	m	4.5	4.5	4.9	4.9	6	6	6	6	4.6	4.5	4.5
Max keel depth	m	1.1	1.1	1.1	1.1	1.1	1.1	0.9	0.9	1.05	1.1	1.1
Keel depth below cone	m	1.02	1.02	1.02	0.78	1.02	1.02	0.82	0.58	0.97	1.02	0.78
Max sail height	m	0.24	0.24	0.17	0.17	0.18	0.18	0.25	0.25	0.22	0.21	0.21
Av keel x-section area	m^2	3.8	3.8	4.24	4.24	3.52	3.52	3.36	3.36	3.41	3.77	3.77
Av sail x-section area	m^2	0.4	0.4	0.41	0.41	0.47	0.47	0.47	0.47	0.38	0.39	0.39
Keel block density	kg.m/3	931	931	933	933	923	923	926	926	931	932	932
Sail block density	kg.m^3	905	905	917	917	906	906	900	900	901	911	911
Porosity		0.32	0.32	0.4	0.4	0.3	0.3	0.27	0.27	0.32	0.35	0.35
Block thickness	mm	50.9	50.9	50.4	50.4	49.5	49.5	50.5	50.5	50	47.2	47.2
Level ice thickness	mm	59.3	59.3	59.3	59.3	59	59	59.6	59.6	59.4	58.6	58.6
Consolidated layer thickness	mm	58.3	58.3	20	20	53.3	53.3				40	40
Level ice flex, initial	kPa	32.5	32.5	34.5	34.5	37.5	37.5	36.5	36.5	37.5	73	73
Level ice flex strength at test	kPa	60.5	60.5	82	82	81.75	81.75	69.5	69.5	74.5	82	82
Block flex strength	kPa	27.5	27.5	20.5	20.5	25.5	25.5	19.5	19.5	15.5	32	32
Consol. core flex strength	kPa	74.5	74.5	81.3	81.3							
Friction angle		36	36	36	36	36	36	36	36	36	36	36
Cohesion	pa	438	438	438	438	438	438	438	438	438	438	438
Cylinder peak X force	N	3110	2650	2170	1080	2760	3110	2440	870	2810	3950	1560
Cone peak X force	N	3370	3060	2790	3520	3010	2930	3160	5300	3340	3650	7070
Total peak X force	N	6130	5350	4670	6290	5720	5940	5300	5980	5530	7110	8330
Cylinder peak Y force (starb.)	N	290	320	340	560	370	570	310	260	390	490	180
Cylinder peak Y force (port)	N	330	370	410	60	400	140	150	150	850	490	180
Cone peak Y force (starb.)	N	470	300	500	1450	600	550	450	1060	910	140	1710
Cone peak Y force (port)	N	400	680	240	50	290	190	270	150	490	470	10
Total peak Y force (starb.)	N	670	470	580	1920	700	790	520	1860	1820	490	2100
Total peak Y force (port)	N	530	850	530	640	500	220	160	900	660		0
Total Z force	N	2980	2610	2840	3940	2440	1760	2390	3760	2280	2530	4850
Penet at peak cyl. X force	m	3.1	2.9	3.1	3.0	3.0	2.6	3.3	2.9	2.7	2.6	2.8
Penet at peak cone. X force	m	2.8	2.4	2.5	3.2	2.6	2.6	3.3	3.2	2.6	3.2	2.2
Penet at peak X force	m	3.1	2.9	3.1	2.5	3.2	3.2	2.8	3.1	3.6	2.6	2.2
Penet at peak Z force	m	3.9	3.9	3.9	3.7	5.2	4.6	4.7	4.6	2.9	2.1	

Diagram labels:

1.825 m
0.605 m
1.75 - 6.0 m
-0.23 - 0.51 m
45
0.28 - 1.03 m
PWC#1 Ridge keel
Sheet ice
0.005 - 0.424 m/s
Cyl. diam = 0.8 m

Table 3.2 (continued).

	JIP	JIP	JIP	JIP	JIP	JIP	JIP	JIP	JIP	JIP
Ice sheet	4	4	5	6	6	7	7	7	8	8
Run	1	2	1	2	1	2	3	4		
Cylinder diameter m	0.8	0.8	0.8	0.8	0.8	1.8	1.8	1.8	1.8	1.8
Cylinder surface	smooth	smooth	rough	smooth	smooth	smooth	smooth	smooth	smooth	smooth
Cone base diameter m	1.825	1.825	1.825	1.825	1.825	1.825	1.825	1.825	1.825	1.825
Cone angle	45	45	45	45	45	45	45	45	45	45
Speed m/s	0.07	0.07	0.07	0.07	0.07	0.07	0.005	0.005	0.07	0.07
Water level to cone base	0.32	0.08	0.08	0.08	-0.23	0.51	0.08	0.08	0.08	0.08
Ridge orientation	90	90	90	90	90	90	90	90		
Keel width m	3.5	3.5	4							
Max keel depth	0.86	0.82	1.11	1.04	0.5	0.59	1.05	0.47	0.66	0.76
Keel depth below cone	0.54	0.74	1.03	0.96	0.5	0.08	1.01	0.77	0.39	0.68
Max sail height	0.12	0.14	0.23	0.25	0.06	0.06	0.12	0.23		
Av keel x-section area m^2	2.495	2.34	2.693	2.693	3.097	3.107	2.378	2.079	0.595	0.761	1.59
Av sail x-section area m^2	0.26	0.302	1	0.559	0.338	0.94	0.303	0.339	0.125	0.089	0.349
Keel block density kg/m^3	903	903	895	895	895	906	906	906	906	913
Sail block density kg/m^3	787	787	746	746	755	755	768	768	768	792
Porosity	0.27	0.27	0	0.16	0.23	0.18	0.18	0.28	0.28	0.05
Block thickness mm	46.8	46.8	50.9	50.9	51.5	51.5	56.4	56.4	56.4	55.3
Level ice thickness mm	56	56	56.2	56.2	51.5	51.5	56.4	56.4	56.4	55.3
Consolidated layer thickness mm					0	0				
Level ice flex when ridge buil kPa	55.5	55.5	59.5	59.5	61.5	61.5	64	64	64	66.5
Level ice flex strength at test kPa			99	99	25	25	80	80	80	166.5
Block flex strength kPa	37.5	37.5	44	44	31.5	31.5	24.5	24.5	24.5	21.5
Consol. core flex strength kPa			81	81	74	74	244.5	244.5	244.5	254.5
Friction angle	36	36	36	36	36	36	36	36		
Cohesion pa	438	438	438	438	438	438	438	438		
Cylinder peak X force N	790	2610	4530	3770	1540		2540	3120	860	610	3520
Cone peak X force N	5290	3780	3190	3290		2600	2840	3230	1910	2010	2810
Total peak X force N	5910	6030	6160	6850	1510	2610	5590	5850	2600	2470	6030
Cylinder peak Y force (port) N	170	720	240	1190	180		130	1060	160	90	360
Cylinder peak Y force (starb.) N	180	120	460	70	590		440	40	30	60	270
Cone peak Y force (port) N	360	860	460	780		1090	470	900	300	350	680
Cone peak Y force (starb.) N	1050	280	340	130		120	310	250	370	300
Total peak Y force (port) N	450	1420	620	1540		1200	380	1660	420	350	900
Total peak Y force (starb.) N	1130	280	490	150	580	10	620	190	520	420	480
Total Z force N	5080	2160	3320	2340		2460	2140	1680	1450	1770	2930
Penet at peak cyl. X force m	2.3	1.7	2.2	2.4	2.7		1.6	1.8	0.8	0.5
Penet at peak cone X force m	2.2	2.4	4.1	3.0		4.8	1.9	2.0	1.9	1.9
Penet at peak st. X force m	2.2	2.4	4.3	6.2	5.3	3.1	4.1	2.1	1.3	2.3
Penet at peak Z force m	2.2	2.4	4.1	4.3	6.2	5.3	3.1	4.1	2.1	1.3	2.3

Cylinder X force vs keel depth
McKenna et al. (1995b), McKenna (1996)

Legend: ○ 0.8 m cylinder, ● 1.8 m cylinder

X axis: Keel depth from cone base (m)
Y axis: Cylinder X force (N) (Thousands)

Cylinder X force vs keel width
McKenna (1995b), McKenna (1996)

Legend: ○ 0.8 m cylinder, ● 1.8 m cylinder

X axis: Keel width (m)
Y axis: Cylinder X force (N) (Thousands)
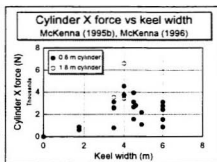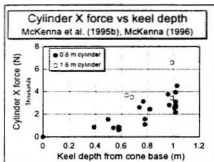
Table 3.2 (continued).

Test program	JIP	JIP	JIP	JIP	JIP	JIP	JIP
Ice sheet	8	8	8	9	9	10	10
Run	2	3	4	1	2	1	2
Cylinder diameter	m	1.8	1.8	1.8	1.8	1.8	
Cylinder surface		smooth	smooth	smooth	smooth	smooth	smooth	smooth
Cone base diameter	m	1.825	1.825	1.825	1.825	1.825	1.825	1.825
Cone angle		45	45	45	45	45	45	45
Speed	m/s	0.07	0.07	0.07	0.07	0.07	0.07	0.07
Water level to cone base	m	0.32	0.32	0.08	-0.23	-0.23	0.32	0.08
Ridge orientation		90	90	90	90	90	90	90
Keel width	m	3.5	1.75	1.75	4	4	4	4
Max keel depth	m	0.75	0.56	0.37	0.99	0.95	0.96	1.07
Keel depth below cone	m	0.43	0.24	0.29	0.99	0.95	0.64	0.99
Max sail height	m	0.23	0.11	0.15	0.22	0.21	0.26	0.22
Av keel x-section area	m^2	1.811	0.642	0.502	2.884	2.906	2.905	3.428
Av sail x-section area	m^2	0.372	0.12	0.091	0.479	0.503	0.480	0.472
Keel block density	kg.m^3	913	913	913	894	894	902	902
Sail block density	kg.m^3	792	792	792	743	743	751	751
Porosity		0.05	0.21	0.21	0.18	0.18	0.24	0.24
Block thickness	mm	47.1	47.1	47.1	49.8	49.8	50	50
Level ice thickness	mm	55.3	55.3	55.3	49.8	49.8	59.2	59.2
Consolidated layer thickness	mm				0	0	36	36
Level ice flex when ridge buil	kPa	66.5	66.5	66.5	60.5	60.5	43	43
Level ice flex strength at test	kPa	166.5	166.5	166.5	16	16	107	107
Block flex strength	kPa	21.5	21.5	21.5	29.5	29.5	28.5	28.5
Consol. core flex strength	kPa	254.5	254.5	254.5	116.5	116.5	232.5	232.5
Friction angle		36	36	36	36	36	36	
Cohesion	pa	438	438	438	438	438	438	
Cylinder peak X force	N				3420		3690	6580
Cone peak X force	N						6030	3110
Total peak X force	N	6510	3100	2690	3730	2460	9270	8890
Cylinder peak Y force (port)	N				1670		1110	1710
Cylinder peak Y force (starb.)	N				340		350	340
Cone peak Y force (port)	N						820	830
Cone peak Y force (starb.)	N						210	250
Total peak Y force (port)	N	2580	560	510	2050	60	1490	2540
Total peak Y force (starb.)	N	120	270	260	390	760	340	260
Total Z force	N	4780	3140	2000	340	10	6570	3510
Penet at peak cyl. X force	m						2.2	2.1
Penet at peak cone. X force	m						3.0	1.8
Penet at peak tot. X force	m	2.0	1.2	1.3	0.2	1.2	1.9	1.8
Penet at peak Z force	m	2.0	1.3	1.8			3.0	3.1

Structure X force verses speed
McKenna (1995b), McKenna (1996)

Cylinder X force verses block strength
McKenna (1995b), McKenna (1996)
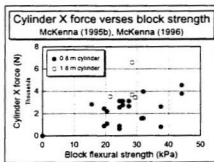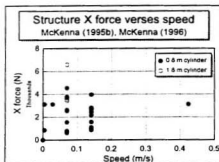
3.5 *In situ* direct shear of ridge keels[1]

3.5.1 Introduction

In this section a technique for direct *in situ* field measurement of rubble shear strength which has been developed and tested in the laboratory is described. The study was prompted by the requirement for accurate full-scale ice rubble properties for predicting ridge loads on structures. The technique involves lowering a ram and associated apparatus into a precut slot in a pressure ridge. This facilitates direct horizontal shear measurements of undisturbed keel ice rubble.

The experiments were conducted in the ice tank at the Institute for Marine Dynamics and were sponsored by the National Energy Board and administered by K.R. Croasdale and Associates. Model ice was used to build partially refrozen ridges, which were then sheared along a horizontal plane just below the consolidated layer using three different direct shear techniques. The apparatus, a scaled model of that proposed for field use, was designed after a rigorous evaluation of the suitability of various types of both direct and indexed shear tests (Croasdale *et al.*, 1996). The robustness of direct shear methods and the unambiguous analysis required to obtain estimates of cohesion and internal friction were important factors in choosing a direct shear technique. The quality of the force-time data, the apparatus configuration and conventions for analysis of Mohr-Coulomb failure criteria were also investigated.

3.5.2 Test conditions

Experimental setup and model ice ridges

The tests were conducted on two ice ridges with parent ice sheet thicknesses of 30 mm and 50 mm. Since the constituent block thickness of ridges in temperate regions is of the order of 0.2 m to 0.5 m, scales ranging from 1:4 to 1:17 were modelled.

EG/AD/S model ice was used to build the ridges. Density and flexural strength were measured at the time of ridge formation and at test time. Fine bubbles were introduced during the freezing process to achieve a realistic density which was 895 kg/m^3 for keel blocks and 750 kg/m^3 for the sail blocks. The flexural strength measured in the level ice varied from 32 kPa to 62 kPa during ridge construction. At test time, keel samples yielded flexural strengths of the order of 30 kPa while sail ice samples ranged from 134 to 266 kPa. The full-scale flexural strength of sea ice ranges from below 300 kPa to 700 kPa.

The ridges were constructed for the present test program using the "dumptruck" technique as briefly described in Section 3.3. In this study a channel 4 m wide, spanning the entire 12 m width of the tank was cut in the level ice and fifty-five metres of level ice from elsewhere in the tank were lifted using the service carriage and dumped into the channel. The ice broke into pieces during placement since repeated drops were made at the centre of the channel. The ridges were supported on the front edge by the adjacent level ice sheet and on the back by a floating dock spanning the width of the tank as shown in Figure 3.22. A cooling cycle following the ridge construction created a refrozen layer within each ridge at the waterline.

Shear box apparatus

The rectangular shear box was constructed of welded aluminum plate with nominal dimensions of 0.75m long x 0.5m wide x 0.4m deep. The box consisted of upper and lower halves of equal depth connected by a slotted runner bearing positioned on overlapping flanges. The shearing action was achieved by relative motion of the two halves. The length of the bottom half of the box was 0.85m to allow the insertion of a spreader device. The assembly is shown in Figure 3.23.

The spreader was a self-contained assembly consisting of a hydraulic ram mounted rigidly to an aluminum plate. Four parallel guide rods were fixed to another plate which slid through holes in the first plate. A button load cell was placed on the end of the piston and a displacement potentiometer ("yoyo" type) was positioned between the spreader plates. The whole unit was easily detachable from the shear box so it could be incorporated into all direct shear options without disturbance of the data acquisition and drive systems.

For a typical sandy soil, laboratory shear devices split the sample across thousands of grains leading to uniform shearing which is representative of continuum behaviour. Ice rubble is, by contrast, a granular material with particles that are orders of magnitude larger. The size of the shear plane which would allow for similar particle kinematics and shear surface uniformity would prohibit direct scaling of soils shear devices. Thus, a consideration of the particle orientation, size and dynamics in a shear box is necessary to adequately model continuum behaviour. These considerations were reviewed as a part of this thesis and it was found that the average ratio of shear plane width to ice block length for 19 ice rubble shear tests in the literature was 6.4. The experiments with the

smallest shear box size-to-block ratios were conducted by Prodanovic (1979) who demonstrated that shear strength was unchanged when the block size was reduced from one half to one quarter of the width of the box. Furthermore, the results were repeatable and have been shown to be representative of results reported more recently. A box width of 0.5 m was chosen giving a box-to-block size ratio of 5.5 for 30 mm ice and 3.3 for 50 mm ice.

The elevation of the horizontal shear plane was selected such that shearing would be initiated below the refrozen core and beyond the reach of blocks frozen into it. As well, the elevation was maintained close to the undersurface of the refrozen layer to minimize the box depth and trenching requirements. Although the shear box could be lowered to any depth within the ridge, it was designed so that it could be conveniently and repetitively placed in the ridges with the shear plane positioned 10 cm below the lower surface of the refrozen layer.

Shear box options 1, 2 and 3

Three direct shear options were considered in the laboratory. In all three cases the apparatus was placed in a pre-cut trench in the ridge. Option 1 involved the use of the entire shear box assembly. Option 2 involved the removal of the lower half of the box and the placement of a reaction plate on the spreader assembly. The objective of this option was to provide a frame that would contain the *in situ* rubble sample and to guide the shear plane along the bottom edge of the box. In this case the shear plane reaction force was carried by the refrozen layer adjacent to the spreader. The absence of the lower half of the shear box reduced the depth of the rubble to be trenched and decreased the size and weight of the apparatus.

Option 3 eliminated the box altogether and relied upon the refrozen core to keep the *in situ* sample intact. Using only the spreader device, option 3 was implemented in three different configurations. In the first arrangement, 500 mm x 350 mm plates were attached to both spreader plates to allow for a larger bearing surface on the ice. In the second, the extra plate bearing against the *in situ* sample was removed and the spreader was moved down to bear directly against the refrozen layer. In the third, the guide rods were removed eliminating all possible sources of apparatus friction. Figure 3.24 is a schematic representation of the experiments showing the site before, and after, the placement of the apparatus for options 1 and 3.

Test plan and procedure

Two ice sheets were used in the test program. The first ridge was built from level ice 30 mm thick and the consolidated layer depth was approximately 40 mm. The second ridge was built from a 50 mm thick sheet and had the same consolidated layer depth. Both ridges were tempered so that the air temperature during testing was near the freezing point.

Before trenching, the ridge sail was levelled to a surface approximately 10 cm above the water level. To aid with the trenching, a template matching the shape of the interior of the shear box was placed over the ridge sail. The pattern was then vertically sawn through the sail core and keel to a predetermined depth below the core around 200 mm. At one end of the trench rectangular sections of the sail core and keel were removed by hand for placement of the spreader unit. At the opposite end of the trench, blocks were removed to allow free translation of the sheared sample.

The shear box was lowered over the undisturbed rubble by hand and keel depth, sail height and box position were measured. To increase vertical stresses in the undisturbed sample, fixed weights were distributed evenly on a plywood board placed on the levelled surface of the sail. Surcharges of approximately 500 Pa and 1000 Pa were achieved by using fixed weights of 20 kg and 40 kg. All tests were conducted at a shear rate of 2.1 cm/s.

Following the complete set of shear experiments on the first ridge (30 mm ice) it was decided that option 2 would be dropped from the second set of tests. As well, options 1 and 3 would be implemented without the spreader guide rods in place (hereafter referred to options 1a and 3a). It was apparent from the tests with the first ridge that the rods were the cause of enhanced friction and binding and did little to orient the spreader plates. Dry runs conducted prior to the second set of tests indicated a significant reduction in no-load box friction for option 1 without the guide rods. By removing the rods, peak friction was reduced by more than half the original 'with-rods' option. For option 3, removal of the guide rods meant that there was no frictional component to the load trace due to the apparatus.

3.5.3   Laboratory results

Ridge geometry

A ridge profile was measured by pushing a graduated aluminum rod through the keel. A length scale was used to measure the height of the sail relative to the service carriage platform. The measured profile for ridge 2 is shown in Figure 3.22.

Block dimensions resulting from the "dumptruck" ridge construction technique were estimated from video images of the floating rubble in a previous study where the same technique was used (McKenna *et al.*, 1995a). In that study, the block length and width dimensions in the plane of the water surface were determined for 160 blocks in a digitized video frame. The means of the length and width were 3.1 and 2.0 times the ice thickness. The smallest block widths were approximately equal to the level ice thickness. The largest block length was between 8 and 9 times the ice thickness. On average, the ratio of the length to the width was 1.6. These statistics are believed to be representative of those for this study since parent ice sheet properties were similar.

Force time series

Figure 3.25 shows force and displacement time series traces, two for option 1a and two for option 3a. Several "dry" runs were conducted to determine the no-load static and dynamic friction characteristics of the shear box. Averaged load traces of the frictional force for each shear option have been subtracted from the force traces and for all subsequent analyses.

Virtually all load traces exhibited a significant oscillatory component. Some fluctuations were more random than others but most were uniform and saw-toothed. During the tests, it was often possible to observe the "skipping" or hopping of the rubble sample corresponding to these load cycles. The frequency was observed to drop with decreasing normal stress, though the relation was not very strong. Option 3 produced both the highest (for original "with guide rods" option) and lowest (without rods) frequencies - apparently an artifact of the spreader mechanics. Oscillation amplitudes were observed to be poorly correlated to normal stress, although a slight trend towards increased

amplitude with apparatus "weight" was noted.

The potential causes of the force oscillations included ice-structure ratchetting, shear box stick-slip action, and ice rubble cyclic dilation. The author believes that the most likely cause was ratchetting in which, periodically, quasi-static forces on an ice-structure interface increase with increased deflection until ice resistance is exceeded, causing ice failure and a relief of loads on the structure. In this case, the appropriate measured force values to use in the interpretation are the peak values since this mechanism is not resonant and will not result in any dynamic amplification of the peak forces.

For options 1 and 2, the peaks of load cycles frequently grew with increased shear box translation. At appreciable box translations there was an increased normal stress due to the decrease in shear area, and the sample tilted into the trench. This may have led to enhanced compression and gouging at the leading and trailing box edges, complicating the analysis for options 1 and 2. Only option 3 (no shear box at all) exhibited a clear tendency for peak loads to repeatedly occur in the first few seconds.

Rubble shear stress

Analysis of the experimental data revealed that subjective decisions were required in order to determine shear strength, even for the least ambiguous of test procedures. Shear stress is often computed by dividing the force required to shear the sample by the instantaneous shear plane area of the box. Difficulty is encountered when forces are cyclic and peaks increase with displacement. The choice must then be made of when, or at what displacement, peak "shear resistance" was encountered. Loads which follow may be greater but may also be artifacts of the shear box mechanics. Furthermore, one may

wish to consider either peak or residual (mobilized) friction angles and, of these, either absolute maxima or mean cyclic values may be selected.

In this study two conventions were adopted. The first was to determine the peak shearing force from the first two seconds or 4.2 cm displacement. The second looked at the first 15 seconds or 30 cm of the force-time histories for a peak. The latter was selected to correspond to some observed trends in the force traces whereas the first was based on the assumption that for typical dilatant soils, shearing peak loads occur at displacements close to but less than one particle thickness. Shear areas were adjusted for box displacement.

Mohr-Coulomb approximation

Normal (vertical) shear plane stresses were determined from the weight of the ice above the surface, the buoyant weight of ice between the surface and the shear plane below and the weights added for surcharge. A plot of the results for the 2-second peak shear for all options is given in Figure 3.26 and for the 15-second peak shear in Figure 3.27. It is evident by comparing Figures 3.26 and 3.27 that using the 2 s instead of the 15 s adjusted shear strength values is probably justified. Increased scatter in the latter underscores the uncertainty about apparatus performance and shear interpretation beyond the first few seconds of each test. The uniform spread of the results for all apparatus options, and the close agreement between options indicates that the 2 s peak is analytically superior. An interesting result is obtained when both the combined 2 s and combined 15 s results are compared. Figure 3.28 shows that the internal friction angle for both was a near perfect match while apparent cohesion was 2/3 higher for the latter case.

Case (1991) reports laboratory results from the ice tank at IMD when a fixed vertical direct shear box was used to shear rubble samples. The ice rubble (similar to that in this study) was formed by a chopping action of the carriage and samples were corralled into the box. The shear rate was twenty times slower than that in the present tests and the timing of tests relative to ice formation was somewhat different. In spite of these differences, the laboratory results are similar. The results for the Case (1991) study for all tests combined were ϕ = 38° and c = 661 Pa whereas the combined results in the present study are ϕ = 41° and c = 873 Pa. This is a strong indication that the direct shear approach is robust and that the influence of block size and test conditions on rubble shear strength in the IMD laboratory are minimal.

3.5.4 Summary and recommendations

The present study has demonstrated the application of various direct shear methods for the measurement of laboratory ice rubble shear strength *in situ*. The averaged results of ϕ = 41° and c = 873 Pa are similar to results reported in the literature. Based on the results of the present experiments, a direct, horizontal shear technique is suitable for determining the *in situ* shear properties of rubble in first year ridge keels. Also, as long as a competent consolidated layer is present, this can be used as a platform for loading the shear plane thus simplifying the testing apparatus. Since trenching around the sides of the ice sample will be a time-consuming operation in the field, the test procedure might be significantly stream-lined by cutting the sides of the ice sample with a slight flare angle. This would eliminate binding of the sample in the hole and enable a single chain saw cut to be used instead of a trench.
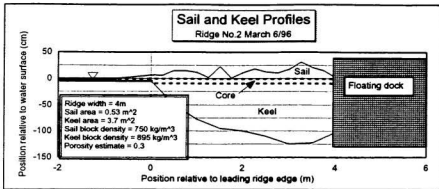
Figure 3.22 Ridge geometry.
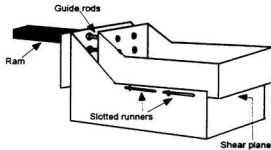
Figure 3.23 Schematic of shear box assembly.
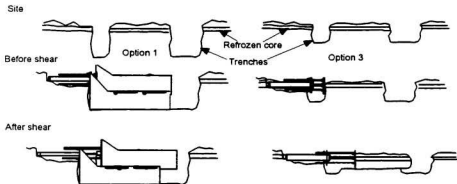
Figure 3.24 Schematic of *in situ* tests, options 1 and 3.

Option 1a, No Surcharge, Run 1
peak force = 789 N
at displacement = 9.7 cm

Option 1a, 20 Kg Surcharge, Run 1
peak force = 598 N
at displacement = 9.6 cm

Option 3a, No Surcharge, Run 2
peak force = 502 N
at displacement = 2.4 cm

Option 3a, 40 Kg Surcharge, Run 1
peak force = 797 N
at displacement = 3.5 cm
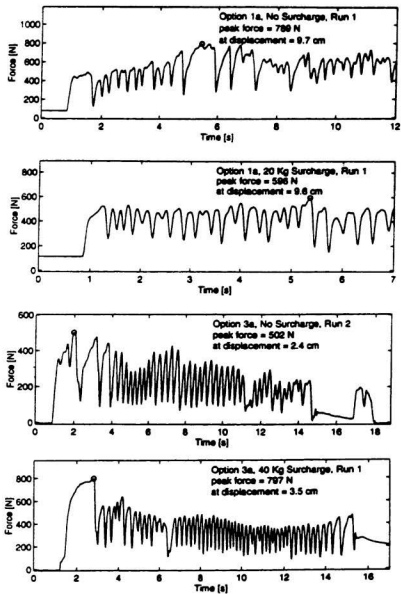
Figure 3.25 Sample force time series.
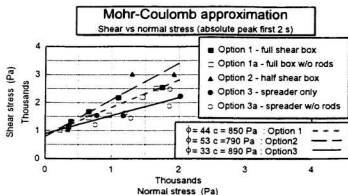
Figure 3.26 Mohr-Coulomb approximation - 2 second peak.
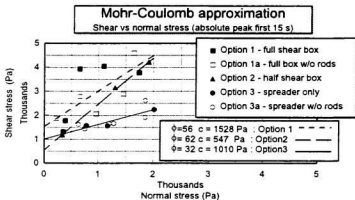
Figure 3.27 Mohr-Coulomb approximation - 15 second peak.
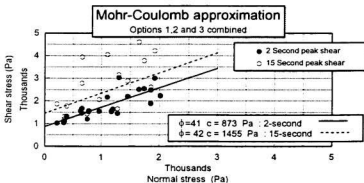
Figure 3.28 Mohr-Coulomb approximation - combined study.

3.6 Summary of exploratory experiments

The experimental programs reviewed in this chapter have significantly expanded the data base for studying first-year ridge keel interactions. Pilot experiments at C-CORE (Section 3.1) demonstrated a transition of failure modes in ridge-structure interactions while looking at both floating and dry rubble in continuous and discrete formations. Rubble properties were determined as it was anticipated that they affect shear strength and the dependency of shear strength on block contact duration and initial temperature was investigated. The pilot program also pioneered the use of sand as an analogue for ice rubble. The sand afforded a level of control not possible with ice and observations and measurements were highly informative about failure modes and force trends. These qualities motivated a second sand test series, undertaken to isolate the effects of ridge obliquity on loads (Section 3.2). Results showed that longitudinal forces were relatively insensitive to ridge obliquity.

A series of ice ridge interaction tests conducted at the Institute for Marine Dynamics are described in Subsections 3.3 and 3.4. The IMD pilot tests in Section 3.3 initiated the testing of unconsolidated ridges at that institution and provided high-quality measurements of test conditions and forces for ridge keel model development. Section 3.4 reviews two large-scale detailed ridge interaction experimental programs which utilized procedures pioneered by the IMD pilot test series. These tests provide the most complete data sets known with extensive video coverage, force and test condition measurements and detailed ridge profiles.

The last experimental program described is one in which a technique for measuring first-year ridge keel shear strength *in situ* was developed. A small-scale model of a proposed apparatus was constructed and tested at IMD providing direction for full-scale tests and adding another set of laboratory ice rubble shear strength data to the literature.

These programs were all directed at diminishing both parametric and force model uncertainties for first-year ridge keel load modelling. In addition to the individual merit of each program, the new data when combined with that from the literature (reviewed in Chapter 2) provides a unique opportunity for the systematic development of an analytical force model. The remainder of this thesis is dedicated to exploiting this opportunity. The first major step described in the next chapter is a regression study. The well-documented and far-reaching data set now assembled permits a broad and meaningful multi-variable regression.

Chapter 4

MODEL DEVELOPMENT I

Regression analyses

The previous chapter describes a series of experimental programs, each providing some data and relationships which should be useful in modelling the forces involved in penetrating a ridge keel. In this chapter results from the experiments in Chapter 3 have been combined with data from the literature for regression analyses. The grouped data sets include those for ridge keel shape, ice rubble shear strength and structure interaction forces. Any individual test program tends to involve a choice of a limited set of parameters which are varied, and often a limited range over which variation occurs. When diverse programs are studied collectively, general results are obtained, removing or reducing biases which result from the limitations of any one test procedure. While collective studies run the risk of oversimplifying some issues they can broaden the applicability of results and, as the following shows, can be a better guide for future work.

4.1 First-year ridge keel shape

Though there have not been any new field data presented in this thesis, this section describes the results of a new regression study of ridge keel shape. The data used are described in the thesis background as reported in Burden and Timco (1995). Burden and Timco (1995) catalogued the dimensions of over 112 first-year and 64 multi-year ridges. The first-year ridges were divided into two groups: those associated with temperate

climates and those from the arctic. The keel data for temperate first-year ridges were considered in this study.

Detailed surveys of ridge cross-sections have shown that keel shapes have varying slopes with both convex and concave curvature. The keel bottom may be pointed and off-centre, rounded or flat. Naturally, there are no simple geometric forms that perfectly define all ridges. For analytical modelling, ridges are typically categorized as triangular or trapezoidal in cross-section because those shapes are easily defined by measured field data; usually width, depth and sometimes slope angle. Though commonly applied, these shapes present some analytical difficulties since they possess slope discontinuities. Discontinuities preclude one from defining the whole keel with a simple, single algebraic formula, a convenience for computing depth across the entire ridge. For this study the replacement of the facetted geometric approximations with that of a half-cycle "sine wave" form has been considered (Figure 4.1). To investigate the quality-of-fit of the "sine" approximation the data sets presented by Burden and Timco have been reanalysed.

Keel width to depth ratio

A total of 44 ridges had both keel width and depth measurements studied. A regression analysis was performed to determine the best linear and non-linear relationship between these measured parameters. The resulting formulas are

$$W = 2.5H + 9.4 \quad and \quad W = 9.2H^{0.525} \quad \text{(1)}$$

where W and H are the keel width and depth in meters. For the linear relation the r^2 value, adjusted for degrees of freedom, was 44.8% and the standard deviation of the somewhat normally distributed residuals was 8.2 m. The power-law fit established through a natural log transform had a standard deviation of the normally distributed log residuals of 0.3471 with an adjusted r^2 value of 38.7%. A linear relationship between the width and depth, fitted with a zero intercept as in Burden and Timco (1995), resulted in the relation, $W = 3.99H$ with an r^2 of 24%. Figure 4.2 is a scatter plot of the ridge data with both fitted linear relations and the power law fit.

Keel angle

Both fore and aft keel angles are listed in Burden and Timco (1995). These terms are understood to be used arbitrarily assigned to differentiate between the two slopes of a given ridge and are in no way a convention for classifying any particular ridge orientation. The method of measurement is not recorded. For 16 first-year temperate region ridges the averages of the angles which were measured are 28.8° and 26.3° respectively, resulting in an overall average of 27.5°. Of the 16, only 8 ridges had width and depth stated. If these 8 ridges were assumed to be either triangular or "sine" shaped, the average slope angle for both is found to be 23.5°, a slight underestimate of the measured average (the average angle for both shapes is computed from the arctan of ridge depth over half the ridge width). The relation between measured and computed slope is investigated further in Figure 4.3. Although both shapes have the same average slope over a half length, the slope of the "sine" shape varied between 0.0 and 33.5° from tip to toe. This range encompasses the measured values above.

Keel area

Through digitization, Burden and Timco determined the cross-sectional area of 18 temperate first-year ridges. Only six of these corresponded to ridges for which both width and depth data were also provided. Width and depth dimensions were estimated from digitized plots so that another 11 of the 18 ridges could be considered in this study. The area under a "sine" shaped approximation ($2HW/\pi$) over-estimates the measured areas by 12%. The area under an isosceles triangle of equal proportions underestimates areas by the same margin (Figure 4.4). When only the six fully-defined ridges are used, the error for the "sine" approximation diminishes to 7% and that for triangular keels increases to 14%.

The "sine" keel shape is a more accurate keel cross-sectional area shape approximation than the isosceles triangle one. When one considers that overstating size results in overestimated loads, which is safer than underestimating, the new "sine" shape may be a better choice for design regardless of the improvement. Further, the continuous and simple form of the "sine" curve may indeed provide easier load modelling by eliminating slope discontinuities[1].

---

[1] Brown and Bruce (1995) conducted a finite element investigation of the stress distribution within a ridge keel during indentation. In that study the stress patterns/contours below the surface of a triangular keel were shown to be parabolic or *sine*-like in shape. This indicated that discontinuities in surface form did not translate to internal stress discontinuities.
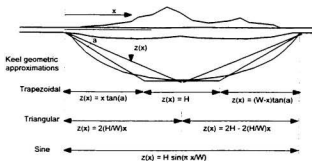
Figure 4.1 Keel geometry approximations.
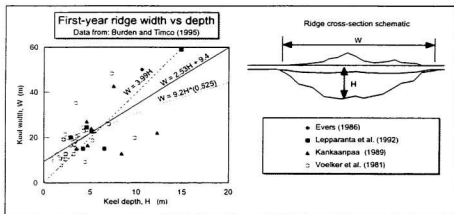
Figure 4.2 Keel width vs depth study.
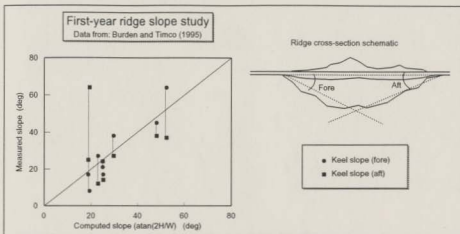
Figure 4.3 Keel slope study.
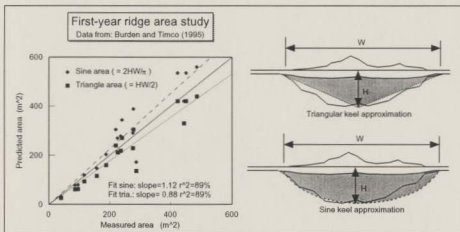
Figure 4.4 Keel cross-sectional area study.

4.2 Ice rubble shear strength

In this section experiments investigating the shear strength of submerged ice rubble are studied. Properties and conditions suspected of influencing shear behaviour are grouped using dimensional analysis. The derived dimensionless ratios, and the original quantities are used in a multiple regression study of rubble shear strength. The inter-dependencies between explanatory variables (independent or control variables) is investigated and the best-fit formulas defining shear strength are quantified.

4.2.1 Dimensional analysis

Regression analyses produce dimensionally homogeneous equations. When the dimensions of control variables on both sides of an equation are not similar, the regression coefficients assume a dimensional form. When developing and classifying generalized equations for scaling it is desireable that the coefficients remain dimensionless. To meet this criteria a dimensional analysis is used to group variables into dimensionless ratios which eliminate all dimensions from the regression analysis. These terms (ratios) may also be used as a means of systematically collecting and converting data from various experimental programs while reducing the number of variables to be investigated.

In a previous chapter, it was explained that ice rubble is broadly assumed (in the literature) to be an isotropic, rigid plastic material which obeys the Mohr-Coulomb yield criterion. Consequently, the shear strength is said to arise from independent frictional and cohesive components. Friction in a granular material arises from interlock, block strength

and surface friction. The conditions which influence friction behaviour include packing density, block shape, size, and gradation, surface roughness, the presence of surface water, particle composition and particle strength. Cohesion in a bulk ice rubble sample was shown to be a function of the freeze-bonding propensity of the ice and would, therefore, be dependent upon heat transfer, block scale, contact pressure, ice impurities, shearing rate, interstitial fluid and other factors.

As pointed out in section 3.3 it appears that the fundamental Mohr-Coulomb plasticity assumption stated above oversimplifies the true nature of ice rubble (Ettema and Uroz-Aguirre, 1991). Due to the apparent stress dependency of ϕ and c terms, and for completeness in the dimensional analysis, both are grouped here with all other explanatory variables for the broadest possible analysis.

The hypothesis tested in the dimensional analysis is

$$\phi . c = f(L_x, L_s, t, S, e, V, \gamma, \sigma_{fl}, \sigma_{max}) \qquad (40)$$

with terms defined as follows:

- block size, median of maximum dimension L_x, and minimum dimension L_s.

- duration, t, of contact between blocks within the bulk sample,

- interstitial water impurity content (salinity mostly), S,

- porosity of bulk sample, e,

- shear speed, V,

- rubble buoyant weight, γ,

- ice block flexural strength, σ_{fl},

- and maximum confinement stress, σ_{max}.

The preceding list was developed after consideration of the various reporting methods and experimental procedures in the literature. Not all of the factors expected to assert some influence can be included in this listing. For instance, temperature and particle grading are omitted due to the absence of reported information. However, while contact duration, t, was poorly reported it does appear in the analysis to ensure that one other significant variable, in addition to velocity, which involves time is included. Its value is set to unity for all data sets as a default value.

Flexural strength was selected (instead of another ice strength index) primarily because it was the most commonly reported ice strength parameter in the literature for rubble shear strength. It may be argued that for *platy* blocks, failure in flexure will occur at lower stresses than pure crushing or tension in an interlocked matrix of blocks being sheared. Under these circumstances flexural strength may be the better choice since it would be closely tied to any threshold for non-linear shear behaviour. Regardless, flexural strength would be significantly related to the other strength indices - thus a regression equation with either strength index would probably have the same parametric significance(s) but possess different coefficients of proportionality.

Figure 4.5 shows the workings of the *matrix technique* for dimensional analysis. This technique (described in Sharp *et al.*, 1992) enables the systematic evaluation of many Π parameters objectively and completely even when large numbers of variables are involved. The dimensionless groups ultimately chosen using this process are as follows:

$$\phi, \; \frac{c}{\sigma_{fl}} = f\left\{ \frac{\gamma L_c}{\sigma_{fl}}, \; \frac{Vt}{L_c}, \; S, \; e, \; \frac{L_c}{L_i}, \; \frac{\sigma_{max}}{\sigma_{fl}} \right\} \tag{41}$$

These are selected because of their physical significance and prior use in the literature. Sensitivity runs confirm the validity of this selection, in particular, the use of flexural strength as a repeating variable for normalization. Both σ_{max} and γL_x were substituted for flexural strength resulting in dimensionless parameters which ultimately yielded poorer correlations than those listed above.

4.2.2 Analysis data set

The values of explanatory variables from all the sources used in the study are listed in Table 4.1. Friction angle and cohesion are usually stated in each literature reference, only a few values are computed here from plotted data. Ordinarily, block size is given, though dimensions are often approximate. The "maximum" block size described by most researchers is typically the average or median of the longest dimension of blocks and not the largest block in the bulk sample. Block thickness (median of minimum block dimension, L_i) and median of the maximum block dimension, L_x, are used independently in this study since it is uncertain which is more important, and the ratio of the two gives an indication of particle shape. The rate of shearing is reported quantitatively in all but one reference. Keinonen and Nyman (1978) use the relative term, "slowly by hand" which is estimated here to be around 25 mm/sec. Some references do not cite a flexural strength for the ice used in tests. Where this is the case values are estimated based on the description of the ice. For instance, freshwater ice near 0° C is assigned a flexural strength of 1 MPa after work by Gow (1977).

The salinity of the fluid in which the rubble is immersed is known to significantly affect ice rubble freeze-bonding (Schaefer and Ettema, 1986). Outside of a laboratory one would expect salinity and flexural strength to be too closely correlated to be considered

independent for multiple regression purposes. However, in the lab flexural strength is controlled to a large extent by the air content of the ice. Bubble layering and spraying are two techniques used to enhance the void ratio of ice allowing flexural strength scaling. Some laboratories use chemical dopants such as urea and EG/AD/S as a substitute for salts. A control experiment has not been done to investigate the effects of these dopants on the freeze-bonding of ice blocks. It is assumed here that the influences of all dopants (salts included) is proportional to the percent weight of the impurity in the water. Experiments in freshwater are assigned an arbitrary impurity of 0.001% since a value of zero prohibits some transformations of variables (logs, square roots, inverses etc.) and is unlikely in any event.

All but two researchers report values of bulk sample porosity. Since porosity is difficult to measure, especially when ice blocks have a lower density out of water when pores drain, the quoted values are usually approximate. Neither Hellmann (1984) or Case (1991) give estimates of bulk porosity so bulk porosity values for those references have been estimated. Since there does not appear to be an obvious relation between porosity and block size, Hellmann's rubble samples are considered here to possess average porosity (35%) as no unusual packing procedures are mentioned. Case (1991) used ice rubble similar to that reported in Section 3.5 (from Bruneau *et al.*, 1996) and so the same value is adopted (30%). The buoyant weight of the rubble sample is computed from bulk porosity, and, ice and water density. Though seemingly correlated, porosity and weight parameters are carried through the dimensional analysis separately and into the regression study, where spurious correlations can be dealt with systematically.

Most rubble shear experiments in the lab involve direct shear devices which produce a

horizontal or vertical failure surface in an ice rubble sample. Where external forces are applied to provide a variation in the normal pressure, stresses from rubble weight or buoyancy are relatively small. Ettema and Urroz-Aquirre (1991) argue that some researchers with vertical direct shear apparati have neglected this buoyant stress which gives rise to a cohesive intercept that should not be there. They suggest that the horizontal confining pressure on a vertical shear plane is

$$\sigma_h < K_p \, \sigma_v \qquad (42)$$

where the σ_v is the rubble (buoyant) hydrostatic pressure, σ_h is the horizontal component of this pressure during shearing and K_p is the Rankine passive pressure coefficient. This assertion implies that during shearing the vertical pressure increases by a factor of K_p. In direct shear tests with soil the vertical pressure is not considered to do this as K_p and K_a are not coefficients for pressures on failure planes. For the experiments by Prodanovic (1979), Weiss et al. (1981), and Hellmann (1984) as cited in Ettema and Urroz (1989) the normal stress was either regulated at a constant value or measured throughout so as to provide instantaneous coincident shear and normal stress values. Other than the platen used to apply the normal stress only friction on the walls of the shear boxes can provide reaction forces adding to normal stresses on the failure plane. Based on shear box dimensions and construction it is unlikely that any significant stress on the failure plane was not measured as a normal stress. Both Prodanovic and Weiss et al. report shear experiments at a confining stress of zero. This is also unlikely, suggesting that either the original static pressure may have been zeroed out of the readings or confinement may have been very low so that it was rounded off to zero. Potentially, the ice rubble may have become self-supporting due to freeze-bonding (cohesion) after being placed in the

shear box so that any relief in the box would relieve measured confinement pressure.

For those shear box tests where the failure planes are vertical the reported normal stresses are used here for all but the zero stress data points. A normal stress value equivalent to one-half the average vertical ($0.5 \, \sigma_v$) is used since the rubble would have to have been confined at least that much in the placement process. Where failure planes are horizontal, normal stress values are elevated here by an amount equivalent to the hydrostatic pressure if it does not appear to have been included. The σ_{max} values in Table 4.1 represent the highest normal stress used in each reference in which ϕ and c are computed.

4.2.3 Regression analysis

Multiple regression techniques have been used to synthesize formulas representing the relationship between ϕ, c and the other explanatory variables listed in Table 4.1. Details of the techniques used are described in Lye (1995). The quality of the fitted formulae was determined by analyzing the residuals for patterns and outliers. Variables were transformed when residual plots appeared skewed - indicating that not all data trends have been identified. Most often the natural logarithms of data were used when residuals were heteroscedastic (the spead of residuals increases with the independent variable). Few trends other than convergence and divergence of residuals were encountered. The most pervasive problem with all data sets was multicollinearity or the undesirable condition where at least one explanatory variable is closely related to one or more other explanatory variables. When explanatory variables are significantly correlated, parameter importance and regression formulas are usually distorted and erroneous.

The Minitab software employed in this regression study is capable of flagging highly correlated explanatory variables so some multicollinearity problems were avoided this way. Variable inflation factors which indicate the multi-variable correlation of each explanatory variable against all others were computed also. Threshold acceptability values (from Lye, 1995) were used to accept or reject some variables for various tests. Matrix plots of scatter diagrams and tables of simple regression results were also employed to screen explanatory variable correlations. Also, "forwards" and "backwards" *stepwise regression* techniques which indicate a type of "regression repeatability" were employed to guard against multicollinearity and to register the best r^2 value, adjusted for the number of explanatory variables (degrees of freedom) in use.

The adjusted r^2 value indicates the percentage of the variation in the dependent variable described by the given formula. The partial **F** test, or **t** test, was used to determine the benefit of any one variable to the overall equation. Registering $|t| > 2.0$ (or $p < 0.05$) indicates a significantly non-zero influence at the 95% confidence level. (**p** representing the actual probability of not meeting this criterion.) Thus $|t| = 2$ was the threshold for accepting or rejecting a given variable. Since **t** values are often highly sensitive to the subtraction or addition of any variable, many combinations of variables were tested to determine those which avoided multi-collinearity and were significant.

General relationships

The linear correlation coefficients for all pairs of variables are listed in Table 4.2 for dimensional and Table 4.3 for non-dimensional terms. At a glance one can see that significant correlations of variables exist (shaded regions) for the data set in general. Even speed, a seemingly independent parameter, is correlated to other control parameters

in the laboratory. Many correlations can be explained by the habits of experimentalists. For instance, larger labs produce larger ridges with larger blocks at higher confinement. There may or may not be similar trends in the field. This type of correlation should be avoided in the laboratory and must be avoided in multiple regression analysis. Correlations between non-dimensional terms in Table 4.3 are even more difficult to understand and so are best avoided completely.

Cohesion

The relation between apparent cohesion and several explanatory variables was investigated. Both dimensional and non-dimensional forms of cohesion were studied. The analysis was carried out with, and without, ϕ in the list of explanatory variables. All formulas yielding a spreading trend in the residuals were transformed using natural logs and a variety of exponents, where applicable.

The formulas yielding the best-fit, with normalized residuals and with the lowest likelihood of multicollinearity (or correlation error) are listed in Table 4.4. Many other combinations of variables were explored, frequently yielding r^2 values much higher than those listed. However, where explanatory variables are strongly related to each other (as the shaded areas of Table 4.2 and Table 4.3 indicate), only one may be considered.

Figure 4.6 is a plot of the best-fit formulation for the relationship between cohesion and maximum normal stress, both normalized by flexural strength. With an r^2 value of 78.3% this dimensionless equation may be suitable for scaling. Cohesion is strongly correlated to block size in this study. Figure 4.7 indicates the best single variable relationship for cohesion (in Pascals) as

$$c = 16240L_i - 7 \qquad \textbf{(43)}$$

where L_i is block thickness (in meters). Apparently, block size is also significantly proportional to the maximum normal stress (see Table 4.2). Thus the relation between block size and cohesion may be influenced by the dependency of cohesion on normal stress or *vice versa*. Table 4.4 identifies the linear and non-linear relationships between cohesion and maximum stress - both yielding r^2 values around 60%.

The regression analysis procedure was repeated with the data sets from Urroz and Ettema (1987), Bruneau (1994a) and McKenna *et al.* (1996) removed. There was no attempt to *improve* results by doing so. These were selected since apparatus and test procedures differed from the rectangular, direct shear devices of the others. Comparing these sensitivity results to the earlier results (both in Table 4.4) shows that moderate increases in r^2 were identified for cohesion, which in the sensitivity study is surprisingly well-defined by block thickness and shear speed (Figure 4.8). The inverse relationship between cohesion and speed may be evidence that cohesive bonds may form relatively fast and that bond strength may be strain-rate dependent.

Internal friction angle

Regression equations resulting from the study of ϕ vs dimensional and non-dimensional parameters are also listed in Table 4.4. Transformation of variables was not required in this case as residuals were normally distributed with linear regression. As Table 4.4 shows the angle of internal friction is influenced by variations in porosity and block size. Figure 4.9 is a scatter plot of the individual relationships and Figure 4.10 is a quality-of-fit diagram for the relation:

$$\phi - (1.22 - 168L_i + 1.37e) \geq 0 \qquad \textbf{(44)}$$

where ϕ is the internal friction angle in degrees, L_i is the block thickness in meters and e is bulk porosity in percent. Both Figures 4.10 and 4.11 demonstrate the apparent weakness of the correlation. The multi-collinearity of maximum normal stress, block size, weight etc. as highlighted in Table 4.2 limited the combinations of parameters possible in the study. Typically around 50% of the variation of ϕ can be explained by one or two explanatory variables. The percentage is higher in the sensitivity run where the elimination of some data sets yields an r^2 of 67.2% for the relation involving cohesion and porosity.

Comments

Apparently, cohesion scales linearly with block thickness, the robust relationship established accounts for around 70% of the variation in c. Taking into account the sensitivity runs, cohesion can be roughly approximated in kPa by $17L_i$, where L_i is the block thickness in meters. The dimensionless ratio c/σ_{fl} is highly correlated to σ_{max}/σ_{fl} (r^2 of 78%) and may be a good choice for scaling cohesion estimates.

Approximately 40% of the scatter in ϕ cannot be accounted for through regression analysis, though porosity appears to be a predominantly significant explanatory variable. Evidently an inverse relation exists between ϕ and c (Table 4.4). This is an indication of a flattening of the Mohr-Coulomb failure envelope at higher mean pressures possibly resulting from particle degradation and the loss of granular shear behaviour.

4.2.4 Shear vs normal stress

The data points from which the ϕ and c terms in Table 4.1 were derived have been collected so that an evaluation of instantaneous shear and normal stress could be made independent of the reported Mohr-Coulomb failure criteria. This study was prompted by the apparent dependency of cohesion and friction angle on normal stress demonstrated in Table 4.2 and Table 4.4.

Figure 4.11 is a plot of shear stress vs normal stress including all data sets used in the previous study. Several other ice rubble shear tests which have been reported in the literature have not been included in the figure. The tests by Wong *et al.* (1987), Sayed (1987), Eranti *et al.* (1992), Cornett and Timco (1996) and others either saw a monotonic increase in shear stress with no specific failure point, involved experiments with dry ice rubble, or were not fully reported. In Figure 4.12 data from Lehmus and Karna (1995) and Cheng and Tatinclaux (1977) have been added to the data from Figure 4.11. From both Figures 4.11 and 4.12 it appears that a lower boundary shear strength exists that it is slightly concave/parabolic. The upper boundary of data appears to be defined by some radical outliers from the data sets of Lehmus and Karna (1995) and also Bruneau (1994a) who were studying consolidation effects, as well as Cheng and Tatinclaux (1977) where there was no attempt to control or measure normal stress (estimated here from rubble depth), and by Weiss *et al.* (1981) who used the largest apparatus and ice blocks. From Figure 4.13 where data is grouped according to ice temperature, speed and contact period it appears that the upper bound may be a feature of cold ice or extended contact.

Since many properties of ice, including strength, vary according to the salinity of the solution in which it is formed it was of interest to discriminate between tests using either

saline, fresh or doped ice. Figure 4.14 provides no particular insights, however, as data for all three types of ice are scattered somewhat evenly.

A dimensional analysis was performed in which the terms for shear and normal stresses, τ and σ_n, were substituted for ϕ, c and σ_{max}. Figure 4.15 indicates the matrix methodology used to formulate dimensionless ratios. Normal stress was selected as a repeating variable instead of flexural strength allowing the dimensionless ratio between shear and normal stress to arise. The derived expression is:

$$\frac{\tau}{\sigma_n} = f\left(\frac{\gamma L_s}{\sigma_A}, \frac{\sigma_A}{\sigma_n}, \frac{Vt}{L_s}, S, e, \frac{L_s}{L_i}\right) \tag{45}$$

Again, multiple regression techniques have been used to synthesize formulas representing the relationship between τ and those explanatory variables as they appear in dimensionless groups above. The base data set used in this study is limited to those for which values of ϕ and c were known in Table 4.1. This means that Lehmus and Karna (1995), and, Cheng and Tatinclaux (1977) were not included. A sensitivity study was carried out later in which these tests were included. The table listing all data point values appears in Appendix A.

Linear regression results for dimensional and non-dimensional terms are tabulated in Table 4.5 and Table 4.6 respectively. For very large data sets the **t** test of significance is not meaningful so only r^2 (adjusted) has been used as a guide for simple correlation and variance inflation factors were once again used to avoid multi-collinearity.

Table 4.7 lists the multiple regression results. Linear and non-linear relations between

τ and σ_n were determined. The distributions of residuals were typically log-normal indicating that a power-law relation for the combined data set was more appropriate than a linear fit. The best power-law fit relationship for shear stress was determined as:

$$\tau = \frac{(\sigma_n)^{0.878} \, (e)^{0.55}}{(\sigma_p)^{0.0851}} \qquad (46)$$

with an r^2 of 80% where all stresses are in Pascals and porosity, e, is in percent. Including Lehmus and Karna (1995), and, Cheng and Tatinclaux (1977) considerably worsened the correlation. Eliminating the "non-standard" direct shear data sets (Urroz and Ettema, 1987, Bruneau, 1994a, and McKenna *et al.*, 1996) did not improve the relation either. Figure 4.16 is a plot of the base data set with the best linear and non-linear single variable correlations shown. The approximate strength of solid ice and loose sand are also plotted as a reference for relative strength. The range of maximum normal stress typical for ridges between 5 and 20 m deep is also plotted so that one may quickly recognise the region of the graph which is of the greatest practical importance for keel modelling.

The best linear fit for ice rubble shear strength yields a friction angle of 31° which is approximately equivalent to that of loose sand. It is conceivable that, in a virtually cohesionless state and with favourable grading and particle size, ice rubble behaves as any other blocky granular material. Invariably though, bonding takes place, the degree to which depends on a great many factors. The average appears to be around 590 Pa (from the linear fit on Table 4.7), however, in the figure one can see cohesion up to 5 kPa was observed in the laboratory and may conceivably reach many times higher according to the degree of consolidation (potentially approaching that of solid ice). The

degree of variation is somewhat masked by the logarithmic representation. A band which covers the main swath of the data points is approximately half an order of magnitude in thickness. Overall, the plot of shear vs normal stress in Figure 4.16 illustrates that ice rubble shear strength is strongly related to normal stress but, is also highly variable.

The significant portion of scatter left unexplained by the preceding analysis underscores the sensitivity of ice rubble shear strength to parameters not reported, differing experimental techniques and natural variability. Measurement error is probably responsible for as much as 10 to 20% of the scatter. As described earlier some of the data used in the analysis was inferred or estimated. This may also have contributed to scatter.

4.2.5 Sensitivity study and comparison to full-scale

The empirical formulas for c, ϕ and τ (Equations 43, 44 and 46) described earlier in this section have been evaluated in a sensitivity study shown in Figure 4.17. Two approaches to calculating rubble shear strength are considered. The "phi-c" approach refers to the use of Mohr-Coulomb criteria (ϕ and c from equations 44 and 43), and the "tau" approach which refers to the fundamental shear (τ) vs normal stress relationship (equation 46). The values of explanatory variables selected in the table accompanying the figure are representative of those of a design ridge in temperate climatic zones. The sensitivity study focusses on the relative effect of porosity, block thickness and keel depth as well as comparing the computed shear strength from both approaches. The average shear strength is assumed here to be that at $2H/3$ from the keel bottom, according to a linear hydrostatic approximation. The horizontal bar graph shows that the "tau" model generally produces higher shear strength estimates than the "phi-c" approach. It is also more

sensitive to keel depth. less sensitive to porosity and does not vary with block thickness. For the "phi-c" approach the extrapolation of laboratory results to the field has apparently resulted in remarkably low estimates of friction angle.

A comparison of computed and measured full-scale rubble shear strengths is reviewed in Figure 4.18. Computed values are compared here with those of Lepparanta and Hakala (1992). In that study the investigators performed a detailed study of ridge keel geometry and composition. Five ridge keels were "punch-sheared" vertically with a 2 m square loading platform to obtain shear resistance. Loads were applied using pumped water, concrete block placement and a hydraulic ram. The first technique failed due to the cumbersome handling of the volume of water required. The second was found to be effective for small and medium ridge keels but again became too difficult to handle for larger ridges. The last technique showed the most promise for larger keels though limited stroke and hydraulic pressure prevented complete ridge keel failure.

In the successful punch tests failure planes were vertical and shear resistance measured from 1.7 to 4+ kPa for keels ranging in depth from 2.3 to 11.7 m. Loading period averaged about 2 hours and displaced the keels less than 0.1 m on average which translates to less than 1 mm per minute. This very slow rate is not representative of the conditions under which the highest failure loads are expected to occur. None-the-less, Lepparanta and Hakala claim that the field results have been backed by both shear box and square punch tests performed in the laboratory. The shear strength in the laboratory was said to vary from 0.9 to 2.6 kPa with a mean friction angle of 8.4 degrees. These results are somewhat puzzling since a calculation based upon information given shows that normal stress varied by as much as 0.34 to 1.5 kPa and shear stress varied from 0.9

to 2.6 kPa. This would suggest a friction angle much higher than that stated.

Figure 4.17 indicates that the "phi-c" computed shear strength provides a closer estimate of the full-scale data than the alternate "tau" approach. The average errors of the estimates were 17% and 33% respectively. The near match for experiment No. 6 is problematic for the "phi-c" approach, however, since the ultimate shear strength of the ridge was not achieved and may not have been approached in that test. In this case the estimate based on the empirical τ formula may be better.

Lavender (1973) also proposed a full-scale cohesion for ice rubble from river ice jams. The technique used for his estimate of 0 to 3800 Pa is not published and conditions are not known. Regardless, the upper bound is certainly of the same order as that in Figures 4.17 and 4.18.

Hudson (1983) describes full-scale observations of extruded first-year ice ridges in the arctic. Ridge extrusion is described as a phenomenon which occurs when there is a high speed collision between flows or ridges and stationary structures. The formation which develops resembles a deflected ocean wave "frozen" in time. The impression of intense pressures and considerable shearing within the rubble body is given. The extruded crests are somewhat circular in shape implying a "virtually cohesionless" material, according to Hudson.

Hudson points out that a 2 m thick ice sheet produces the same size ice rubble as a 5 m thick sheet which suggests that first-year ridge cohesion may reach some asymptotic limit that could be in the range of 25 to 35 kPa for severe arctic first-year ridges. These

estimates are highly consistent with the block size relation for cohesion here.

At present, the limited data from the field appear to support the prediction of ice rubble shear strength using Mohr-Coulomb failure criteria obtained in the laboratory. Considerable caution should be exercised in doing so, however. As was mentioned in Chapter 2, first-year ridge keel rubble, over long contact periods, may undergo many changes via erosion, freezing, creep, brine transport, melting etc. These processes have not been, and cannot be, adequately modelled in the laboratory so that the range of reported shear strengths may not be fully representative of field conditions. To provide reliable parametric input for ridge keel models it is imperative that efforts be placed in field studies, through methods such as the *in situ* direct shear technique suggested in Section 3.5.

Table 4.1 Laboratory ice rubble shear data for regression analysis.

Reference	Friction angle φ deg	Cohesion c Pa	Block thickness Li m	Block length Lx m	Shear Speed V m/s	Block Flexural strength σfl Pa	Pore fluid salinity S % wt	Bulk porosity e %	Buoyant weight γ N/m^3	Maximum Normal stress σmax Pa
Keinonan and Nyman (1978)	47	11.3	0.02	0.064	0.025	15000	0.6	35	669	1470
Prodanovic (1979)	47	250	0.019	0.152	0.000106	19500	5.5	37.5	735	2710
	53	560	0.038	0.294	0.001185	17500	5.5	37.5	735	2710
Weiss et al. (1981)	34	4100	0.2	0.6	0.005	83000	5.5	45	647	29000
	24	3400	0.2	0.6	0.025	83000	5.5	45	647	21000
	26	2300	0.15	0.45	0.003	55000	5.5	31	812	25000
	25	1400	0.15	0.45	0.024	55000	5.5	31	812	21000
	13	1700	0.08	0.24	0.004	45000	5.5	27.5	853	31000
	11	1200	0.08	0.24	0.025	45000	5.5	27.5	853	8000
Hellmann (1984)	54	580	0.01	0.025	0.0109	1000000	0.001	35	542	3200
	61	420	0.01	0.025	0.0016	1000000	0.001	35	542	3250
	44	280	0.025	0.055	0.0107	1000000	0.001	35	542	4220
	64	1	0.005	0.015	0.0107	50000	0.001	35	542	1800
Fransson&Sandkvist (1985)	34	550	0.039	0.18	0.01	1000000	0.001	20	667	1600
	14	450	0.046	0.15	0.01	780000	0.001	20	667	3000
	13	240	0.008	0.07	0.01	37000	0.6	20	706	850
Urroz and Ettema (1987)	34	1	0.038	0.095	0.002	1000000	0.001	36	533	260
	51	1	0.016	0.038	0.002	1000000	0.001	39	508	480
	38	1	0.018	0.018	0.002	1000000	0.001	23	642	380
	27	1	0.038	0.095	0.002	1000000	0.001	41	492	170
	55	1	0.038	0.038	0.002	1000000	0.001	40	500	290
	33	1	0.018	0.018	0.002	1000000	0.001	31	575	410
	49	1	0.016	0.038	0.002	1000000	0.001	40	500	290
	39	1	0.018	0.018	0.002	1000000	0.001	36	533	310
Case (1991)	48.9	523	0.03	0.096	0.001	34400	0.5	30	446	1780
	37.6	597	0.03	0.096	0.001	27500	0.5	30	446	1630
	34.8	674	0.03	0.096	0.001	19750	0.5	30	446	2400
	27.2	824	0.03	0.096	0.001	15800	0.5	30	446	1500
Bruneau (1994a)	54	2460	0.018	0.035	0.001	2000000	0.001	40	588.6	1250
	59	720	0.018	0.035	0.001	1000000	0.001	40	588.6	1250
McKenna et al. (1996)	36	438	0.05	0.153	0.07	25000	0.5	26	784	625
Bruneau et al. (1996)	41	873	0.04	0.123	0.021	30000	0.5	30	687	2050

Table 4.2 Explanatory variable correlation analysis for ϕ and c terms.

Key: r²adj = r² adjusted for the number of explanatory variables; t-ratio, |t| > 2 = significant; p, p < 0.05 means significant within 95% confidence limits. Shading represents significant correlation.

Each cell lists: r²adj / t-ratio / p

(row variable)	Friction angle ϕ	Cohesion c	Block thickness t	Block length L_x	Shear speed V	Flexural strength σ_{fl}	Pore fluid salinity S	Bulk porosity e	Buoyant weight
Cohesion c	4.8 / -1.63 / 0.112								
Block thickness t	18.1 / -2.88 / 0.007	70.1 / 8.58 / 0							
Block length L_x	17 / -2.78 / 0.009	65.3 / 7.94 / 0	92.7 / 20.43 / 0						
Shear speed V	0 / -0.88 / 0.388	0 / 0.37 / 0.716	2.2 / 1.32 / 0.198	1.8 / 1.26 / 0.216					
Flexural strength σ_{fl}	6.5 / 1.82 / 0.078	1.4 / -1.21 / 0.236	11.2 / -2.27 / 0.03	19.6 / -3.01 / 0.005	10.3 / -2.19 / 0.036				
Pore fluid salinity S	12.2 / -2.36 / 0.024	37.4 / 4.55 / 0	53.8 / 6.27 / 0	68.3 / 8.49 / 0	0 / 0.5 / 0.621	26.4 / -3.58 / 0.001			
Bulk porosity e	17.3 / 2.82 / 0.008	6.4 / 1.81 / 0.08	1.8 / 1.27 / 0.214	0 / 1.01 / 0.322	9.4 / 1.42 / 0.044	3 / 0.99 / 0.165	0 / / 0.33		
Buoyant weight	15.7 / -2.67 / 0.012	8 / 1.97 / 0.058	16.7 / 2.76 / 0.01	24.4 / 3.41 / 0.002	22.2 / 3.27 / 0.003	13.9 / -2.51 / 0.017	43.1 / 5.1 / 0	9.3 / -2.09 / 0.044	
Maximum normal stress σ_{max}	17.4 / -2.82 / 0.008	61.2 / 7.28 / 0	73.6 / 9.64 / 0	68.7 / 8.57 / 0	0 / 0.3 / 0.764	10.5 / -2.21 / 0.034	60.8 / 7.22 / 0	0 / 0.85 / 0.4	24.7 / 3.44 / 0.002

Table 4.3 Dimensionless explanatory variable correlation analysis for ϕ and c terms.

Key: r²adj = r² adjusted for the number of explanatory variables; t-ratio, |t| > 2 = significant; p, p < 0.05 means significant within 95% confidence limits. Shading represents significant correlation.

Each cell lists: r²adj / t-ratio / p

(row variable)	ϕ	c/σ_{fl}	$\gamma L_x/\sigma_{fl}$	$(V \cdot t)/L_x$	σ_{max}/σ_{fl}	S	e
c/σ_{fl}	13.2 / -2.45 / 0.02						
$\gamma L_x/\sigma_{fl}$	1.7 / -1.26 / 0.219	47.2 / 5.52 / 0					
$(V \cdot t)/L_x$	7.6 / 1.93 / 0.063	2 / -1.97 / 0.058	1.1 / -1.3 / 0.204				
σ_{max}/σ_{fl}	0 / 0.44 / 0.662	24.5 / -3.43 / 0.002	19.8 / -3.02 / 0.005	1.1 / -1.16 / 0.253			
S	12.2 / -2.36 / 0.024	42.2 / 5.01 / 0	71.9 / 8.49 / 0	4.3 / -1.58 / 0.124	13.4 / -2.47 / 0.019		
e	17.3 / 2.82 / 0.008	0 / 0.25 / 0.807	0.45 / / 0.654	0 / -0.93 / 0.357	7.6 / 1.93 / 0.063	0 / 0.99 / 0.33	
L_x/L_i	0 / -0.92 / 0.363	1.7 / 1.25 / 0.219	27 / 3.63 / 0.001	0 / -0.45 / 0.656	15.5 / -2.66 / 0.012	1.5 / 2.34 / 0.025	1.5 / -1.23 / 0.228

Table 4.4 Overview of regression analysis results for ϕ and c terms.

Explanatory variables	Regression formula	r^2(adj)	Standard dev[*]	F test
Cohesion				
$c = f(\gamma L_j, J\sigma, Vol_{\sigma H}, S, c, \phi, Ar, \sigma_{min}/\sigma_H)$	$c/\sigma_H = 0.33(\sigma_{min}/\sigma_H)^{1.07}$	78.3	7.01*	120
$c = f(L_j, L_s, \phi, V, \sigma_H, S, c, \gamma, \sigma_{min})$	$c = 1624(L_j) - 7$	70.1	555	73.5
Friction angle				
$\phi = f(\gamma L_j, J\sigma, Vol_{\sigma H}, c/\sigma_H, S, c, Ar, \sigma_{min}/\sigma_H)$	$\phi = 0.77 - 2.52(S) + 1.16(c) + 27.7(Vol_{\sigma H})$	45.5	10.6	10.2
$\phi = f(L_j, L_s, \phi, V, \sigma_H, S, c, \gamma, \sigma_{min})$	$\phi = 1.22 - 16(d_L) + 1.37(c)$	56.4	9.69	21.0
Sensitivity runs (see correlation table also)				
$c = f(\sigma_{min})$	$c = 277 + 0.0897(\sigma_{min})$	62	62.5	51.62
$c = f(\sigma_{min})$	$c = 0.00004(\sigma_{min})^{1.47}$	59.8	1.98**	47.1
$\phi = f(\gamma L_j/\sigma_H)$	$\phi = 39.25(\gamma L_j/\sigma_H)^{.58}$	68.8	10.4*	73.7
excl. Ureuz and Bruma (1987), Brinson (1994a), McKinnN et al (1996)				
$c = f(\gamma L_j, J\sigma, Vol_{\sigma H}, S, c, \phi, Ar, \sigma_{min}/\sigma_H)$	$c/\sigma_H = 0.023 - 0.048(Vol_{\sigma H}) - 0.00006(J\sigma/\sigma_{min})$	55.4	0.0116	14.64
$c = f(L_j, L_s, \phi, V, \sigma_H, S, c, \gamma, \sigma_{min})$	$c = 162 + 171(d_L) - 1870(V)$	89.8	344	887.8
$\phi = f(L_j, L_s, \phi, V, \sigma_H, S, c, \gamma, \sigma_{min})$	$\phi = -16.1 - 0.0129(c) + 1.96(c)$	67.2	9.18	21.48

* Standard deviation of natural logarithms.

Table 4.5 Explanatory variable correlation analysis for τ terms.

Key: r^2 adj
r^2 (adj) > 50%
r^2 (adj) > 30%

τ	σn	Li	Lx	V	σ_{fl}	S	e	
77.1								
47.4	45.3							
46.2	43	95						
2.3	1.9	0.7	0.9					
3.1	3.2	15.2	21.8	28.6				
36	37.9	52.8	62.7	1.7	16.5			
3.7	1.6	1.2	0.7	14.1	10.8	4		
5.4	8.3	14.6	18.4	4.2	17	24	33.1	γ

Table 4.6 Explanatory variable correlation analysis for τ terms.

Key: r^2 adj
r^2 (adj) > 50%
r^2 (adj) > 30%

$\tau/\sigma n$	$\gamma Lx/\sigma n$	V*t/Lx	$\sigma_{fl}/\sigma n$	S	e	
9.9						
3	3.8					
0	14.3	8.8				
0.3	0.4	7.3	6.6			
0	0.4	11.1	11.3	4		
0	2.2	0	10.8	14.8	1.3	Ar

Table 4.7 Overview of regression analysis results for τ terms.

Explanatory variables	Regression formula	r^2(adj)	Standard dev*	F test
Shear stress				
$\tau = f(\sigma_v)$	$\tau = 3.52(\sigma_v)^{0.832}$	75.6	0.7221*	1344
$\tau = f(\sigma_v)$	$\tau = 588 + 0.598(\sigma_v)$	77.1	1541	1461
$\tau = f(\sigma_v, I_a, I_b, V, \sigma_p, S, c, \gamma)$	$\tau = 1.05(\sigma_v)^{0.816}\sigma_p^{0.370}(\sigma_p)^{0.086}$	80.3	0.6482*	591.5
Non-dimensional terms				
$\tau/\sigma_v = f(\gamma L_s/\sigma_v, Vol_s, S, c, At, \sigma_i/\sigma_p)$	$\tau/\sigma_v = 0.651(\sigma_p/\sigma_v)^{0.30})(Vol_s/L_s)^{0.30})\sigma_v)^{0.068}$	25.2	0.6531	37.37
Sensitivity Runs (incl. or excl. from base data set)				
incl. Cheng and Tatsuoka (1973), Lehmus and Karna (1995)				
$\tau = f(\sigma_v)$	$\tau = 1099 + 0.574(\sigma_v)$	50.9	2295	628.1
$\tau = f(\sigma_v)$	$\tau = 47.9(\sigma_v)^{0.492}$	31.1	1.192*	274.4
$\tau = f(\sigma_v, I_a, I_b, V, \sigma_p, S, c, \gamma)$	$\tau = -748 + 0.506(\sigma_v) + 57.3(c)$	52.1	2267	339.9
excl. Urroz and Ettema (1987), Brincun (1994a), McKenna et al. (1996)				
$\tau = f(\sigma_v)$	$\tau = 1106 + 0.565(\sigma_v)$	73.7	2297	487.5
$\tau = f(\sigma_v)$	$\tau = 18.54(\sigma_v)^{0.606}$	73.3	0.5307*	478.2
$\tau = f(\sigma_v, I_a, I_b, V, \sigma_p, S, c, \gamma)$	$\tau = 0.259(\sigma_p)^{0.552}(\sigma_v)^{1.29}$	80.0	0.4594*	348.57

* Standard deviation of natural logarithms

Figure 4.5 Matrix method dimensional analysis for ϕ and c terms.
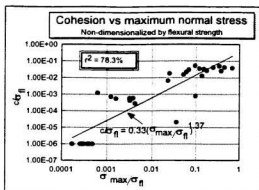
Figure 4.6 Normalized cohesion best-fit regression result.
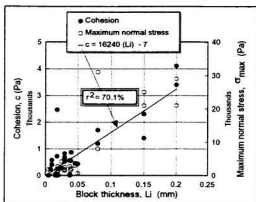
Figure 4.7 Cohesion vs block thickness regression results.
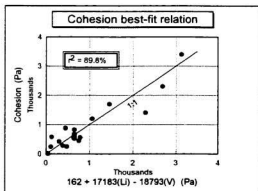
Figure 4.8 Cohesion sensitivity study regression results.
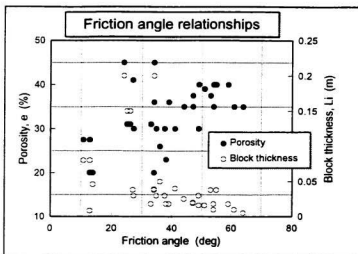
Figure 4.9 Friction angle vs porosity and block thickness.
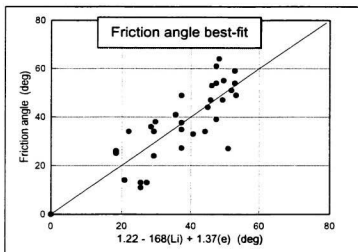
Figure 4.10 Friction angle best-fit regression result.
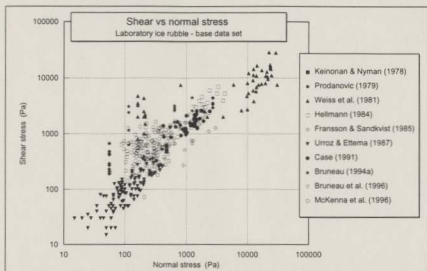
Figure 4.11 Laboratory ice rubble shear vs normal stress data - by author.
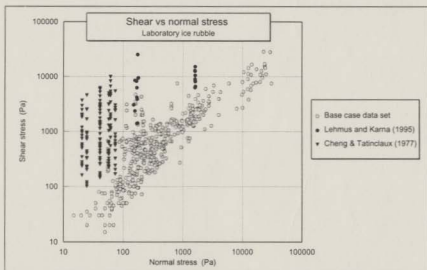
Figure 4.12 Laboratory ice rubble shear vs normal stress data with extreme data.
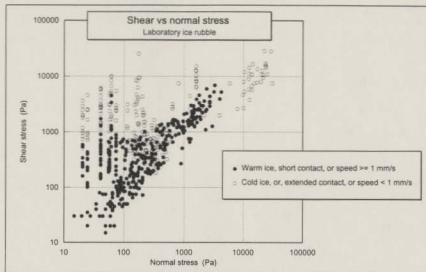
Figure 4.13 Ice rubble shear sensitivity study - temperature, duration and speed.
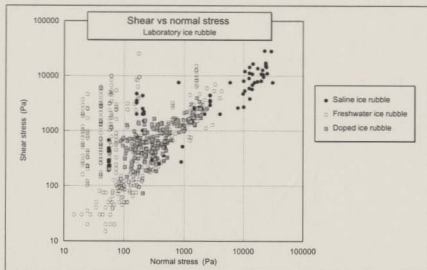
Figure 4.14 Ice rubble shear sensitivity study - ice type.

Steps:
1) Determine rank m of dimension matrix with n parameters (n1 m)
2) Choose m repeating variables from self B at n (includes matrix A unit remainder B (partition matrix)
3) Invert m x m dimensional matrix A to get C
4) Multiply C and D to get output matrix D
5) Extract the n - m Pi parameter (subsort) from D

RELATED PARAMETERS AND THEIR FUNDAMENTAL UNITS

Figure 4.15 *Matrix method dimensional analysis for 7 terms.*

Figure 4.16 Laboratory ice rubble regression results summarized.

Quantity	Units	Default values	Porosity high	low	Block size thick	thin	Depth deep	shallow
Porosity	%	35	45	25	35	35	35	35
Max. block size	m	1	1	1	1.5	0.7	1	1
Min. block size	m	0.2	0.2	0.2	0.3	0.15	0.2	0.2
Flexural strength	Pa	300000	300000	300000	300000	300000	300000	300000
Keel depth	m	15	15	15	15	15	20	10
Block density	Kg/m^3	900	900	900	900	900	900	900
Water density	Kg/m^3	1025	1025	1025	1025	1025	1025	1025
Buoy. weight	N/m^3	797	674	920	797	797	797	797
Av. vert. stress (2H/3)	Pa	7971	6744	9197	7971	7971	10628	5314
Max. vert. stress (H)	Pa	11956	10117	13795	11956	11956	15941	7971
COMPUTED								
Cohesion	Pa	3241	3241	3241	4866	2429	3241	3241
Friction angle	Deg	16	29	2	0	24	16	16
Phi-c - av. horiz. shear	Pa	5462	7022	3542	4866	5973	6203	4722
Phi-c - max. horiz. shear	Pa	6573	8912	3692	4866	7745	7683	5462
Tau - av. horiz. shear	Pa	6436	6382	6065	6436	6436	8286	4509
Tau - max. horiz. shear	Pa	9189	9111	8659	9189	9189	11829	6436

Computed shear strength
Sensitivity analysis

Shear strength (Pa)
Thousands

0   2   4   6   8   10

Default
High porosity
Low porosity
Thicker blocks
Thinner blocks
Deep keel
Shallow keel

■ Phi-c computed shear
▥ Tau computed shear
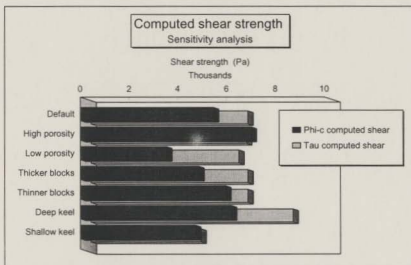
Figure 4.17 Computed ice rubble shear strength - sensitivity study.

Quantity	Units	Lepparanta and Hakala (1992)				
		2	3*	4	5	6*
Porosity	%	23	28	32	33	28
Max. block size	m		0.75	0.6		0.7
Min. block size	m	0.2	0.2	0.11	0.1	0.23
Flexural strength	Pa	300000	300000	300000	300000	300000
Keel depth	m	3.3	3.6	3.9	3.8	11.7
Block density	Kg/m^3	880	880	880	880	880
Water density	Kg/m^3	1025	1025	1025	1025	1025
Buoy. weight	N/m^3	1095	1024	967	953	1024
Av. vert. stress (2H/3)	Pa	2410	2458	2515	2414	7988
Max. vert. stress (H)	Pa	3614	3687	3772	3622	11983
COMPUTED						
Cohesion	Pa	3241	3241	1780	1617	3729
Friction angle	Deg	-1	6	27	30	1
Phi-c - av. horiz. shear	Pa	3205	3499	3038	2990	3860
Tau - av. horiz. shear	Pa	1787	2027	2225	2184	5704
MEASURED (from ref.)						
Av. shear strength	Pa	1700	3400	3400	2400	4000

* Failure did not occur therefore stated shear strength is lower bound

Averages:
Measured = 2980 Pa
Phi-c = 3320 Pa
Tau = 2790 Pa
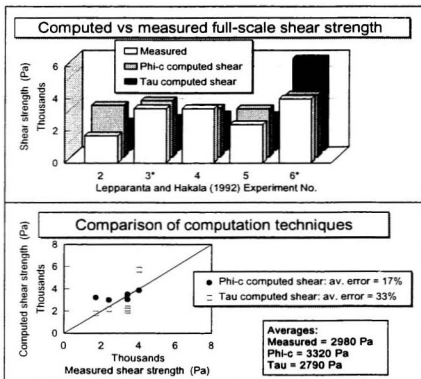
Figure 4.18 Computed ice rubble shear strength - full-scale study.

4.3 Ridge/structure interaction forces

Physical modelling of the interaction between vertical structures and ice rubble has been carried out as part of the work included in this thesis (Bruneau, 1994a, McKenna *et al.*, 1995b, and McKenna, 1996). The purpose has been to establish a basis for load model development. The results of similar work in the literature as reviewed in Section 2.3 have been combined in a regression study in this section. This attempts to determine the correlation between control variables and their relevance to forces measured in laboratory ice rubble/structure interactions. The results provide an empirical basis for theoretical load model development and aid in the systematic scaling of forces.

4.3.1 Dimensional analysis

A dimensional analysis was performed using the "matrix technique" (Sharp *et al.*, 1992) as described earlier. Parameters were selected based on their appearance in existing load models (as reviewed in Section 2.4) and the empirical relations seen in the data reported in Chapter 3. The hypothesis tested in the dimensional analysis was

$$F = f(D, H, W, \phi, c, \gamma, V) \tag{47}$$

with terms defined as follows:

- structure diameter or width, D,

- maximum depth of rubble interacting with structure, H,

- the width of the rubble accumulation, W, (in path of structure)

- ice rubble shear strength, ϕ and c,

- rubble buoyant weight, γ, and

- interaction speed, V.

The shear strength failure criteria are assumed to capture the effect of parameters such

as block size and porosity.

The following dimensionless ratios were formed as shown in Figure 4.19 (with some rearrangements):

$$\frac{F}{\gamma H^2 D} = f\left[\frac{c}{\gamma H}, \; \phi, \; \frac{W}{D}, \; \frac{H}{D}, \; \frac{W}{H}\right] \tag{48}$$

The last three terms are not mutually independent so that only (any) two of three are of practical importance in a given study.

An alternate approach (Figure 4.20) aimed at involving *speed* in the dimensionless terms yielded

$$\frac{F}{H^2 V^2 \rho} = f\left[\frac{c}{\rho V^2}, \; \phi, \; \frac{H}{D}, \; \frac{W}{D}, \; \frac{A}{HW}, \; \frac{gD}{V^2}\right] \tag{49}$$

where g is the gravitational constant, A is ridge cross-sectional area, and ρ is rubble bulk density.

4.3.3 Analysis data set

Table 4.8 is a summary of laboratory ridge/structure interaction data sets. The boundary conditions varied between two-dimensional (wall-to-wall) and three-dimensional (isolated cylinder) indentation, and, from interactions with continuous rubble (modelling a rubble field) to discrete rubble accumulations (modelling a ridge). Also, experiments varied from unconfined (no core present) to confined (with core) horizontal surfaces at the waterline. Cheng and Tatinclaux (1977) did not determine a friction angle for the rubble they used but Mellor (1980) suggested that it was around 46° with very low cohesion

(essentially zero) arbitrarily selected here as 1 Pa. The experiments by Hellmann (1984) involved ploughing a circular vertical plate through rubble under the surface. The boundary condition in this case has been categorized as non-confined although it differs somewhat from those experiments in which structures extend up and out of the water. All experimental results which provide the database for the regression studies reported here are tabulated in Appendix B.

Six scatter plots in Figure 4.21 illustrate the dependency of peak interaction force on the key explanatory variables. A measurement of shear strength is obviously not sufficient for a prediction of interaction forces. There is considerable scatter in the data particularly in the plot of force vs speed, ridge width, rubble buoyant weight and shear strength.
It may be possible to argue from these data for a dependency of force on structure diameter, and ridge width but the clearest correlation is a power-law dependency of force on rubble depth. The upward curvature is distinct even without normalization of the other factors. It is important to emphasize that these plots do not isolate the effects of single variables so that no correlations were ruled out prior to the regression study.

4.3.4 Regression study

Multiple regression techniques have been used to synthesize formulas representing the relationship between measured force and the explanatory variables described above. Two groups of dimensionless ratios were investigated for best-fit. The quality of the fitted formulae were determined by the same methods used in the study of ice rubble shear in Section 4.2. Matrix plots and variance inflation factors were used to identify and avoid spurious correlations and multicollinearity problems.

All data sets were grouped for the initial analysis. In the second trial two data sets (Timco and Cornett, 1995, and Bruneau, 1994a "dry tests") were removed. In Timco and Cornett (1995), uncertainty surrounds the non-direct measurement of rubble forces and in Bruneau (1994a) "dry" ice rubble was not submerged. Furthermore neither program had a specified shear strength for ice rubble (in the state tested). In the third trial only those experiments associated with this thesis and reviewed in Chapter 3 were included (Bruneau, 1994a "wet", McKenna *et al.*, 1995a and b, and McKenna, 1996). These tests also correspond to the only data sets which involved discrete ridges for which ridge width and sectional area were reported.

Dummy variables, as suggested by Draper and Smith (1966), were used to quantify the influence of boundary conditions. The three boundary conditions which were identified for this study are, as described above (Subsection 4.3.3): the longitudinal extent or width of the rubble, the lateral extent of the structure and the degree of rubble confinement at the waterline.

Results

A qualitative regression study of the laboratory ridge/structure interaction boundary conditions indicated that only the confinement of the rubble at the waterline significantly affected loads. Neither rubble width nor structure extent were significant factors in measured loads. This result comes as some surprise since the boundary condition which receives the least attention in load models (confinement at the waterline) is the only one of importance in the lab. Results here must be viewed cautiously, however, since the boundary conditions are closely correlated to other laboratory conditions which may also be influential.

Correlation analyses results for all explanatory variables and for each of the three data set groupings are listed in Tables 4.9 to 4.11. Force formulations from the regression analysis are summarized in Table 4.12. Included are the best-fit formulas for both dimensional and non-dimensional explanatory variables. Results which were near best-fit but involved fewer or alternate variables are also given. Both linear and power law best-fit formulas are given with and without intercepts for all three data set groupings.

All data sets

Single variable linear regression results listed in Table 4.9 indicate that force is predominantly influenced by rubble depth and structure diameter. These terms are key elements in "earth pressure" force formulas, $0.5\gamma H^2 D$, and so this was the form (including the 0.5 coefficient) of the normalizing term exploited for subsequent regression tests.

Table 4.12 lists the most significant multi-variable regression results. Although velocity shows up as a significant variable in the first formulation in Table 4.12 it appears later to have an opposite effect (with a different data set). This conflicting result indicates that the significant correlations with velocity are probably arbitrary and coincidental. For most multi-variable regression trials involving dimensional variables those terms associated with hydrostatic "earth pressure" force were again dominant. The term, $0.5\gamma H^2 D$ is the most significant and often the only significant parameter in the regression equations for ridge indentation force. The dependency of indentation force on this term is demonstrated in Figure 4.22 where all data sets are identified by author. The best-fit linear and non-linear formulations involving only this term are shown in Figure 4.23. According to linear regression results, 93% of the variation in interaction force can be

explained by the following:

$$F - 11.5 \frac{\gamma H^2 D}{2} + 150 \qquad (50)$$

The power law relation for the same data set resulted in a 55.7% r^2. The residuals for both are not normally distributed and so the r^2 values are skewed. The plotted results in Figure 4.23 clarify this problem by showing the deviations of both curves from the data points. When the intercept is fixed at zero (for which an r^2 value cannot be interpreted) the apparent fit is better, particularly with the larger scale tests. The formula becomes

$$F - 12 \frac{\gamma H^2 D}{2} \qquad (51)$$

All data sets minus Timco and Cornett (1995) and Bruneau (1994a) "dry"

The data set was reduced in size by eliminating the data from Bruneau (1994a) "dry" and Timco and Cornett (1995). Table 4.10 indicates that force is significantly correlated to depth, diameter and internal friction angle. However, ϕ is also correlated to depth and diameter and therefore cannot appear with them as a control term in a multi-variable regression analysis. Regression results indicated an improved linear fit over the previous result. With an $r^2 = 96\%$ the following formula was determined:

$$F - 11.6 \frac{\gamma H^2 D}{2} + 103 \qquad (52)$$

The skewness of the residuals for both the transformed power law and linear formulas was diminished somewhat from the previous trial. Plotted results in Figure 4.24 again indicate that the best-fit for the larger scale experiments was a zero-intercept formula with a proportionality coefficient of 12.

Chapter 3 data only (Bruneau, 1994a, McKenna et al., 1995a and b, and McKenna, 1996)

The third regression study was performed on those data sets which involved the indentation of discrete piles of rubble, not continuous rubble fields. Data sets were limited to those reviewed in Chapter 3. Table 4.11 indicates the single variable relationships for this data set and is a guide for avoiding multi-collinearity. Both linear and power-law fits resulted in r^2 values better than 95%. The linear relation established was

$$F = 11.8 \frac{\gamma H^2 D}{2} + 55 \tag{53}$$

and is shown in Figure 4.25. Again the zero intercept relationship was identical to that for other data sets with a coefficient of 12. Essentially the data sets in this last grouping are directly proportional to hydrostatic earth pressure and form a boundary above which all the other data sets, with quite different boundary conditions, were scattered.

Despite expectations that the width and shear strength of ice rubble accumulations were important factors in determining loads on structures in the lab, regression results indicate otherwise. The non-significant correlations in the multi-variable analysis for these parameters are qualified, however. The close correlation between shear strength and normal stress (a function of rubble buoyant weight and depth) has made the rubble strength terms inseparable from the $0.5\gamma H^2 D$ term. Also, ridge width has a non-zero correlation to depth and so is also inseparable. The robust linear relationship between measured force and $0.5\gamma H^2 D$ with the coefficient of around 12 simply cannot be further reduced or broken down to include other explanatory variables because of these and other

parametric correlations.

4.3.5 Conclusions

In this section a review of experimental results has elucidated the form of fundamental equations describing ridge keel failure forces on vertical structures. Though known, the values of the proportionality coefficients remain somewhat unexplained. The correlation between some of the important experimental conditions has made explaining them difficult. This is a problem for generalizing and scaling results since factors such as ridge width, which may be significant in the laboratory but buried in the proportionality coefficient, may or may not be a significant factor at full-scale.

Motivated by the success of previous "sand keel" tests the next chapter describes a set of control experiments which attempt to reconcile the regression formulas described here with physical modelling results. The rationale is that testing with a material for which shear strength is time-independent and well understood, and with techniques that permit accurate measurements of key experimental conditions, can provide a definitive data set for constructing a working keel force model. A model developed from sand tests would substantially improve existing modelling practices if it could be adapted and calibrated for ice ridge application and still retain the sensitivites to boundary conditions, keel size *etc.* learned with sand.

Table 4.8 Summary of Laboratory ice rubble indentation experiments.

Reference	Boundary conditions Rubble extent**	Structure Waterline width	confine.	Range of Structural width m	Range of Rubble width m	Range of Rubble depth m	Range of Rubble area m^2	Range of Speed m/s	Range of Peak load N	Range of Friction angle deg	Range of Cohesion Pa
Cheng and Tatinclaux (1977)	C	2-D	N	0.91	Contin*	0.076-0.22	-na-	0.00015-0.0028	19-366	46	1
Keinonen & Nyman (1978)	C	2-D	N	0.3	Contin	0.174	-na-	0.025	24	47	10
Prodanovic (1979)	C	2-D	N	0.152-0.304	Contin	0.09-0.28	-na-	0.001-0.009	8-285	50	500
Hellmann (1994)	D	3-D	N	0.1	Contin	0.2-0.8	-na-	0.001-1.25	60-600	54-61	580-420
Timco and Cornett (1995)	D	3-D	N	0.333	0.8-1	0.003-0.45	0.002-0.4	0.09-0.27	70-1900		
Bruneau (1994) - wet	D	3-D	Y	0.114	0.3-contin	0.1-0.25	.06-0.112	0.006	7.5-50	50	1500
Bruneau (1994) - dry	D	3-D	Y	0.114	0.3-contin	0.1-0.2	0.02-0.09	0.006	52-250		
McKenna et al. (1995a)	D	3-D	Y	0.32	2-3	0.58-0.67	0.59-1	0.02-0.19	331-852	36	500
McKenna et al. (1995a)	D	3-D	Y	0.8	4.5-6	0.59-1.02	3.4-4.2	0.03-0.14	870-3950	36	500
McKenna (1996)	D	3-D	Y	0.8-1.8	1.75-6	0.01-1	0.014-3.1	0.049-0.079	810-6580	36	873

* Contin. means that rubble was continuous in the direction of structure displacement.
** Rubble extent is either continuous (C) or discrete (D) in the direction of travel

Table 4.9 Explanatory variable correlation analysis - all data sets.

Force (F)	Speed (V)	Depth (H)	Diam (D)	Weight (γ)
20.8				
67.1	30.7			
40.4	3.6	16.8		
0.5	1.7	1.7	4.2	

Key: r^2 adj
r^2 adj > 50%
r^2 adj > 30%

Table 4.10 Correlation analysis for all data minus Timco and Cornett (1995), and Bruneau (1994a) "dry".

Force (F)	Speed (V)	Depth (H)	Diam (D)	Weight (γ)	Friction (φ)	Cohesion (c)
22.6						
68.5	43.6					
40.6	5.7	14.9				
1.8	0.4	0	0			
30.4	28.4	36.2	40.4	3.8		
3.4	0	0	25.3	0	8.8	

Key: r^2 adj
r^2 adj > 50%
r^2 adj > 30%

Table 4.11 Correlation analysis of Chapter 3 data sets only.

Key: r^2 adj
r^2 adj > 50%
r^2 adj > 30%

Force (F)	Speed (V)	Depth (H)	Diam (D)	Weight (γ)	Friction (φ)	Cohesion (c)	Area (A)	Width (W)
1.9								
59.2	24.4							
62.3	0	28.1						
3.1	5.7	0	5.7					
8.5	16.4	43.7	13.1	10.2				
33.8	12.5	56.5	43	1.8	45			
36.2	28.3	80.9	23.8	2.4	14.7	43.6		
33	19.7	63	36.7	0	34.9	55.3	81.3	

Table 4.12 Summary of regression results for structure interaction tests.

Structure tests: explanatory variables	Regression formula	r^2 (adjusted)	Std. dev*	F test
All data sets				
$F = f(D, H, V, \gamma, \rho)$	$F = 4820 H^{0.696} \rho^{0.85} V^{0.302}$	68.0	0.9426*	85.86
$F = f(\gamma HD, H/D, gD/V^2)$	$F = 11,500.5\gamma HD/\gamma + 49.1(H/D) + 82.6$	93.1	304	810
	$F = 3370.5\gamma H^2 D^{0.85}(H/D)^{0.302}(gD/V^2)^{0.85}$	66.9	0.9386*	82.0
	$F = 11,560.5\gamma HD + 150$	92.8	310	151.9
	$F = 82,30.5\gamma HD^{0.806}$	55.7	1.11*	
$F = f(\gamma HD)$ without intercept	$F = (0.5\gamma HD)^{1.6}$		3.796*	137.4
	$F = 12.1 * 0.5\gamma HD$		337	1800
Minus: Tinto and Cornell (1995), Brumau (1994a) "dry"				
$F = f(D, H, V, \gamma, \rho, \phi, \nu)$	$F =$	88.9	412	203
$F = f(\gamma HD, H/D, gD/V^2, \phi, \nu)$	$F = 341H + 171HD + 3.43\gamma + 62.3\phi - 6528$	86.8	0.6357*	166.4
	$F = 780 H^{1.71} D^{ac} \gamma^{0.85} \rho^{0.85}$			
	$F = 11,700.5\gamma HD + 60.2H(H/D) + 16.2$	96.8	220	1539
	$F = 11,660.5\gamma HD + 103$	96.4	236	2671
	$F = 47,000.5\gamma HD^{0.78}$	84.7	0.6636*	599
$F = f(\gamma HD)$ without intercept	$F = (0.5\gamma HD)^{1.6}$		3.0*	344
	$F = 12.0 * 0.5\gamma HD$		252	3185
Chapter 3 data sets only: Brumau(1994a) "wet", McKenna et al (1995), McKenna (1996)				
$F = f(D, H, V, \gamma, \rho, \phi, \psi, W, A)$	$F = 38.1\chi^{0.708} H^{0.8} \rho^{0.900}$	97.3	0.3103*	412
$F = f(\gamma HD, H/D, gD/V^2, \phi, \psi, W/D, A/WH)$	$F = 15,460.5\gamma HD^{0.966}$	97.4	0.3035*	1291
	$F = 11,400.5\gamma HD + 54.6$	95.3	348	693.34
$F = f(\gamma HD)$ without intercept	$F = (0.5\gamma HD)^{1.6}$		1.232*	1064
	$F = 12.0 * 0.5\gamma HD$		344	1697

* Standard deviation of natural logarithm

Steps
1) Determine rank m of dimensions matrix with n parameters (n1 m)
2) Choose m repeating variables from set of m, creates matrix A and remainder B (partitions matrix)
3) Invert m x n dimensional matrix A to get C
4) Multiply C and D to get output matrix D
5) Extract the n - m Pi parameter (ratios) from D

RELATED PARAMETERS AND THEIR FUNDAMENTAL UNITS

Figure 4.19 *Matrix method* dimensional analysis no. 1 for interaction force terms.

Figure 4.20 *Matrix method dimensional analysis no. 2 for interaction force terms.*
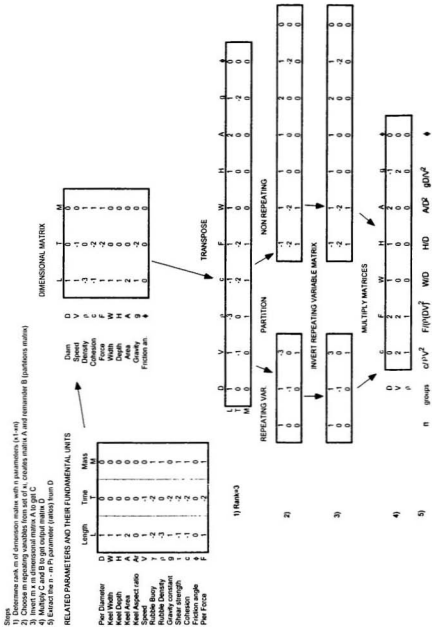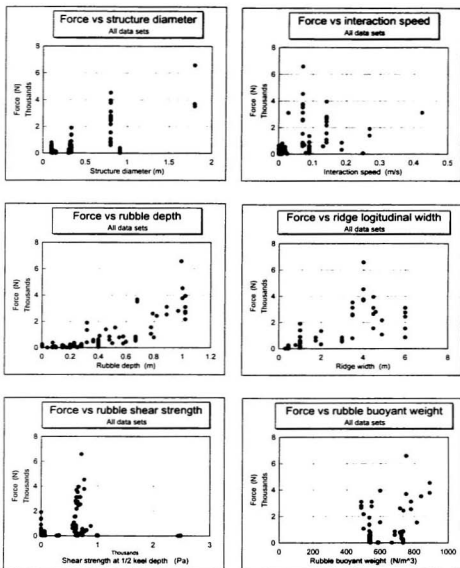
Figure 4.21 Scatter plots of force versus key variables.
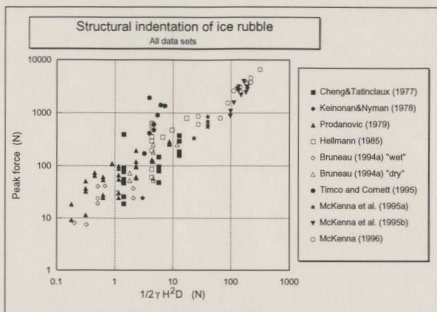
Figure 4.22 Ice rubble indentation force vs $1/2\gamma H^2 D$ term - by author.
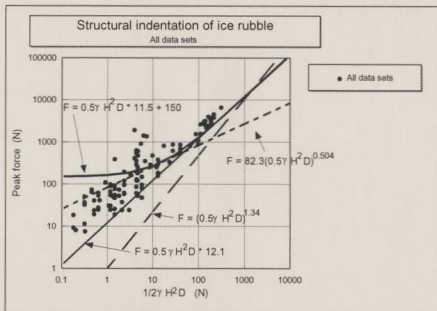
Figure 4.23 Ice rubble indentation force vs $1/2\gamma H^2 D$ term - regression results.
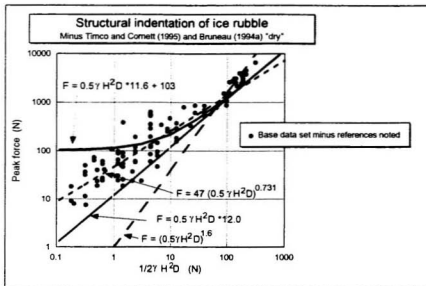
Figure 4.24 Ice rubble indentation force vs $1/2\gamma H^2D$ term - sensitivity study.
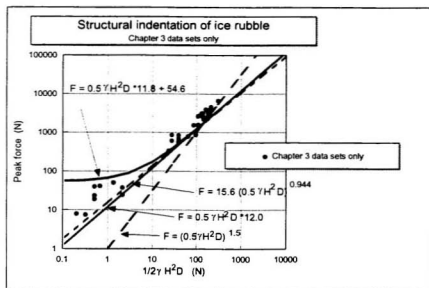
Figure 4.25 Ice rubble indentation force vs $1/2\gamma H^2D$ term - sensitivity study.

Chapter 5

MODEL DEVELOPMENT II

Sand tests

In Chapter 4 the shear strength of ice rubble was analyzed using regression techniques. The strength was shown to be a complex function of confinement stress which is inseparable from block size in the reported laboratory results. Varying experimental techniques, and the correlation of many experimental conditions distort the relative importance of control variables and underscore the need for direct field measurement of parametric inputs in force prediction models.

Structure interaction experiments were also reviewed in Chapter 4. For most combinations of data sets, interaction forces were shown to be strongly related to hydrostatic earth pressure. For the trials involving the data sets reviewed in Chapter 3 it was shown that the only parameters with significant influence on interaction force were rubble depth, weight and structure diameter. Again the problem of correlated variables was prevalent as rubble strength could be defined by rubble depth, ridge width by ridge depth *etc.*.

In this chapter an attempt is made to decipher the composition of the proportionality coefficients for the force models in Chapter 4. Experiments have been conducted using piles of dry sand that model, in inverted form, a rubble ice keel. It is conjectured in this study that the plastic deformation of "sand keels" in the laboratory may provide a simple

but effective analogue for natural ridge failure processes. Though no scaling of loads is intended, the "sand keel" approach sheds light on fundamental failure mechanisms and force trends for the indentation of keel-like accumulations of a granular material. The ease and simplicity of systematic testing with sand is in sharp contrast to experimenting with floating ice rubble in the lab. Sand also has roughly the same lower bound shear strength as ice rubble and the literature points out that failure modes in soils are not significantly influenced by cohesion. In the present chapter, a load model is developed for vertical and sloped structures in sand providing a basis for understanding the results in Chapter 4.

5.1 Keel replication experiments

5.1.1 Introduction

In this section experiments are described in which ice rubble keels created in the IMD laboratory using the "dumptruck" technique in McKenna *et al.* (1995b) (reported in Section 3.4) are replicated with sand and indented at reduced scale. The purpose is twofold: to compare force patterns so that ice rubble indentation force can be contrasted against a purely frictional material, and, to justify the use of sand as a substitute for ice rubble in experiments where elucidating general failure patterns and load trends are the objectives. Only the submerged portions of the ridges interacting with the cylindrical part of the structure in McKenna (1995b) are considered in this study.

Figure 5.1 is a plot of laboratory ice rubble shear data from Chapter 4. The theoretical behaviour of a loose and dense sand (from Bowles, 1984) and plastic blocks (from Urroz

and Ettema, 1987) is shown for comparison. The figure indicates that the lower bound strength (or weakest state) of ice rubble undergoing shear is similar to that of loose sand. As described earlier, the scatter in the upper portion is attributable to various degrees of inter-block bonding or rubble *cohesion*. The absence of cohesion in sand tests is not expected to adversely influence the applicability of experimental results. Jumakis (1984) states, "Consideration of stress condition in soil shows that cohesion of a ϕ-c soil does not affect the position of the rupture surface.". Also, in the study of soil failure in front of tines it has been observed that rupture distance (leading extent of failure pattern) is substantially independent of cohesion (Osman, 1964) and moisture content in sand (Rajaram and Oida, 1992).

5.1.2 Experimental program

The keel replication experiments were performed at C-CORE. All experiments were conducted with silica sand Type '0' with internal friction angle equal to 32° and weight of 13880 N/m³ when loosely deposited. The 1 m square tank apparatus constructed for experiments in Section 3.1 was used. The same mechanical drive arm was employed for horizontally translating the 60 mm diameter plastic model structure. The structure was vertically supported by two cantilever load cells and, when translated, maintained a constant clearance of 4 mm with a sandpaper-covered false floor. All tests were conducted at 6 mm/s.

"Sand keels" were constructed by placing piles of loose sand across the tank floor in front of a model structure. Precise shaping was achieved using plywood trowels cut out to the shape of the ridge keels profiled in the McKenna *et al.* (1995b) "PWC" study. The trowels were dragged over the loose piles, creating the desired prismatic keel form. The

average profile reported for each of the six ridges and adjusted for the position of the cone was used. Sand was mixed and consistently replaced before each experiment to maintain a consistent density. A total of eleven ice interaction tests were performed in McKenna *et al.* (1995b), two for each ridge except for ridge number five in which only one ice interaction experiment was performed. Eight of these are considered in this study. The "cone low" experiments are omitted because the cone extends down into the keel so that the integrity and shape of the keel portion interacting with the cylinder are more likely to be disturbed.

5.1.3 Experimental results

Force traces for all eight tests have been normalized by peak force and plotted in Figures 5.2 to 5.9. Also plotted are the keel profile and force trace for the corresponding ice ridge interaction experiments. The horizontal position of the ice ridge force traces (relative to the keel) was based on the positioning reported in McKenna (1995b). The horizontal position of the sand traces in the figures was established by shifting them until the start of force increase coincided with that of the ice ridge. This procedure was required since the two force curves were not in phase, perhaps a result of the forward displacement of the ice ridge keels during interactions. Doing so improved the clarity (and probably the positional accuracy) of the superimposed curves. Although force traces may not be in proper phase position with the keel profile, the horizontal scale is correct and so one can easily make correlation observations.

In general, sand and ice force trace patterns are quite similar. The exceptions are that sand force traces are typically less steep on the decline (trace RHS) and have a broader peak than ice force traces. Also ice force traces are characteristically bi-modal when the

keels are this way. Some of these differences can be accounted for by assuming that in the ice ridge experiments very little surcharge develops during interactions at medium and high speeds[1]. If displaced ice blocks are not settled enough to create a surcharge one may expect the force traces to follow the contours of the original undisturbed keel form. Dynamic model scaling is in no way achieved in the sand tests so that a very different fluid dynamic regime exists. Displaced sand which accumulates and flows around the structure settles immediately and provides an instantaneous surcharge. Thus one would expect higher relative loads particularly after the peak where ploughed sand may obstruct the structure even after leaving the original ridge site.

It appears that at high speeds an even greater disparity exists between sand and ice force traces. The most notable dissimilar trace was that for the high speed test PWCPEI1-1 where the trace appeared to be "eroded" over the first half of the curve. This may be the result of the *suspension* of previously undisturbed submerged ice rubble blocks. Fluid accelerating around the advancing structure may shear off ice blocks on the outer surface of the keel in the steepest flow gradient regions. Flow speeds easily exceed that which is critical for the suspension of ice blocks in the PWCPEI experiments (block terminal speed is around 0.26 m/s). At very high speeds engaging blocks may be analogous to spooning tea leaves in a stirred-up cup.

Evidently, the best force trace match is that for the slowest interaction speed (PWCPEI3-2) which lends support to the transient surcharge assumption. For that test the bi-modal keel is not reflected in the ice force trace as prominently as in others at medium speed.

---

[1] This appears to be consistent with video records taken during IMD tests. Fluid dynamic considerations supporting this assumption are also discussed later in Chapter 7.

including PWCPEI3-1 for the same ridge. The slope matches that of the sand where it was observed that ploughed material ahead of the advancing structure had settled into the keel trough.

Generally, ice force traces are more jagged than sand traces. Although, seemingly smooth sand does tend to fail in "blocks", the ice ridge trace has a higher frequency failure mode which may be a feature of a different compressibility and the failure of cohesive freeze-bonds. These effects do not appear to substantially influence the general similitude of patterns.

5.1.4 Conclusions

The force traces from "sand keel" indentation experiments appear to be representative of those for ice rubble interactions over a limited range of interaction speeds. The suitability of results from all sand tests must be considered in light of this sensitivity. The success of modelling ridge keels with sand here, and in Chapter 3, presents an opportunity for more advanced experiments described in following sections.

197
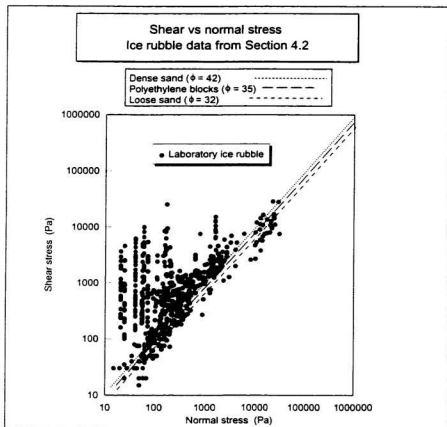
Figure 5.1 Shear vs normal stress: ice rubble, sand, and plastic blocks.
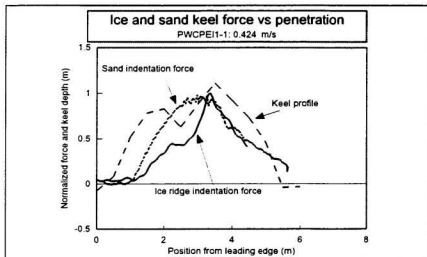
Figure 5.2 Force patterns and keel shape - PWCPEI1-1.
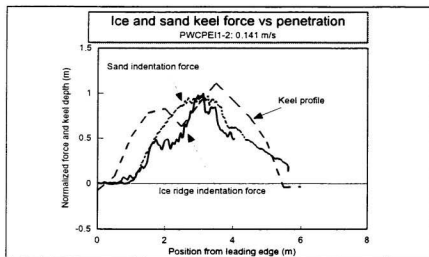
Figure 5.3 Force patterns and keel shape - PWCPEI1-2.
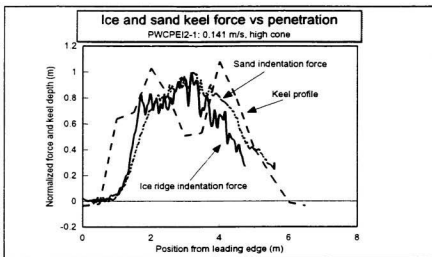
Figure 5.4 Force patterns and keel shape - PWCPEI2-1.
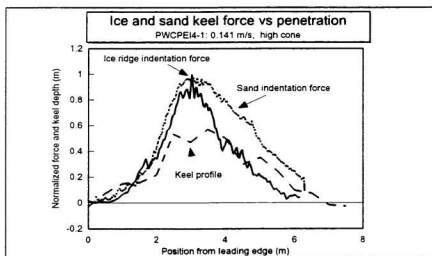
Figure 5.5 Force patterns and keel shape - PWCPEI4-1.
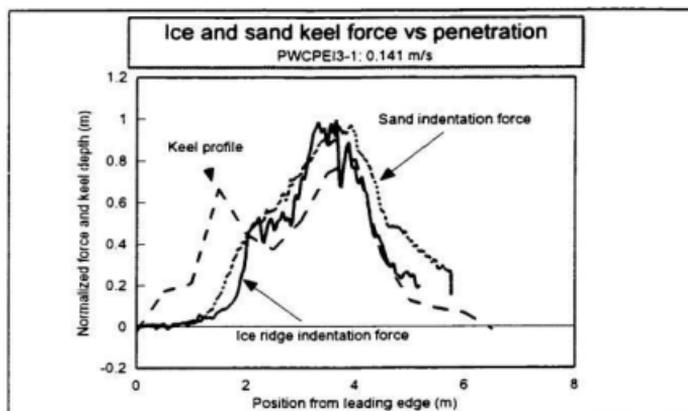
Figure 5.6 Force patterns and keel shape - PWCPEI3-1.
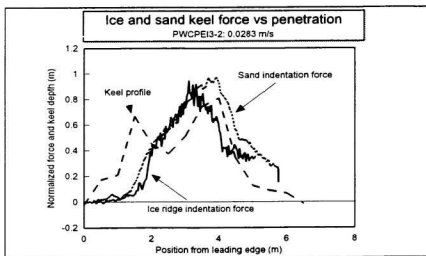
Figure 5.7 Force patterns and keel shape - PWCPEI3-2.
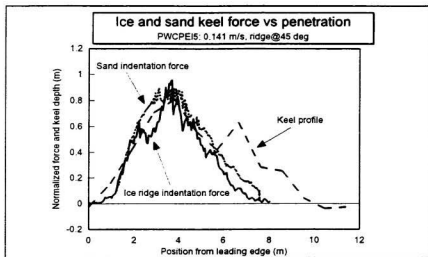
Figure 5.8 Force patterns and keel shape - PWCPEI5.
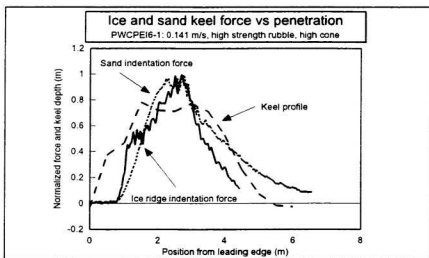
Figure 5.9 Force patterns and keel shape - PWCPEI6-1.

5.2 Sand-modelling of ice rubble forces on vertical structures[1]

5.2.1 Introduction

In Chapter 4 the regression study of ice rubble interaction experiments was unable to elucidate the relative importance of ridge width, rubble strength and other explanatory variables. In the literature it is apparent that two-dimensional earth pressure and draught formulae used in geotechnical and agricultural engineering practice are limited in their capacity to help. The force required to break through a discrete sand pile may be considerably less than that for retaining structures or steady-state ploughing conditions for a continuous horizontal layer. Also the indentation of keels is more complicated than passive pressure on retaining walls because a non-linear, transient surcharge may develop and clearing processes are activated.

This section describes controlled experiments using sand which are undertaken to determine the relative influence of keel shape, and, structure shape and aspect ratio. Also systematic testing of "sand keels" of various aspect ratios which enable the point of incipient plug failure and peak load to be correlated and formulated are carried out. The measurement of the horizontal load and failure patterns with penetration into continuous sand layers is also undertaken to provide a basis for the formulation of a force prediction model for "sand keels".

---

[1] A version of this section *Bruneau, S.E. (1996) Modelling first-year ice ridge keels with sand*, has been presented at the 49th Geotechnical Conference of The Canadian Geotechnical Society, Sept. 1996, St. John's, Nf.

5.2.2 Experimental program

Experiments were carried out using the same apparatus and similar testing procedures as described in Sections 3.1 and 5.1. Several additional plastic model structures and plywood "keel" trowels were constructed. Refer to Appendix C for a full listing of experimental conditions for all sand tests reported in this section.

For structures indenting symmetrical trapezoid keel formations dimensional analysis yields:

$$\frac{F}{\gamma H^2 D} = f\left[\alpha, \delta, \phi_I, \phi, \frac{W}{D}, \frac{H}{D}, \frac{P_{en}}{D}\right] \qquad (54)$$

where F is horizontal force, γ is bulk weight, α is the slope of the structure, δ is soil surface slope, ϕ_I is the soil-structure friction angle, ϕ is the angle of internal friction, W and H are the "sand keel" width and depth, D is the structure projected width and P_{en} is structure penetration from the "sand keel" leading edge. For tines indenting soil there is a critical depth aspect ratio (rubble depth to structure width) above which material is displaced forwards, sideways and upwards, and below which no upward movement occurs. Reported values for the critical depth aspect ratio vary widely with a median value around 7 (Godwin and Spoor, 1977). This study is aimed at applications where aspect ratio is typically no greater than 3, remaining above the critical depth.

5.2.3 Experimental results

Figure 5.10 illustrates the relative influence of "sand keel" shape on peak load and penetration at peak. All five keels (shown beneath the bar graph) had the same sectional

area and two different widths were used. Loads were normalized against the 320 mm-wide trapezoid "sand keel" because it resulted in the highest load and was also the preferred default shape in subsequent tests. Generally, the wider shorter keels resulted in lower loads and significantly greater penetrations at peak. There was little difference between the loads on keels of similar width.

Figures 5.11 and 5.13 illustrate the influence of structural shape on peak indentation force for both trapezoidal "sand keels" and for a continuous sand layer (steady-state loading achieved). Each model shape (shown in Figure 5.11) had the same projected frontal width. The load on the circular cylinder was used to normalize loads for the trapezoidal indentation tests and the square section was similarly used for the continuous layer tests because each produced the respective maxima. The results which show little variation for trapezoidal indentation and moderate differences for continuous layer indentation are in stark contrast to the substantial variation in drag of similar, two-dimensional bodies in a fluid. Force traces for the three structure shapes are superimposed on Figure 5.13. That for the square section has the steepest incline whereas the force trace for the triangular structure is the most gradual.

To establish the quantity of load attributable to "edge effects" flat vertical structures of width D, $2D$, and $3D$ were translated through "sand keels". Peak indentation force for each test was normalized against that for the structure of width D (Figure 5.12). By extrapolating to the normalized force intercept, one obtains a force at an effective width of zero. In this study the edge effect force was 50% of the total indentation force for the structure of width D where the keel was $2.8D$ wide and $2/3D$ deep. Thus, the *effective* width of the structure, D_{eff}, was

$$D_{eff} = D \left[1 + \frac{1.5H}{D} \right] \tag{55}$$

which is necessarily limited by critical depth considerations to around $2D$. It is remarkable that if one inverts the aspect ratio coefficient in the above formula it becomes essentially equivalent to Dolgopolov's shape factor reviewed in Section 2.4. Sample force traces for the three widths are plotted in Figure 5.13.

The relative penetration to peak load has been determined for a range of W/D and H/D ratios for vertical cylinders indenting trapezoidal "sand keels" (Figure 5.14). The penetration at peak force may not be independent of structure roughness and sand density, however, these parameters were not varied in this study. Multiple regression techniques were applied to determine the expression

$$\frac{P_m}{D} = 0.113 \left[\frac{W}{D} \right]^{1.63} \left[\frac{H}{D} \right]^{-0.42} \tag{56}$$

which has a goodness-of-fit adjusted r^2 value of 97%.

Lastly, continuous sand layers were indented until steady state conditions arose. The point at which steady state failure occurred was approximated because it is a cyclic collapse mechanism (as described by Rajaram and Oida, 1992). Forward rupture distance, r, side rupture distance, s, surcharge height at the structure, H_{sur}, and horizontal force were measured at 5 cm penetration intervals for a range of H/D (Figure 5.15). Expressions for r, s, and H_{sur} have been formulated using multiple regression techniques yielding,

$$\frac{H_{sur}}{D} = 0.818 \left[\frac{H}{D}\right]^{0.43} \left[\frac{(P_{en}/D)^2}{(P_{en}/D)^2 + (H/D)}\right]^{1.89} \qquad (57)$$

$$\frac{r}{D} = 2.01 \left[\frac{H}{D}\right]^{0.509} \left[\frac{(P_{en}/D)^2}{(P_{en}/D)^2 + (H/D)}\right]^{1.11} \qquad (58)$$

$$\frac{s}{D} = 1.39 \left[\frac{H}{D}\right]^{0.554} \left[\frac{(P_{en}/D)^2}{(P_{en}/D)^2 + (H/D)}\right]^{2.17} \qquad (59)$$

with r^2 values (adjusted for degrees of freedom) of 96.5, 98.2 and 92.4 % respectively. The basic form of these equations was developed from first principles as described in Appendix D. Patterns of increase and stabilization are the same for all measured quantities. Measurements of r and s required some judgement since rupture form was slightly asymmetric at times and the cyclic formation of leading rupture edges meant that these dimensions ratchetted as the structure advanced.

5.2.4 Development of a load model: cylindrical structures, trapezoidal keels

When a cylindrical structure penetrates a "sand keel", the sand accumulates in a raised crescent around the leading edge with the rupture distance extending further from the structure as surcharge deepens (Figure 5.15). The failure surface is rounded and cusp-like until shear planes, flaring from the structure to the back of the keel, form.

Failure patterns were observed and sketched (Figure 5.13) from time-lapsed photographs taken through a window with a model structure brushing past. For the trapezoidal "sand keel" in Figure 5.13, the failure surface extended upwards at a steep angle from position

0 through to some time after position 1. At that point a transition occurred whereby the sand within the main body of the pile ahead of the structure became fully mobilized. This transition in failure mode appears to mark the point where the classical local passive failure system collapses with the diminished confining stresses at the rear of the pile - promoting an outward instead of upward displacement of sand. In Figure 5.13 it can be seen that this transition between local and plug-like failure also marks the zone in which peak load occurs.

An algorithm for computing peak load requires modelling of only one of the failure modes described above because the point of incipient plug failure is now known from the results in Figure 5.14. Thus, the well established passive earth pressure formula representing the local failure mode has been used and adapted for computing forces in this study as follows:

$$F = \frac{\gamma H_t^2 K_p D_{eff}}{2} \tag{60}$$

where γ is the bulk weight of the sand (measured as 13880 N/m^3), H_t is the total height of sand at the structure ($H_{sur} + H$), D_{eff} is the effective width of the structure, and K_p (from Jumakis, 1984) is the effective passive pressure coefficient defined as

$$K_p = \frac{\cos^2(\phi + \alpha)}{\cos^2\alpha\cos(\alpha - \phi_1)\left(1 - \sqrt{\dfrac{\sin(\phi + \phi_1)\sin(\phi + \delta)}{\cos(\alpha - \phi_1)\cos(\alpha - \delta)}}\right)^2} \tag{61}$$

where α is the slope of the structure, δ is soil surface slope, ϕ_l is the soil-structure friction angle (0.6ϕ for sand and plastic, after Audibert *et al.*, 1984) and ϕ is the angle of internal friction ($\approx$ 32° for loose sand tested after Paulin, 1992). This formulation is described in more detail in **Appendix D**.

The average surface slope, δ, was approximated as $atan(H_s/2r)$ by observing in continuous layer indentation that overburden was approximately level over half of the rupture distance before sloping to the toe of the surcharge pile. From the results of experiments here and in Chapter 3 it was concluded that the effects of varying ridge cross-sectional shape, ridge obliquity and structure cross-sectional shape were not great enough to justify inclusion in this force model.

Indentation force has been computed as a function of penetration using two approximations for effective width, D_{ef} (Figure 5.15(d)). The first, method "A", is $D(1+3H/2D) \leq 2D$ from above. Method "B" is an attempt to reconcile the computational procedure with observed failure shape. During local failure the cusp-like wedge of mobilized sand appears to have a uniform vertical cross-section (Figure 5.15). The whole displaced sand body can thus be approximated geometrically by sweeping a vertical wedge of unit width circumferentially at either side of the cylinder projected width. Since the failure surface is approximately straight between the bottom of the structure and the surcharge pile toe, one can integrate the wedge sides and add to the structure diameter as follows:

$$D_{ef} = D + \int_{-\beta}^{\beta} \frac{r}{2}\cos(\theta)d\theta = (D + r\sin(\beta)) \quad ; \quad \beta = atan(s/r) \qquad (62)$$

to get the effective frontal width of the failure surface.

Measured forces are modelled slightly better by method "A" than "B" though both approximations are quite sound. Method "A" matched results with an r^2 value of 96.7% and Method "B" had an r^2 value of 93.2%. The Method "A" D_{eff} is also more appealing than the other owing to its simplicity, not requiring rupture distance values. The peak indentation load for any trapezoidal "sand keel" is obtained from Figure 5.15(d) by determining the penetration at peak for H/D and W/D from Figure 5.14. Alternatively, the dimensionless formulas for surcharge height, peak force penetration and effective structure width may be used to obtain the same result.

5.2.5 Conclusions

A model of the interaction forces for prismatic structures indenting "sand keels" has been successfully developed and tested. The procedure, based on passive earth pressure, provides a framework for understanding the role of several key explanatory variables. Ridge width, for example, influences the depth of the sand at which peak load occurs. It was not possible to establish this relationship with the ice rubble data sets. The procedures outlined are limited in application to full-scale by an inability to model global inertia, compressibility, fluid dynamic and boundary compliancy effects. The degree to which these effects influence force modelling is investigated, in part, in the following chapters where the procedure developed in this section is applied to ice rubble for load prediction.

With additional sand testing semi-empirical relations for r, s, and H_{sur} may be found for sloping structures including some cones. This is of interest since cones have been used

as ice shields in the Northumberland Strait Bridge Project. Though models for the flexural failure of an ice sheet are well-established, the effects of structure slope on rubble clearing are not well-defined. Analytical solutions similar to those described in this section for vertical structures are possible for cones since conical structures approach cylindrical form with increased slope angle. An alternate modelling procedure may be necessary for cones with a gradual slope.
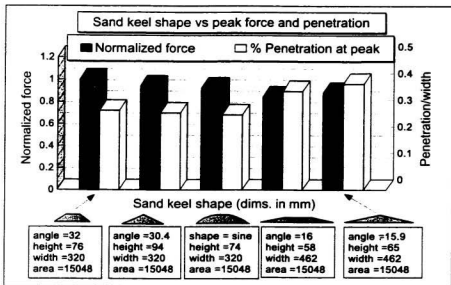
Figure 5.10 "Sand keel" shape study.
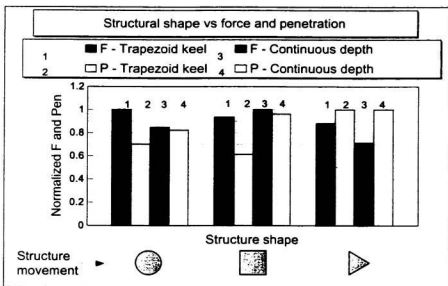
Figure 5.11 Structure cross-sectional shape study.
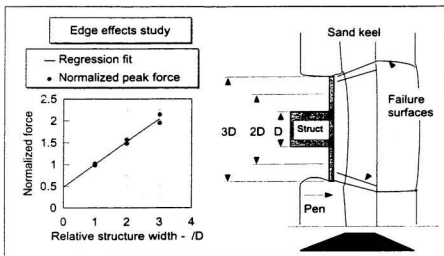
Figure 5.12 Study of edge effects for development of effective width formula.
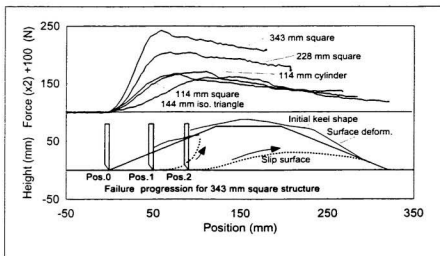
Figure 5.13 Force trace and failure pattern study.

$$(Pen/D) = 0.113\ (W/D)^{1.63}(H/D)^{-0.42}$$
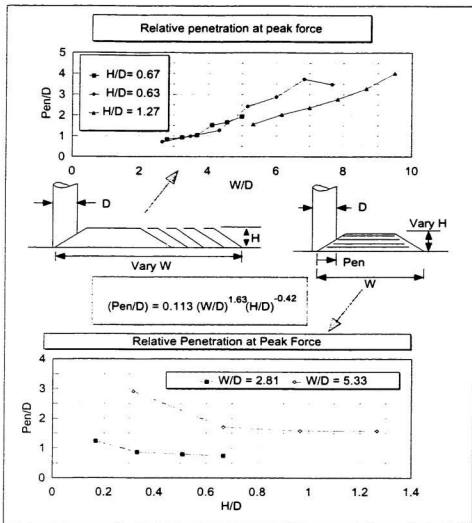
Figure 5.14 Keel penetration at peak force study.
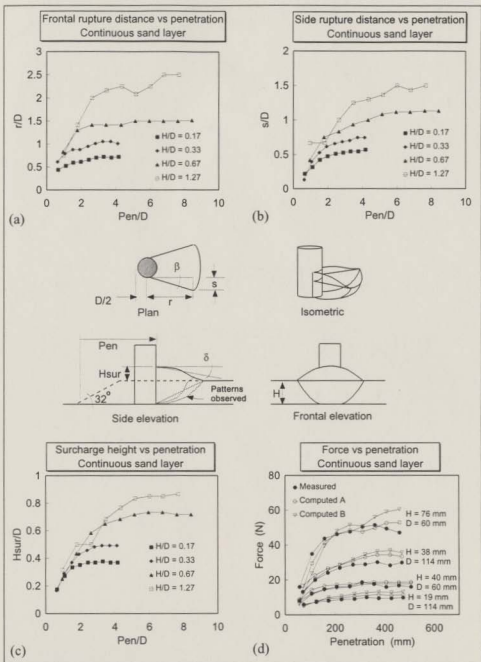
Figure 5.15 Rupture surface evolution, and, measured vs predicted forces.

5.3 Sand-modelling of ice rubble forces on conical structures

5.3.1 Introduction

As described in Section 2.4 competent sea ice crushes, spalls and buckles against vertical structures while for sloping structures it fails at much lower loads in flexure. Sloping structures, such as cones, also diminish the threat of structural resonance but tend to increase vertical loads, underwater exposure and construction complexities. Probabilistic design calculations for the Northumberland Strait Crossing Project (Cammaert *et al.*, 1993) indicated that when efficient upward breaking conical structures are placed in a dynamic first-year sea ice environment design ice loads may be governed by ridges which are keel-dominated. The relative importance of loads from the refrozen core, ordinarily a formidable obstacle for vertical structures, is diminished by the cone. The failure modes and load levels associated with submerged and above water ice rubble interacting with upward breaking cones is not well-understood. This study describes an investigation with a conical structure similar to the investigation in the previous section for vertical structures. There sand was substituted for ice rubble in scaled experiments from which fundamental failure mechanisms were determined and a load prediction model was developed.

Two additional complexities of modelling ice rubble loads on cones vs vertical prismatic structures below water level are that the slope of the structure is an extra control variable, and, in nature, there is a rubble weight discontinuity at the waterline above the base of the cone. In this study only one cone slope was tested (55.7°) and there was no

water present. The failure mode examined in these experiments is thus analogous to ice rubble failure only when upward sloping structures lift rubble and when downward sloping structures depress it. For instance, in cases where upward and downward rubble failure occurs on a single continuous sloping structure (such as a steep cone extending well below sea level) these experiments may not be applicable unless the two failure modes can be treated separately. In the cases where the waterline passes through the rubble bearing on the conical structure and a discontinuity in the confining stress gradient exists, an approximation of effective stress may be required.

5.3.2 Experimental program

Tests were conducted to determine the sensitivity of indentation force and penetration to keel shape. Also, the relative penetration at peak force for keels of various aspect ratios and the evolution of load and failure patterns with penetration into continuous sand layers were tested. Experiments were performed with similar procedures and equipment to those in Section 5.2. For a full listing of test conditions refer to Appendix C.

For conical structures indenting symmetrical trapezoid keel formations dimensional analysis yields:

$$\frac{F}{\gamma H^2 D_{av}} = f\left(\alpha, \delta, \phi_t, \phi, \frac{W}{D_{av}}, \frac{H}{D_{av}}, \frac{P_{en}}{D_{av}}\right) \tag{63}$$

where F is horizontal force, γ is bulk weight, α is the slope of the structure, δ is soil surface slope, ϕ_t is the soil-structure friction angle, ϕ is the angle of internal friction. W and H are the "sand keel" width and depth, D_{av} is the average cone diameter over H, and P_{en} is structure penetration from the "sand keel" leading edge.

5.3.3 Experimental results

Figure 5.16 illustrates the relative influence of "sand keel" shape on peak load and penetration at peak as in Section 5.2. All five keels (shown beneath the bar graph) had the same sectional area and two different widths were used. Loads were normalized against the 320 mm wide "sine" shaped "sand keel" because it resulted in the highest load. The wide short trapezoidal keel showed the least resistance to indentation. There was little difference between the loads on keels of similar width.

The relative penetration of the leading edge of the cone to the position of peak load has been determined for a range of W/D_{av} and H/D_{av} ratios (Figure 5.17). Multiple regression techniques were applied to determine the relation ($r^2 = 78\%$):

$$\frac{P_m}{D_{av}} = 0.57 \left[\frac{W}{D_{av}} \right]^{0.723} \left[\frac{H}{D_{av}} \right]^{-0.0471} \tag{64}$$

which enables one to interpolate the approximate point of peak load for interaction with keels of various aspect ratios.

Continuous sand layers were indented as far as the apparatus permitted which approached steady-state conditions. Rupture distances and maximum surcharge heights were measured for lateral, forward and oblique (45°) positions around the cone as shown in Figures 5.18 to 5.20. Measurements were made at 5 cm penetration intervals so as to track the development of these parameters and three different sand depths were used. Rupture distances were measured relative to the cone neck and surcharges were measured from the cone base to the top of the sand on the cone. The leading sand pile often crested higher a small distance from the cone surface so the height at that point was recorded.

Multiple regression techniques were used to define longitudinal rupture distance, r_o, and the maximum sand height on the cone, H_{ro} in dimensionless forms as follows:

$$\frac{r_o}{D_{av}} = 0.535 + 2.06 \left[\frac{H}{D_{av}}\right] \frac{\left[\frac{P_{en}}{D_{av}}\right]^2}{\left[\frac{P_{en}}{D_{av}}\right]^2 + \left[\frac{H}{D_{av}}\right]} \tag{65}$$

$$\frac{H_{ro}}{D_{av}} = 1.59 * \left[\frac{H}{D_{av}}\right]^{0.652} \left[\frac{\left[\frac{P_{en}}{D_{av}}\right]^2}{\left[\frac{P_{en}}{D_{av}}\right]^2 + \left[\frac{H}{D_{av}}\right]}\right]^{1.07} \tag{66}$$

with adjusted r^2 values of 94.1% and 98.4% respectively. Patterns of increase and stabilization were the same for other measured rupture distances and surcharge heights. The development of these equations is reviewed in Appendix D.

5.3.4 Development of a cone load model: trapezoidal keels

When a conical structure penetrates a "sand keel", the sand accumulates in a raised crescent around the leading edge with the rupture distance extending further from the structure as surcharge deepens. The failure surface is more rounded and cusp-like than that for cylinders. Plug failure is evident when shear planes, flaring from the structure to the back of the keel, form. It was shown in Section 5.2 that the point of plug-like failure corresponds to the point of peak load for vertical structures and the same is assumed here. Thus an algorithm for computing peak load need only model the local failure mechanism at the point of incipient plug failure.

The passive earth pressure formula representing the local failure mode was used and adapted for computing forces in this study as follows:

$$F = \frac{\gamma H_{so}^2 K_p D_{eff}}{2} \tag{67}$$

where γ is the bulk weight of sand (measured as 13880 N/m^3), H_{so} is the greatest depth of sand on the cone, D_{eff} is the effective width of the cone structure, and K_p

$$K_p = \frac{\cos^2(\phi+\alpha)}{\cos^2\alpha\cos(\alpha-\phi_1)\left[1-\sqrt{\dfrac{\sin(\phi+\phi_1)\sin(\phi+\delta)}{\cos(\alpha-\phi_1)\cos(\alpha-\delta)}}\right]^2} \tag{68}$$

is the effective passive pressure coefficient where ϕ is the internal friction angle ($\approx 32°$ for loose sand used), α is the slope of the structure ($\approx 34.3°$ from vertical), ϕ_1 is the soil-structure friction angle (0.6ϕ for sand and plastic), and, δ is the soil surface slope. Ridge keel shape and orientation have been excluded from the formulation because previous experiments here, and in Chapter 3, indicated that these conditions had a minor influence on forces. Refer to Appendix E for the development of the force equation and to the top Figure 5.18 for conventions and parameter definitions.

The average surface slope, δ, was estimated since the surcharge accumulated in a curved form similar to a cosine function between 0 and $\pi/2$. The sectional area of the sand accumulation was approximately $2/\pi(mH_{so})$. A triangular accumulation with the same height and area provides an estimate of δ as

$$\delta = atan\left(\frac{H_{sur}}{m\,4/\pi}\right) \tag{69}$$

where m is the cone frontal rupture distance defined on the top of Figure 5.18 and H_{sur} is the surcharge height $(H_{o} - H)$.

The effective width D_{eff} of the conical structure was estimated in two ways. The first, method "A", involves adapting the aspect ratio (effective width) formula developed in Section 5.2 for prismatic structures as follows:

$$D_{eff} = D_{av}\left[1 + \frac{3H}{2D_{av}}\right] \leq 2 \qquad (70)$$

where D_{av} is the average diameter of the structure below the original sand depth H.

During local failure the raised crescent of mobilized sand appears to have a uniform vertical cross-section (see top of Figure 5.18 "Isometric"). The whole body can thus be approximated geometrically by sweeping a vertical wedge of unit width circumferentially from one side of the cone to the other. Since the rupture surface extends approximately linearly outward from the cone base up to the sand surface, the effective structural width may be approximated as follows: (Method "B")

$$D_{eff} = \int_{-\beta}^{\beta} B\cos\theta\, d\theta \quad ; \quad B = \frac{r_o + D_z/2 + D_b/2}{2} \quad ; \quad \beta = a\sin\left[\frac{r_{45}}{r_o}\right] \qquad (71)$$

where $B\, d\theta$ is the average horizontal projected width of a soil wedge, β is the approximate angle over which the unit wedge is swept either side of the axis of symmetry. Integrating one obtains

$$D_{eff} = 2B\sin(\beta) \qquad (72)$$

Computed forces using both effective width methods predict measured forces quite well as shown in Figure 5.21. This figure includes two measured force traces for each depth. Method "A" slightly under-predicts loads with an average (for both measured traces) adjusted r^2 value of 99.2% while Method "B" both over- and under-predicts with an average r^2 value of 98.8%.

Predicting a peak load for any given trapezoidal "sand keel" starts with predicting the penetration for peak force using Equation (64) with approximate aspect ratios H/D and W/D. Using Equation (66) the maximum height of sand acting on the cone can then be determined at that penetration. The surcharge slope and effective structure width are then computed from Equations (69) and (70). Forces are then calculated utilizing Equations (67) and (68).

5.3.5 Conclusions

In this section an analytical procedure that predicts forces on conical structures indenting homogeneous "sand keels" is outlined. The study shows an excellent agreement between measured and computed forces. The applicability of the "sand keel" force model to ice force modelling is limited to conical structures with a slope near that which was tested. Also the introduction describes how other failure modes and rubble stress distributions may affect the applicability of results.

In the next chapter the validity of the sand force prediction models for both vertical and sloping structures is tested for ice rubble forces using data from Chapters 3.
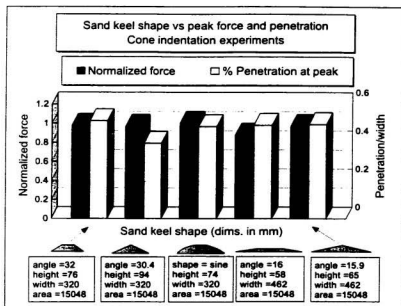
Figure 5.16 "Sand keel" shape sensitivity - cone tests.
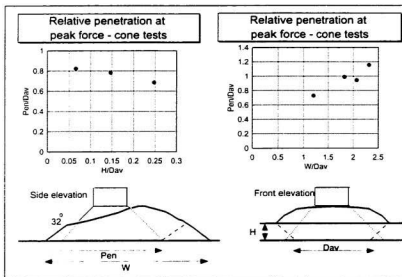
Figure 5.17 Peak force penetration study - cone tests.

Figure 5.18 Failure patterns for cone penetration - $H/D_{av} = 0.110$.
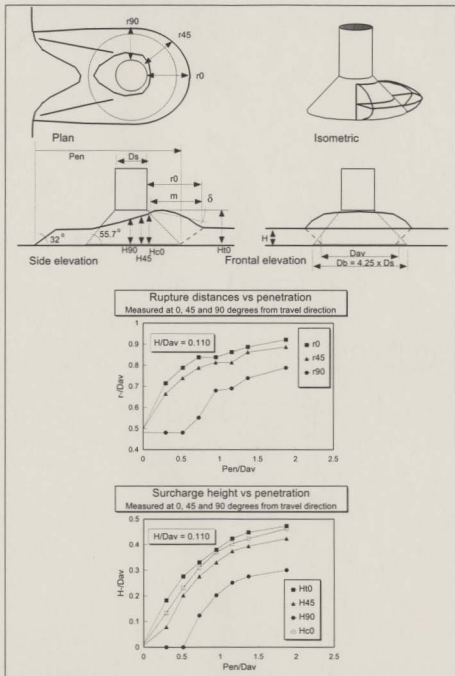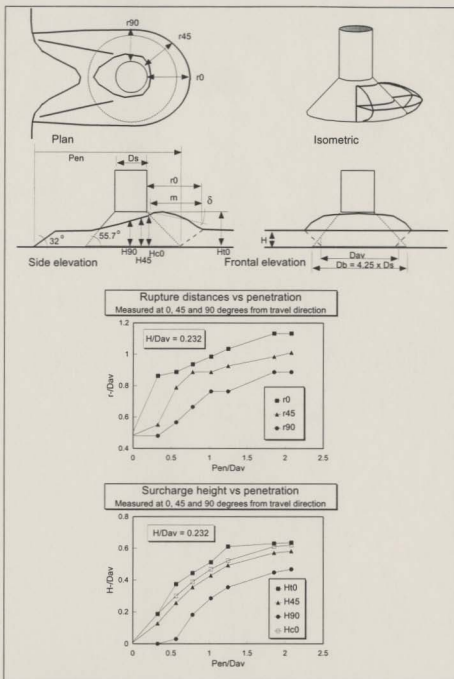
Figure 5.19 Failure patterns for cone penetration - $H/D_{av} = 0.232$.
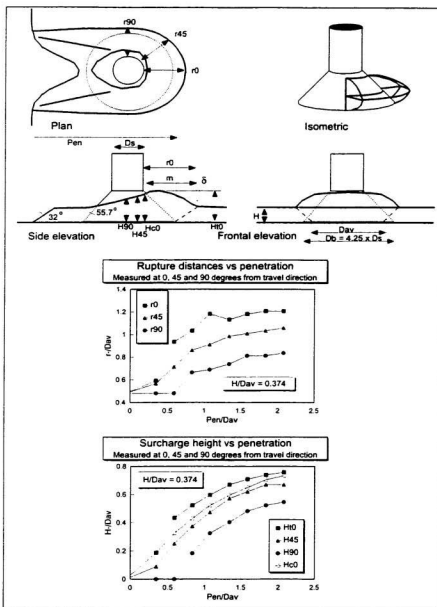
Figure 5.20 Failure patterns for cone penetration - $H/D_{av} = 0.374$.
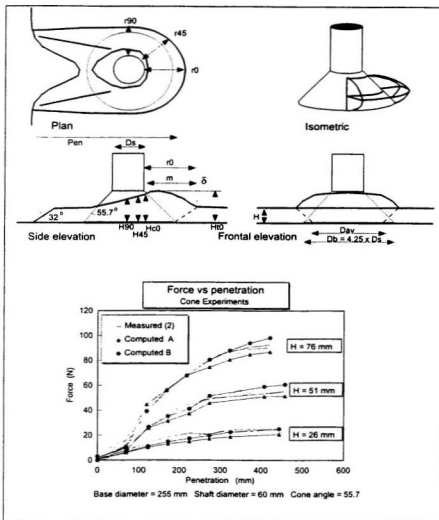
Figure 5.21 Measured and computed force vs penetration - cone tests.

Chapter 6

MODEL DEVELOPMENT III

Application to ice rubble

In Chapter 5 detailed measurements were used to develop force models for structure interactions with "sand keels" analogous to first-year ridge keels. The validity of applying these force models to ice rubble-structure interaction experiments is tested in this chapter. Force data reviewed in Chapter 4 are used in this study which first considers vertical structures and later examines forces on cones.

6.1 Vertical structure interaction model

Section 5.2 describes the procurement of sand tests aimed at elucidating keel failure mechanics. A force prediction model developed for sand performed well and so it is tested in this section against laboratory results for ice rubble-structure interactions. Computed forces are compared to measured forces using regression techniques and recommendations for better modelling are given.

6.1.1 Model application procedure

The sand force model described in Section 5.2 can be extended to include the effects of cohesion (after Jumikis, 1984) and thus has been adapted for this study as follows:

$$F = \frac{1}{2}\gamma H_p^2 D_{eff} K_p + 2 c H_p D_{eff} \sqrt{K_p} \tag{73}$$

where γ is the buoyant weight of submerged rubble, H_p is rubble depth at the point of peak load, D_{ef} is effective structure width, K_p is the passive pressure coefficient and c is cohesion. Rubble buoyant weight is computed here as

$$\gamma = (\rho_w - \rho_i)(1-e)g \qquad (74)$$

where ρ_w and ρ_i are water and ice densities, e is bulk porosity and g is the gravitational constant.

In Section 5.1 arguments which support the omission of surcharge effects underwater for ice rubble laboratory experiments are presented. Video observations from IMD tests show that displaced rubble sometimes accumulates in front of the structure but often appears "suspended". In the present study the hypothesis tested is that displaced rubble does not create a surcharge. Thus for data from those studies where continuous ice rubble layers were indented, H_p, is assumed to be the far field depth. Where discontinuous ridges were indented, depth is computed as a function of penetration into a "sine-shaped" keel (as described in Section 4.1) as follows:

$$H_p = H\left(\sin\frac{\pi P_m}{W}\right) \qquad (75)$$

where H and W are the keel depth and width and P_m is the penetration at peak force determined using the relationship derived in the sand tests (section 5.2) as

$$\frac{P_m}{D} = 0.113\left[\frac{W}{D}\right]^{1.63}\left[\frac{H}{D}\right]^{-0.42} \qquad (76)$$

The effective diameter of the laboratory structures is approximated by the formula

$$D_{ef} = D \left[1 + \frac{3H}{2D} \right] \leq 2D \tag{77}$$

derived in Section 5.2.

The internal friction angle and cohesion used in this study are those reported in each reference source. For comparison, values of ϕ and c estimated from the regression equations derived in Section 4.2 are also used:

$$\phi = 1.22 - 168L_i + 1.7e \quad ; \quad c = 16242L_i - 7 \tag{78}$$

where L_i is block thickness.

The passive pressure coefficient K_p defined in Equation (61) is used here. For this study structure slope was 0° for all data sets. The dynamic ice-structure friction angle, ϕ_I, was determined from friction coefficients, $\tan(\phi_I)$, where quoted in the reference source. Coefficients were estimated for IMD studies (McKenna *et al.*, 1995a and 1995b, and McKenna, 1996) to be 0.03, Keinonen and Nyman (1978) estimated a value of 0.158 and a value of 0.13 (equivalent to the IMD cone) has been assigned where no specific information was given. The surface slope, δ, of the rubble in the path of the indenting structure was estimated by the same model used in section 5.2 for the sand tests:

$$\delta = atan \left[\frac{H}{W} \right] \tag{79}$$

where it has been assumed that the rupture surface extends from the structure to the rear of the ridge keel at peak force. Where a continuous layer of rubble was indented a slope of 0° was assumed.

6.1.2 Measured vs computed forces

All interaction data sets from Section 4.2 for which a ϕ and c were stated (excludes Timco and Cornett, 1995 and Bruneau, 1994a "dry") have been used in this comparative study. Forces measured in these tests are plotted in Figure 6.1 against forces predicted using the above procedure. The "perfect match" (1:1) line has also been drawn. Only the data sets from Chapter 3 are plotted in Figure 6.2. Computed forces are generally conservative (higher than measured) with most data points lying to the left of the 1:1 line. The poorest matching data appear to come from Cheng and Tatinclaux (1977) and Bruneau (1994a) "wet". In Figure 6.3 and 6.4 computed values of ϕ and c (from Section 4.2) were substituted for reported values. Both Cheng and Bruneau data sets appear closer to the rest in Figure 6.3 than in Figure 6.1, suggesting that the reported failure criteria may be inappropriate. This, however, is not an entirely satisfactory explanation since other data sets move away from the best-fit line when computed values of ϕ and c are used. Most importantly the McKenna *et al.* (1995b) and McKenna (1996) data which feature prominently in this thesis are negatively affected (Figure 6.4 compared to Figure 6.2).

To test the performance of the modelling technique quantitatively, ordinary least squares fitting has been applied to the data from Figures 6.1 and 6.3. Both linear and power law fits are shown in Figures 6.5 and 6.6. Due to the significant range of force experiments the larger scale tests are weighted heavier in the linear comparison. It is readily observed

in Figure 6.5 that the linear relation for the "computed ϕ-c" forces is inferior to that for the "referenced ϕ-c" force estimates (77% to 91%). Power law fits favour the "computed ϕ-c" results by a ratio of 83% to 66%. On average, the predicted forces were 18% higher than the measured for the "referenced ϕ-c" force estimates, and 33% higher for the "computed ϕ-c" force estimates. The results for the Chapter 3 data plotted in Figures 6.2 and 6.4 feature linear r^2 values of 89% (for the referenced ϕ-c force estimates) and 65% (for the "computed ϕ-c" force estimates) respectively (Figure 6.6).

Isolating the two large-scale experiment data sets, McKenna et al., (1995b) and McKenna (1996), it is possible to investigate model performance further as shown in Figure 6.7. Only predicted forces using the "referenced ϕ-c" values are considered. The plot shows that forces from the first experiment are over-predicted by a wider margin than those of the second, which practically straddle the 1:1 fit line. The goodness-of-fit linear r^2 value is 81% as shown in the figure. With zero intercept the best fit line has slope of 0.967, suggesting almost no conservatism in the estimates overall.

Figure 6.8 shows that interaction speeds have little effect on predictions. Slow and fast experiments alike fall near the match line. Note that the higher of the two medium speeds were all from the data set McKenna et al. (1995b). Figure 6.9 separates the experiments based on the vertical position of the conical ice shield relative to the waterline. The cone base marks the top of the cylinder considered here. It may be argued that the cone positioned low in the water would tend to interfere more with the keel below it. This assertion is supported by all but one data point so cone position relative to keel depth may be a valid consideration for ice load modelling.

Figure 6.10 shows that block strength has little or no effect on interaction forces. Weak and strong rubble blocks alike constituted ridges which were both over and under-predicted. Two additional data points have been singled out on Figure 6.10. These represent the interaction force for the experiment with no refrozen core and, an oblique (45°) ridge test. As can be seen in the figure neither are anomalous in the prediction of forces. In summary, the separation of McKenna et al. (1995b) and McKenna (1996) data sets revealed in Figure 6.7 is not explained in this study.

6.1.3 Conclusions

The force prediction technique developed for sand in Chapter 5, does offer a viable prediction model for ice ridge keel forces. The technique performs well when the surcharge observed in the sand tests is left out. The model involves utilizing an effective structure width and approximated keel shape developed earlier in the thesis. These adaptations now provide some insight into the composition of the proportionality coefficients of the regression formulas established in Chapter 4.

Many variables contribute to error in force prediction. In general, one might expect a non-bias cumulative error in the variables to result in a uniform scatter of the predicted data. But trends in the residuals from comparative studies suggest that a factor causing some bias may be involved. The over-estimation of interaction forces in the broad base data set may be partially explained by the limitations of the passive earth pressure formula. This formulation is developed from a force equilibrium on a theoretical failure wedge shape which differs slightly from that typically observed (Siemens et al. 1965). The equilibrium of forces used also assumes that shear resistance acts over the entire failure surface instantaneously. This roughly approximates the physics of the failure

though actual failure is more likely to be progressive, initiated at the high stress zones first. In geotechnical engineering it is recognised that in computations of embankment stability, for instance, failure over the entire slip surface is non-simultaneous (Kosar, 1996). An effective shear strength is used to avoid complex numerical methods which are required to attempt precise physical modelling.

For ice ridge keels progressive failure *is* likely so that the force equilibrium method of determining forces on the surfaces of a failure wedge becomes an approximation of the actual physics. Maattanen (1994b) points out that a progressive failure index typical for sand-steel interactions is 0.8 so that one may expect applied forces to be 20% less than those computed using classical force equilibrium methods. In this study it is shown that predicted forces are, on average, 18% higher than measured forces for the entire data set. Progressive failure may be partially responsible. There is little doubt that a similar progressive failure process influences the results of direct shear box tests. The action of shearing a bulk rubble sample by applying pressure at one or both ends of a box or ring replicates the conditions for non-simultaneous failure. A consideration of box size and mechanics becomes important if one is to determine the degree to which progressive failure is an intrinsic factor in the computed ϕ and c values.

The quality-of-fit reported in the multi-variable regression analysis in section 4.2.4 was somewhat better than that reported for the analysis above. This is not surprising since it is unusual to out-perform the best-fit formulas with analytical models developed from the same data set. The fundamental problem with regression formulas is that they provide very little guidance for extrapolation. Using an analytical model based on sound principles and validated through experimental studies provides a more sound approach

for load prediction. This study has justified the use of passive earth force modelling techniques already in the literature, and demonstrates that combined with empirical formulations for effective structure width, keel shape, and the penetration at peak force, this approach can be a potent load estimating tool for ridge keel/structure interactions.
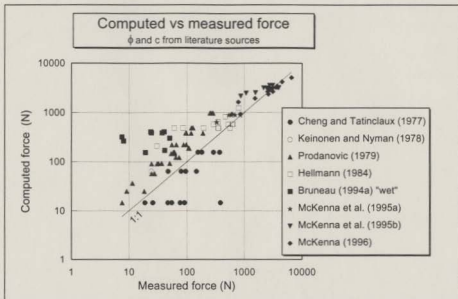
Figure 6.1 Force prediction study for "referenced ϕ-c" - by reference, base data set.
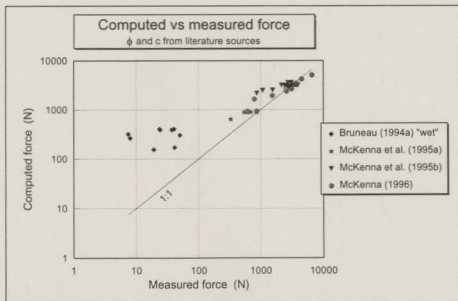
Figure 6.2 Force prediction study for "referenced ϕ-c" - Chapter 3 data.
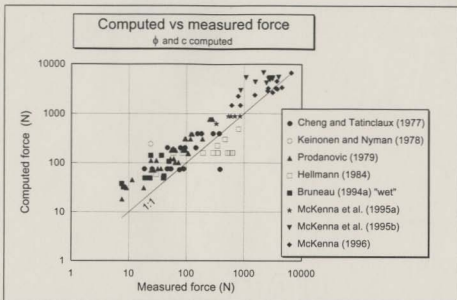
Figure 6.3 Force prediction study for "computed φ-c" - by reference, base data set.
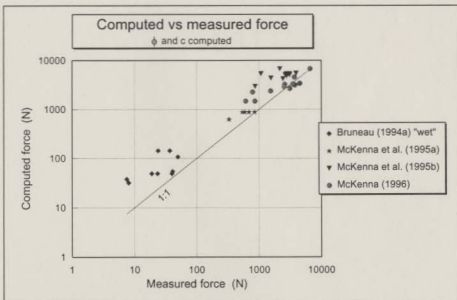
Figure 6.4 Force prediction study for "computed φ-c" - Chapter 3 data.
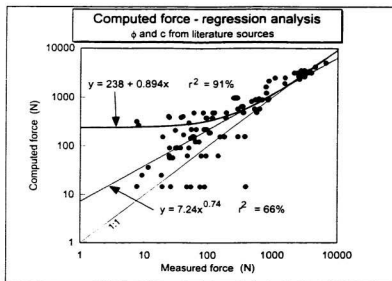
Figure 6.5 Force prediction study regression results "referenced ϕ-c" - base data set.
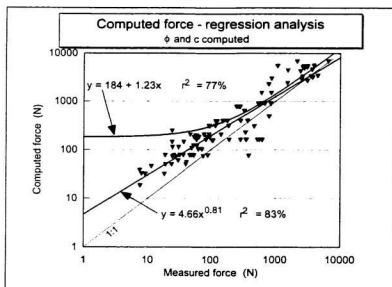
Figure 6.6 Force prediction study regression results "computed ϕ-c" - base data set.
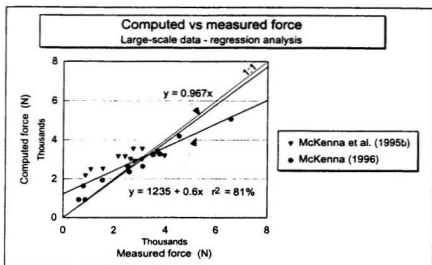
Figure 6.7 Force prediction study regression results - large-scale data sets.
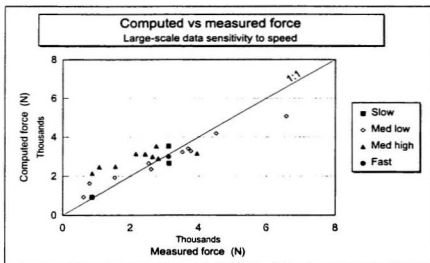
Figure 6.8 Force prediction study - large-scale data speed sensitivity.
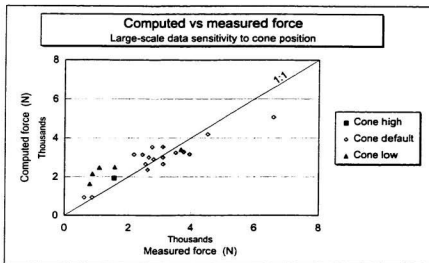
Figure 6.9 Force prediction study - large-scale data cone height sensitivity.
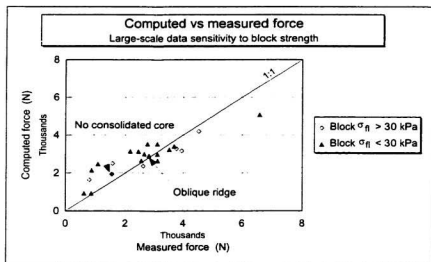
Figure 6.10 Force prediction study - large-scale data block strength sensitivity.

6.2 Conical structure interaction model

In the following study the cone interaction model developed for the sand tests in Section 5.3 is used to compute forces for the cone tests reported in Section 3.4 from McKenna *et al.* (1995b) and McKenna (1996). The results are compared with the measured forces and recommendations based on performance are given.

6.2.1 Model application procedure

The model described in Section 5.3 used to predict loads in sand was adapted and extended to include the effects of cohesion (after Jumikis, 1984) as follows:

$$F_{cone} = \frac{1}{2}\gamma_{eff}H_{ro}^2 D_{eff}K_p + 2cH_{ro}D_{eff}\sqrt{K_p} \qquad (80)$$

In applying the above formula the effective ice rubble weight was estimated by

$$\gamma_{eff} = 9.81 \frac{((\rho_s H_s + \rho_k(H - H_{wl}))}{2(H_s + H_{wl})} \qquad (81)$$

where H_s is the height of the sail above the waterline, H is the depth of the keel below the waterline, H_{wl} is the height of the waterline above the cone base, and, ρ_s and ρ_k are the bulk sail and keel densities (which include porosity). This formula represents an approximate average rubble weight based on the hydrostatic sail pressure at waterline (maximum) and the hydrostatic keel pressure at the leading edge of the cone base. Refer to Appendix F for details on this formulation.

Video records (McKenna and Bruneau, 1997) show that surcharge develops on upward breaking ice cones in a fashion similar to that observed in sand tests in Section 5.3. Thus the depth of the rubble H_{ro} acting on the cone can be approximated using the formula

derived in Section 5.3 which considers a non-linear build up of surcharge as follows:

$$H_{to} - D_{av} = 0.59 \left[\frac{H_{se}}{D_{av}} \right]^{0.652} \left[\frac{\left[\frac{P_{en}}{D_{av}} \right]^2}{\left[\frac{P_{en}}{D_{av}} \right]^2 + \left[\frac{H_{se}}{D_{av}} \right]} \right]^{1.07} \tag{82}$$

where D_{av} is the average cone diameter between the waterline and the cone base. The sail height used, H_{se}, is the height of a "trapezoid-shaped" sail with a cross-sectional area matching the measured value. This adaptation is necessary to match the shape of the "sand keels" for which the expression for total depth above was derived. Thus H_{se} was determined from the following expression

$$A_{sail} = H_{se} \left(W - \frac{H_{se}}{\tan(32)} \right) \tag{83}$$

where A_{sail} is the sail cross-sectional area, W is the ridge width. The penetration into the ridge at peak load, P_{en}, is estimated from sand tests (Section 5.3) using the formula:

$$\frac{P_{en}}{D_{av}} = 0.57 \left[\frac{W}{D_{av}} \right]^{0.723} \left[\frac{H_{se}}{D_{av}} \right]^{-0.0471} \tag{84}$$

The effective diameter the cone structure can be estimated by the formula

$$D_{eff} = D_{av} \left[1 + \frac{3H_{to}}{2D_{av}} \right] \leq 2D_{av} \tag{85}$$

which was derived in Section 5.2 for vertical structures in sand.

The applicable form of the passive pressure coefficient K_p is that defined earlier in Section 5.3, Equation 68. The internal friction angle (and cohesion) used for the comparison were those reported in McKenna *et al.* (1996) where $\phi = 36°$ and $c = 438$ Pa. The cone slope was 45° and the ice-structure friction coefficient $\tan(\phi_i)$ was 0.14 from McKenna (1995b). The slope of the surcharge was estimated by the same model used in Section 5.3 for the sand tests and adapted as follow:

$$\delta = -atan\left[\frac{H_{ro}-H_{wl}}{r_o 4/\pi}\right] \tag{86}$$

This recognises that the overburden is humped in the shape of a cosine curve, for which this equation gives an average slope over the rupture distance, r_o, approximated from sand tests as:

$$r_o = D_{av}\left[0.535 + 2.06\left[\frac{H_{se}}{D_{av}}\right]\frac{\left[\frac{P_{en}}{D_{av}}\right]^2}{\left[\frac{P_{en}}{D_{av}}\right]^2 + \left[\frac{H_{se}}{D_{av}}\right]^2}\right] \tag{87}$$

6.2.2 Comparative study results

The preceding force computation procedure has been tested against measured force data. In Figure 6.11 predicted forces are plotted against measured forces for all cone longitudinal horizontal forces reported in Section 3.4 (after McKenna *et al.* 1995b and McKenna 1996). Forces are predicted reasonably well ($r^2 = 67\%$) though some scatter

exists which is pronounced for higher force data points. From Figure 6.12 and 6.13 one can see that the instances where the model significantly under-predicts are limited to tests where the cone was positioned low in the water and where flexural strength was high. To possibly explain these trends recall that with the cone positioned low in the water measured loads were lower than computed forces on the cylinder. The higher measured forces seen here may be compensating for this. The influence of the protruding cone base on rubble below it may explain these inconsistencies. An "effective depth" for the cone may be a consideration for future modelling. High flexural strength may influence the shear strength of rubble in the laboratory at IMD though this effect has not been recognised in the ϕ and c terms used in this force study.

Figure 6.14 shows that interaction speed does not influence the prediction of cone forces. It is important to note that inertia forces are not scaled linearly in the laboratory so that much higher speeds are required to examine this effect in practice. Nevertheless, speed effects which *may* have resulted from shear strength or surcharge formation dependencies are not evident in this study. The data points for both high and low speed tests are clustered around the 1:1 line.

The refrozen core flexural force component has not been removed from the measured forces in this study. This would tend to shift the points to the left in Figures 6.11 to 6.14. The force traces in McKenna (1995b) for the cone "X" force (the component considered here) appear, from video observation, to have a frequency component corresponding to flexural failure. Typically this component has an amplitude between 10 and 20% of the total transient ridge force. If the flexural resistance momentarily vanishes immediately after the collapse of a load cycle when the newly broken core ice becomes

indistinguishable from the accumulated rubble, then the flexural component is probably 10 to 20% of the forces shown. Figure 6.12 indicates the effect of rubble strength on the model performance and also shows the single data point which represents a test in which there is no refrozen core. The position of this point does not support the "core component" argument above, however, it is only one point and it also corresponds to the lowest cone position tested.

6.2.3 Conclusions

This study has successfully demonstrated the applicability of the sand cone model to ice rubble experiments. Sensitivities to cone position relative to the keel are noted. Speed had little influence on forces but higher block strength resulted in higher forces. The cone model presented has some intrinsic weaknesses which are difficult to overcome. For instance, the ice cone is not as steep as the sand cone and the formulas for surcharge height, rupture distance and penetration at peak are based on the sand cone. The effective diameter formula used for the cone was derived from vertical structure experiments in sand. Also the ice cone was not as high as the sand cone so that more rubble interacted with the cylindrical neck above the cone in ice than was the case in sand. Despite these limitations the procedure works well, is closed form, and does not require very much input data.

In the next chapter the application of the laboratory analytical models to full-scale is discussed. Considerations of speed effects resulting from fluid dynamics and global inertia are considered. A sensitivity trial calculation of full-scale forces on vertical structures is presented and a comparison of those results with full-scale data is attempted.
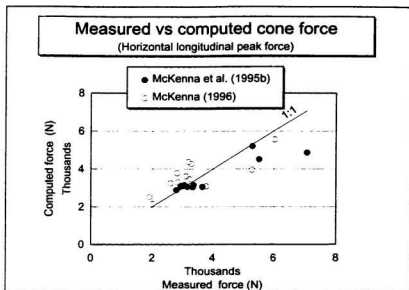
Figure 6.11 Cone force prediction study - by reference.
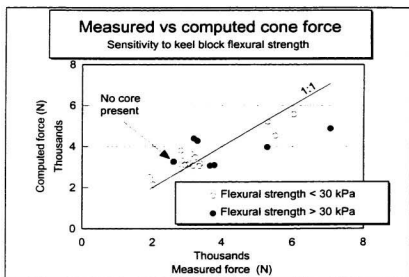
Figure 6.12 Cone force prediction study - block strength sensitivity.
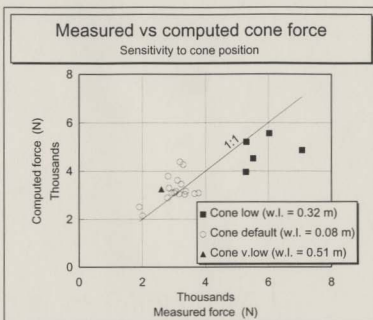
Figure 6.13 Cone force prediction study - cone position sensitivity.
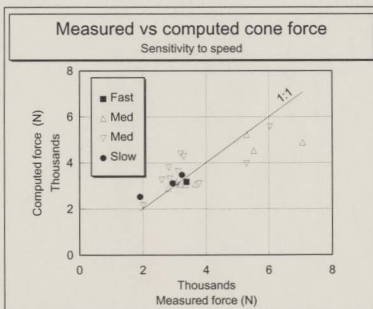
Figure 6.14 Cone force prediction study - interaction speed sensitivity.

Chapter 7

MODEL DEVELOPMENT IV

Application to full-scale

Considered in this chapter is the final phase of model development - the application of the new keel load model for vertical structures to full-scale. The influence of interaction speed which has fluid dynamic and global inertia consequences is discussed theoretically and suggestions for modelling are given. A trial sensitivity study of the new model at full-scale is then described. Performance is compared to other models in the literature. Until now, only laboratory data have been used for model development and calibration, primarily because of the scarcity of field data. In this chapter the full-scale ridge factor and line load data from Section 2.3 are revisited and the results of the thesis model sensitivity study are reviewed in light of this information.

7.1 Fluid dynamic considerations

In Section 5.1 it was suggested that the acceleration of fluid around a structure in steady state flow may affect ice block stability. Also, blocks and ice debris uplifted in the early stages of an interaction may not settle soon enough to create a surcharge. This argument is further developed in this section.

Suspension of a block

The suspension of an ice block from the surface of a ridge keel may be caused by fluid rushing out of a compressed zone, or fluid rushing past the surface. The total force

247

required to accelerate a body through a fluid is the sum of the fluid resistance forces (drag and inertia) plus the inertia force of the body (mass times acceleration). In the case of a rubble block roughly circular in shape, square-edged and oriented perpendicular to the direction of acceleration, it can be shown (Sarpkaya and Garrison, 1982, Bruneau, 1992) that the force required to accelerate such a body is

$$F(t) = \frac{1}{2}\rho(\pi r_a^2)V(t)^2 C_d + (M_b + (\frac{8}{3}\rho r_a^3))\frac{dV}{dt}C_m \qquad (88)$$

where r_a is the radius of the block, M_b is the mass of the block, $V(t)$ is instantaneous speed and C_d and C_m represent the drag and inertia coefficients for uniformly accelerated flow.

A stationary body perpendicular to flow may be suspended in a surrounding fluid if the flow rate exceeds a critical velocity. The critical velocity in the case of a rubble block may be equated to the terminal velocity which is determined by ignoring the inertia term above (in Equation 88) and equating the drag term to body weight. Thus for a block of ice 1 m in diameter and 0.2 m thick, suspension occurs when axial flow velocity reaches 0.58 m/s (when $C_d = 1.15$, $\rho_i = 910$ kg/m³, $\rho_w = 1010$ kg/m³). In air, the terminal velocity for the same block would be 50 m/s ($\rho_{air} = 1.25$ kg/m³) which underscores the near weightlessness of ice under water.

For a block lying flat, suction forces may be considered. According to Bernoulli's equation, the term $[\rho V^2/2 + P]$ is constant where P is the ambient pressure. If it is assumed that the fluid flow is zero on one side of the block and equal to V on the other, then the uplift pressure is equal to the $\rho V^2/2$ (dynamic pressure) term. For the submerged

submerged block (1 m diameter, 0.2 m thick), the speed required for uplift is approximately 0.55 m/s. This number is close to the suspension or terminal velocity computed above, so it unlikely that a block lifted under these circumstances would settle very soon.

Velocity field around cylinder

The velocity field around a circular cylinder may be determined for incompressible potential flow from a closed form solution of Navier-Stokes equation. The longitudinal, u, and lateral, v, velocity components as shown in Figure 7.1 are defined by

$$u = -U_o \left[\frac{r_a^2}{R^2} \cos 2\theta - 1 \right] \quad ; \quad v = -U_o \frac{r_a^2}{R^2} \sin 2\theta \qquad (89)$$

where U_o is the far field relative velocity, r_a is the radius of the cylinder, and R and θ are the radial and angular distance to the point of interest (Davenport, 1989). The maximum velocity is $2U_o$ and occurs on the sides of the cylinder at $\theta = 90°$ and $270°$ where pressure is also a minimum. The maximum lateral velocity is equivalent to the far field velocity ($v_{max} = U_o$) and occurs at $\theta = \pm 45°$, $\pm 135°$. Typically, flow separates and boundary layers are present so flow is not potential, however, upstream (approximately the front half of the cylinder) where separation does not occur the approximation of potential flow is a good one.

Keel interaction dynamics

It has been shown that a body in a fluid may be suspended through the action of drag and suction. We have also seen that fluid accelerates around a cylinder reaching a peak lateral speed equal to the approach speed and doubling the longitudinal speeds around the

structure sides. It is assumed here that blocks at rest on the surface of a ridge keel are engaged with one another as a result of buoyant and cohesive forces (assuming that friction is essentially absent at the surface). Two cases are now considered: in the first a 1 m diameter circular block is projected half way out of a frictionless planar keel surface approaching a large cylindrical structure, in the second, a similar block lies flat on the keel surface (Figure 7.2).

When an interaction commences consider the fluid at $\theta = 135°$ and $225°$ (Figure 7.1) near the structure where the lateral fluid speed is a maximum (U_o), acceleration is zero and thus the fluid dynamic forces result from drag and suction. If we consider bulk cohesion to act evenly over all block surfaces it can be shown that cohesion must exceed 450 Pa to avoid uplift of the prostrate block due to suction if U_o is 1 m/s. For the upright block if bulk cohesion alone were holding it in place (on one side) then it would have to exceed 580 Pa. As the region in which these blocks are located approaches the surface of the structure near the sides the "absolute" speed almost doubles. Ignoring inertia momentarily, this would increase the drag and uplift forces by a factor of four. It is entirely possible that in a natural first-year ridge keel a block may be inclined so as to produce some added lift component as well which would further upset the equilibrium of forces holding the block in place.

Though approximate and highly idealized, the scenarios in the preceding review demonstrate the sensitivity of keel ice block stability to interaction speeds and the importance of cohesion at the keel surface. There are other fluid dynamic factors which must also be considered during interactions. Of particular interest are fluid dynamic and body inertia forces.

Inertia considerations

If a large mass of rubble, such as a "plug", were displaced from rest in a stationary fluid it can be shown that substitution of the relative body parameters (effective dimensions, coefficients, etc.) into Equation (88) yields the total inertia and drag force on that body. In soil mechanics an inertia term analogous to that above has been formulated for the horizontal inertia of displaced soil in front of an advancing tine:

$$F_i = \rho D_f H_f V^2 \frac{\sin\alpha\cos(45-\phi/2)}{\sin(\alpha+45-\phi/2)} \tag{90}$$

where ρ is the density of the material displaced, α is the rake angle (to forward horizontal), D_f is effective width over the furrow depth, H_f, V is the speed and ϕ is the internal friction angle of the soil (Stafford, 1984).

It would be quite easy to apply a "plug" inertia factor like these to ridge failure forces but it may not be correct to do so. Though increased interaction speed is associated with increased accelerations causing inertial forces it also diminishes block engagement pressures as described earlier. Figure 7.3 illustrates the competing force processes on a ridge keel interacting with a structure. Though the position and relative strength of individual curves is somewhat arbitrary it is entirely possible that the net speed effect is near zero as shown. This is supported in the laboratory by the results reported in Chapter 3, the regression results of Chapter 4 and the detailed analysis in Chapter 6. Not shown in the figure are the effects of alternate failure modes or simply the adjustment of the assumed failure shape that would likely result from significant speed changes. This brief study does not provide closure to this topic but speed effects will not be considered further here. This will likely be a fruitful area of research for future analytical work.
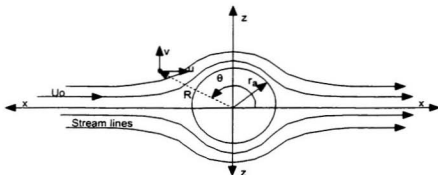
Figure 7.1 Potential flow around a cylinder.
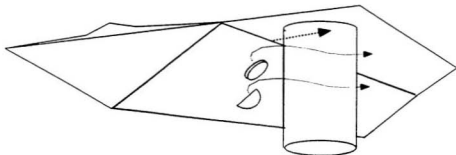
Figure 7.2 Keel block suspension scenarios.
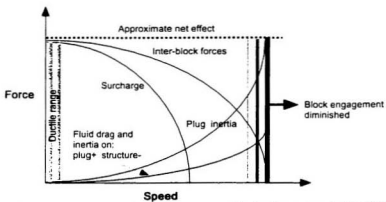
Figure 7.3 Competing fluid dynamic force processes for keel-structure interactions.

7.2 Full-scale load sensitivity study: vertical structures

Table 7.1 presents the results of a sensitivity study for full-scale loads. It is assumed here that the design ridges considered are keel-dominated and that the keel failure mechanism is shear as described Section 2.2. Also it has been assumed here that the keel and core failure processes can be modelled separately as described in Section 2.4. Progressive failure is assumed to be incorporated into the effective shear strength parameters as discussed in Section 6.1. Default values for the ridge geometry and properties are somewhat representative of design conditions for the Northumberland Strait. The analytical technique described and tested in Section 6.1 is described here as the "thesis" model. Two other load models are tested: the "friction plug" model first proposed by Croasdale in 1980 and revised in 1994, and the "Dolgopolov" model from Dolgopolov et al. (1975). Both models feature prominently in the Northumberland Strait Crossing Project design load calculations (Cammaert et al. (1993) and are reviewed in detail in Section 2.4. Initially they were considered individually, then together as competing mechanisms in the so-called cross-over technique. Note that, as in the thesis model, there is no assumed accumulation of displaced rubble (surcharge) in the Dolgopolov model, though a range was suggested by Dolgopolov et al. (1975).

Fourteen load scenarios are listed on Table 7.1. They feature independent variations of structure diameter, keel depth and width, block thickness, porosity and rubble shear strength. From the figure it is apparent that the thesis model has sensitivities and responses which resemble the Dolgopolov model. The listed values for the coefficient of variance and range support this assertion. On average the thesis model forecasts loads 15% lower than the Dolgopolov model and is somewhat more sensitive to structure

diameter. less sensitive to keel depth and is uniquely sensitive to changes in ridge width. The friction plug model predicts loads which are on average 36% of the thesis model values. The form of the plug model selected has no cohesion term which eliminates related responses and significantly affects the coefficient of variation for model output.

To compare the results of this sensitivity analysis to the model sensitivity study in Section 2.4, Scenario 4 on Table 7.1 is considered. This scenario is chosen because it is the only one that matches the "default" conditions of all the models reviewed in Figure 2.15, including the values quoted for the numerical simulations by Brown and Bruce (1995) and Sayed (1995). Remarkably, the average default value for all these models was 6.5 MN which is equivalent to the load predicted here by the thesis model. This unwitting endorsement by a broad range of experts strengthens the relevancy of the model.

There are a few distinct advantages to the thesis model over the others reviewed in this study. The thesis model demonstrates a sensitivity to ridge width which is not realized in the Dolgopolov model unless it is analytically "truncated" via plug shear models or otherwise. The model also utilizes an assumed shape for ridge keels which better approximates natural ridges than other modelling approaches. Surcharge effects are implicit in the thesis model whereas a broad range of possible values are suggested for the other models. Also in the thesis model an empirical effective structure width formula is used. Most importantly, the thesis model is based on fundamental equilibrium mechanics, uses regression equations based on a broad range of new and old data, and has demonstrated a high degree of success predicting forces in the laboratory. To examine sensitivity results further, the next section revisits full-scale load data from Chapter 2.

Table 7.1   Sensitivity analysis of thesis model at full-scale.

Scenario	Diameter D (m)	Depth H (m)	Width* W (m)	Block thick t (m)	Porosity n (%)	Friction** ϕ (deg)	Coh.*** c (Pa)	Thesis mod.**** Force MN	Friction plug***** Force MN	Didsgov****** Force MN
1 "Default settings"	10	15	47.4	0.2	35	15.57	3241	4.30	1.26	5.05
2 Diameter increased	10	15	47.4	0.2	35	15.57	3241	6.16	1.58	6.31
3 Diameter decreased	5	15	47.4	0.2	35	15.57	3241	2.33	0.95	3.79
4 Depth increased	10	20	47.4	0.2	35	15.57	3241	6.52	2.49	9.14
5 Depth decreased	10	10	47.4	0.2	35	15.57	3241	2.50	0.51	2.34
6 Width increased	10	15	60.0	0.2	35	15.57	3241	5.49	2.34	5.05
7 Block thickness increased	10	15	34.7	0.3	35	15.57	3241	3.67	2.67	4.35
8 Block thickness decreased	10	15	100.0	0.1	35	15.57	3241	3.07	0.00	6.51
9 Porosity increased	10	15	47.4	0.2	40	15.57	4866	5.10	2.87	6.86
10 Porosity decreased	10	15	47.4	0.2	25	15.57	1817	3.19	2.15	3.78
11 Average shear (all labs)	10	15	47.4	0.2	35	32.37	3241	3.62	0.17	5.11
12 Sample friction only	10	15	47.4	0.2	35	31	598	6.00	2.72	8.36
13 Sample cohesion only	10	15	47.4	0.2	35	0	5000	3.75	0.09	4.63
14 Sample friction and cohesion	10	15	47.4	0.2	35	45	5000	12.25	4.53	15.60
							Average	5.22	1.89	6.19
							Std Dev	2.92	1.48	3.15
							C.O.V	0.56	0.78	0.51
							Max	14.58	4.53	15.60
							Min	2.33	0.00	2.34
							Range	12.25	4.53	13.26

Notes:
* Ridge width is computed in all scenarios except it from Section 2.1. $W = 2.53H + 9.4$
** Friction angle is computed for scenarios 1 - 10 from Section 4.1. $\phi = 1/2Z - 16R/L + 1.37e$
*** Cohesion is computed for scenarios 1 - 10 from Section 4.1. $c < N/2K0L - 7$
**** Friction plug model as per Section 2.1 - no surcharge, w/ shape factor
***** Didsgov et al (1970) model as per Section 2.1 - no surcharge.

Force MN

□ Thesis model
● Friction plug model
■ Didsgov model

Scenario labels (left axis, top to bottom):
"Default settings"
Diameter increased
Diameter decreased
Depth increased
Depth decreased
Width increased
Block thickness increased
Block thickness decreased
Porosity increased
Porosity decreased
Average shear (all labs)
Sample friction only
Sample cohesion only
Sample friction and cohesion

X-axis: 0   5   10   15   20

7.3 Discussion of full-scale loads

As described in subsection 2.3.1 the value of a ridge factor as a design tool is significantly compromised by the unknown state of the refrozen core in a first-year ridge. Without any knowledge of the core competency the relative contributions of the ridge elements cannot be accurately determined. Nevertheless ridge factors do provide useful guidelines for bounding load estimates and, with some assumptions about the core, may reveal approximate average load values for first-year ridge keels.

The information in Table 2.4 indicated a maximum range of ridge factors of 1 to 4 with an average of 2.3 for the references cited. Table 2.4 also shows that the range of line loads is 500 to 1024 kN/m (where quoted) with an average of 800 kN/m. Figure 7.4 shows how these values have been interpreted. The ratio of refrozen core resistance to level ice resistance has been plotted against the maximum, mean and minimum rubble line loads for each of the maximum, mean and minimum ridge factors. Though the contribution of the refrozen core to the total line load has been varied between the maximum limits, this probably exceeds the condition for most first-year ridges over the period in which it is likely that force measurements were made. Acknowledging the varied structural geometries, ice conditions and limited references, some basic observations may be drawn from the figure.

- If one assumes that the refrozen core in the ridges studied in the field were approximately equal in strength to the surrounding level ice field, then on average the rubble portion of the ridge contributes approximately 57% of the interaction force or 450 kN/m.

- If a ridge had a core which generated twice the resistance of the surrounding level

ice then, on average, the rubble line load would be closer to 100 kN/m.

- If there were no core present or if it did not provide any significant resistance then the average rubble line load would be 800 kN/m, and the upper and lower line load limits would be approximately 1000 kN/m and 500 kN/m respectively.

For a 10 m wide structure, the forces due to rubble would vary from 1 to approximately 10 MN for the cases considered above. If the refrozen core and level ice are equal in resistance then, for the average condition in which the ridge factor is 2.3 and the line load is 800 kN/m, the force on a 10 m wide structure would be 4.5 MN.

A highly favourable condition arises when the results from the sensitivity study in section 7.2 are considered in light of the results in Figure 7.4. Figure 7.5 shows the sensitivity study results for the thesis model superimposed on the ridge factor study. The mean and standard deviation line loads from the sensitivity study are shown as horizontal parallel lines. The shaded region outlines the entire range of outcomes from the ridge factor study with the darker intensity indicating a higher probability of occurrence.

The ratio of refrozen core resistance (including sail effects) to level ice resistance with the highest probability of occurrence is assumed here to be 1. This value is representative, at some time, of all ridges with cores which become thicker and stronger than level ice. For these ridges, which may also be keel-dominated, the insulation effects of snow and ice restrict rapid core growth and warm that which does form. Also, the downward growth of a refrozen layer through a random rubble matrix results in a highly variable core thickness. This condition may reduce the strength of a thickened core since the weakest parts will attract failure and possibly alter failure modes. A core ratio less than 1 is also possible since those design ridges which have been shown under some

conditions (NSCP) to be keel-dominated may have no core at all. Since the ridge factor data are for a broad range of structure geometries and ice conditions, the core failure mode may vary appreciably. Thus considering the ranges of age, geometry and failure mode for those ridges measured, an average core resistance ratio of 1 has been assumed.

A dashed white ellipse marks the region surrounding the mean ridge factor and mean line load - centred on the darkest shaded region corresponding to a core resistance ratio of 1. As can be seen in the figure the line which marks the mean thesis model line load from the sensitivity study almost bisects the ellipse. Furthermore, the point of intersection between this line and that for the mean ridge factor and line load is well within the region of high occurrence probability for full-scale loads. The sensitivity study line load is slightly greater (14%) than that which has been calculated as the average for full-scale loads. This study shows that the thesis model results are highly consistent with the full-scale load data available.

As demonstrated here and in Section 6.1 the proposed analytical model was unable to precisely match laboratory ice rubble experiments. The errors introduced through measurement and analysis are only partially responsible. Underlying many processes is a natural variability that is, and will remain, beyond reasonable deterministic modelling capabilities. Recognising this, probabilistic modelling techniques have been developed and are now an integral part of most load forecasting projects. Like others, the thesis model is closed-form and may conveniently be incorporated into probabilistic modelling algorithms. There, distributions replace specific values for input parameters and random sampling simulations or distribution manipulation techniques provide return period load estimates for risk analysis.
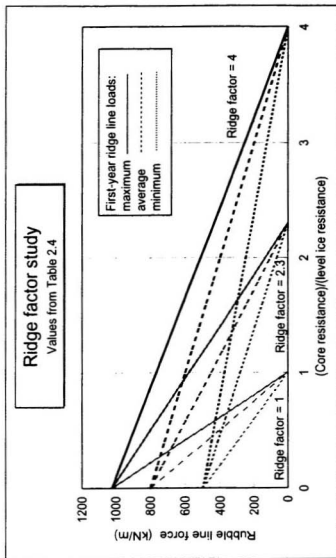
Figure 7.4 Interpretation of full-scale load data.
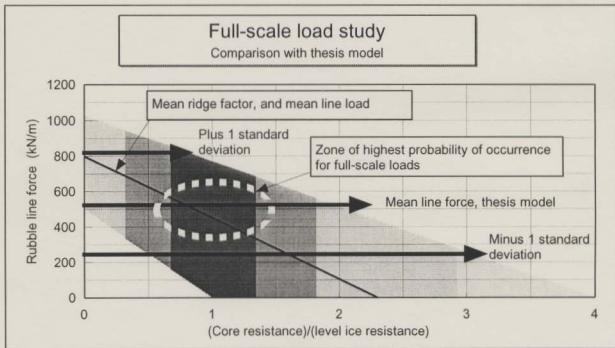
Figure 7.5 Comparison of full-scale data with the thesis model sensitivity study.

Chapter 8
SUMMARY AND CONCLUSIONS

Keel load modelling is a complex and multifaceted problem which has not been fully understood, in spite of many investigations. This thesis documents the development of a new approach to first-year ridge keel load modelling. Insight into the keel load prediction problem was gained through a series of investigations which involved the organisation and analysis of prior work and new experimental investigations. The body of work in this thesis is partitioned into background research, exploratory experimentation and model development phases.

In the background chapter a detailed research effort is described in which many literature sources are interpreted, grouped and examined. The topics included parent ice properties and physical characteristics of ridges, a review of ice rubble shear strength, a study of laboratory and full-scale ridge load investigations and a review and sensitivity study of ridge keel force models in the literature. This background study laid the groundwork for subsequent investigations by demonstrating the scarcity of controlled experimental results, and by exposing parametric and force model uncertainties.

Following the background chapter exploratory experiments are described, the first of which was a multiphased pilot ridge study involving work with both ice blocks and sand. Subsequent larger scale ice ridge/structure interaction experiments provided detailed information into both cylinder and cone shaped structure interaction mechanics. A program in which an *in situ* technique for determining the shear strength of ridge keels

was then developed and tested in the laboratory. All of these programs provided direction for future tests and new data sets, which were grouped with those from the literature for a composite regression study.

The regression study was concerned with developing best-fit empirical formulas which avoided the theoretical trappings of pre-existing models and dealt with variable multi-colinearities and some laboratory scale effects. Focus was primarily on ice rubble shear strength and structure interaction forces. Ridge keel shape was also briefly examined in this chapter insofar as it was demonstrated that a "sine" shaped keel approximation was more suitable than the traditional triangular shape in matching measured cross-sectional areas and for use in analytical modelling. In the study of ice rubble shear strength, state-dependencies and high variability were revealed and quantified. Best-fit empirical models for Mohr-Coulomb yield criteria were ascertained from the composite data set and a more fundamental study of shear data provided a non-linear interpretation of the behaviour of ice rubble strength.

The study of earlier and recent structure interaction experiments collectively, led to the conclusion that the most significant parametric grouping describing ridge forces was based on hydrostatics as used in earth pressure formulas. Though highly significant and effective, the raw form of the regression formulas did not provide guidance on the composition of the proportionality coefficients. This weakened confidence in predicting forces outside the range of the laboratory tests considered. Because of this, a new series of experiments which were sensitive to the unique boundary conditions and alignments of ridge/structure interactions were undertaken. They involved the substitution of sand for ice rubble in indentation tests which afforded a level of control and measurement that

enabled the development and calibration of a highly effective force model.

The specific goals of the sand experiments were to investigate "sand keel" failure modes, structure shape effects, effective structure width, keel shape sensitivities, ridge indentation at peak load and the evolution of rupture surfaces and debris accumulations with penetration. A parallel series of tests was performed in which a cone-shaped model was used since there is considerable interest in industry in this structural shape. There was no attempt to scale sand indentation forces. Analysis of the sand tests collectively made it possible to adapt and calibrate the time-tested passive earth pressure formula as a load prediction model for sand ridge interactions. This highly successful model application provided a solid geotechnical base solution which was then exploited for the ice ridge problem.

The model developed for vertical structures using sand tests was tested against the laboratory ice ridge results. The absence of displaced rubble accumulation (surcharge) underwater in the ice ridge experiments supported the omission of this effect in the model. Uncertainty over the parametric values for ice rubble shear strength promoted the use of two different sets of yield criteria. Both yield criteria from literature sources and values derived empirically in this study were used in the model and the merits of both were discussed. Ultimately, the model developed in this thesis performed very well by consistently predicting loads within 20% of measured values. The measured versus predicted force comparisons showed a higher scatter for the cone tests than those for the vertical structure, even though average interaction forces were well predicted by both.

The analytical advantage of the first-year ridge keel modelling approach developed in this

thesis is that the ridge shape is better approximated, ridge width is a factor, surcharge effects are considered, an effective structure width model was developed and implemented, and the model was effectively tested against a large body of new data. Also the model is closed form and singular, has been successfully applied to vertical and conical structures, and is based on fundamental earth pressure equilibrium mechanics as are other approaches already in the literature. A further advantage is that the input yield criteria have been critically examined so that parametric uncertainties are quantified and reduced.

The last chapter of this thesis considers fluid dynamics, inertia effects and the application of the new load model to full-scale force prediction. Though only a review, it was demonstrated that fluid dynamics can play a significant role in ice rubble behaviour underwater at larger scales. It is pointed out that there is no significant evidence of speed related fluid dynamic of fluid inertial effects on interaction forces in the laboratory. Thus these effects are not considered in the full-scale sensitivity study, though it is recommended that they be the focus of future research thrusts.

The full-scale load prediction performance of the model developed in this thesis was considered in light of other models from the literature, Dolgopolov *et al.* (1975) and Croasdale (1994). The load values from the new load model were consistently in the range of the loads expected when one considers the *cross-over* technique which employs both of the other models. A comparison of model sensitivity results with the average ridge factor and ridge keel line loads from field data sources shows excellent agreement for the new model. By way of comparison, for design conditions analogous to those for the Northumberland Strait, the thesis model predicted a force which was equivalent to

the average of the forces predicted by 10 other models from the literature.

There are many opportunities to improve upon and advance the work thrusts described in this thesis. Of these opportunities two feature prominently; detailed investigations of ridge keel fluid dynamics/inertia effects, and, field work. Field experiments feature as the most significant and probable source of new information. Verification of failure modes, measurements of ridge geometries, *in situ* tests of rubble shear strength, and ultimately, full-scale force measurements should, and will, have the greatest influence over future model developments. Without question, field studies such as these should be the immediate focus of organized research efforts.

REFERENCES

Acres International Ltd. (1987) **Northumberland Strait Bridge Ice Forces Report**. Public Works Canada, April, 1987, 101 p.

Allyn, N. (1994) **Review of First Year Ridge Keel Loads on Bridge Piers**. Westmar Consultants Inc. Communication to Strait Crossing Joint Venture, Project No. 94678, June 15, 1994, 22 p.

Audibert, J.M.E. Nyman, D.J. and O'Rourke, T.D. (1984) **Differential Ground Movement Effects on Buried Pipelines**. Guidelines for the Seismic Design of Oil and Gas Pipeline Systems, ASCE, 1984, pp. 161-179.

Blenkarn, K.A. (1970) **Measurement and Analysis of Ice Forces on Cook Inlet Structures**. Offshore Technology Conference, Dallas Texas. Paper no 1261, pp. II 365-379.

Bowles, J.E. (1984) *Physical and Geotechnical Properties of Soils*. McGraw Hill, Inc. USA, 578 p.

Bridgwater, (1987) *Attrition of Bulk Particulate Solids*, Tribology in Particulate Technology. Edited by Briscoe and Adams, IOP Publishing Limited, 1987, Ch.4 Sec.4.

Brinch Hansen, J (1961) **The Ultimate Resistance of Rigid Piles Against Transverse Forces**. Geoteknisk Institut, The Danish Geotechnical Institute Bulletin No. 12. Copenhagen. 1961, 9 p.

Broms, B.B. (1964) **Lateral Resistance of Piles in Cohesive Soils**. Journal of the Soil Mechanics and Foundations Division, Proceedings of the American Society of Civil Engineers. March, 1964, pp. 27-63.

Brooker, E.W. and Ireland, H.O. (1965) **Earth Pressures at Rest Related to Stress History**. Canadian Geotechnical Journal, Vol.2, No.1, pp. 1-15.

Brown T.G. and Bruce J.R. (1995) **Finite Element Analysis of First-Year Ridge Interactions**. F.G. Bercha and Associates for Public Works Canada and NRC, January 1995, 60 p.

Brown T.G. (1989) **Northumberland Strait Ridge Investigation** - Interim Report, Bercha and Associates for Delcan/Stone and Webster Joint Venture, April 1989, 70 p.

Bruneau, S.E. (1992) "The Hydrodynamics of Oscillating Porous Disks". M.E.Sc. Thesis The University of Western Ontario, Boundary Layer Wind Tunnel Laboratory, 128 p.

Bruneau, S.E. (1994a) **Ice Load Models for First Year Ridges and Rubble Fields - Physical Laboratory Tests**. Prepared for K.R.Croasdale and Associates in response to The National Energy Board solicitation no. XSC (84084-3-0214/000/A). 79 p.

Bruneau, S.E. (1994b) **The Indentation of Sand Formations**. Prepared for K.R.Croasdale and Associates on behalf of Public Works Canada for The Northumberland Strait Crossing Project, 51 p.

Bruneau S.E. (1995a) "Development of a First-Year Ridge Keel Load Model - PhD Proposal". Faculty of Engineering and Applied Science, Memorial University of Newfoundland, January 1995, 33 p.

Bruneau S.E. (1995b) Personal Communication to CODA on matters related to the Northumberland Strait Bridge Project.

Bruneau, S.E. (1996) **Modelling First-Year Ridge Keels With Sand**. The 49th Canadian Geotechnical Conference of the Canadian Geotechnical Society, Sept. 1996, St.John's, Nf, Canada, pp. 287-294.

Bruneau, S.E., McKenna, R.F., Croasdale, K.R., Crocker, G.B. and King, A.D. (1996) *In Situ Direct Shear of Ice Rubble in First-Year Ridge Keels*. The 49th Canadian Geotechnical Conference of the Canadian Geotechnical Society, Sept. 1996, St.John's, Nf, Canada, pp. 269-278.

Burden R.P. and Timco G.W. (1995) **A Catalogue of Sea Ice Ridges**. NRC-IMD report TR-1995-27, April, 1995, 72 p.

CAN/CSA-S471-92 **Code for the Design, Construction and Installation of Fixed Offshore Structures**. Canadian Standards Association, Rexdale, Ontario, Can. (1992).

Cammaert, A.B. and Muggeridge, D.B. (1988) *Ice Interaction with Offshore Structures*. Van Nostrand Reinhold, New York, 432 p.

Cammaert, A.B., Jordaan, I.J., Bruneau, S.E., Crocker, G.B., McKenna, R.F. and Williams, S.A. (1993) **Analysis of Ice Loads on Main Span Piers for the Northumberland Strait Crossing**. Contract Report for J.Muller International - Stanley Joint Venture Inc., CODA Contract Number 5022.01, 108 p.

Case, P.C. (1991) **A Continued Study of the Frictional and Cohesive-Like Behaviour of Floating Model Ice Rubble**. Laboratory Memorandum LM-1991-27, National Research Council of Canada, Institute for Marine Dynamics, 76 p.

Chao J.C. (1993) **An analysis of Ice Rubble Shear Strength Data**. Proceedings of the Third (1993) International Offshore and Polar Engineering Conference, Singapore, 6-11

June 1993, pp. 607-612.

Cheng, S.T. and Tatinclaux, J.C. (1977) **Compressive and Shear Strengths of Fragmented Ice Covers**. Iowa Institute of Hydraulic Research Iowa City, Aug. 1977, 43 p.

Clough H.F. and Vinson, T.S. (1986) **Ice Forces on Fixed Conical Structures**. OMAE, 1986, Vol. IV, pp. 507-514.

Coon, M.D., Echert, D.C. and Knoke, G.S. (1995) **Force-Displacement Measurements of a First-Year Pressure Ridge Keel**. ASME Ice Mechanics, 1995, 16 p.

Cornett, A.M. and Timco, G.W. (1996) **Mechanical Properties of Dry Saline Ice Rubble**. ISOPE (6th), Los Angels, 1996, Vol.2, pp 297-303.

Croasdale, K.R. (1980) **Ice Forces on Fixed, Rigid Structures**. Working Group on Ice Forces on Structures. State of the art Report. E., U.S.Army CRREL, Hanover, NH, Special Report 80-26: 153p.

Croasdale, K.R. Allyn, N.F.B. and Marcellus R.W. (1990) **Thermal Response of Ice Rubble: Predictions and Observations**. IAHR Ice Symposium, Espoo, pp. 153-167.

Croasdale, K.R. (1993 - 94) Personal communication, March, 1994.

Croasdale K.R. Metge, M., C.M.E.L Ent. Ltd and Wright, B. (1994) **Overview of Load Transmission Through Grounded Ice Rubble**. Contract report for The National Research Council of Canada (G.Timco), March 1994, 95 p.

Croasdale K.R. and Associates (1995) **Ice Load Models for First-Year Pressure Ridges and Rubble Fields - Phase 1**. Joint Industry Project report for National Energy Board and PERD. April, 1995, 192 p.

Croasdale K.R. and Associates (1996) **In Situ Strength Measurements of First-Year Ridge Keels for Interaction Models**. Joint Industry Project Report for NEB, April, 1996, 210 p.

Davenport, A.G. (1989) Personal Communication and Class Notes, Industrial Aerodynamics, The University of Western Ontario.

Dinkla, E. and Sluymer, T.J (1970) **Ice Pressure Against Structures**. IAHR Ice Symposium, Reykjavik, Iceland, 1970, Sec. 6.6, 7 p.

Dolgopolov, Y.V. Afanasiev V.P. Koren`kov V.A. Panfilov D.F. (1975) **Effect of Hummocked Ice on the Piers of Marine Hydraulic Structures**. 3rd International

Symposium on Ice Problems, IAHR'75. Hanover, NH. USA, pp. 463-477.

Draper. N.R. and Smith, H. (1966) *Applied Regression Analysis*. John Wiley and Sons, Inc, 193 p.

Eranti, E., Lehmus, E. and Nortala-Hoikkanen, (1992) **First Year Ice Ridge Characteristics and Loads on Offshore Structures**. 2nd International Offshore and Polar Engineering Conference, San Francisco, CA, pp. 681-687.

Ettema, R. and Urroz, G.E. (1989) **On the Internal Friction and Cohesion in Unconsolidated Ice Rubble**. Cold Regions Science and Technology, Vol 16, pp. 237-247.

Ettema, R. and Urroz-Aguirre, G.E. (1991) **Friction and Cohesion in Ice Rubble Reviewed**. Cold Regions Engineering, Proceedings of International Specialty Conference, Hanover, NH, pp. 316-325.

Evers, K., (1986) - **Erste Eisbrechtechnische Expedition mit F.S. Polarstern. Schlussbericht**, Band III, Kap. 13: Geometrie und Konsolidierungsgrad der von "Polarstern" durchbrochenen Presseisrucken, Hamburg, Germany, April 1986.

Fransson, L. Sandkvist, J. (1985) **Brash Ice Shear Properties - Laboratory Tests**. POAC'85, Narssarsuaq, Greenland, pp. 75-87.

Frederking, R.M.W. (1994) Communication to Strait Crossing Joint Venture regarding main bridge pier ice loads, June 14, 1994, 1 p.

Frederking, R.M.W. and Sayed, M. (1994) **Review of Ice Force Report - Northumberland Strait Crossing**. National Research Council Canada, Client Report to Strait Crossing Joint Venture, July 1994 IERT Report No:C6T01, 6 p.

Gale, A.D. Sego, D.C. and Morgenstern, N.R. (1986) **Behaviour of Cohesionless Broken Ice**. Proceedings of the Third Canadian Conference on Marine Geotechnical Engineering, St. John's, Nf., pp. 485-502.

Gladwell, R.W. (1976) **Field Studies of Eight First-year Sea Ice Pressure Ridges**. APOA Report No.75-1, 101 p.

Godwin, R.J. and Spoor, G. (1977) **Soil Failure with Narrow Tines**. Journal of Agricultural Engineering Res., Vol. 22, pp. 213-228.

Gow, A.J. (1977) **Flexural Strength of Ice on Temperate Lakes**. Journal of Glaciology, Vol. 19, No. 81, pp. 247-256.

Hellmann, J.H. (1984) **Basic Investigations of Mush Ice**. IAHR '84, 7th International Symposium on Ice, Hamburg, Germany, Vol. 3, pp. 37-55.

Hettiaratchi, D.R.P., Witney, B.D. and Reece, A.R. (1966) **The Calculation of Passive Pressure in Two-Dimensional Soil Failure**. Journal of Agricultural Engineering Research, 1966, No.11 (2), pp. 89-107.

Hibler, W.D., Weeks, W.F. and Mock, S.J. (1972) **Statistical Aspects of Sea-Ice Ridge Distributions**. Journal of Geophysical Research, Vol. 77, No.30, Oct. 20, 1972, pp. 5954-5970.

Hobbs, P.V. (1974). *Ice Physics*. Clarendon Press, Oxford, 837 p.

Hoikkanen, J (1985) **Measurements and Analysis of Ice Force Against a Conical Offshore Structure**. 8th conference on Port and Ocean Engineering under Arctic Conditions (POAC'85), Narssarssuaq. Vol.3, pp. 1203-1220.

Hudson, R.D. (1983) **Observations of the Extrusion of Sea Ice Rubble**. Conference on Port and Ocean Engineering under Arctic Conditions (POAC'83), Helsinki, Finland, pp. 99-108.

Joensuu, A. (1981) **Arktisille Merialueille Soveltuvat Oljynja Kaasunporaustasanteet**. Diplomityo. Helsingin Teknillinen Korkeakoulu, Koneinsinooriosasto. Otanniemi 1981. 130 p. (cit. Krankkala, T. and Maattanen, M., 1984)

Jumakis, A.R. (1984) *Soil Mechanics*. Robert E. Krieger Publishing Company Inc., Florida, 576 p.

Kankaanpaa, P. (1989) **Structure of First Year Pressure Ridges in the Baltic Sea**. POAC'89. pp. 87-102.

Keinonen, A. (1977) **Measurements of Physical Characteristics of Ridges on April 14 and 15, 1977**. Styrelsen for vintersjo-fartsforskning, 22, 9 p.

Keinonen, A. and Nyman, T. (1978) **An Experimental Model-Scale Study on the Compressive, Frictional and Cohesive Behaviour of Broken Ice Mass**. Proceedings. International Association for Hydraulics Research Ice Symposium, Lulea, Sweden, Part 2, pp. 335-353.

Keinonen, A. (1979) **An Analytical Method for Calculating the Pure Ridge Resistance Encountered by Ships in First-Year Ice Ridges**. Helsinki University of Technology, Ship Hydrodynamics Laboratory, Report No. 17.

Kitazawa T. and Ettema, R. (19) **Rubble-Ice Resistance For Ships Moving With**

Creeping Speed. Proceedings of the 5th OMAE, 1986, Vol. 4. pp. 593-600.

Kolymbas. D. (1987) **Ice Forces on Conical Offshore Strucutres.** Computer Methods in Applied Mechanics and Engineering, North-Holland, 60, (1987) pp. 217-231.
Kosar, K. (1996) Personal communication, C-CORE, St.John's Nf.

Kovacs, A. (1972) **On Pressure Sea Ice.** In: T. Karlsson (Ed.) Proceedings of International Sea Ice Conference. National Research Council, Reykjavik, Iceland, 1971, pp. 276-295.

Kovacs, A. and Mellor, M. (1974) **Sea Ice Morphology and Ice as a Geologic Agent in Southern Beaufort Sea.** Reprint from Coast and Shelf of the Beaufort Sea. The Arctic Institue of North America, CRREL, 1974. 164p.

Krankkala, T. and Maattanen, M (1984) **Methods for Determining Ice Forces Due to First- and Multi-Year Ridges.** IAHR Ice Symposium, Hamburg, 1984, pp. 263-287.

Lavender, S.T. (1973) **Analysis of Ice Cover Stability.** Acres Employee Development Committee Seminar Notes (unpublished), January, 1973.

Lehmus, E. and Karna, T. (1995) **Shear Strength of Ice Rubble in Laboratory Tests.** Proceedings of the Fifth (1995) International Offshore and Polar Engineering Conference. The Hague. Netherlands, June 11-16, 1995, pp. 323-329.

Lepparanta, M. (1981) **Statistical Features of Sea Ice ridging in the Gulf of Bothnia.** Winter Navigation Research Board. Report No. 32, Board of Navigation, Helsinki, Finland, 51 p.

Lepparanta, M. and Hakala, R. (1992) **The Structure and Strength of First-Year Ice Ridges in the Baltic Sea.** Cold Regions Science and Technology, 20, (1992), pp. 295-311.

Lepparanta, M, Lensu, M., Kosloff, P. and Veitch, B. (1995) **The Life Story of a First-Year Sea Ice Ridge.** Cold Regions Science and Technology, 23, (1995), pp. 279-290.

Lewis, E.L. and Perkin, R.G. (1986) **Ice Pumps and Their Rates.** Journal of Geophysical Research, Vol. 91, No. C10, pp. 11756-11762.

Loset, S. and Sayed, M. (1993) **Proportional Strain Tests of Fresh-Water Ice Rubble.** Journal of Cold Regions Engineering, ASCE., Vol.7, No.2, June 1993, pp. 44-61

Lye. L.M. (1995) Personal communication and course notes "Similitude and Modelling". Memorial University of Newfoundland, ENG.9710.

Maattanen, M. (1983) **Design Recommendations for Ice Effects on Aids-Navigation,** 3rd Draft. Oulu, 1983. IALA Technical Committee: Ice Effects on Lighthouses, 15 p.

Maattanen, M. (1986) **Test Cone Project, Technical Research Centre of Finland.** Polartech´86, Helsinki, Finland, Vol.1, pp. 749-761.

Maattanen, M. and Hoikkanen, J. (1990) **The Effect of Ice Pile-up on the Ice Force of a Conical Structure.** IAHR Ice Symposium 1990, Espoo, pp. 1010-1021.

Maattanen, M. (1994a) **Ice Force Design and Measurement of a Conical Structure.** IAHR Ice Symposium, Trodheim, Norway, Vol.1, pp. 401-410.

Maattanen, M. (1994b) **PEI Bridge Project -Answers to Keel Load Questions.** Personal communications to Strait Crossing Joint Venture, June 7 and 8, 1994, 6 p.

Marshall A.R. Jordaan, I.J. and McKenna, R.F. (1991) **A Two Dimensional Model of Grounded Ice Rubble.** Conference on Port and Ocean Engineering under Arctic Conditions, St.John's, Nf, Canada, Vol. 1, pp. 428-444.

McKenna, R.F, Bruneau, S.E. Guzzwell, J. Hill, B. and Kirby, C. (1995a) **Pilot Experiments with a cylindrical Structure in Unconsolidated Ridges.** Report for the National Energy Board by the National Research Council of Canada IMD Report, TR-1995-20, 32 p.

McKenna, R.F. Williams, F.M. Hill, B. and Kirby, C.S. (1995b) **Forces on the Northumberland Strait Bridge Piers due to Ice Ridge Keels.** Report for Public Works Canada by the National Research Council, IMD Report No. TR-1995-38, 36 p.

McKenna, R.F., Bruneau. S.E. and Williams, F.M. (1996) **In Situ Shear Strength Measurements of Model Ice Rubble Using a Punch Technique.** The 49th Canadian Geotechnical Conference of the Canadian Geotechnical Society, Sept, 1996, St.John's, Nf. pp. 279-286.

McKenna R.F. (1996) **First-Year Ice Ridge Forces on an Upward Breaking Conical Structure.** C-CORE Report No.96-C11 for National Research Council of Canada, IMD, St.John's, Nf.

McKenna, R.F. and Bruneau S.E. (1997) **Ice Rubble Build-Up on Conical Structures During Ridge Interactions.** In Press for POAC/OMAE, 1997 Yokohama, Japan.

McKenna, R.F. Bruneau, S.E., Guzzwell, J. (1997) **Modelling Unconsolidated Rubble Forces on a Cylindrical Structure.** In press for POAC/OMAE 1997, Yokohama, Japan.

Mellor, M. (1980) **Ship Resistance in Thick Brash Ice.** Cold Regions Science and

Technology, Vol.3, (1980) 304-321.

Michel, B. (1978) *Ice Mechanics*. Les Presses de l'Universite Laval, 499 p.

Molgaard, J. (1991) **Mechanisms of Ice Friction**. IUTAM-IAHR Symposium St. John's Newfoundland, Canada, 1991, pp. 385-403.

Molgaard, J. and Jordaan I.J. (1994) Personal communication and class notes from Eng 9051. Memorial University of Newfoundland.

Osman, M.S. (1964) **The Mechanics of Soil Cutting Blades**. Journal of Agricultural Engineering Research, Vol.9, No.4, pp. 313-328.

Palosuo, E. (1975) **Formation and Structure of Ridges in the Baltic**. Styrelson for vintersjofartsforskning, University of Helsinki, Report No.12, 54p.

Palosuo, E. (1970) **The Structure of an Ice Ridge in The Baltic**. Proceedings from IAHR Ice Symposium, Reykjavik, Iceland, Sept. 8-10, 1970, Sec. 3.10, 13 p.

Parmerter, R.R. and Coon, M.D. (1972) **Model of Pressure Ridge Formation in Sea Ice**. Journal Geophysical Research. Vol.77 (33), pp. 6565-6575.

Parmerter, R.R. and Coon, M.D. (1973) **On the Mechanics of Pressure Ridge Formation in Sea Ice**. Offshore Technology Conference, American Institute of Mining and Technology, Dalas Texas, 1973, pp. 733-739.

Paulin, M. (1992) "Physical Model Analysis of Iceberg Scour in Dry and Submerged Sands". M.Eng Thesis, Memorial University of Newfoundland, Faculty of Engineering and Applied Science, 1992, 324 p.

Peschansky, I.S. (1963) **Glaciology and Ice Engineering**. Morskoi Transport, 1963. (cit. Dolgopolov *et al.*, 1975).

Pilkington, G.R. O'Rourke, J.C. Steen, J.W, and Banke, E.G. (1982) **Ridge Keel Observations**. Proceedings of the Workshop on Sea Ice Ridging and Pile-Up, October 1980, National Research Council Technical Memorandum No. 134, pp. 2-8.

Poplin, J.P. and Weaver, J.S. (1992) **Ice Force and Rubble-Related Research Studies at Isserk I-15**. OMAE 1992Vol. IV, Arctic/Polr Technology ASME, pp. 75-84.

Pounder, E.R., (1965) *Physics of Ice*. Pergamon Press, Oxford, pp. 109-113.

Prodanovic, A., (1979) **Model tests of Ice Rubble Strength**. Port and Ocean Engineering Under Arctic Conditions, (POAC'79), Vol. 1, pp. 89-105.

Prodanovic, A. (1981) **Upper Bounds of Ridge Pressure on Structures**. 6th International Conference on Port and Ocean Engineering under Arctic Conditions, Quebec City, PQ, Vol.3, pp. 1288-1302.

Rajaram, G. and Oida, A. (1992) **Deformation of Sand Caused by Tine Implements**. Journal of Terramechanics, Vol. 29, No.1, pp. 149-159.

Ralston, T.D. (1980) **Plastic Limit Analysis of Sheet Ice Loads on Conical Structures**. Physics and Mechanics of Ice, P. Tryde, ed., Springer-Verlag, New York, 1980, pp. 289-308.

Rogachco, S.I., Evdokimov, G.N. and Burdjug, T.P. (1994) **The Action of Sea Ice on Offshore Construction**. OMAE, Vol.4, Arctic/Polar Technologoy, ASME (1994), pp. 93-96.

Roggensack, W.D. (1975) **Large Scale Laboratory Direct Shear Tests on Ice**. Canadian Geotechnical Journal, Vol. 12, pp. 169-178.

Sanderson, T. (1984) **Theoretical and Measured Ice Forces on Wide Strucutres**. Proc. IAHR Ice Symposium, Hamburg, Vol. 3, pp. 151-207.

Sanderson, T. (1988) *Ice Mechanics - Risks to Offshore Structures*. Graham and Trotham Ltd., London, UK, 253 p.

Sarpkaya, T. and Garrison, C. (1982) **Vortex Formation and Resistance in Unsteady Flow**. Journal of Applied Mechanics, Vol. 30, Series E, No.1, pp. 16-24.

Sayed, M., Frederking, R.M.W., and Croasdale, K.R. (1986) **Ice Stress Measurements in a Rubble Field Surrounding a Caisson-Retained Island**. Ice Technology (1986), Cambridge, Mass., USA, pp. 255-262.

Sayed, M. (1987) **Mechanical Properties of Model Ice Rubble**. Proceedings, Materials and Member Behaviour, ASCE, Orlando, Fl., pp. 647-659.

Sayed, M. and Frederking, R.M.W. (1988) **Model of Ice Rubble Pile-up**. Journal of Engineering Mechanics, ASCE, Vol. 114, No. 1, pp. 149-160.

Sayed, M., Timco, G.W. and Sun, L. (1992) **Testing Model Ice Rubble Under Proportional Strains**. Proceedings of the 11th OMAE, ASME, pp. 335-341.

Sayed, M (1995) **Numerical Simulation of The Interaction Between Ice Ridges and Bridge Piers**. National Research Council of Canada, TR-1995-08, 13 p.

Schaefer, J.A. and Ettema, R. (1986) **Experiments on Freeze-bonding Between Ice**

Blocks in Floating Ice Rubble. IAHR Ice Symposium 1986, Iowa, pp. 401-413.

Sharp, J.J. Deb, A. and Deb M.K. (1992) **Applications of matrix manipulation in dimensional analysis involving large numbers of variables.** Marine Structures, 5 (1992), pp. 333-348.

Shinde, S.B. and Kemp T.S. (1983) **Natural Ice Rubble Studies: Vol 2.** Esso Resources Canada, APOA Report No. 185-02, Calgary, Ab, 83 p.

Siemens, J.C. Weber, J.A. and Thornburn, T.H. (1965) **Mechanics of Soil as Influenced by Model Tillage Tools.** Transactions of the ASAE, Vol.8, No.1., pp. 1-7.

Stafford, J.V. (1984) **Force Prediction Models for Brittle and Flow Failure of Soil by Draught Tillage Tools.** Jounal of Agricultural Engineering Research 1984, Vol.29, No.1, pp. 51-60.

Timco, G.W. and Sayed, M. (1986) **Model Tests of the Ridge-building Process in Ice.** Proc. IAHR Symposium on Ice Problems, Iowa City, IA, Vol.1, pp. 591-602.

Timco G.W. and Cornett, A.M. (1995) **Model Tests of Ridge Interaction With a Bridge Pier for the Northumberland Strait Crossing.** National Research Council of Canada, IMD Report TR-1995-02.

Tucker, W.B. and Govoni, J.W. (1981) **Morphological Invetigations of First-Year Sea Ice Pressure Ridge Sails.** Cold Regions Science and Technology, Vol.5, pp. 1-12.

Tucker, W.B.III, Sodhi, D.S. and Govoni, J.W. (1984) **Structure of First-Year Pressure Ridge Sails in the Prudhoe Bay Region.** In P.W.Barnes, D.M.Schell and E.Reimnitz (editors), The Alaskan Beaufort Sea - Ecosystems and Environments, Academic Press, New York, pp. 115-135.

Urroz, G.E. and Ettema, R. (1987) **Simple Shear Box Experiments with Floating Ice Rubble.** Cold Regions Science and Technology, Vol. 14, pp. 185-199.

Vaudrey (1983) **Characterization of Offshore and Coastal Ice Conditions.** Design for Ice Conditions, S.R. Caldwell Eds., ASCE, New York, pp. 3-16.

Veitch, B., Lensu, M., Riska, K., Kosloff, P., Keiley, P., Kujala, P. (1991a) **Field Observations of Ridges in the Baltic Sea.** 11th Conference on Ort and Ocean Engineering under Arctic Conditions (POAC'91), St.John's, Nf, Canada, pp. 381-400.

Veitch, B., Kujala, P., Kosloff, P., Lepparanta, M. (1991b) **Field Measurements of the Thermodynamics of an Ice Ridge.** Helsinki University of Technology, Laboratory of Naval Architecture and Marine Engineering Internal Report, 1991-M-114, 53 p.

Veitch, B. Kujala, P., Keiley, P. and Lehmus, E. (1991c) **Ice Tank Experiments on the Thermodynamics of Deformed Ice**. Helsinki University of Technology, Laboratory of Naval Architecture and Marine Engineering Internal Report, 1991-M-110, 46 p.

Vesic, A.S. (1971) **Breakout Resistance of Objects Embedded in Ocean Bottom**. Journal of Soil Mechanics and Foundations Division, Proceedings of The American Society of Civil Engineers, Sept. 1971, pp. 1183-1205.

Voelker R.. DeBord, F.W., Nelka, J.J., Jacobi, J.W. and Coburn, J.L (1981) **Assessment of Ice Conditions in the South Bering Sea Based on April 1980 USCG Polar Class Trafficability Test Data. Vol. 1 and 2**, U.S. Maritime Administration Artec. Inc. Springfield, VA, USA (cit. Burden and Timco, 1995)

Wang, Yung-shih, (1984) **Analysis and Model Tests of Pressure Ridges Failing Against Conical Structures**. IAHR Ice Symposium, Hamburg, 1984, pp. 67-76.

Weeks, W.F. and Kovaks, A (1970) **The Morphology and Physical Properties of Pressure Ridges: Barrow Alaska, April 1969**. IAHR Ice Symposium, Icelend, pp. 1-8.

Weiss, R.T. Prodanovic, A. and Wood K.N. (1981) **Determination of Ice Rubble Properties**. In Proc of International Association for Hydraulic Research, International Symposium on Ice. Quebec, Canada, July 27-31, pp. 860-870.

Williams, F.M. Crocker, G. and Butt, S. (1993) **Northumberland Strait Ice Properties Measurements**. National Research Council of Canada, IMD Report TR-1993-06, 15 p.

Wong, T.T., Gale, A.D. Sego, D.C. and Morgenstern, N.R. (1987) **Shear Box Tests on Broken Ice**. 9th International Conference on Port and Ocean Engineering Under Arctic Conditions, Fairbanks, Alaska, USA, Aug. 17-22, 1987, Vol 3, pp. 97-107.

Wong, T.T. (1990) **The Mechanical Properties of Broken Ice**, PhD. Thesis University of Alberta, Edmonton, 186 p.

Wright, B.D. Hnatiuk, J. and Kovacs, A. (1978) **Sea Ice Pressure Ridges in The Beaufort Sea**. Part 1, Proc of International Association for Hydraulic Research, International Symposium on Ice Problems, pp. 249-271.

Wright, B.D. and McGonigal, D. (1982) **Features of First and Multi-Year Ridges**. Proceedings of the Workshop on Sea Ice Ridging and Pile-Up, Oct.1980, National Research Council Technical Memorandum No. 134, pp. 2-8.

Zanegin, V.G. Khrapaty, N.G. and Lyubimov (1990) **Investigation of Sea Ice Shear Properties**. Proceedings of The First (1990) European Offshore Mechanics Symposium, Tronheim, Norway, 20-22, Aug. 1990, pp. 550-555.

APPENDIX A

Table A.1 lists laboratory ice rubble shear data from literature sources referred to in Subsection 4.2.4 - ice rubble regression analysis.

Table A.1 Ice rubble shear data from literature sources.

Auth/Ref	Ice block Min L Li m	Median of Max L Lx m	Shear Speed V m/s	Ice block Flex σ fl Pa	Pore fluid Sal./impur. S % wt	Bulk Porosity e %	Buoyant Weight γ N/m^3	Stress Normal σ n Pa	Stress Shear τ Pa
Keinonen & Nyman (1978)	0.02	0.064	0.025	15000	0.6	35	670	475	475
	0.02	0.064	0.025	15000	0.6	35	670	475	500
	0.02	0.064	0.025	15000	0.6	35	670	475	505
	0.02	0.064	0.025	15000	0.6	35	670	475	605
	0.02	0.064	0.025	15000	0.6	35	670	1375	1375
	0.02	0.064	0.025	15000	0.6	35	670	1375	1425
	0.02	0.025		15000	0.6	35	670	1375	1580
	0.02	0.064	0.025	15000	0.6	35	670	1375	1580
Prodanovic (1979)	0.019	0.152	0.000106	19500	5.5	37.5	736	55.9	270
	0.019	0.152	0.000106	19500	5.5	37.5	736	55.9	290
	0.019	0.076	0.001185	19500	5.5	37.5	736	55.9	190
	0.019	0.152	0.008854	19500	5.5	37.5	736	55.9	210
	0.019	0.076	0.008854	19500	5.5	37.5	736	55.9	230
	0.019	0.152	0.001185	19500	5.5	37.5	736	2710	3360
	0.019	0.076	0.001185	19500	5.5	37.5	736	1470	1840
	0.019	0.152	0.001185	19500	5.5	37.5	736	1470	1730
	0.019	0.076	0.001185	19500	5.5	37.5	736	2710	2920
	0.0368	0.2944	0.001185	17500	5.5	37.5	736	55.9	480
	0.0368	0.1472	0.001185	17500	5.5	37.5	736	55.9	440
	0.0368	0.2944	0.001185	17500	5.5	37.5	736	55.9	670
	0.0368	0.1472	0.001185	17500	5.5	37.5	736	1470	2440
	0.0368	0.2944	0.001185	17500	5.5	37.5	736	1470	2600
	0.0368	0.1472	0.001185	17500	5.5	37.5	736	2710	2550
	0.0368	0.2944	0.001185	17500	5.5	37.5	736	2710	3520
	0.0368	0.2944	0.001185	17500	5.5	37.5	736	2710	4360
	0.0368	0.1472	0.001185	17500	5.5	37.5	736	2710	4400
Weiss et al. (1981)	0.2	0.6	0.004	83000	5.5	45	647	161.865	2000
	0.2	0.6	0.004	83000	5.5	45	647	161.865	3200
	0.2	0.6	0.004	83000	5.5	45	647	161.865	3500
	0.2	0.6	0.004	83000	5.5	45	647	800	7500
	0.2	0.6	0.004	83000	5.5	45	647	14000	10800
	0.2	0.6	0.004	83000	5.5	45	647	14300	16500
	0.2	0.6	0.004	83000	5.5	45	647	21400	10500
	0.2	0.6	0.004	83000	5.5	45	647	29200	28000
	0.2	0.6	0.004	83000	5.5	45	647	22300	28500
	0.2	0.6	0.025	83000	5.5	45	647	161.865	800
	0.2	0.6	0.025	83000	5.5	45	647	161.865	4700
	0.2	0.6	0.025	83000	5.5	45	647	10000	8000
	0.2	0.6	0.025	83000	5.5	45	647	10500	12000
	0.2	0.6	0.025	83000	5.5	45	647	14000	6800
	0.2	0.6	0.025	83000	5.5	45	647	17000	7800
	0.2	0.6	0.025	83000	5.5	45	647	17200	13600
	0.2	0.6	0.025	83000	5.5	45	647	20800	12700
	0.15	0.45	0.003	55000	5.5	31	812	203	1000
	0.15	0.45	0.003	55000	5.5	31	812	203	2900
	0.15	0.45	0.003	55000	5.5	31	812	203	4300
	0.15	0.45	0.003	55000	5.5	31	812	5900	7500
	0.15	0.45	0.003	55000	5.5	31	812	12700	3800
	0.15	0.45	0.003	55000	5.5	31	812	12400	5900
	0.15	0.45	0.003	55000	5.5	31	812	12300	9000
	0.15	0.45	0.003	55000	5.5	31	812	12500	11200
	0.15	0.45	0.003	55000	5.5	31	812	24900	11000
	0.15	0.45	0.003	55000	5.5	31	812	23600	15000
	0.15	0.45	0.003	55000	5.5	31	812	23700	16000
	0.15	0.45	0.003	55000	5.5	31	812	23600	17000
	0.15	0.45	0.024	55000	5.5	31	812	203	400
	0.15	0.45	0.024	55000	5.5	31	812	203	2000
	0.15	0.45	0.024	55000	5.5	31	812	10000	2700
	0.15	0.45	0.024	55000	5.5	31	812	9800	4700
	0.15	0.45	0.024	55000	5.5	31	812	11400	5300
	0.15	0.45	0.024	55000	5.5	31	812	12600	14300
	0.15	0.45	0.024	55000	5.5	31	812	19700	8000
	0.15	0.45	0.024	55000	5.5	31	812	21600	9500
	0.15	0.45	0.024	55000	5.5	31	812	19900	10800
	0.15	0.45	0.024	55000	5.5	31	812	24200	14400
	0.08	0.24	0.005	45000	5.5	27.5	853	213	2000
	0.08	0.24	0.005	45000	5.5	27.5	853	2000	2500

Table A.1 Ice rubble shear data from literature sources (continued).

Author/Yr	Ice block Min L (m) L1	Ice block Max L (m) L2	Median of L (m) L*	Shear Speed V (m/s)	U' (m/s)	Shear Stress σ' (Pa)	Pore fluid S	Bulk Porosity η (%wt)	Buoyant Weight γ (N/m³)	Stress Normal (Pa)	Stress Shear (Pa)
Hellmann (1984)	0.08	0.24	0.005	45000	1000000	0.001	5.5	853	4000	2000	
	0.08	0.24	0.005	45000	1000000	0.001	5.5	853	13800	5700	
	0.1	0.24	0.005	45000	1000000	0.001	27.5	853	5540	5490	
	0.1	0.24	0.0159	45000	1000000	0.001	27.5	853	2590	2290	
	0.1	0.24	0.0159	45000	1000000	0.001	27.5	853	2290	2090	
	0.1	0.24	0.0159	45000	1000000	0.001	27.5	853	1460	1450	
	0.1	0.24	0.0159	45000	1000000	0.001	27.5	853	1090	980	
	0.1	0.24	0.0159	45000	1000000	0.001	27.5	853	720	540	
	0.08	0.24	0.0159	45000	1000000	0.001	5.5	853	1800	1170	
	0.08	0.24	0.0159	45000	1000000	0.001	5.5	853	3200	2400	
	0.08	0.24	0.0159	45000	1000000	0.001	5.5	853	4250	2390	
	0.08	0.24	0.0159	45000	1000000	0.001	5.5	853	4660	2550	
	0.1	0.24	0.0159	45000	1000000	0.001	27.5	853	350	390	
	0.1	0.24	0.0159	45000	1000000	0.001	27.5	853	5990	6690	
	0.25	0.55	0.107	1000000	1000000	0.001	35	542	5400	2400	
	0.25	0.55	0.107	1000000	1000000	0.001	35	542	1450	990	
	0.25	0.55	0.107	1000000	1000000	0.001	35	542	790	880	
	0.25	0.55	0.107	1000000	1000000	0.001	35	542	720	800	
	0.25	0.55	0.107	1000000	1000000	0.001	35	542	1090	1270	
	0.25	0.55	0.107	1000000	1000000	0.001	35	542	1200	1650	
	0.25	0.55	0.107	1000000	1000000	0.001	35	542	1650	1060	
	0.25	0.55	0.107	1000000	1000000	0.001	35	542	1570	1570	
	0.25	0.55	0.107	1000000	1000000	0.001	35	542	2990	1270	
	0.25	0.55	0.107	1000000	1000000	0.001	35	542	4750	1480	
	0.01	0.16	0.0016	1000000	1000000	0.001	35	542	390	550	
	0.01	0.16	0.0016	1000000	1000000	0.001	35	542	560	560	
Fransson & Sandkvist (1985)	0.005	0.18	0.01	32000	1000000	0.6	20	667	3880	1630	
	0.005	0.18	0.01	32000	50000	0.6	20	667	1330	360	
	0.15	0.18	0.01	78000	1000000	0.001	20	667	575	150	
	0.15	0.18	0.01	78000	1000000	0.001	20	667	625	800	
	0.15	0.18	0.01	78000	1000000	0.001	20	667	660	570	
	0.15	0.18	0.01	78000	1000000	0.001	20	667	1300	750	
	0.15	0.18	0.01	78000	1000000	0.001	20	667	960	750	
	0.15	0.18	0.01	78000	1000000	0.001	20	667	1650	660	
	0.18	0.18	0.01	37000	0.6	0.5	20	667	650	700	
	0.18	0.18	0.01	37000	0.6	0.5	20	667	450	260	
Urroz and Ettema (1987)	0.08	0.09	0.002	1000000	0.001		36	534	708	510	
	0.08	0.09	0.002	1000000	0.001		36	534	28	30	
	0.08	0.09	0.002	1000000	0.001		36	534	38	30	
	0.08	0.09	0.002	1000000	0.001		36	534	70	45	
	0.08	0.09	0.002	1000000	0.001		36	534	64	64	
	0.08	0.09	0.002	1000000	0.001		36	534	95	95	
	0.08	0.09	0.002	1000000	0.001		36	534	80	80	
	0.08	0.09	0.002	1000000	0.001		36	534	78	80	
	0.08	0.09	0.002	1000000	0.001		36	534	125	90	
	0.08	0.09	0.002	1000000	0.001		36	534	110	150	
	0.08	0.09	0.002	1000000	0.001		36	534	150	150	
	0.08	0.09	0.002	1000000	0.001		36	534	180	95	
	0.08	0.09	0.002	1000000	0.001		36	534	170	160	
	0.08	0.09	0.002	1000000	0.001		36	534	64	60	
	0.08	0.09	0.002	1000000	0.001		36	534	170	170	
	0.08	0.09	0.002	1000000	0.001		36	534	205	155	
	0.08	0.09	0.002	1000000	0.001		36	534	230	159	
	0.015	0.28	0.002	1000000	0.001		39	509	85	95	
	0.015	0.28	0.002	1000000	0.001		39	509	180	95	

Table A.1 Ice rubble shear data from literature sources (continued).

Author/Ref	Ice block Min L. m	Median or Max L. Lx m	Shear Speed V m/s	Ice block Flaw σf Pa	Pore fluid Sal./temp. S %wt	Bulk Porosity e %	Buoyant Weight b' kg/m³	Stress Normal σn Pa	Stress Shear τ Pa
	0.016	0.038	0.002	1000000	0.001	39	509	85	120
	0.016	0.038	0.002	1000000	0.001	39	509	68	125
	0.016	0.038	0.002	1000000	0.001	39	509	65	125
	0.016	0.038	0.002	1000000	0.001	39	509	120	115
	0.016	0.038	0.002	1000000	0.001	39	509	130	170
	0.016	0.038	0.002	1000000	0.001	39	509	140	130
	0.016	0.038	0.002	1000000	0.001	39	509	145	150
	0.016	0.038	0.002	1000000	0.001	39	509	200	150
	0.016	0.038	0.002	1000000	0.001	39	509	180	215
	0.016	0.038	0.002	1000000	0.001	39	509	185	220
	0.016	0.038	0.002	1000000	0.001	39	509	260	340
	0.016	0.038	0.002	1000000	0.001	39	509	260	340
	0.016	0.038	0.002	1000000	0.001	39	509	320	520
	0.016	0.038	0.002	1000000	0.001	39	509	400	520
	0.016	0.038	0.002	1000000	0.001	39	509	475	560
	0.018	0.018	0.002	1000000	0.001	23	642	45	75
	0.018	0.018	0.002	1000000	0.001	23	642	85	80
	0.018	0.018	0.002	1000000	0.001	23	642	95	90
	0.018	0.018	0.002	1000000	0.001	23	642	100	100
	0.018	0.018	0.002	1000000	0.001	23	642	130	130
	0.018	0.018	0.002	1000000	0.001	23	642	180	175
	0.018	0.018	0.002	1000000	0.001	23	642	180	185
	0.018	0.018	0.002	1000000	0.001	23	642	260	195
	0.018	0.018	0.002	1000000	0.001	23	642	255	290
	0.018	0.018	0.002	1000000	0.001	23	642	290	260
	0.018	0.018	0.002	1000000	0.001	23	642	350	290
	0.018	0.018	0.002	1000000	0.001	23	642	380	275
	0.095	0.095	0.002	1000000	0.001	41	492	15	30
	0.095	0.095	0.002	1000000	0.001	41	492	25	20
	0.095	0.095	0.002	1000000	0.001	41	492	25	35
	0.095	0.095	0.002	1000000	0.001	41	492	40	30
	0.095	0.095	0.002	1000000	0.001	41	492	45	30
	0.095	0.095	0.002	1000000	0.001	41	492	50	20
	0.095	0.095	0.002	1000000	0.001	41	492	50	15
	0.095	0.095	0.002	1000000	0.001	41	492	50	20
	0.095	0.095	0.002	1000000	0.001	41	492	60	30
	0.095	0.095	0.002	1000000	0.001	41	492	70	30
	0.095	0.095	0.002	1000000	0.001	41	492	95	45
	0.095	0.095	0.002	1000000	0.001	41	492	105	85
	0.095	0.095	0.002	1000000	0.001	41	492	110	50
	0.095	0.095	0.002	1000000	0.001	41	492	115	85
	0.095	0.095	0.002	1000000	0.001	41	492	160	50
	0.038	0.038	0.002	1000000	0.001	40	500	40	50
	0.038	0.038	0.002	1000000	0.001	40	500	40	65
	0.038	0.038	0.002	1000000	0.001	40	500	50	65
	0.038	0.038	0.002	1000000	0.001	40	500	55	75
	0.038	0.038	0.002	1000000	0.001	40	500	60	75
	0.038	0.038	0.002	1000000	0.001	40	500	65	80
	0.038	0.038	0.002	1000000	0.001	40	500	65	100
	0.038	0.038	0.002	1000000	0.001	40	500	90	110
	0.038	0.038	0.002	1000000	0.001	40	500	100	130
	0.038	0.038	0.002	1000000	0.001	40	500	90	130
	0.038	0.038	0.002	1000000	0.001	40	500	80	130
	0.038	0.038	0.002	1000000	0.001	40	500	130	200
	0.038	0.038	0.002	1000000	0.001	40	500	130	230
	0.038	0.038	0.002	1000000	0.001	40	500	180	230
	0.038	0.038	0.002	1000000	0.001	40	500	195	350
	0.038	0.038	0.002	1000000	0.001	40	500	210	330
	0.038	0.038	0.002	1000000	0.001	40	500	285	350
	0.038	0.038	0.002	1000000	0.001	31	575	90	85
	0.038	0.038	0.002	1000000	0.001	31	575	85	85
	0.038	0.038	0.002	1000000	0.001	31	575	80	50
	0.018	0.018	0.002	1000000	0.001	31	575	100	90
	0.018	0.018	0.002	1000000	0.001	31	575	125	75
	0.018	0.018	0.002	1000000	0.001	31	575	140	100
	0.018	0.018	0.002	1000000	0.001	31	575	165	100
	0.018	0.018	0.002	1000000	0.001	31	575	175	95
	0.018	0.018	0.002	1000000	0.001	31	575	200	120

Table A.1 Ice rubble shear data from literature sources (continued).

Auth/Ref	Ice block Min L Li m	Median of Max L Lx m	Shear Speed V m/s	Ice block Flex σ fl Pa	Pore fluid Sal./Impur. S % wt	Bulk Porosity e %	Buoyant Weight γ N/m^3	Stress Normal σ n Pa	Stress Shear τ Pa
	0.018	0.018	0.002	1000000	0.001	31	575	205	150
	0.018	0.018	0.002	1000000	0.001	31	575	275	175
	0.018	0.018	0.002	1000000	0.001	31	575	295	190
	0.018	0.018	0.002	1000000	0.001	31	575	370	220
	0.018	0.018	0.002	1000000	0.001	31	575	360	250
	0.018	0.018	0.002	1000000	0.001	31	575	410	260
	0.016	0.038	0.002	1000000	0.001	40	500	35	40
	0.016	0.038	0.002	1000000	0.001	40	500	65	40
	0.016	0.038	0.002	1000000	0.001	40	500	65	65
	0.016	0.038	0.002	1000000	0.001	40	500	65	75
	0.016	0.038	0.002	1000000	0.001	40	500	80	70
	0.016	0.038	0.002	1000000	0.001	40	500	85	50
	0.016	0.038	0.002	1000000	0.001	40	500	75	100
	0.016	0.038	0.002	1000000	0.001	40	500	75	105
	0.016	0.038	0.002	1000000	0.001	40	500	120	120
	0.016	0.038	0.002	1000000	0.001	40	500	180	220
	0.016	0.038	0.002	1000000	0.001	40	500	160	275
	0.016	0.038	0.002	1000000	0.001	40	500	290	300
	0.018	0.018	0.002	1000000	0.001	36	534	20	30
	0.018	0.018	0.002	1000000	0.001	36	534	35	50
	0.018	0.018	0.002	1000000	0.001	36	534	50	50
	0.018	0.018	0.002	1000000	0.001	36	534	55	50
	0.018	0.018	0.002	1000000	0.001	36	534	60	55
	0.018	0.018	0.002	1000000	0.001	36	534	60	45
	0.018	0.018	0.002	1000000	0.001	36	534	150	100
	0.018	0.018	0.002	1000000	0.001	36	534	140	125
	0.018	0.018	0.002	1000000	0.001	36	534	145	130
	0.018	0.018	0.002	1000000	0.001	36	534	200	215
	0.018	0.018	0.002	1000000	0.001	36	534	250	215
	0.018	0.018	0.002	1000000	0.001	36	534	310	200
Case (1991)	0.03	0.096	0.001	21840	0.5	30	446	1000	2100
	0.03	0.096	0.001	21840	0.5	30	446	1330	1860
	0.03	0.096	0.001	21840	0.5	30	446	420	1380
	0.03	0.096	0.001	25935	0.5	30	446	1360	2170
	0.03	0.096	0.001	25935	0.5	30	446	870	1210
	0.03	0.096	0.001	25935	0.5	30	446	1390	1930
	0.03	0.096	0.001	25935	0.5	30	446	1180	1400
	0.03	0.096	0.001	25935	0.5	30	446	560	870
	0.03	0.096	0.001	25935	0.5	30	446	540	1320
	0.03	0.096	0.001	25935	0.5	30	446	1380	2090
	0.03	0.096	0.001	25935	0.5	30	446	720	1630
	0.03	0.096	0.001	25935	0.5	30	446	960	1250
	0.03	0.096	0.001	25935	0.5	30	446	1240	1470
	0.03	0.096	0.001	25935	0.5	30	446	1140	1560
	0.03	0.096	0.001	25935	0.5	30	446	1510	1290
	0.03	0.096	0.001	24570	0.5	30	446	1750	2610
	0.03	0.096	0.001	24570	0.5	30	446	1650	1870
	0.03	0.096	0.001	24570	0.5	30	446	2410	2530
	0.03	0.096	0.001	24570	0.5	30	446	1460	2220
	0.03	0.096	0.001	24570	0.5	30	446	1020	1060
	0.03	0.096	0.001	21840	0.5	30	446	990	1220
	0.03	0.096	0.001	21840	0.5	30	446	980	970
	0.03	0.096	0.001	21840	0.5	30	446	820	930
	0.03	0.096	0.001	21840	0.5	30	446	1310	1390
	0.03	0.096	0.001	21840	0.5	30	446	670	1330
	0.03	0.096	0.001	21840	0.5	30	446	430	880
	0.03	0.096	0.001	23478	0.5	30	446	1900	2580
	0.03	0.096	0.001	23478	0.5	30	446	790	1440
	0.03	0.096	0.001	23478	0.5	30	446	1430	1700
	0.03	0.096	0.001	23478	0.5	30	446	1900	1690
	0.03	0.096	0.001	23478	0.5	30	446	1490	1290
Bruneau (1994a)	0.018	0.035	0.001	2000000	0.001	35	542	115	2407
	0.018	0.035	0.001	2000000	0.001	35	542	115	3095
	0.018	0.035	0.001	2000000	0.001	35	542	638	2849
	0.018	0.035	0.001	2000000	0.001	35	542	640	3177
	0.018	0.035	0.001	2000000	0.001	35	542	1250	4452
	0.018	0.035	0.001	1500000	0.001	35	542	115	632
	0.018	0.035	0.001	1500000	0.001	35	542	640	1629

Table A.1 Ice rubble shear data from literature sources (continued).

Auth/Ref	Ice block Min L, Li, m	Median of Max L, Lx, m	Shear Speed, V, m/s	Ice block Flex, c fl, Pa	Pore fluid Sal./Impur., S, % wt	Bulk Porosity, %	Buoyant Weight, γ, N/m^3	Stress Normal, σn, Pa	Stress Shear, τ, Pa
	0.018	0.035	0.001	1000000	0.001	35	542	115	1160
	0.018	0.035	0.001	1000000	0.001	35	542	640	2620
	0.018	0.035	0.001	1000000	0.001	35	542	1250	2604
Bruneau et al. (1996)	0.018	0.035	0.001	1000000	0.001	35	542	436	896
	0.03	0.0918	0.021	30000	0.5	30	687	662	1672
	0.03	0.0918	0.021	30000	0.5	30	687	392	1321
	0.03	0.0918	0.021	30000	0.5	30	687	354	1117
	0.03	0.0918	0.021	30000	0.5	30	687	1103	2168
	0.03	0.0918	0.021	30000	0.5	30	687	1746	2539
	0.03	0.0918	0.021	30000	0.5	30	687	343	1042
	0.03	0.0918	0.021	30000	0.5	30	687	1309	3018
	0.03	0.0918	0.021	30000	0.5	30	687	1924	3003
	0.03	0.0918	0.021	30000	0.5	30	687	784	1537
	0.03	0.0918	0.021	30000	0.5	30	687	2019	2222
	0.03	0.0918	0.021	30000	0.5	30	687	1175	1524
	0.05	0.153	0.021	30000	0.5	30	687	661	1461
	0.05	0.153	0.021	30000	0.5	30	687	964	1543
	0.05	0.153	0.021	30000	0.5	30	687	1655	2506
	0.05	0.153	0.021	30000	0.5	30	687	222	1012
	0.05	0.153	0.021	30000	0.5	30	687	1459	2200
	0.05	0.153	0.021	30000	0.5	30	687	757	1201
	0.05	0.153	0.021	30000	0.5	30	687	1201	1624
	0.05	0.153	0.021	30000	0.5	30	687	1862	2475
	0.05	0.153	0.021	30000	0.5	30	687	640	1559
	0.05	0.153	0.021	30000	0.5	30	687	1855	1875
	0.05	0.153	0.021	30000	0.5	30	687	1287	1444
McKenna et al. (1995b) PWC	0.0473	0.144738	0.069	18	0.5	32	547	150	175
	0.0473	0.144738	0.068	18	0.5	32	547	213	371
	0.0473	0.144738	0.073	18	0.5	32	547	139	281
	0.0473	0.144738	0.148	18	0.5	32	547	134	259
	0.0473	0.144738	0.13	18	0.5	32	547	191	383
	0.0473	0.144738	0.149	18	0.5	32	547	233	673
	0.0473	0.144738	0.068	18	0.5	32	547	115	675
	0.0473	0.144738	0.064	18	0.5	32	547	183	729
	0.0473	0.144738	0.068	18	0.5	32	547	96	529
	0.0473	0.144738	0.145	18	0.5	32	547	93	678
	0.0473	0.144738	0.145	18	0.5	32	547	115	653
	0.0473	0.144738	0.074	18	0.5	32	547	88	639
	0.0473	0.144738	0.074	18	0.5	32	547	134	194
	0.0473	0.144738	0.074	18	0.5	32	547	142	181
	0.0473	0.144738	0.074	18	0.5	32	547	57	200
	0.0471	0.144126	0.073	32	0.5	32	594	104	216
	0.0471	0.144126	0.07	32	0.5	32	594	271	274
	0.0471	0.144126	0.075	32	0.5	32	594	172	188
	0.0471	0.144126	0.075	32	0.5	32	594	140	703
	0.0471	0.144126	0.07	32	0.5	32	594	232	351
	0.0471	0.144126	0.075	32	0.5	32	594	104	309
	0.0471	0.144126	0.15	32	0.5	32	594	98	737
	0.0471	0.144126	0.139	32	0.5	32	594	187	552
	0.0471	0.144126	0.149	32	0.5	32	594	142	497
	0.0471	0.144126	0.07	32	0.5	32	594	154	388
	0.0471	0.144126	0.068	32	0.5	32	594	240	417
	0.0471	0.144126	0.076	32	0.5	32	594	107	378
	0.0471	0.144126	0.156	32	0.5	32	594	110	434
	0.0471	0.144126	0.135	32	0.5	32	594	217	593
	0.0471	0.144126	0.153	32	0.5	32	594	229	332
	0.051	0.15606	0.053	27.5	0.5	32	474	220	630
	0.051	0.15606	0.06	27.5	0.5	32	474	242	909
	0.051	0.15606	0.048	27.5	0.5	32	474	216	872
	0.051	0.15606	0.047	27.5	0.5	32	474	279	734
	0.051	0.15606	0.055	27.5	0.5	32	474	230	463
	0.0504	0.154224	0.059	34.5	0.5	40	406	276	258
	0.0504	0.154224	0.059	34.5	0.5	40	406	179	593
	0.0504	0.154224	0.066	34.5	0.5	40	406	177	394
	0.0504	0.154224	0.06	20.5	0.5	40	406	292	462
	0.0504	0.154224	0.057	20.5	0.5	40	406	177	1332
	0.0504	0.154224	0.059	20.5	0.5	40	406	231	472
	0.0495	0.15147	0.066	35.5	0.5	30	542	136	570
	0.0495	0.15147	0.058	35.5	0.5	30	542	282	619

Auth/Ref	Ice block Min L, Li, m	Median of Max L, Lx, m	Shear Speed, V, m/s	Ice block Flex, σfl, Pa	Pore fluid Sal./Impur., S, % wt	Bulk Porosity, e, %	Buoyant Weight, γ, N/m^3	Stress Normal, Pa	Stress Shear, τ, Pa
	0.0495	0.15147	0.065	35.5	0.5	30	542	203	618
	0.0495	0.15147	0.065	25.5	0.5	30	542	179	710
	0.0495	0.15147	0.065	25.5	0.5	30	542	293	1167
	0.0495	0.15147	0.064	25.5	0.5	30	542	236	461
	0.0505	0.15453	0.063	37.5	0.5	27	544	166	548
	0.0505	0.15453	0.063	37.5	0.5	27	544	297	554
	0.0505	0.15453	0.074	37.5	0.5	27	544	109	485
	0.0505	0.15453	0.062	19.5	0.5	27	544	185	723
	0.0505	0.15453	0.055	19.5	0.5	27	544	223	1521
	0.0505	0.15453	0.068	19.5	0.5	27	544	161	449
	0.05	0.153	0.077	36.5	0.5	32	474	111	144
	0.05	0.153	0.072	36.5	0.5	32	474	230	188
	0.05	0.153	0.071	36.5	0.5	32	474	173	310
	0.05	0.153	0.076	36.5	0.5	32	474	206	72
	0.05	0.153	0.071	15.5	0.5	32	474	159	688
	0.05	0.153	0.073	15.5	0.5	32	474	128	461
	0.05	0.153	0.07	15.5	0.5	32	474	173	648
	0.0479	0.146574	0.067	73	0.5	35	446	158	488
	0.0479	0.146574	0.058	73	0.5	35	446	239	719
	0.0479	0.146574	0.063	73	0.5	35	446	152	681
	0.0479	0.146574	0.072	32	0.5	35	446	156	829
	0.0479	0.146574	0.061	32	0.5	35	446	216	1285
	0.0479	0.146574	0.065	32	0.5	35	446	163	646
McKenna (1996) JIP	0.0497	0.152082	0.056	55.5	0.5	20.7	786	491	733
	0.0497	0.152082	0.049	55.5	0.5	20.7	786	437	1052
	0.0497	0.152082	0.064	55.5	0.5	20.7	786	301	541
	0.0497	0.152082	0.049	37.5	0.5	20.7	786	363	1235
	0.0497	0.152082	0.051	37.5	0.5	20.7	786	354	1275
	0.0497	0.152082	0.055	37.5	0.5	20.7	786	367	640
	0.0497	0.152082	0.055	37.5	0.5	20.7	786	363	1231
	0.0497	0.152082	0.065	37.5	0.5	20.7	786	221	903
	0.0497	0.152082	0.066	37.5	0.5	20.7	786	147	964
	0.0497	0.152082	0.053	37.5	0.5	20.7	786	344	1127
	0.0497	0.152082	0.056	37.5	0.5	20.7	786	290	1303
	0.047	0.14382	0.061	117	0.5	26.5	714	266	415
	0.047	0.14382	0.066	117	0.5	26.5	714	357	531
	0.047	0.14382	0.075	117	0.5	26.5	714	143	412
	0.047	0.14382	0.049	117	0.5	26.5	714	152	445
	0.047	0.14382	0.054	117	0.5	26.5	714	362	805
	0.047	0.14382	0.066	117	0.5	26.5	714	276	748
	0.047	0.14382	0.053	81.5	0.5	26.5	714	393	994
	0.047	0.14382	0.069	81.5	0.5	26.5	714	332	650
	0.047	0.14382	0.067	81.5	0.5	26.5	714	161	549
	0.047	0.14382	0.055	81.5	0.5	26.5	714	411	575
	0.047	0.14382	0.061	81.5	0.5	26.5	714	388	573
	0.047	0.14382	0.051	81.5	0.5	26.5	714	317	1635
	0.047	0.14382	0.05	81.5	0.5	26.5	714	410	901
	0.047	0.14382	0.072	81.5	0.5	26.5	714	156	545
	0.047	0.14382	0.07	81.5	0.5	26.5	714	125	709
	0.047	0.14382	0.053	81.5	0.5	26.5	714	486	1334
	0.047	0.14382	0.066	81.5	0.5	26.5	714	308	1067
	0.051	0.15606	0.064	59.5	0.5	15	892	301	489
	0.051	0.15606	0.069	59.5	0.5	15	892	301	396
	0.051	0.15606	0.059	59.5	0.5	15	892	452	486
	0.051	0.15606	0.066	59.5	0.5	15	892	458	280
	0.051	0.15606	0.053	59.5	0.5	15	892	519	599
	0.051	0.15606	0.062	59.5	0.5	15	892	513	835
	0.051	0.15606	0.065	44	0.5	15	892	323	514
	0.051	0.15606	0.065	44	0.5	15	892	329	333
	0.051	0.15606	0.055	44	0.5	15	892	508	927
	0.051	0.15606	0.063	44	0.5	15	892	519	324
	0.051	0.15606	0.05	44	0.5	15	892	575	924
	0.051	0.15606	0.055	44	0.5	15	892	603	667
	0.052	0.15912	0.075	61.5	0.5	22.5	813	193	493
	0.052	0.15912	0.077	61.5	0.5	22.5	813	224	353
	0.052	0.15912	0.068	61.5	0.5	22.5	813	336	400
	0.052	0.15912	0.071	61.5	0.5	22.5	813	236	404
	0.052	0.15912	0.069	61.5	0.5	22.5	813	310	477
	0.052	0.15912	0.072	61.5	0.5	22.5	813	290	409

Table A.1 Ice rubble shear data from literature sources (continued).

Auth/Ref	Ice block Min L Li m	Median of Max L Lx m	Shear Speed v m/s	Ice block Flex σfl Pa	Pore fluid Sal./impur. S % wt	Bulk Porosity e %	Buoyant Weight γ N/m3	Stress Normal σn Pa	Stress Shear τ Pa
	0.05	0.153	0.064	24.5	0.5	22.5	730	370	593
	0.05	0.153	0.066	24.5	0.5	22.5	730	356	308
	0.05	0.153	0.067	24.5	0.5	22.5	730	294	683
	0.05	0.153	0.071	24.5	0.5	22.5	730	303	337
	0.05	0.153	0.073	24.5	0.5	22.5	730	165	579
	0.05	0.153	0.076	24.5	0.5	22.5	730	173	406
	0.047	0.14382	0.069	21.5	0.5	12.25	/ree	112	1258
	0.047	0.14382	0.064	21.5	0.5	12.25	766	225	263
	0.047	0.14382	0.065	21.5	0.5	12.25	766	236	605
	0.047	0.14382	0.072	21.5	0.5	12.25	766	340	241
	0.047	0.14382	0.074	21.5	0.5	12.25	766	153	449
	0.047	0.14382	0.057	21.5	0.5	12.25	766	149	322
	0.05	0.153	0.064	29.5	0.5	18	869	358	477
	0.05	0.153	0.075	29.5	0.5	18	869	342	182
	0.05	0.153	0.053	29.5	0.5	18	869	516	1109
	0.05	0.153	0.06	29.5	0.5	18	869	516	643
	0.05	0.153	0.063	29.5	0.5	18	869	500	433
	0.05	0.153	0.067	29.5	0.5	18	869	471	828
	0.05	0.153	0.064	29.5	0.5	18	869	434	382
	0.05	0.153	0.066	29.5	0.5	18	869	326	303
	0.05	0.153	0.071	29.5	0.5	18	869	304	255
Lehmus and Karna (1995)	0.047	0.188	0.01	1000000	0.001	33	559	168	8200
	0.047	0.188	0.01	1000000	0.001	31	575	173	3870
	0.037	0.1295	0.01	1000000	0.001	32	567	170	6280
	0.037	0.1295	0.01	1000000	0.001	42	484	1585	12820
	0.037	0.1295	0.01	1000000	0.001	30	584	175	25190
	0.045	0.2025	0.01	1000000	0.001	28	600	180	9400
	0.045	0.2025	0.01	1000000	0.001	37	525	1598	6300
	0.045	0.2025	0.01	1000000	0.001	32	567	1610	8080
	0.045	0.2025	0.01	1000000	0.001	37	525	158	8480
	0.045	0.2025	0.01	1000000	0.001	39	509	1593	12520
	0.048	0.192	0.01	1000000	0.001	29	592	178	9380
	0.048	0.192	0.01	1000000	0.001	37	525	1598	8980
	0.04	0.18	0.01	1000000	0.001	30	584	175	1420
	0.041	0.1845	0.01	1000000	0.001	40	500	150	3050
	0.041	0.1845	0.01	1000000	0.001	37	525	158	2350
	0.041	0.1845	0.01	1000000	0.001	32	567	170	1400
	0.042	0.189	0.01	1000000	0.001	32	567	170	4150
	0.042	0.189	0.01	1000000	0.001	31	575	1613	6610
	0.042	0.189	0.01	1000000	0.001	36	534	1600	11160
	0.042	0.189	0.01	1000000	0.001	34	550	1605	10490
	0.042	0.189	0.01	1000000	0.001	35	542	1603	8300
Cheng and Tatinclaux (1977)	0.008	0.038	0.00025	1000000	0.001	35	542	25	2632
	0.008	0.038	0.0005	1000000	0.001	35	542	25	960
	0.008	0.038	0.001	1000000	0.001	35	542	25	400
	0.008	0.038	0.001993	1000000	0.001	35	542	25	200
	0.008	0.038	0.002999	1000000	0.001	35	542	25	200
	0.008	0.038	0.003999	1000000	0.001	35	542	25	120
	0.008	0.038	0.004996	1000000	0.001	35	542	25	101
	0.008	0.038	0.005995	1000000	0.001	35	542	25	101
	0.008	0.038	0.00025	1000000	0.001	35	542	41	2841
	0.008	0.038	0.0005	1000000	0.001	35	542	41	720
	0.008	0.038	0.001	1000000	0.001	35	542	41	175
	0.008	0.038	0.001993	1000000	0.001	35	542	41	151
	0.008	0.038	0.002999	1000000	0.001	35	542	41	144
	0.008	0.038	0.003999	1000000	0.001	35	542	41	161
	0.008	0.038	0.004996	1000000	0.001	35	542	41	175
	0.008	0.038	0.00025	1000000	0.001	35	542	58	3067
	0.008	0.038	0.0005	1000000	0.001	35	542	58	1656
	0.008	0.038	0.001	1000000	0.001	35	542	58	605
	0.008	0.038	0.001993	1000000	0.001	35	542	58	398
	0.008	0.038	0.002999	1000000	0.001	35	542	58	394
	0.008	0.038	0.003999	1000000	0.001	35	542	58	228
	0.008	0.038	0.004996	1000000	0.001	35	542	58	221
	0.008	0.038	0.005995	1000000	0.001	35	542	58	221
	0.008	0.038	0.0005	1000000	0.001	35	542	74	2438
	0.008	0.038	0.001	1000000	0.001	35	542	74	2385
	0.008	0.038	0.001993	1000000	0.001	35	542	74	562

Table A.1 Ice rubble shear data from literature sources (continued).

Auth/Ref	Ice block Min L Li m	Median of Meas L Lk m	Shear Speed v m/s	Ice block Flex σ fl Pa	Pore fluid Sal./Impur. S %wt	Bulk Porosity e %	Buoyant Weight N/m^3	Stress Normal σ n Pa	Stress Shear Pa
	0.008	0.038	0.002999	1000000	0.001	35	542	74	322
	0.008	0.038	0.003999	1000000	0.001	35	542	74	240
	0.008	0.038	0.004996	1000000	0.001	35	542	74	202
	0.008	0.038	0.005995	1000000	0.001	35	542	74	168
	0.008	0.038	0.00025	1000000	0.001	35	542	25	1666
	0.008	0.038	0.0005	1000000	0.001	35	542	25	780
	0.008	0.038	0.001	1000000	0.001	35	542	25	720
	0.008	0.038	0.001999	1000000	0.001	35	542	25	433
	0.008	0.038	0.002999	1000000	0.001	35	542	25	331
	0.008	0.038	0.003999	1000000	0.001	35	542	25	227
	0.008	0.038	0.004996	1000000	0.001	35	542	25	221
	0.008	0.038	0.005995	1000000	0.001	35	542	25	221
	0.008	0.038	0.00025	1000000	0.001	35	542	41	3000
	0.008	0.038	0.0005	1000000	0.001	35	542	41	1502
	0.008	0.038	0.001	1000000	0.001	35	542	41	696
	0.008	0.038	0.001999	1000000	0.001	35	542	41	446
	0.008	0.038	0.002999	1000000	0.001	35	542	41	331
	0.008	0.038	0.003999	1000000	0.001	35	542	41	302
	0.008	0.038	0.004996	1000000	0.001	35	542	41	259
	0.008	0.038	0.005995	1000000	0.001	35	542	41	259
	0.008	0.038	0.00025	1000000	0.001	35	542	58	4517
	0.008	0.038	0.0005	1000000	0.001	35	542	58	2371
	0.008	0.038	0.001	1000000	0.001	35	542	58	1022
	0.008	0.038	0.001999	1000000	0.001	35	542	58	379
	0.008	0.038	0.002999	1000000	0.001	35	542	58	451
	0.008	0.038	0.003999	1000000	0.001	35	542	58	288
	0.008	0.038	0.004996	1000000	0.001	35	542	58	259
	0.008	0.038	0.005995	1000000	0.001	35	542	58	235
	0.008	0.038	0.001	1000000	0.001	35	542	74	2688
	0.008	0.038	0.001999	1000000	0.001	35	542	74	778
	0.008	0.038	0.002999	1000000	0.001	35	542	74	595
	0.008	0.038	0.003999	1000000	0.001	35	542	74	446
	0.008	0.038	0.004996	1000000	0.001	35	542	74	446
	0.008	0.038	0.005995	1000000	0.001	35	542	74	446
	0.008	0.038	0.00025	1000000	0.001	35	542	25	4569
	0.008	0.038	0.0005	1000000	0.001	35	542	25	2481
	0.008	0.038	0.001	1000000	0.001	35	542	25	902
	0.008	0.038	0.001999	1000000	0.001	35	542	25	398
	0.008	0.038	0.002999	1000000	0.001	35	542	25	322
	0.008	0.038	0.003999	1000000	0.001	35	542	25	230
	0.008	0.038	0.004996	1000000	0.001	35	542	25	230
	0.008	0.038	0.005995	1000000	0.001	35	542	25	110
	0.008	0.038	0.00025	1000000	0.001	35	542	41	4377
	0.008	0.038	0.0005	1000000	0.001	35	542	41	2803
	0.008	0.038	0.001	1000000	0.001	35	542	41	1397
	0.008	0.038	0.001999	1000000	0.001	35	542	41	600
	0.008	0.038	0.002999	1000000	0.001	35	542	41	499
	0.008	0.038	0.003999	1000000	0.001	35	542	41	403
	0.008	0.038	0.004996	1000000	0.001	35	542	41	300
	0.008	0.038	0.005995	1000000	0.001	35	542	41	252
	0.008	0.038	0.00025	1000000	0.001	35	542	58	4973
	0.008	0.038	0.0005	1000000	0.001	35	542	58	3144
	0.008	0.038	0.001	1000000	0.001	35	542	58	1286
	0.008	0.038	0.001999	1000000	0.001	35	542	58	643
	0.008	0.038	0.002999	1000000	0.001	35	542	58	427
	0.008	0.038	0.003999	1000000	0.001	35	542	58	427
	0.008	0.038	0.004996	1000000	0.001	35	542	58	322
	0.008	0.038	0.005995	1000000	0.001	35	542	58	322
	0.008	0.038	0.00025	1000000	0.001	35	542	74	5400
	0.008	0.038	0.0005	1000000	0.001	35	542	74	3000
	0.008	0.038	0.001	1000000	0.001	35	542	74	1608
	0.008	0.038	0.001999	1000000	0.001	35	542	74	888
	0.008	0.038	0.002999	1000000	0.001	35	542	74	667
	0.008	0.038	0.003999	1000000	0.001	35	542	74	557
	0.008	0.038	0.004996	1000000	0.001	35	542	74	557
	0.008	0.038	0.005995	1000000	0.001	35	542	74	557
	0.004	0.025	0.000198	1000000	0.001	35	542	21	3651
	0.004	0.025	0.000378	1000000	0.001	35	542	21	2466
	0.004	0.025	0.000808	1000000	0.001	35	542	21	1018

Table A.1 Ice rubble shear data from literature sources (continued).

Auth/Ref	Ice block Min L Li m	Median of Max L Lx m	Shear Speed V m/s	Ice block Flax σfl Pa	Pore fluid Sal./Impur. S %wt	Bulk Porosity e %	Buoyant Weight γ N/m^3	Stress Normal σn Pa	Stress Shear τ Pa
	0.004	0.025	0.001183	1000000	0.001	35	542	21	546
	0.004	0.025	0.001667	1000000	0.001	35	542	21	341
	0.004	0.025	0.000378	1000000	0.001	35	542	41	6207
	0.004	0.025	0.000808	1000000	0.001	35	542	41	2698
	0.004	0.025	0.001183	1000000	0.001	35	542	41	1732
	0.004	0.025	0.001667	1000000	0.001	35	542	41	313
	0.004	0.025	0.000808	1000000	0.001	35	542	62	6616
	0.004	0.025	0.001183	1000000	0.001	35	542	62	4481
	0.004	0.025	0.001667	1000000	0.001	35	542	62	3384
	0.004	0.025	0.000198	1000000	0.001	35	542	21	1946
	0.004	0.025	0.000378	1000000	0.001	35	542	21	833
	0.004	0.025	0.000808	1000000	0.001	35	542	21	495
	0.004	0.025	0.001183	1000000	0.001	35	542	21	252
	0.004	0.025	0.001667	1000000	0.001	35	542	21	160
	0.004	0.025	0.000198	1000000	0.001	35	542	41	5798
	0.004	0.025	0.000378	1000000	0.001	35	542	41	2103
	0.004	0.025	0.000808	1000000	0.001	35	542	41	1125
	0.004	0.025	0.001183	1000000	0.001	35	542	41	568
	0.004	0.025	0.001667	1000000	0.001	35	542	41	399
	0.004	0.025	0.000198	1000000	0.001	35	542	62	9958
	0.004	0.025	0.000378	1000000	0.001	35	542	62	4842
	0.004	0.025	0.000808	1000000	0.001	35	542	62	2040
	0.004	0.025	0.001183	1000000	0.001	35	542	62	1288
	0.004	0.025	0.001667	1000000	0.001	35	542	62	1088
	0.004	0.025	0.000198	1000000	0.001	35	542	21	2926
	0.004	0.025	0.000396	1000000	0.001	35	542	21	1805
	0.004	0.025	0.000805	1000000	0.001	35	542	21	955
	0.004	0.025	0.001201	1000000	0.001	35	542	21	587
	0.004	0.025	0.001634	1000000	0.001	35	542	21	235
	0.004	0.025	0.000396	1000000	0.001	35	542	41	5182
	0.004	0.025	0.000805	1000000	0.001	35	542	41	3141
	0.004	0.025	0.001201	1000000	0.001	35	542	41	1278
	0.004	0.025	0.001634	1000000	0.001	35	542	41	503
	0.004	0.025	0.000195	1000000	0.001	35	542	62	9847
	0.004	0.025	0.000396	1000000	0.001	35	542	62	5333
	0.004	0.025	0.000805	1000000	0.001	35	542	62	1877
	0.004	0.025	0.001201	1000000	0.001	35	542	62	1162
	0.004	0.025	0.001634	1000000	0.001	35	542	62	543
	0.004	0.025	0.000195	1000000	0.001	35	542	21	2034
	0.004	0.025	0.000396	1000000	0.001	35	542	21	1180
	0.004	0.025	0.000805	1000000	0.001	35	542	21	737
	0.004	0.025	0.001201	1000000	0.001	35	542	21	539
	0.004	0.025	0.001634	1000000	0.001	35	542	21	277
	0.004	0.025	0.000195	1000000	0.001	35	542	41	5937
	0.004	0.025	0.000396	1000000	0.001	35	542	41	3610
	0.004	0.025	0.000805	1000000	0.001	35	542	41	1452
	0.004	0.025	0.001201	1000000	0.001	35	542	41	698
	0.004	0.025	0.001634	1000000	0.001	35	542	41	535
	0.004	0.025	0.000198	1000000	0.001	35	542	62	8221
	0.004	0.025	0.000396	1000000	0.001	35	542	62	4489
	0.004	0.025	0.000805	1000000	0.001	35	542	62	1711
	0.004	0.025	0.001201	1000000	0.001	35	542	62	1142
	0.004	0.025	0.001634	1000000	0.001	35	542	62	772

APPENDIX B

Table B.1 lists laboratory ice rubble/structure interaction data from literature sources referred to in Subsection 4.3.3 - ridge/structure interaction regression analysis.

Table B.1 Ice rubble/structure interaction data.

Reference	Dummy variables	Rubble extent* contin.=1 disc.=2	Structure confine 2d=1 3d=2	Waterline confine N=1 Y=2	Structural diameter m	Keel width m	Keel depth m	Keel area m²	Speed m/s	Peak load N	Friction angle deg	Cohesion c Pa	Buoyant weight N/m³
Cheng and Tatinclaux (1977)	1	1	1	1	0.0944	0.0762			0.000155	386.4	46	–	542
	1	1	1	1	0.0944	0.0762			0.000283	76.1	46	–	542
	1	1	1	1	0.0944	0.0762			0.000347	90.7	46	–	542
	1	1	1	1	0.0944	0.0762			0.000366	54.3	46	–	542
	1	1	1	1	0.0944	0.0762			0.000655	46.5	46	–	542
	1	1	1	1	0.0944	0.0762			0.000978	25.5	46	–	542
	1	1	1	1	0.0944	0.0762			0.001323	18.7	46	–	542
	1	1	1	1	0.0944	0.1524			0.000652	146.5	46	–	542
	1	1	1	1	0.0944	0.1524			0.001042	95.0	46	–	542
	1	1	1	1	0.0944	0.1524			0.001445	78.9	46	–	542
	1	1	1	1	0.0944	0.1524			0.002226	47.3	46	–	542
	1	1	1	1	0.0944	0.2286			0.00006	371.9	46	–	542
	1	1	1	1	0.0944	0.2286			0.001286	291.9	46	–	542
	1	1	1	1	0.0944	0.2286			0.001829	183.0	46	–	542
	1	1	1	1	0.0944	0.174			0.002807	156.5	46	–	542
Kein and Ny (1978) Prodanovic (1979)	1	1	1	1	0.3	0.3			0.025	24.0	47	11	669
	1	1	1	1	0.152		0.075	0.00854	0.008654	11.4	47	260	736
	1	1	1	1	0.152		0.145	0.00854	0.008654	24.3	47	260	736
	1	1	1	1	0.152		0.145	0.00854	0.008654	30.4	47	260	736
	1	1	1	1	0.152		0.075	0.00854	0.008654	31.9	47	260	736
	1	1	1	1	0.152		0.09	0.00854	0.008654	36.5	53	580	736
	1	1	1	1	0.152		0.04	0.00854	0.008654	73.0	53	580	736
	1	1	1	1	0.152		0.075	0.00854	0.008654	87.4	53	580	736
	1	1	1	1	0.152		0.145	0.00854	0.008654	97.3	53	580	736
	1	1	1	1	0.152		0.145	0.00854	0.008654	127.7	53	580	736
	1	1	1	1	0.152		0.09		0.001185	7.6	53	580	736
	1	1	1	1	0.152		0.145		0.001185	50.2	53	580	736
	1	1	1	1	0.152		0.28		0.001185	63.8	53	580	736
	1	1	1	1	0.152		0.04		0.001185	54.7	53	580	736
	1	1	1	1	0.152		0.145		0.001185	65.4	53	580	736
	1	1	1	1	0.152		0.145		0.001185	120.1	53	580	736
	1	1	1	1	0.304		0.28		0.001185	9.1	53	580	736
	1	1	1	1	0.304		0.075		0.001185	53.2	53	580	736
	1	1	1	1	0.304		0.09		0.001185	106.4	53	580	736
	1	1	1	1	0.304		0.28		0.001185	97.3	53	580	736
	1	1	1	1	0.304		0.18		0.001185	118.6	53	580	736
	1	1	1	1	0.304		0.28		0.001185	264.5	53	580	736
	1	1	1	1	0.304		0.28		0.001185	282.7	47	260	736
	1	1	1	1	0.304		0.075		0.001185	18.2	47	260	736
	1	1	1	1	0.304		0.075		0.001185	24.3	47	260	736
	1	1	1	1	0.304		0.075		0.001185	27.4	47	260	736

Table B.1 Ice rubble/structure interaction data (continued).

Reference	Dummy variables	Rubble extent contin.=1 disc.=2	Structure 2-d=1 3-d=2	Waterline confine N=1 Y=2	Structural diameter m	Keel width m	Keel depth m	Keel area m²	Speed m/s	Peak load N	Friction angle deg	Cohesion c Pa	Buoyant weight N/m³
Hellmann (1984)	1	1	1	2	0.304		0.145		0.001185	57.8	47	260	736
	1	1	1	2	0.304		0.145		0.001185	60.8	53	580	736
	1	1	1	2	0.304		0.075		0.001185	60.8	53	580	736
	1	1	1	2	0.304		0.09		0.001185	109.4	53	580	736
	1	1	1	2	0.304		0.145		0.001185	94.2	53	580	738
	1	1	1	2	0.304		0.145		0.001185	191.5	53	580	736
	1	1	1	2	0.304		0.28		0.001185	252.3	53	580	736
	1	1	1	2	0.304		0.28		0.001185	285.8	53	580	736
Bruneau (1996a) Submerged rubble	1	2	2	2	0.1	0.45	0.3	0.09	0.0105	352.0	54	420	542
	1	2	2	2	0.1	0.45	0.4		0.0105	345.0	54	420	542
	1	2	2	2	0.1	0.3	0.4	0.045	0.0105	470.0	54	580	542
	1	2	2	2	0.1	0.45	0.4	0.06	0.0105	800.0	54	580	542
	1	2	2	2	0.1		0.4	0.09	0.0105	630.0	54	580	542
	1	2	2	2	0.1		0.4		0.0012	525.0	61	420	542
	1	2	2	2	0.1		0.8		0.0022	290.0	61	420	542
	1	2	2	2	0.1	0.45	0.8	0.1125	0.0045	565.0	54	580	542
	1	2	2	2	0.1		0.4		0.0102	555.0	54	580	542
	1	2	2	2	0.1		0.4		0.0102	195.0	54	580	542
	1	2	2	2	0.114		0.4		0.02	85.0	55	2400	588
	1	2	2	2	0.114		0.2		0.023	60.0	55	2400	588
	1	2	2	2	0.114		0.2		0.25	40.0	55	2400	588
	1	2	2	2	0.114		0.1		0.006	42.5	55	2400	588
	1	2	2	2	0.114		0.1		0.006	7.5	55	900	588
	1	2	2	2	0.114		0.25		0.006	19.0	55	900	588
	1	2	2	2	0.114		0.25		0.006	50.0	55	900	588
	1	2	2	2	0.114		0.2		0.006	41.0	55	900	588
	1	2	2	2	0.114	0.45	0.2		0.006	24.0	55	900	588
	1	2	2	2	0.114		0.2		0.006	37.0	55		588
	1	2	2	2	0.114		0.2		0.006	180.0	55		588
Dry rubble	1	2	2	2	0.114	0.45	0.2	0.09	0.006	120.0	55		5297
	1	2	2	2	0.114	0.45	0.2	0.09	0.006	52.0	55		5297
	1	2	2	2	0.114	0.45	0.2	0.09	0.006	57.0	55		5297
	1	2	2	2	0.114		0.1	0.045	0.006	250.0	55		5297
	1	2	2	2	0.114	0.45	0.1	0.0225	0.006	250.0	55		5297
	1	2	2	2	0.114		0.1		0.006	52.0	55		5297

Table B.1 Ice rubble/structure interaction data (continued).

Reference	Dummy variables	Boundary conditions Rubble extent disc = 1 contin = 2	Boundary conditions Structure 2-d or 3-d 2-d = 1 3-d = 2	Boundary conditions Waterline confirm N = 1 Y = 2	Structural diameter m	Keel width m	Keel depth m	Keel area m^2	Speed m/s	Peak load N	Friction angle deg	Cohesion c Pa	Buoyant weight N/m^3
Timco and Cornett (1995)	1	2	2	2	0.333	2	0.318	0.636	0.09	1350.0			536
		2	2	2	0.333	1	0.318	0.318	0.09	450.0			536
		2	2	2	0.333	1	0.363	0.363	0.09	470.0			536
		2	2	2	0.333	1	0.003	0.003	0.09	70.0			536
		2	2	2	0.333	1	0.003	0.003	0.09	180.0			536
		2	2	2	0.333	1	0.273	0.273	0.09	900.0			536
		2	2	2	0.333	1	0.408	0.408	0.09	270.0			536
		2	2	2	0.333	0.8	0.003	0.0024	0.09	270.0			536
		2	2	2	0.333	1	0.363	0.363	0.09	1400.0			536
		2	2	2	0.333	1	0.453	0.453	0.27	1900.0			536
McKenna et al. (1995a)		2	2		0.32	2	0.58	0.59	0.019	331.0	36	438	725
		2	2		0.32	3	0.58	0.59	0.187	852.0	36	438	725
		2	2		0.32	3	0.67	1	0.187	592.0	36	438	725
		2	2		0.32	3	0.67	1	0.131	262.0	36	438	725
		2	2		0.32	3	0.67	1	0.019	541.0	36	438	725
McKenna et al. (1995b)		2	2		0.8	4.5	3.8	3.8	0.424	3110.0	36	438	487
		2	2		0.8	4.9	3.8	3.8	0.141	2170.0	36	438	402
		2	2		0.8	4.9	4.24	4.24	0.141	1080.0	36	438	900
		2	2		0.8	4.9	4.24	4.24	0.141	2760.0	36	438	500
		2	2		0.8	6	3.52	3.52	0.0263	3110.0	36	438	549
		2	2		0.8	6	3.36	3.36	0.141	2440.0	36	438	738
		2	2		0.8	6	3.36	3.36	0.141	870.0	36	438	738
		2	2		0.8	4.6	3.41	3.41	0.141	2610.0	36	438	738
		2	2		0.8	4.5	3.77	3.77	0.141	3950.0	36	438	599
		2	2		0.8	3.5	3.77	3.77	0.141	1560.0	36	438	599
McKenna (1996)		2	2		0.8	3.5	1	2.154	0.07	790.0	36	438	716
		2	2		0.8	4	1	2.491	0.07	2010.0	36	438	890
		2	2		0.8	3.5	0.89	3.101	0.07	4530.0	36	438	816
		2	2		0.8	1.75	0.89	1.938	0.07	3770.0	36	438	780
		2	2		1.8	1.75	0.89	1.938	0.07	1540.0	36	438	780
		2	2		1.8	3	0.48	0.553	0.07	2540.0	36	438	685
		2	2		1.8	4	0.645	0.553	0.07	3120.0	36	438	685
		2	2		1.8	4	0.68	1.418	0.07	860.0	36	438	839
		2	2		1.8	3.5	0.68	1.831	0.07	610.0	36	438	753
		2	2		1.8	4	0.99	2.848	0.07	3520.0	36	438	753

APPENDIX C

The tables listed in this appendix are referred to in Sections 5.2 and 5.3 - Sand tests.
Table C.1 lists the test conditions and results for the sand test experiments with vertical
structures and C.2 lists those for conical structures.

Table C.1 Sand test conditions for vertical structures.

Element	Parameter	Test	Keel Shape & size	Pier Shape & size	Pier diameter mm	Keel width mm	Keel depth mm	Depth/diam	Wid/diam	Maximum force N	Dist. to max. F m
KEEL	Shape	NS01	Trap 320	Cyl 114	114	320	76	0.67	2.81	35.4	0.118
		NS02	Tria 320	Cyl 114	114	320	94	0.82	2.81	33.23	0.093
		NS03	Sin 320	Cyl 114	114	320	74	0.65	2.81	32.62	0.091
		NS04	Trap 450	Cyl 114	114	450	58	0.51	3.95	29.84	0.168
		NS05	Tria 450	Cyl 114	114	450	65	0.57	3.95	31.11	0.180
KEEL	Wid/Dia	01,20,21,3	Trap 320	Cyl 114	114	320	76	0.67	2.81	35.3	0.094
		NS06	Trap320+50	Cyl 114	114	370	76	0.67	3.25	45.92	0.106
		NS07	Trap320-100	Cyl 114	114	420	76	0.67	3.68	57.34	0.118
		NS08	Trap320-150	Cyl 114	114	470	76	0.67	4.12	59.33	0.174
		NS09	Trap320-200	Cyl 114	114	520	76	0.67	4.56	69.77	0.190
		NS10	Trap320-250	Cyl 114	114	570	76	0.67	5.00	71.68	0.221
		NS12	Trap 160	Cyl 60	60	160	38	0.63	2.67	5.2	0.043
		NS13	Trap 160+50	Cyl 60	60	210	38	0.63	3.50	7.64	0.059
		NS14	Trap 160-100	Cyl 60	60	260	38	0.63	4.33	10.56	0.077
		NS15	Trap 160-150	Cyl 60	60	310	38	0.63	5.17	11.18	0.146
		NS16	Trap 160-200	Cyl 60	60	360	38	0.63	6.00	13.37	0.173
		NS17	Trap 160+50	Cyl 60	60	410	38	0.63	6.83	12.89	0.224
		NS18	Trap 160-300	Cyl 60	60	460	38	0.63	7.67	14.02	0.209
		NS70	Trap320	Cyl 60	60	320	76	1.27	5.33	22.4	0.094
		NS71	Trap320+50	Cyl 60	60	370	76	1.27	6.17	29.84	0.122
		NS72	Trap 320-100	Cyl 60	60	420	76	1.27	7.00	35.27	0.142
		NS73	Trap 320-150	Cyl 60	60	470	76	1.27	7.83	39.84	0.167
		NS74	Trap 320-200	Cyl 60	60	520	76	1.27	8.67	44.15	0.167
		NS75	Trap 320-250	Cyl 60	60	570	76	1.27	9.50	46.16	0.241
KEEL	Dep/Dia	NS20	Trap 320/76	Cyl 114	114	320	76	0.67	2.81	33.65	0.084
		NS21	Trap320/58	Cyl 114	114	320	58	0.51	2.81	30.35	0.090
		NS22	Trap320/38	Cyl 114	114	320	38	0.33	2.81	20.22	0.098
		NS23	Trap320/19	Cyl 114	114	320	19	0.17	2.81	9.14	0.141
		NS24	Trap320/19	Cyl 60	60	320	19	0.32	5.33	4.45	0.174
		NS25	Trap320/40	Cyl 60	60	320	40	0.67	5.33	12.22	0.102
		NS26	Trap320/76	Cyl 60	60	320	76	1.27	5.33	23.76	0.094

Table C.1 Sand test conditions for vertical structures (continued).

Element	Parameter	Test	Keel Shape & size mm	Pier Shape & size mm	Pier Diameter mm	Keel width mm	Keel depth mm	Depth/diam	Widt/diam	Maximum force N	Dist. to max. F m
Structure	Shape	NS1,20,21,3	Trap 320	Cyl 114	114	320	76	0.67	2.81	35.3	0.094
		NS40	Contin 38	Cyl 114	114		38	0.33	1.40	31	0.354
		NS41	Trap 160	Sqa 114	114	160	76	0.67	2.81	7.8	0.095
		NS41a	Trap 320	Sqa 114	114	320	76	0.67	2.81	32.74	0.068
		NS42	Trap 320	Sqa 114	114	320	76	0.67	2.81	33.34	0.068
		NS43	Contin 38	Sqa 114	114		38	0.33	1.40	36.56	0.414
		NS44	Trap 160	Sqa 114	114	160	38	0.33		7.52	0.121
		NS44	Trap 320	Tria 114	114		38	0.33	2.81	31.12	0.141
		NS45	Contin 38	Tria 114	114		76	0.67	2.81	28.1	0.430
		NS46	Trap 320	Tria 114	114	320	76	0.67		31.14	0.127
	Edge	NS50	Contin 38	Sqa 114	114		38	0.33		37.28	0.4016
		NS51	Contin 38	Sqa 114	114		38	0.33		36.89	0.0803
		NS52	Contin 38	Sqa 114	114		76	0.67	2.81	34.07	0.0732
		NS53	Trap 320	Flat 228	228	320	38	0.33		52.54	0.354
		NS54	Contin 38	Flat 228	228		38	0.17	1.40	73.27	
		NS55	Contin 38	Flat 228	228		38	0.17		76.9	
		NS56	Trap 320	Flat 343	343	320	76	0.33	1.40	49.44	0.732
Effective width		NS57	Trap 320	Flat 343	343	320	76	0.22	0.93	71.58	0.0612
		NS58	Contin 38	Flat 343	343		38	0.11		110.49	
		NS59	Contin 38	Flat 343	343		38	0.11		109.3	0.29
		NS60	Trap 320	Flat 343	343	320	76	0.22	0.93	65.1	0.0548

Table C.1 Sand test conditions for vertical structures (continued).

Development of local failure Shape & size mm	Test	Pier shape & size mm	Width or diam mm	Depth mm	Depl/diam	Dist to measurement mm	Front breakout mm	Side breakout mm	Height h cyl base mm	Force N	Relative Surcharge hour	Relative F Rupture s/D	Relative S Rupture s/D	Relative Penetration Dmf/D
Contin 19	NS30a	Cyl114	114	19	0.17	74	50	26	39	5.010	0.18	0.44	0.22	0
		Cyl114	114	19	0.17	124.8	60	36	50	7.333	0.27	0.53	0.32	1.09
		Cyl114	114	19	0.17	174	68	48	57	8.025	0.33	0.60	0.42	1.53
		Cyl114	114	19	0.17	220.9	54	54	59	8.82	0.35	0.61	0.47	1.97
		Cyl114	114	19	0.17	277.5	80	60	61	9.02	0.37	0.70	0.53	2.43
		Cyl114	114	19	0.17	326.6	80	62	61	9.93	0.37	0.70	0.54	2.86
		Cyl114	114	19	0.17	375.7	80	62	61	9.44	0.37	0.70	0.54	3.30
		Cyl114	114	19	0.17	474	82	65	61	9.81	0.37	0.72	0.57	4.16
Contin 38	NS31a	Cyl114	114	38	0.33	70.5	90	15	57	13.15	0.00	0.79	0.13	0.00
		Cyl114	114	38	0.33	119.9	90	45	71	19.06	0.29	0.79	0.39	0.62
		Cyl114	114	38	0.33	171.2	108	70	80	24.01	0.43	0.88	0.61	1.05
		Cyl114	114	38	0.33	218.5	115	75	90	26.85	0.46	0.95	0.66	1.50
		Cyl114	114	38	0.33	271.8	115	80	93	28.64	0.49	0.95	0.70	1.92
		Cyl114	114	38	0.33	321.2	115	85	94	28.67	0.49	0.95	0.75	2.38
		Cyl114	114	38	0.33	370.5		85	94	28.28	0.49	1.00	0.75	2.82
		Cyl114	114	38	0.33	421.8		85	94	28.28	0.49	1.01	0.75	3.25
		Cyl114	114	38	0.33	474								3.70
Contin 40	NS34a	Cyl60/60	60	36	0.60	56.9	50	25	51	8.056	0.00	0.83	0.00	0.00
		Cyl60/60	60	36	0.60	106	78	45	66	12.1	0.43	1.30	0.75	0.95
		Cyl60/60	60	40	0.67	156.9	85	60	75	15.72	0.58	1.42	1.00	1.77
		Cyl60/60	60	40	0.67	206	90	67	81	15.94	0.65	1.42	1.12	2.67
		Cyl60/60	60	40	0.67	256.9	90	67	83	16.27	0.68	1.50	1.12	3.43
		Cyl60/60	60	40	0.67	306.9	91	68	83	16.03	0.73	1.50	1.13	4.31
		Cyl60/60	60	40	0.67	356.9				15.87	0.72	1.50		5.13
		Cyl60/60	60	40	0.67	406				16	0.72	1.52		5.95
		Cyl60/60	60	40	0.67	456.9								6.77
		Cyl60/60	60	40	0.67	506								7.62
Contin 76	NS35la	Cyl60/60	60	76	0.60	57.7	85	40	55	15.98	0.00	0.96	0.00	0.00
		Cyl60/60	60	76	1.10	107.7	110	65	85	34.9	0.52	1.42	0.67	0.96
		Cyl60/60	60	76	1.27	157.7	130	78	106	43.65	0.68	1.80	1.00	1.80
		Cyl60/60	60	76	1.27	207	135	82	117	46.14	0.78	2.17	1.25	2.63
		Cyl60/60	60	76	1.27	260.3	150	86	122	47.51	0.83	2.25	1.37	3.46
		Cyl60/60	60	76	1.27	310.3	150	90	126	50.35	0.85	2.08	1.50	4.34
		Cyl60/60	60	76	1.27	360.3			127	51.44	0.85	0.80	1.50	5.01
		Cyl60/60	60	76	1.27	410.3			127	47.08	0.87	2.50	1.50	6.01
		Cyl60/60	60	76	1.27	460.3								6.80
		Cyl60/60	60	76	1.27									7.67

Table C.1 Sand test conditions for vertical structures (continued).

Development of Keel failure

Test	Keel Shape & size (edge objects)	Pier Shape & size	Width or diam mm	Depth mm	Depth/dm	Dist to measurement mm	Front breakout mm	Side breakout mm	Height of cyl. base mm	Force N	Relative Surcharge Hsur	Relative F Rupture rfD	Relative S Rupture srD	Relative Penetn. Dist/D
NS51	Contin 38	Sqe 114	114	38	0.33	68	100	25	58	13.13	0.00	0.00	0.00	0.00
		Sqe 114	114	38	0.33	119.3	120	40	76	23.48	0.18	0.88	0.22	0.60
		Sqe 114	114	38	0.33	168.6	130	54	88	28.15	0.33	1.05	0.35	1.05
		Sqe 114	114	38	0.33	218	140	60	96	32.44	0.44	1.14	0.47	1.48
		Sqe 114	114	38	0.33	269.3	140	75	105	32.72	0.51	1.23	0.53	1.91
		Sqe 114	114	38	0.33	318.6	150	80	107	36.05	0.59	1.23	0.66	2.36
		Sqe 114	114	38	0.33	369.9	160	80	108	36.65	0.61	1.32	0.70	2.79
		Sqe 114	114	38	0.33	417.3				35.98	0.61	1.40	0.70	3.24
														3.66
NS55	Contin 38	Flat 228	228	38	0.17	73.2	105	28	58	29.57	0.09	0.46	0.12	0.21
		Flat 228	228	38	0.17	120.6	135	45	75	39.56		0.66	0.20	0.32
		Flat 228	228	38	0.17	170.6	150	55	90	48.81	0.25	0.81	0.26	0.53
		Flat 228	228	38	0.17	220.6	150	65	98	58	0.26	0.81	0.29	0.75
		Flat 228	228	38	0.17	272.3	160	65	107	67.92	0.30	0.83	0.35	0.97
		Flat 228	228	38	0.17	323.2	180	80	116	75.55	0.37	0.83		1.20
		Flat 228	228	38	0.17	373.2	190		123		0.37			1.42
														1.64
NS59	Contin 38	Flat 343	343	38	0.11	70.6	105	30	56	42.59	0.05	0.31	0.09	0.21
		Flat 343	343	38	0.11	123.2	135	45	64	64.51	0.08	0.39	0.12	0.36
		Flat 343	343	38	0.11	172.3	155	55	76	79.99	0.14	0.52	0.16	0.50
		Flat 343	343	38	0.11	221.5	170	65	85	91.92	0.13	0.54	0.18	0.65
		Flat 343	343	38	0.11	274.1	185	70	91	107.24	0.17	0.54	0.20	0.80
		Flat 343	343	38	0.11	323.2	245	75	102	107.91	0.17	0.71	0.22	0.94

Continuous Layer keel failure

Test	Keel Shape & size	Pier diameter mm	Keel depth mm	Depth/D	Dist-steady force mm	Max F N	Relative surcharge Hsur	Relative F rupture rDia	Relative S Rupture sfDia	Relative penetn. DistD
NS30	Contin 19	114	19	0.17	285.1		0.37	0.72	0.54	2.50
NS30a	Contin 19	114	19	0.17	300.2		0.37	0.61	0.63	2.63
NS31	Contin 38	114	38	0.33	354.1		0.49	1.03	0.54	3.11
NS31a	Contin 38	114	38	0.33	295.36	31.99	0.49	1.03	0.70	2.59
NS32	Contin 58	114	58	0.61	347.7	30.55	0.55	0.92	0.92	3.60
NS33	Contin 58	114	58	0.67	433.3	98	0.60	1.58	1.02	3.61
NS34	Contin 40	114	58	0.67	277.7	17.37	0.73	1.58	1.12	4.63
NS34a	Contin 40	60	40	0.67	364.2	13.66	0.84			4.92
NS35	Contin 58	60	58	0.97	400.3	33.06		1.50		6.07
NS36	Contin 76	60	76	1.27	364.2	51.67	0.85	2.50	1.50	6.07
NS36a	Contin 76	60	76	1.27	339.22	52.50		2.50	1.50	5.65

Table C.2 Sand test conditions for conical structures.

	Notes	Test	Diameter cone base Db mm	Keel width W mm	Keel depth H mm	Average diameter Dav mm	H/Dav	W/Dav	Maximum force N	Dist. to max. F m	P/Dav
Repeat tests	trap 320	con01.dat	255	320	76	203	0.374	1.575	36.4	0.165	0.812
	trap 320	con02.dat	255	320	76	203	0.374	1.575	37.3	0.184	0.905
	trap 320	con03.dat	255	320	76	203	0.374	1.575	34.9	0.157	0.774
	trap 320	con04.dat	255	320	76	203	0.374	1.575	36.5	0.179	0.881
	trap 320	con05.dat	255	320	76	203	0.374	1.575	35.8	0.154	0.759
	trap 320	con10.dat	255	320	76	203	0.374	1.575	36.6	0.147	0.724
		AVERAGE	255	320	76	203	0.374	1.575	36.2	0.164	0.809
Keel Shape	tri 320	con06.dat	255	320	94	191	0.492	1.676	35.9	0.127	0.664
	sin 320	con07.dat	255	320	74	205	0.362	1.566	37.1	0.155	0.756
	trap 460	con08.dat	255	462	58	215	0.269	2.144	32.6	0.227	1.052
	tri 460	con09.dat	255	462	65	211	0.309	2.193	36.0	0.229	1.086
Pent to Peak Force	width	con24.dat	255	244	76	203	0.374	1.201	23.9	0.148	0.729
		con21.dat	255	370	76	203	0.374	1.821	48.3	0.201	0.989
		con22.dat	255	420	76	203	0.374	2.067	55.2	0.192	0.944
		con23.dat	255	470	76	203	0.374	2.313	66.7	0.235	1.158
	depth	con30.dat	255	320	54	218	0.248	1.467	32.0	0.149	0.684
		con31.dat	255	320	34	232	0.147	1.380	21.8	0.181	0.782
		con32.dat	255	320	16	244	0.066	1.311	11.6	0.201	0.823

Table C.2 Sand test conditions for conical structures (continued).

Continuous indentation

[all measures are 4 mm high (hbu to model placement)]

con50.dat

Cone Db mm	Width W	Depth H	H/Db	Dist. to measure cm	Keel penetra. mm	Force N	r0 mm	r45 mm	r90 mm	H0 top mm	H0 cone mm	H45 mm	H90 mm
255	contin	0	0.000	0.0	-13	0.4	97.5	97.5	97.5	0	0	0	0
255	contin	43.42642	0.170	8.2	70	17.9	120	115	115	42	42	22	41
255	contin	74.25697	0.291	17.9	110	29.0	145	145	135	70	70	45	70
255	contin	76	0.298	18.1	168	42.4	210	175	140	110	100	80	62
255	contin	76	0.298	23.6	218	71.9	240	185	155	125	125	130	76
255	contin	76	0.298	33.6	273	72.9	240	195	160	148	135	130	90
255	contin	76	0.298	38.5	332	86.9	240	205	165	154	147	140	102
255	contin	76	0.298	43.4	422	92.6	245	215	170	158	153	140	115

con51.dat

Cone Db mm	Width W	Depth H	H/Db	Dist. to measure cm	Keel penetra. mm	Force N	r0 mm	r45 mm	r90 mm	H0 top mm	H0 cone mm	H45 mm	H90 mm
255	contin	0	0.000	0.0	-5	0.3	97.5	97.5	97.5	0	0	0	0
255	contin	44.55318	0.175	0.0	71	16.4	115	112	112	42	42	30	41
255	contin	51	0.200	17.6	124	28.0	175	160	160	83	65	56	70
255	contin	51	0.200	22.9	171	38.3	180	180	165	99	104	76	76
255	contin	51	0.200	27.9	224	45.2	200	190	165	128	128	104	85
255	contin	51	0.200	41.3	408	53.4	210	200	165	154	132	120	95
255	contin	51	0.200	46.3	458	55.2	230	205	180	158	133	122	99

con52.dat

Cone Db mm	Width W	Depth H	H/Db	Dist. to measure cm	Keel penetra. mm	Force N	r0 mm	r45 mm	r90 mm	H0 top mm	H0 cone mm	H45 mm	H90 mm
255	contin	0	0.000	0.0	0	0.0	97.5	97.5	97.5	0	0	0	0
255	contin	26	0.102	7.7	70	7.8	145	135	110	41	41	20	29
255	contin	26	0.102	13.9	123	14.1	160	155	115	51	51	51	45
255	contin	26	0.102	17.9	172	18.6	170	160	112	67	67	66	55
255	contin	26	0.102	23.2	225	21.5	175	165	138	81	86	71	55
255	contin	26	0.102	28.1	345	20.7	175	165	140	86	99	81	59
255	contin	26	0.102	33.2	444	24.7	180	170	150	93	104	84	60
255	contin	26	0.102	44.9	442	25.0	187	180	160	100	130	90	65

APPENDIX D

Curve fitting for measured quantities

An equation was required which could describe in closed-form the shape of the "length measurement" versus penetration curve for the structure indentation experiments in sand. The length measurements include the side and frontal rupture distances and the surcharge height (force traces were also of the same form). The boundary conditions required to fit the observed trends were:

$$P_{en} = 0 \rightarrow Y = 0$$
$$P_{en} \rightarrow \infty \rightarrow Y = constant \qquad \text{(D.1)}$$

where P_{en} is penetration from initial contact and Y is the measured length quantity as a function of P_{en}. Also, at zero penetration the curve is observed to be tangent to the $Y = 0$ line.

A geometric curve which meets these criteria is of the form:

$$Y = Amp \frac{x^2}{\left(x^2 + \left[\frac{Amp^2}{PP} - Amp^2 \right] \right)} \qquad \text{(D.2)}$$
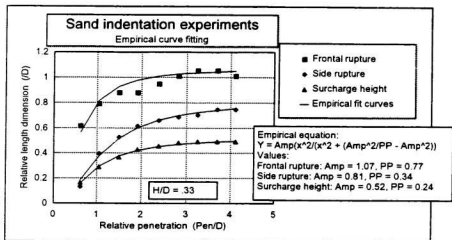
where Amp is the amplitude of the maximum asymptote line. The height of the curve at a penetration equal to Amp is PP times Amp. Thus PP defines the gradient or rate at which the curve approaches the upper asymptote.

While conducting regression analyses of the sand test results a form of the above equation was found to fit force, surcharge, and rupture distance data better than any
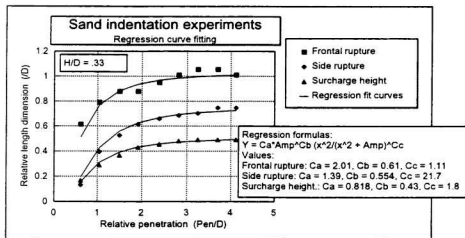
other. It was of the form:

$$Y = C_a Amp^{C_b} \left[\frac{x^2}{x^2 + Amp} \right]^{C_c} \qquad \text{(D.3)}$$

where the constants C_a, C_b and C_c were determined analytically. This equation is analogous to the pure geometric form above and retains all boundary condition qualities. Figures D.1 and D.2 illustrate the performance of the above equations for curve fitting. Arbitrarily selected for this study was an experiment in which a 114 mm diameter cylinder indented a 38 mm deep sand layer (the sand was inclined at 32° at the front). In Figure D.1 the geometric formula (Equation D.2) was fitted using trial and error. All three measured data sets, frontal rupture distance, side rupture distance and surcharge height, were studied and show strong agreement with the curve form. In Figure D.2 the formulas determined using regression analysis were applied. The quality of fit for these traces is as good as or better than the trial and error fit confirming the that the regression curve fitting procedure is a valid one.

Figure D.1 Curve fitting using basic geometric formula.

Sand indentation experiments
Empirical curve fitting

- Frontal rupture
- Side rupture
- Surcharge height
- Empirical fit curves

Empirical equation:
$Y = Amp \cdot x^2/(x^2 + (Amp^2/PP - Amp^2))$
Values:
Frontal rupture: Amp = 1.07, PP = 0.77
Side rupture: Amp = 0.81, PP = 0.34
Surcharge height: Amp = 0.52, PP = 0.24

H/D = .33

Relative length dimension (l/D)
Relative penetration (Pen/D)

Figure D.2 Curve fitting using regression analysis.

Sand indentation experiments
Regression curve fitting

- Frontal rupture
- Side rupture
- Surcharge height
- Regression fit curves

Regression formulas:
$Y = Ca \cdot Amp \cdot Cb \ (x^2/(x^2 + Amp))^{Cc}$
Values:
Frontal rupture: Ca = 2.01, Cb = 0.61, Cc = 1.11
Side rupture: Ca = 1.39, Cb = 0.554, Cc = 21.7
Surcharge height.: Ca = 0.818, Cb = 0.43, Cc = 1.8

H/D = .33

Relative length dimension (l/D)
Relative penetration (Pen/D)

Appendix E

Passive earth pressure (Jumikis 1984, Bowles 1984)

Lateral earth pressure is the force which is exerted by a soil mass acting upon an earth retaining structure, for instance a retaining wall. The *passive* earth pressure indicates the maximum value of the force which can develop upon the motion of the retaining structure towards the earth mass - a force which the soil must resist before it ruptures. The surface upon which the broken-away or sheared off soil slides is termed the *rupture*, or *sliding* surface.

The magnitude of passive earth pressure can be solved graphically or determined analytically using Coulomb's earth pressure theory. According to Coulomb's theory for a frictional soil, passive force per unit length of wall is calculated by means of the following equation:

$$F = \int_0^H K_p \gamma z \, dz = \frac{1}{2} \gamma H^2 K_p \qquad \text{(E.1)}$$

where F is the maximum horizontal force on the structure, γ is the unit weight of the backfill, H is the height of wall on which the soil acts, z is vertical position below surface, and K_p is the dimensionless passive earth pressure coefficient.

Consideration of the stress condition in soil shows that cohesion, c, of a (ϕ-c) soil does not affect the position of the rupture surface. Hence the earth pressure of a cohesive (ϕ-c) soil can be approximately determined by the method used for non-cohesive soils. On this basis the total passive pressure F of a ϕ-c soil per unit length is

$$F = \frac{1}{2}\gamma H^2 K_p + 2cH\sqrt{K_p} \qquad (E.2)$$

When a uniform surcharge acts on the soil backfill the effect is taken care of analytically by modifying the unit weight of soil ($\gamma_{new} = \gamma_{old} + \gamma_{sur}$).

For earth pressure systems where the structure is sloped and there is a non-zero soil-structure friction angle, the solution for K_p may be determined by a static equilibrium of the forces acting on the ruptured soil wedge as shown in Figure E.1. The system of two equations for calculating the unknowns ω (rupture angle) and F is

$$F = \left[w \frac{\sin(\omega + \phi)}{\sin(\xi + \omega + \phi)} \right]_{min} \qquad (E.3)$$
$$\frac{dF}{d\omega} = 0$$

where ϕ is the soil internal friction angle, ϕ_l is the soil-structure friction angle, α is the structure slope from vertical, $\xi = 90° - \alpha + \phi_l$ and w is the weight of the soil wedge:

$$w = \frac{1}{2}\gamma H^2 \left(\frac{\cos(\delta - \alpha)}{\cos^2\alpha} \right) \left(\frac{\cos(\omega - \alpha)}{\sin(\omega - \delta)} \right) \qquad (E.4)$$

where δ is the slope of the soil surface. Jumikis (1984) has determined a general closed-form solution for this two equation system which yields:

$$K_p = \frac{\cos^2(\phi + \alpha)}{\cos^2\alpha \cos(\alpha - \phi_l) \left[1 - \sqrt{\frac{\sin(\phi + \phi_l)\sin(\phi + \delta)}{\cos(\alpha - \phi_l)\cos(\delta - \alpha)}} \right]^2} \qquad (E.5)$$

and reduces to the more familiar form of K_p for vertical frictionless structures in level soil:

$$K_p = \frac{1 + \sin\phi}{1 - \sin\phi} = \tan^2\left[\frac{\pi}{4} + \frac{\phi}{2}\right] \qquad \text{(E.6)}$$

In cases where backfill is sloped in a discontinuous or curved manner a solution for K_p may be found by a lengthy graphical plotting procedure. Otherwise an approximation of the would-be linear slope, δ, that preserves the weight of the mobilized soil block (w) and the height of the soil at the wall (H_{sur}) has been approximated (in the formulation for K_p above, δ only influences w in the force equilibrium). In the vertical structure case where the slope was discontinuous as shown in Figure E.2, the slope approximation was determined as

$$\delta = atan\left[\frac{H_{sur}}{2r}\right] \qquad \text{(E.7)}$$

In the sloping (conical) structure case where backfill was sloped in the form of a cosine curve as shown in Figure E.3 the slope was approximated as

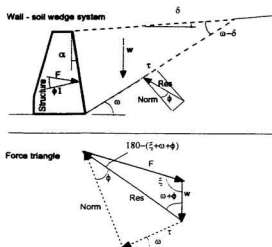$$\delta = atan\left[\frac{H_{sur}}{m4/\pi}\right] \qquad \text{(E.8)}$$

Figure E.1 Force equilibrium for passive earth pressure (Jumikis, 1984).
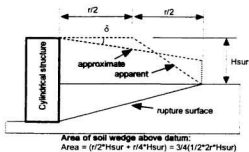

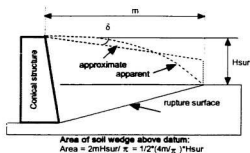**Figure E.2** Surface slope approximation for vertical structure indentation.

Figure E.3 Surface slope approximation for conical structure indentation.

Appendix F

Cone force model notes

Effective weight

The effective rubble weight utilized in the cone load approximation model reflects the probable stress distribution in the region of failure. Typically surcharge is dealt with in passive earth pressure problems by adjusting the effective weight of the soil mass (Jumikis, 1984). A surcharge may be considered a heavy, very thin layer of soil on top of soil body. When ice rubble is failed upwards by a cone which extends below the water the submerged rubble effect is analogous to adding a negative surcharge to the base of the rubble layer. The problem with applying the usual surcharge correction is that it does not recognise the depth over which the buoyant rubble acts. As a result an alternate technique has been applied. An effective stress distribution has been assumed where

$$\gamma_{\text{eff}} = 9.81 \left[\frac{\rho_s H_s + \rho_k (H - H_{wl})}{2(H_s + H_{wl})} \right] \qquad \text{(F.1)}$$

representing a linear distribution which has a maximum stress equal to the average of the maximum sail stress at waterline and the rubble stress at the cone base as shown in Figure F.1.

Sail geometry

The development of surcharge on the cone in the IMD laboratory (described in Chapter 6, Section 2) has been approximated using the results of the sand tests. In the sand tests trapezoidal sails were indented. The developed surcharge height was modelled

analytically with great success using regression techniques with a preselected geometric equation (Appendix D). Thus the sails in the IMD tests have been analytically transformed to a trapezoidal shape which preserves the original sail width and area but adjusts the height. This is reflected in Figure F.2. Note that the trapezoidal sail approximation is used for the computation of cone surcharge height only.
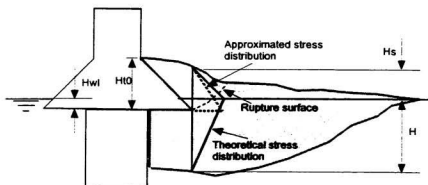
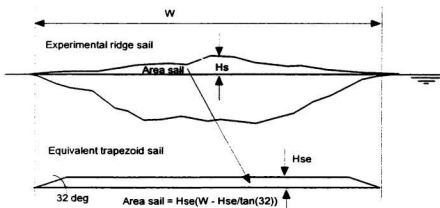**Figure F.1** Effective weight of rubble for cone force model.

Figure F.2 Trapezoidal sail approximation.